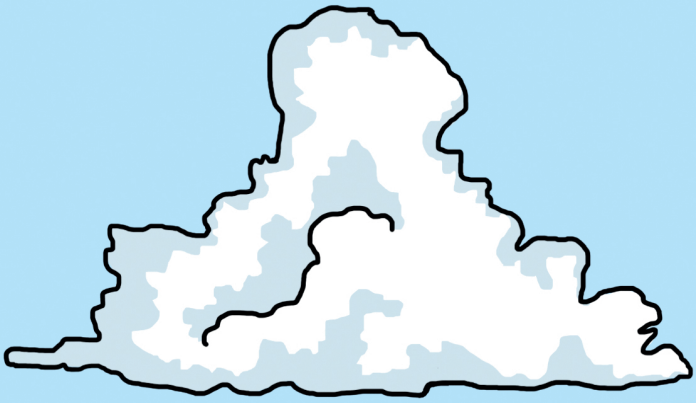


# BETWEEN STOMATA AND CLOUDS

Unveiling vegetation–atmospheric boundary layer interactions with high resolution observations and modeling

Raquel González Armas



## Propositions

1. Within-canopy air properties govern ecosystem responses.
   (this thesis)

2. Vegetation measurements require more effort than atmospheric measurements.
   (this thesis)

3. Idealized conceptual models are as valuable as complex realistic models.

4. Marketing language undermines scientific integrity.

5. Leisure is not a privilege.

6. Perfectionism is a poor strategy to attain excellence.

Propositions belonging to the thesis entitled

**Between stomata and clouds: Unveiling vegetation-atmospheric boundary layer interactions with high resolution observations and modeling**

Raquel González Armas
Wageningen,
1 July 2026

# Between stomata and clouds: Unveiling vegetation-atmospheric boundary layer interactions with high resolution observations and modeling

Raquel González Armas

**Thesis committee**

**Promotors**
Prof. Dr J. Vilà-Guerau de Arellano
Professor of Meteorology
Wageningen University & Research

Prof. Dr H. J. de Boer
Professor of Geoscience
Utrecht University

**Other members**
Prof. Dr K. M. de Beurs, Wageningen University & Research
Dr F. Lohou, University Paul Sabatier, France
Dr L. Nuijens, Delft University of Technology
Prof. Dr K. Rebel, Utrecht University

This research was conducted under the auspices of the Graduate School for Socio-Economic and Natural Sciences of the Environment (SENSE)

# Between stomata and clouds: Unveiling vegetation-atmospheric boundary layer interactions with high resolution observations and modeling

Raquel González Armas

**Thesis**
submitted in fulfilment of the requirements for the degree of doctor at
at Wageningen University
by the authority of the Rector Magnificus,
Prof. Dr C. Kroeze,
in the presence of the
Thesis Committee appointed by the Academic Board
to be defended in public
on July 1, 2026
at 3:30 p.m. in the Omnia Auditorium.

Raquel González Armas
Between stomata and clouds: Unveiling vegetation-atmospheric boundary layer interactions with high resolution observations and modeling
xii+213 pages.

PhD thesis, Wageningen University, Wageningen, NL (2026)
With references, with summary in English and Spanish

DOI https://doi.org/10.18174/681656

# Summary

Vegetation covers a large proportion of the world's land. On those areas, vegetation and atmosphere interact by exchanging energy, heat, water vapor, carbon dioxide ($CO_2$), and other chemical compounds. These interactions importantly alter both the state of the vegetation and the state of the lower atmosphere, the so-called atmospheric boundary layer. While these interactions have been studied for many years, challenges on its understanding and representation in Earth system models still abound. A major challenge is reducing the current uncertainties on the exchanges of energy and matter, which requires the study of the vegetation and atmosphere as a coupled and continuum system. To meet that goal, research approaches need to represent the relevant biophysical processes across scales and scientific disciplines.

In this thesis, we contribute to the understanding of vegetation-atmosphere interactions by linking leaf-scale ecophysiology, canopy microclimate, turbulence, radiation, and cloud processes within a unified diurnal and multi-scale framework. We do so by conducting studies that combine comprehensive observational datasets and modeling approaches at kilometric spatial scales. In terms of observations, we participated in field campaigns in three diverse ecosystems: an agricultural alfalfa field (La Cendrosa site, Spain), a tropical Amazon rainforest site (ATTO site, Brazil), and a temperate forest site (Loobos site, The Netherlands). Studying multiple sites enabled us to investigate the vegetation-atmosphere interactions across canopy structures and atmospheric regimes. To investigate the interactions, we used multiple model approaches: (1) a conceptual atmospheric mixed-layer model (CLASS model) which is structurally analogous to a grid cell in a global Earth system model, (2) a multi-layer canopy scheme which captures vertical variability often neglected in land-surface schemes, and (3) a canopy-resolving Large-Eddy Simulation model (can-DALES model) which attains high realism by explicitly solving air transport within and above canopies.

As a first step, **Chapter 2** examines how four canopy environmental variables - photosynthetically active radiation (PAR), vapor pressure deficit (VPD), air temperature (T), and atmospheric $CO_2$ concentration ($C_a$) - control leaf level and canopy-scale exchanges of water and $CO_2$. Our objective was to understand the influence of atmospheric conditions on stomatal regulation, photosynthesis, and transpiration at the leaf level, and to assess how these responses propagate to the ecosystem scale. To this end, we develop a mathematical framework that quantifies how leaf level exchange processes depend explicitly on atmospheric drivers. Results revealed that the diurnal evolution of stomatal regulation, photosynthesis, and tran-

spiration was primarily governed by PAR, T, and VPD, with $C_a$ minimally contributing. The framework enabled us to disentangle interactions between the atmospheric boundary layer and the vegetation. For example, we could differentiate how cloud shading reduced $CO_2$ assimilation through both diminished radiation and associated temperature decreases. As such, the proposed framework proved a useful tool to analyze temporal vegetation exchange dynamics in weather and climate models.

In **Chapter 3**, we investigated the diurnal and vertical variability of forest microclimate, transpiration and $CO_2$ assimilation for a tropical Amazon forest. Building on the temporal perspective of Chapter 2, this chapter introduces vertical variability within the canopy as a key dimension controlling ecosystem exchange. The study integrates (1) observations acquired in a tropical Amazon forest, and (2) a multi-layer canopy approach which is driven by the acquired measurements, during a cloudy day. We found distinctive observed vertical profiles of leaf traits and microclimate, which were maintained during most of the daytime. In particular, we found a persistent inversion of temperature within the canopy, which hindered air mixing between the upper third of the canopy and the lower layers. The modeling approach revealed that the forest transpiration and $CO_2$ assimilation was dominated by the dynamics of the upper third of the canopy. Differences between the modeled $CO_2$ assimilation and the observed $CO_2$ surface transport underscored the importance of $CO_2$ storage and ventilation events within the canopy, particularly during the morning.

In **Chapter 4**, we focused on a key microclimatic factor for ecosystem fluxes, radiation. Solar shortwave radiation drives the surface heating and the evapotranspiration, while a part of it, the PAR radiation, controls the photosynthesis. In turn, longwave radiation emitted by the vegetation, soil and sky regulates air and canopy temperatures. In this chapter, we investigated how radiation is transmitted through the vegetation by improving and evaluating a canopy radiative transfer scheme for a canopy-resolving Large-Eddy Simulation model. The scheme simulates shortwave and longwave radiation, and make the important step of accounting for the plant preferential use of radiation by resolving four shortwave spectral bands: ultraviolet (280-400 nm), PAR (400-700 nm), far-red (700-750 nm), and near infrared (750-4000 nm). We also explored how the shortwave radiative transfer varied depending on external forcings, related to the sun position and the direct and diffuse proportion of solar radiation, and on internal canopy factors, related to the leaf biomass and its distribution across the canopy. Results showed that the scheme reproduced spectral differences in canopy reflectance and vertical profiles of the radiative fluxes. The canopy radiative transfer scheme now enables the investigation of the effect of ultraviolet and far-red radiation on photosynthesis and surface fluxes.

In **Chapter 5**, we explored the forest-atmosphere interactions by integrating four interconnected aspects of the coupled system: forest microclimate, leaf-scale fluxes, ecosystem-scale fluxes, and the clear-to-cloudy boundary-layer transition. To that end, we combined (1) observations acquired in a tropical Amazon forest and (2) a canopy-resolving Large-Eddy Simulation. This work builds upon the previous chapters by simultaneously linking, at diurnal scales, leaf ecophysiology, vertical structured canopy microclimates, and detailed ra-

diative canopy transfer with canopy-scale and atmospheric boundary layer-scale turbulence. Additionally, to our knowledge, this study reports the first canopy-resolving Large-Eddy Simulation which includes boundary layer clouds. The simulation results validated well for the four themes, demonstrating its realism. The simulation reproduced a stable air layer within the canopy which expanded and shrunk following a diurnal cyle, and which affected the storage and ventilation of within canopy air. Furthermore, the simulation captured the transition from clear sky to a shallow-cumulus regime while resolving canopy-scale turbulence that modulates the surface forcings. This study paves the way to future studies regarding radiative and turbulent vegetation-cloud feedbacks.

In **Chapter 6**, we analyzed the diurnal variability of carbon cycle tracers ($CO_2$, $O_2$, and $\delta^{13}C$-$CO_2$) in a tropical Amazon forest site and a temperate forest site. Carbon cycle tracers are often used to infer information about the biosphere by tracking the movement of carbon between the atmosphere and land. To contribute to interpret the atmospheric signals of the carbon cycle tracers, we focused on determining which (surface or atmospheric) processes are responsible for their diurnal variability. For doing so, we employed both (1) observations and (2) numerical experiments performed by the CLASS model. We calculated the diurnal range of the carbon cycle tracers and quantified the contribution of surface and atmospheric processes to that range. Results revealed the importance of atmospheric processes, namely entrainment of free tropospheric air, subsidence, and cloud ventilation, in shaping the diurnal variations of the carbon cycle tracers. The findings underscored the utility of using the diurnal range as a metric to evaluate atmospheric tracer transport models.

Finally, **Chapter 7** synthesizes the key findings of Chapters 2-6, placing them into context and identifying future research opportunities and practical applications. Future research directions include extending this work to nighttime conditions; deepening the exploration of turbulent and radiative vegetation-cloud feedbacks; incorporating horizontal heterogeneity in vegetation structure; investigating interactions during and after precipitation events; and including particles emitted by vegetation that act as cloud condensation nuclei.

In conclusion, this thesis shows that vegetation-atmosphere interactions are mediated by a tight coupling between canopy ecophysiology, microclimate, turbulence, and cloud processes, operating across leaf, canopy, and atmospheric boundary layer scales, and evolving strongly over the diurnal cycle. By combining comprehensive observational datasets with modeling approaches, this dissertation highlights the importance of understanding and representing diurnal and vertical variability within and above canopies when studying land-atmosphere exchange. The results underscore the potential of canopy-resolving approaches to bridge ecosystem-scale processes and atmospheric dynamics, offering new ways to improve the physical realism of land-surface schemes in Earth system models.

# Resumen

La vegetación ocupa una gran proporción de la superficie terrestre. En esas áreas, vegetación y atmósfera interaccionan intercambiando energía, calor, vapor de agua, dióxido de carbono y otros compuestos químicos. Estas interacciones alteran tanto el estado de la vegetación como el de la parte inferior de la atmósfera, conocida por el nombre de capa límite atmosférica. Aunque estas interacciones han sido estudiadas a lo largo de décadas, todavía existen retos en cuanto a su comprensión y descripción en modelos atmosféricos y climáticos. Un gran reto existente es reducir la incertidumbre en las estimaciones de intercambios de energía y materia entre la vegetación y la atmósfera. Para afrontarlo, es necesario estudiar la vegetación y atmósfera como un sistema acoplado y continuo, lo cual solo es posible mediante la integración de procesos biofísicos a diferentes escalas espaciales.

En esta tesis doctoral, contribuimos a la comprensión y a una mejor representación de las interacciones entre vegetación y atmósfera a través de integrar la ecofisiología de las hojas, los microclimas de la vegetación, la turbulencia atmosférica, la radiación, y los procesos asociados a las nubes. Todo ello es estudiado bajo un marco metodológico que combina observaciones y modelos a escala diurna. En cuanto a observaciones, hemos participado en campañas de campo en tres ecosistemas diversos: un campo agrícola de alfalfa (La Cendrosa, España), un bosque tropical amazónico (ATTO, Brazil), y un bosque templado (Loobos, Países Bajos). El estudio de múltiples lugares nos permitió investigar las interacciones en diferentes estructuras de follaje y bajo diferentes condiciones atmosféricas. Para investigar las interacciones, usamos múltiples modelos: (1) un modelo conceptual de la capa límite (modelo CLASS), el cual es análogo a una celda de un modelo atmosférico global, (2) un modelo de superficie multi-capa, el cual captura la variabilidad vertical en bosques, y (3) una simulación de flujos turbulentos (can-DALES) que resuelve el transporte turbulento tanto dentro como encima del bosque a la vez que simula nubes bajas.

En un primer acercamiento a la materia, el **Capítulo 2** examina cómo cuatro variables atmosféricas - la radiación fotosintéticamente activa, la humedad, la temperatura, y el dióxido de carbono atmosférico - regulan los intercambios de agua y dióxido de carbono a las escalas de hoja y de ecosistema. El objetivo de este estudio era dual. Por una parte, queríamos incrementar nuestra comprensión de la influencia de las condiciones atmosféricas en la regulación de los estomas (poros superficiales de las hojas), de la fotosíntesis y la transpiración de agua a nivel de hoja. Por otra parte, queríamos evaluar cómo estas respuestas a nivel de hoja se propagaban a nivel del ecosistema. Con este fin, desarrollamos un modelo matemático que

cuantifica el grado en el que los intercambios a nivel de hoja dependen de las variables atmosféricas. Los resultados revelaron que la evolución diurna de la apertura de los estomas, la fotosíntesis, y la transpiración dependía primordialmente de la radiación fotosintéticamente activa, la humedad, y la temperatura, mientras que la dependencia con el dióxido de carbono era mínima. Este estudio también nos permitió distinguir diferentes procesos en las interacciones entre vegetación y atmosféra. Por ejemplo, pudimos cuantificar cómo la presencia de nubes disminuía la absorción de carbono de la vegetación mediante dos procesos que ocurren simultáneamente: la reducción de radiación, y la reducción de temperatura. A modo de conclusión, los métodos desarrollados en este capítulo demostraron ser útiles para analizar tendencias temporales en las dinámicas de la vegetación en modelos atmosféricos.

En el **Capítulo 3**, investigamos la variabilidad diurna y vertical del microclima forestal, la transpiración y la asimilación de dióxido de carbono en un bosque tropical amazónico. Basándonos en la perspectiva temporal adquirida en el Capítulo 2, en este nuevo capítulo introducimos la variabilidad vertical dentro del bosque como un factor clave en la regulación de los intercambios de energía y materia. Este estudio integra: (1) observaciones de un bosque tropical amazónico, y (2) un modelo multi-capa del bosque, durante un día nuboso. Las observaciones revelaron variaciones verticales tanto en características de las hojas como en el microclima. Las variaciones en el microclima se mantuvieron a lo largo del día. En concreto, las observaciones mostraban un inversión térmica persistente dentro del bosque, la cual impedía que el aire de la parte inferior del bosque se mezclase con el aire de la parte superior. El modelo reveló que la parte superior del bosque era la que más contribuía a la transpiración de agua y la asimilación de dióxido de carbono. Basándonos en las diferencias entre las observaciones y el modelo, descubrimos la importancia del almacenamiento de dióxido de carbono dentro de la foresta y de su posterior ventilación.

En el **Capítulo 4**, nos centramos en una factor ambiental clave para los ecosistemas, la radiación. La radiación de onda corta (280-4000 nm) controla el calentamiento de la superficie y del aire adjacente, y la transpiración. Además, una parte de la radiación de onda corta, la radiación fotosintéticamente activa (400-700 nm), determina la fotosíntesis. Por otro lado, la radiación de onda larga (3-100 $\mu$m), la cual es emitida por la vegetación, el suelo, y el cielo, regula las temperaturas de la superficie. En este capítulo, investigamos como la radiación es transmitida a través de la vegetación. Por ese motivo, desarrollamos y evaluamos un modelo de transferencia radiativa a través de la vegetación para un modelo de simulación de flujos turbulentos. El modelo desarrollado simula la transferencia de radiación de onda corta y larga, realizando la importante contribución de incluir el uso preferencial de la radiación por parte de la vegetación. Para ello, simulamos cuatro bandas espectrales de radiación de onda corta: la radiación ultravioleta (280-400 nm), la radiación fotosintéticamente activa, la radiación roja lejana (700-750 nm), y la radiación infrarroja cercana (750-4000 nm). En este estudio, exploramos cómo la transmisión de radiación a través de la vegetación varía dependiendo de factores estructurales de la vegetación y de factores atmosféricos. Los resultados revelaron que el modelo era capaz de reproducir la diferencias entre bandas espectrales y los perfiles verticales característicos del ambiente radiativo de los bosques. Este nuevo modelo permite investigar los efectos de la radiación ultravioleta y la radiación roja lejana en la

fotosíntesis y en los flujos de superficie.

En el **Capítulo 5**, estudiamos las interacciones entre vegetación y atmósfera integrando cuatro temas interconectados del sistema: el microclima forestal, los flujos a nivel de hoja, los flujos a nivel de ecosistema, y la capa límite atmosférica. Con ese fin, combinamos: (1) observaciones de un bosque tropical amazónico y (2) una simulación de flujos turbulentos que representa el bosque. En este capítulo combinamos las herramientas adquiridas con anterioridad a través de integrar simultáneamente la ecofisiología de la hoja, la variabilidad vertical del microclima del bosque, y la transferencia radiativa dentro del bosque con un nuevo elemento, la turbulencia atmosférica. Además, este estudio es, según tenemos entendido, el primer estudio que incluye una simulación de flujo turbulento que simula tanto nubes como el transporte de aire dentro de la vegetación de manera acoplada. Los resultados de la simulación representaron las observaciones para los cuatro temas, demostrando el realismo de la simulación. La simulación representó una capa estable de aire dentro del bosque, la cual se expandía y reducía a lo largo del ciclo diurno. Esta capa estable influía en el almacenamiento y ventilación del aire dentro del bosque. A parte de esto, la simulación pudo representar la evolución de las nubes a la vez que representaba la turbulencia cerca y dentro del bosque con exactitud. Este estudio supone una contribución a futuras investigaciones sobre las interacciones turbulentas y radiativas entre vegetación y atmósfera.

En el **Capítulo 6**, analizamos la variabilidad diurna de marcadores del ciclo de carbono ($CO_2$, $O_2$, y $\delta^{13}$C-$CO_2$) en un bosque tropical amazónico y en un bosque templado. Los marcadores del ciclo del carbono son usualmente utilizados para inferir información sobre la biosfera, a través de rastrear el movimiento del carbono entre la atmósfera y la superficie terrestre. Para contribuir a la interpretación de las señales atmosféricas de estos marcadores, nos centramos en determinar qué procesos (atmosféricos o superficiales) gobernaban su ciclo diurno. Para ello, empleamos tanto (1) observaciones como (2) experimentos numéricos realizados con el modelo CLASS. Determinamos el rango diurno de los marcadores y cuantificamos cuánto de ese rango era debido a procesos superficiales y cuánto a procesos atmosféricos. Los resultados revelaron la importancia de los procesos atmosféricos, entre ellos: la entrada de aire troposférico, la subsidencia, y la ventilación de aire creada por las nubes. Este estudio destaca la utilidad de usar los rangos diurnos para evaluar modelos atmosféricos.

Finalmente, en el **Capítulo 7** sintetizamos las conclusiones de los Capítulos 2-6, poniéndolas en contexto e identificando futuras oportunidades de investigación y de aplicaciones prácticas. Futuros caminos de investigación son: la extensión de este trabajo a condiciones nocturnas, el profundizar en las interacciones radiativas y turbulentas entre vegetación y atmósfera, el incorporar variabilidad horizontal en la estructura de los bosques, y el incluir procesos biofísicos como las interacciones con lluvia o con aerosoles emitidos por la vegetación.

En conclusión, esta tesis demuestra que las interacciones entre vegetación y atmósfera están mediadas por un acoplamiento entre la ecofisiología de la vegetación, el microclima forestal, la turbulencia, y las nubes. Dicho acoplamiento varía fuertemente a lo largo del ciclo diurno. Combinando observaciones y modelos, este trabajo científico destaca la importancia de tener en cuenta la variabilidad diurna y vertical dentro y encima de la vegetación

cuando se estudian las interacciones entre vegetación y atmósfera. La tesis también resalta el potencial de las simulaciones de flujo turbulento para conectar los procesos biofísicos de los ecosistemas terrestres y las dinámicas atmosféricas. Estos modelos pueden constituir una útil herramienta para el mejoramiento de las representaciones superficiales en otros modelos atmosféricos.

# Contents


Page

Summary v

Resumen ix

Chapter 1 General introduction 1

Chapter 2 Diurnal dynamics of water and carbon dioxide exchange at leaf and canopy levels 17

Chapter 3 Microclimate, and water and carbon dioxide exchange within and above a forest 51

Chapter 4 Radiative transfer within vegetation canopies 85

Chapter 5 Forest-atmosphere coupling in cloudy conditions revealed by canopy-resolving large eddy simulations and observations 115

Chapter 6 Diurnal evolution of the carbon cycle tracers 147

Chapter 7 Synthesis 177

References 191

Acknowledgements 209

List of publications 211

About the author 213

# Chapter 1

# General introduction

## 1.1 Motivation

Vegetation covers approximately 72 % of the world's land (Latham et al., 2014). Over these vegetated areas, plant canopies crucially influence the atmospheric physics and chemistry, modifying wind speeds and turbulent structures, surface energy fluxes, water evapotranspiration, and the exchange of other chemical compounds such as $CO_2$ and volatile organic compounds (Finnigan et al., 2009; Williams & Torn, 2015; Artaxo et al., 2022; Fehsenfeld et al., 1992). Through these influences, the vegetation can also impact on atmospheric convective regimes, affecting the onset and evolution of low clouds. In turn, the lower atmosphere, in which the vegetation is embedded, provides environmental conditions that regulate the vegetation biology. The surface solar radiation, air temperature, humidity, $CO_2$ concentration, and wind, all impact vegetation biological processes, altering plant photosynthesis and water transpiration. Given the strong connections between vegetation and atmosphere (McPherson, Jun 2007), representing land-atmosphere interactions has been and continues to be a priority on global, regional, and high resolution Earth system models (Bonan, 2008; Santanello et al., 2018).

Yet, challenges on the representation and understanding of vegetation-atmosphere interactions still abound. Substantial discrepancies between observed and modeled exchanges of heat, water, and $CO_2$ still remain (Holtslag et al., 2013; Best et al., 2015; Renner et al., 2021), hindering our capacity of foreseeing how the interactions will evolve under a changing climate. Representing and quantifying the vegetation-atmosphere interactions is challenging as it requires the integration of many biophysical processes across scales. This integration of biophysical processes is often hindered by the lack of detailed observations that enable us to characterize the vegetation. An example of this occurs at small spatial scales, where land-surface models need to represent the stomatal regulation of the leaf gas exchange. In that regard, leaf gas exchange measurements are key to test the land-surface models (Bonan et al., 2026). Nonetheless, many land-surface model evaluations lack leaf gas exchange measurements because they are labor-intensive and typically limited to short time periods.

Apart from observational scarcity, our understanding and representation of vegetation-atmosphere interactions is also hampered by the omission of some biophysical processes in model formulations. A clear example is the simplification of the vertical-dimension of vegetation canopies in land-surface schemes. The prevailing strategy of land-surface models has been to represent vegetation canopies as a bulk layer, simplifying their rich vertical structure in terms of microclimate and vegetation features. This view is slowly shifting as land-surface models incorporating vertical structure are proving to provide accurate results while improving the physical representation (Bonan et al., 2021). Although not yet widely used, multi-layer land-surface approaches are opening up new possibilities to understand and represent land-atmosphere interactions. For instance, they encourage us to explore beyond the surface exchanges and to investigate further the processes taking place within the canopy (Bonan et al., 2026). Representing within canopy air fosters an holistic view of the vegetation-atmosphere system, as it tightly couples the plant ecophysiology with its immedi-

ate atmospheric environment.

Another challenge in the understanding of vegetation-atmosphere interactions is the representation of the influence of clouds. Clouds are ubiquitous over land, covering approximately 60 % of the Earth's land surface at any given moment (Chi et al., 2024). They alter the radiation reaching the surface, introducing horizontal heterogeneity in form of shading and radiation enhancements, and modifying the amount of direct and diffuse radiation (Mol et al., 2024). These cloud-induced radiative perturbations cause rapid changes in temperature and humidity, which together modify the surface energy fluxes, canopy $CO_2$ assimilation, and evapotranspiration. Apart from radiative perturbations, clouds also alter the state of the atmosphere by modifying atmospheric transport or by precipitating water, which eventually impacts the state of the vegetation. Despite the relevance of clouds in land-atmosphere interactions, cloud-vegetation feedbacks are often underexplored due to a lack of spatially extended network of observations and a lack of simultaneous detailed representation of both vegetation and clouds (Vilà-Guerau de Arellano et al., 2023). These cloud-vegetation feedbacks are relevant in climate change scenarios, in which elevations in air temperature and $CO_2$ affect plant ecophysiology in non-linear manners (Sikma et al., 2019). The non-stationary nature of these interactions further amplifies the need for process-based investigations of the vegetation-atmosphere coupling.



We argue that to improve our representation of vegetation-atmosphere interactions we need detailed studies which represents biophysical processes across scales (from leaf to ecosystem to the atmospheric boundary layer) and which combine high quality model and observations under clear sky and cloudy conditions. That specific niche is what we intend to provide in this thesis. In particular, we attempt to gain understanding of vegetation-atmosphere interactions at the diurnal and the kilometric temporal and spatial scales.

> The aim of this thesis is to investigate, describe and quantify how coupled biophysical and atmospheric processes regulate the interactions between the vegetation and the atmospheric boundary layer over the diurnal cycle, with a particular focus on leaf ecophysiology, canopy microclimate, turbulence, radiation and shallow-cumulus clouds.

We consider that the diurnal cycle is a natural laboratory where we can observe how the vegetation and atmosphere interact. The diurnal cycle is a dominant mode of land-atmosphere interactions because many of the involved processes operate at this scale. The diurnal solar cycle regulates the Earth's surface fluxes, controlling plant photosynthesis, and surface heating which triggers convection and mixing of air throughout the lower part of the atmosphere. Models often misrepresent the timing and strength of diurnal processes, such as the diurnal signature of surface fluxes. These errors can, in principle, cascade into biases at larger temporal scales and, for example, provide erroneous low cloud cover or precipiation patterns. Athough other temporal and spatial scales also play a role on the biospheric processes, they are out of the scope of this dissertation. Nonetheless, we consider that the process under-

standing provided in this thesis can be extended and used at larger temporal and spatial scales.

In this dissertation, we aim at deepening our understanding of vegetation-atmosphere interactions thanks to comprehensive observational field campaigns and a hierarchy of modeling approaches. The approach we adopt is based on first principles, meaning that we attempt to break down the complexity of the vegetation-atmosphere system on foundational building blocks that can afterwards be combined. As such, this dissertation constitutes a bottom-up initiative to understand the interactions between vegetation and atmosphere. In the following section, we define and introduce the system under study, laying the basis and terminology that are used throughout this dissertation. Afterwards, we present the methodological approach used in this thesis, introducing the observational and modeling strategy. We finalize this chapter with an outline of the content of the thesis, highlighting the individual but complementary objectives that each content chapter (Chapters 2, 3, 4, 5, and 6) addresses.

## 1.2 The soil-vegetation-air-cloud continuum: a coupled system

Soil, vegetation, air, and clouds interact with each other by exchanging energy, momentum, water, $CO_2$, and other chemical species. These four elements and their interactions compose our object of study, the "coupled system" which we describe in this section. In the following sections we lay down the main concepts and terms that compose the different subsystems: the land (composed by the soil and vegetation), the air, and the clouds.

### 1.2.1 The land: soil and vegetation

Over our study areas, the land surface is comprised by the soil and the vegetation atop. The soil is a thin outer layer of the Earth which is composed by minerals, organic matter, water, air, and countless organisms, and which also provides the substrate for vegetation to grow. The vegetation comprises the collective plant life that covers the surface, including diverse plant types such as trees, shrubs, grasses, crops, lianas, etc. The vegetation also shelters the soil below, protecting it from erosion, enhancing soil structure, decreasing the radiation reaching the soil, and buffering soil temperatures.

Both vegetation and soil exchange matter and energy with the atmosphere. In terms of energy, the energy available at the surface - which is a balance of the solar, sky and terrestrial radiation - is transferred through the vegetation-atmosphere system in diverse ways. Part of it is transferred to deeper layers of the soil and vegetation, whereas the rest is transferred to the atmosphere by heating the adjacent air layer ("sensible heat"), or by evaporating water ("latent heat"). How much of the energy is transformed into sensible heat or into latent heat is determined by surface properties. Over vegetated areas, the latent heat flux tends

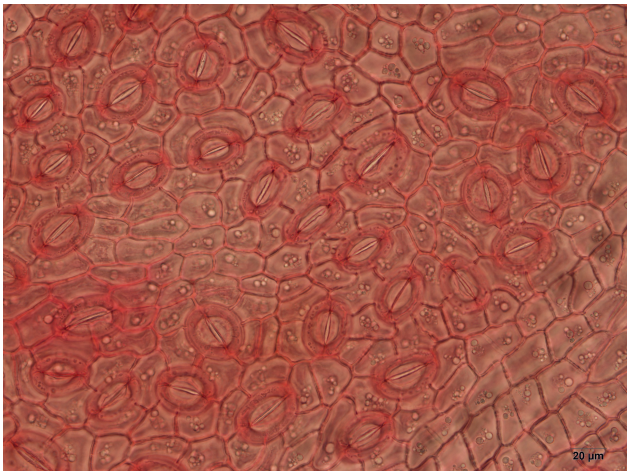



**Figure 1.1:** Microscopic photograph of the stomata of Eucalyptus jacksonii. Through the stomatal pores, plants absorb atmospheric $CO_2$ and, at the same time, transpire water. The photograph was taken at 400x magnification. The representative scale bar is plotted in the lower right-hand corner of the image. The photo was taken by H. J. de Boer.



to dominate over the sensible heat flux, as vegetation tends to transpire large quantities of water. As a rough estimate, a square meter of vegetation transpires between 1 to 10 l of water in a day. The transfer of heat and water between the land and the atmosphere crucially influences the state of the atmosphere. As such, it comprises a key biophysical process in atmospheric and Earth system models.

Apart from energy and water, the Earth's surface also exchanges matter. In that regard, a very important chemical compound is carbon dioxide ($CO_2$). Plants use atmospheric $CO_2$, together with sunlight and water, to produce chemical energy in the process known as photosynthesis. In turn, they can as well emit $CO_2$ through respiration processes. In a similar fashion, soils also emit $CO_2$ to the atmosphere as a consequence of the respiration of the soil organisms.

For the vegetation, the water and $CO_2$ exchanges are coupled, as a large part of these exchanges occurs through the same pores - the stomata - which are located on the surface of leaves, Fig. 1.1. The stomata respond to environmental factors, trying to balance the $CO_2$ uptake gain and the water loss. This tight coupling between water and $CO_2$ at leaf level scales up to larger scales, and makes stomata regulation a central biophysical process when studying land-atmosphere interactions.

### 1.2.2 The atmospheric boundary layer

The "air" that we treat within this thesis is that pertaining to the atmospheric boundary layer, also known as the planetary boundary layer. The atmospheric boundary layer is the

lowest part of the troposphere, extending from the Earth's surface to a height that ranges between dozens of meters and a couple of kilometers, depending on the local meteorological conditions. It is defined as that part of the atmosphere that directly experiences the presence of the Earth's surface, responding to surface forcings in a timescale of approximately 1 hour or less (Stull, 1988). The study of the atmospheric boundary layer is immensely important as it is the part of the atmosphere that we, humans, but also the ecosystems, experience. In other words, the atmospheric boundary layer sets the microclimatic conditions of life on Earth. Its understanding is also crucial for predicting weather patterns and air quality, and for the successful practical implementation of wind and solar renewable energy.

The atmospheric boundary layer is highly dynamic, being mainly characterized by its turbulent nature. Turbulence is generated mechanically and generated or supressed by buoyancy. Mechanical turbulence is caused by wind shear and by the roughness of the Earth's surface. Buoyancy generates or suppresses turbulence depending on atmospheric factors such as temperature gradients, humidity gradients and water phase changes. For example, during daytime and over land, the energy reaching the surface warms the adjacent air layer (thorugh the sensible heat flux) and, fuels evaporation and transpiration, moistening the air (through the latent heat flux). As the near surface air is warmer and more humid that the surrounding air, it also becomes less dense, and therefore, it rises . This upward convective air movement, which is often termed as a thermal, causes mixing of the atmospheric boundary layer. The turbulence state dictates the stability of the atmospheric boundary layer, defining whether the layer is stable (with little vertical mixing and with stratified air layers), neutral (with moderate vertical mixing and with some air stratification), or unstable (with strong vertical mixing and no air stratification). Over land, the stability and depth of the atmospheric boundary layer have a marked diurnal cycle, with, generally, shallow stable noctural boundary layers which transition to deeper convectively-driven unstable boundary layers during daytime.

The atmospheric boundary layer communicates with the surface at its lowermost end but also with another atmospheric layer at its top, the so-called "free troposphere". The free troposphere is a prevailingly stable layer, which extends until the top of the troposphere, and which has not the clear diurnal signatures of the atmospheric boundary layer. During daytime, the thermals originated by the surface heating reach the boundary layer top, engulfing first air from a residual layer, remnant of the previous day's convective boundary layer, and later from the free troposphere, in a process known as entrainment. Entrainment introduces air with different properties (generally warmer, drier, and $CO_2$ depleted) to the atmospheric boundary layer. Close to the zone where entrainment occurs, known as "entrainment zone", is also where low clouds inhabit, either spanning within the atmospheric boundary layer (stratocumulus clouds) or sitting on top of its upper limit (shallow cumulus clouds).

### 1.2.3 The clouds

Clouds come in many sizes and shapes. Broadly, they are categorized as low, middle, and high clouds depending on where their cloud bases and tops are located. Clouds are a crucial component of the Earth system, covering, as mentioned above, a large portion (approximately 60 %) of the Earth's surface at any given moment. Clouds control the water availability at the surface through their precipitation patterns. They also importantly alter the radiative equilibrium of the planet by diverse feedbacks, which results in cooling and warming effects depending on the cloud type and structure (Siebesma et al., 2020). Additionally, clouds perturb the radiation reaching the surface, initiating a chain of events in which they simultaneously alter the the ecosystem $CO_2$ exchange, the surface energy fluxes, and the state of the atmospheric boundary layer.



From all types of clouds, shallow cumulus clouds have played a prominent role in the study of land-atmosphere interactions. Their relevance stems from diverse factors. Firstly, these predominantly non-precipitating clouds represent an initial state of deep convective precipitating clouds. Secondly, these clouds modify surface radiation through different mechanisms: (1) by reducing total surface irradiance, (2) by altering the direct and diffuse partition of radiation, and (3) by introducing heterogeneous patterns of shades and light enhancements. These radiation perturbations alter the surface fluxes of heat, water, and $CO_2$. Additionally, due to their proximity to the surface, their lifetime and evolution are significantly affected by the same surface fluxes that they alter. As such, the coupling between shallow cumulus and land is bidirectional, and as with the surface fluxes, it has a marked diurnal evolution. Given their relevance, atmospheric models aim to capture how shallow cumulus clouds influence weather and climate. Nonetheless, shallow cumulus are elusive to study as their characteristic horizontal length is of the order of 1 km, and many global and mesoscale atmospheric models cannot resolve with enough spatial resolution their driving mechanisms. However, high resolution atmospheric models such as large eddy simulations (LES), are able to resolve this type of clouds with enough detail (e.g., Xiao et al., 2018; Veerman et al., 2020), offering the possibility to improve our understanding of the vegetation and shallow cumulus clouds coupling.

### 1.2.4 The interplay between soil, vegetation, air, and clouds

In this thesis, we focus on the interplay between the vegetation and the atmospheric boundary layer under clear and shallow cumulus dominated skies. We do so by integrating observations and modeling strategies across spatial scales ranging from the leaf to the ecosystem and to the atmopheric boundary layer scales. To explore how the vegetation and atmosphere interact, we pay attention to the leaf and ecosystem exchanges of energy, water, and $CO_2$. Additionally, we investigate how these exchanges are transferred through the atmosphere via turbulent transport. Finally, we also examine the microclimate within and near canopies as well as atmospheric boundary layer processes, and how they relate with the surface exchanges.

## 1.3 Observational and modeling strategies

In this thesis, we carried out five studies (Chapters 2, 3, 4, 5, and 6) by combining observations with models, which sampled the vegetation-atmosphere continuum at leaf, ecosystem, and atmospheric boundary layer scales. In terms of observations, we relied on comprehensive observational datasets acquired during three measurement field campaings, in which we participated. These field campaigns were: (1) the Land surface Interactions with the Atmosphere over the Iberian Semi-arid Envrionment (LIAISE) field campaign, which took place in summer 2021; (2) the Loobos field campaign, which took place 17 and 18 May 2022; and (3) the CloudRoots-Amazon22 field campaign, which took place in August 2022. During these field campaigns, many measurement instruments were deployed, ensuring a detailed description of the vegetation-atmosphere continuum.

These field campaigns enabled us to study three diverse ecosystems: (1) an agricultural alfalfa crop, (2) a tropical rainforest, and (3) a temperate forest. The geographic location of these sites and their appearances are introduced in Fig. 1.2. Studying multiple sites enabled us to investigate the vegetation-atmosphere interactions across canopy structures and atmospheric regimes.

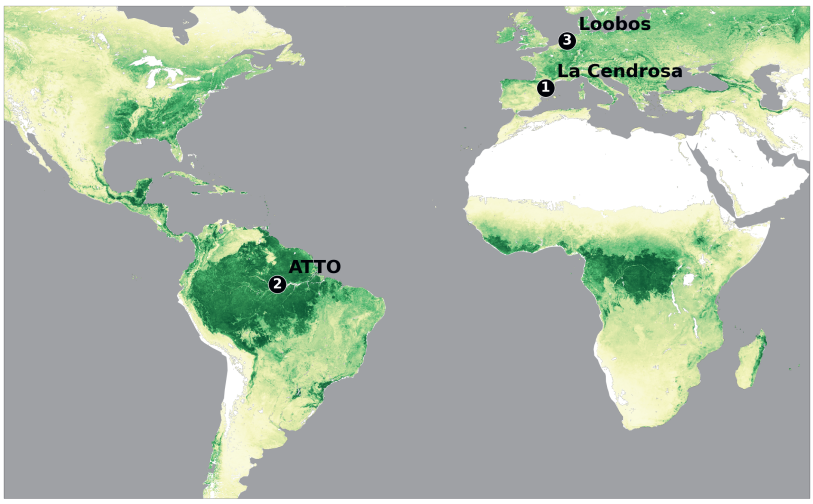
The next sections encompass the main observational and modeling strategies used to represent each of the spatial levels: leaf level, ecosystem level, and atmospheric boundary layer level. Fig. 1.3 offers a glimpse of the observational strategies deployed at each spatial level, whereas Fig. 1.4 depicts some of the modeling approaches used in this dissertation.

*Leaf level*

To characterize the leaf level, we measured and modeled the leaf gas exchange of water (leaf transpiration), and $CO_2$ (leaf assimilation). In terms of observations, we carried out measurements of stomatal conductance in a controlled closed leaf chamber with a LiCOR-6400XT instrument (Fig. 1.3 left main and inset panels). Similarly, we modeled stomatal conductance, leaf transpiration and $CO_2$ assimilation with a leaf gas exchange scheme, known as the "A-$g_s$ model" (Goudriaan et al., 1985).

Apart from characterizing the leaf gas exchange, we also characterized the properties of the leaves. Through additional measurements acquired with the LiCOR-6400XT system (response curve measurements), we determined leaf traits which affected the vegetation photosynthetic capacity. This characterization was used to inform the land-surface models regarding the particular leaf ecophysiological state of the vegetation at each of the sites. Furthermore, in one of the studies, we also took leaf samples that provided another source of independent information regarding the leaf gas exchange. Finally, we also relied in open-source observational datasets of leaf optical properties.

Regarding leaf-scale modeling, we used schemes with different degrees of complexity in terms of the processes controlling leaf temperature and the effect of the wind.




**1. La Cendrosa site**
Agricultural land



*Chapter 2*

**2. ATTO site**
Amazon rainforest



*Chapters 3, 4, 5, and 6*

**3. Loobos site**
Temperate forest



*Chapter 6*

**Figure 1.2:** Overview of the greographical locations studied in this thesis: an agricultural field (La Cendrosa), a tropical rainforest (ATTO site), and a temperate forest (Loobos site). The upper panel shows a portion of the global map with vegetation presence indicated in green shades. The different shades of green represent the leaf area index, which is a parameter that quantifies leaf area density. Darker green colors represent dense vegetation whereas white represents no vegetation. The leaf area index was retrieved from the global dataset GIMMS LAI4g (Cao et al., 2023), and it represents the vegetation state during the second-half of May 2020. The lower row shows pictures of each of the study sites, together with an indication of which chapter of the thesis deals with each site.

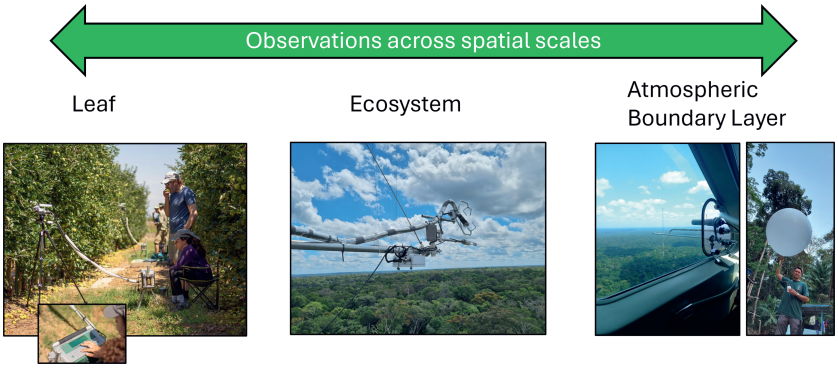



**Figure 1.3:** This panel exemplifies some of the measurement techniques used in this thesis. The observational strategy covers three spatial scales: leaf level (left main and inset pictures), ecosystem level (central picture), and atmospheric boundary layer level (right pictures). At leaf level, the left pictures showcase leaf gas exchange measurements being carried out in an apple orchard with a LiCOR-6400XT system. At ecosystem level, the central picture showcases an eddy-covariance system above a tropical forest. This system measures fast fluctuations of wind and scalars, enabling an estimation of turbulent transport. Finally, at the atmospheric boundary layer level, the right pictures show, starting from the left: part of the measurement system aboard an aircraft flying above a tropical forest, and the launching of a radiosonde, which also monitors the atmospheric state above the tropical forest.

*Ecosystem level*

To characterize the ecosystem level, we relied on multiple observational and methodological approaches. Observations measured soil properties and fluxes (e.g., soil respiration $CO_2$ efflux), within and above canopy microclimate (e.g., radiation fluxes, air temperature, air humidity, atmospheric $CO_2$, and wind), vertical turbulent fluxes (e.g., sensible heat flux; latent heat flux; and $CO_2$ flux acquired by eddy-covariance systems, central panel Fig. 1.3), and canopy structural properties (e.g., leaf area index, canopy height, and leaf area density).

In terms of ecosystem-scale modeling approaches, we used a hierarchy of land-surface schemes with diverse degrees of complexity. We employed both “big-leaf” and “multi-layer” canopy approaches, which differ in how much vertical detail of canopy microclimate and structure is included. We also improved a canopy radiative transfer scheme for an existing atmospheric model, which advances the representation of the radiative environment within canopies.

*Atmospheric boundary layer level*

To characterize the observed atmospheric boundary layer level, we relied on measurements acquired with radiosonde sensors, sensors onboard aircraft, sensors placed at instrumental

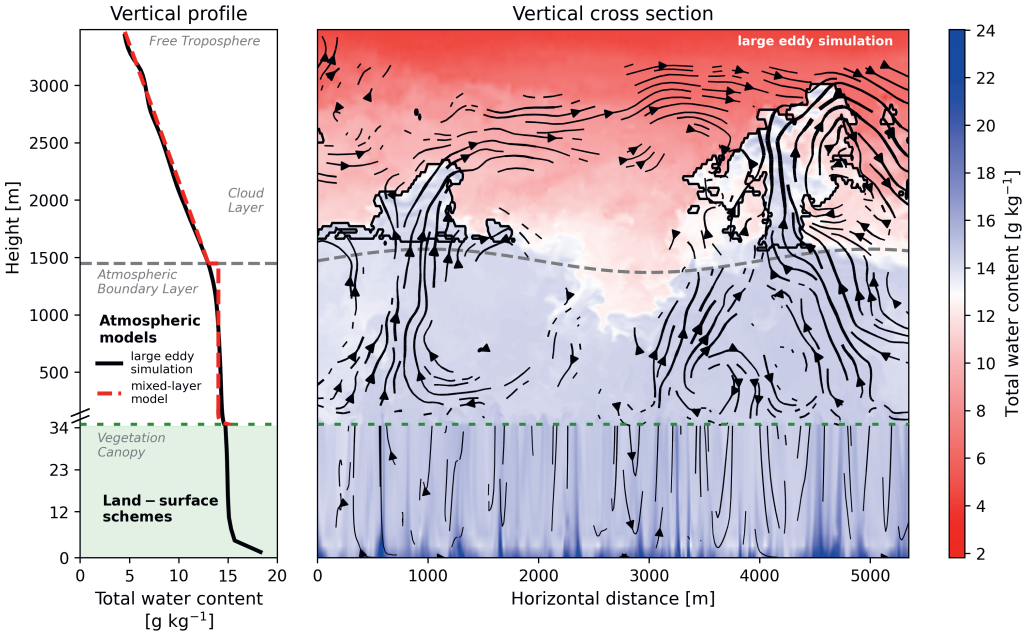



**Figure 1.4:** A glimpse of the atmospheric modeling approaches used in this dissertation: a mixed-layer model (CLASS model, left column), and a large eddy simulation model (the canopy-resolving version of DALES model, left and right columns). The right panel shows the total water content in the atmosphere above a tropical forest (above the dotted horizontal green line), and within the forest (below the dotted horizontal green line) at midday (12 local time). Two buoyantly active shallow cumulus clouds are visible and their contours are depicted in black lines. Air flow is indicated also in black lines, whose thickness is proportional to the wind speed, and whose arrows indicate the air flow direction. The left panel shows the horizontally-averaged vertical profiles of total water content, which, due to the convective vertical mixing, are well-mixed within the atmospheric boundary layer. The atmospheric boundary layer height is indicated as a dashed grey line. Within the forest canopy (below the dotted horizontal green line), we use diverse modeling approaches that communicate with the atmospheric models, and which are known as “land-surface schemes”.

tall towers, and ground remote sensing approaches.

In terms of modeling approaches, we used two distinct atmospheric models: the Chemistry Land-surface Atmospheric Soil Slab model (CLASS model; Vilà-Guerau de Arellano et al., 2015), and the multi-layer canopy Dutch Atmospheric Large Eddy Simulation model (referred in this thesis as can-DALES; Pedruzo-Bagazgoitia et al., 2023), Fig. 1.4. The CLASS model is an atmospheric mixed-layer model which represents the convective atmospheric boundary layer. The left panel of Fig. 1.4 depicts a well-mixed profile of total water content and how the CLASS model represents it. The CLASS model can be regarded as a proxy of a single grid cell of a climate or large-scale model. In that way, it offers a baseline against which to compare more elaborated atmospheric models.

The can-DALES model comprises a more sophisticated modeling approach which is able to solve to a large extent the turbulent transport and cloud processes. The multi-layer canopy representation of can-DALES enables a detailed characterization of canopy microclimates, with high temporal and spatial three-dimensional resolution.

Combining the wealth of observations and modeling approaches described above enabled us to explore the vegetation-atmosphere interactions from a wide perspective. Apart from the modeling strategies mentioned above, in this thesis we also developed some new analytical techniques and metrics. Two deserve special mention: the tendency equations of the leaf gas exchange (Chapter 2), and the diurnal range of carbon cycle tracers (Chapter 6).

## 1.4 Research questions and thesis outline

To enhance our understanding of the vegetation-atmosphere interactions, this dissertation addresses five key research questions. Each research question is explored in a specific chapter (chapters 2, 3, 4, 5, and 6), and the research findings are used as a basis for the subsequent chapters. To facilate the comprehension of this dissertation as a whole, we provide Fig. 1.5. In this figure, we showcase the key elements provided by each content chapter. The thesis is outlined as follows.

In **Chapter 2**, we address the question:

*Which environmental factors drive the daytime cycle of transpiration and $CO_2$ assimilation at leaf and canopy level? To what extent?*

To address this question, we examine how four atmospheric variables - photosynthetically active radiation, air temperature, vapor pressure deficit, and atmospheric $CO_2$ - influence the $CO_2$ assimilation and water transpiration at the leaf and canopy levels. To do so, we develop a technique that quantifies how these four atmospheric variables shape the temporal evolution of the stomatal conductance, leaf $CO_2$ assimilation, and leaf transpiration. Additionally, we explore how these influences propagate to the ecosystem canopy level. The study is based on an agricultural monoculture, being an excellent test bed due to its relatively simple canopy composition.

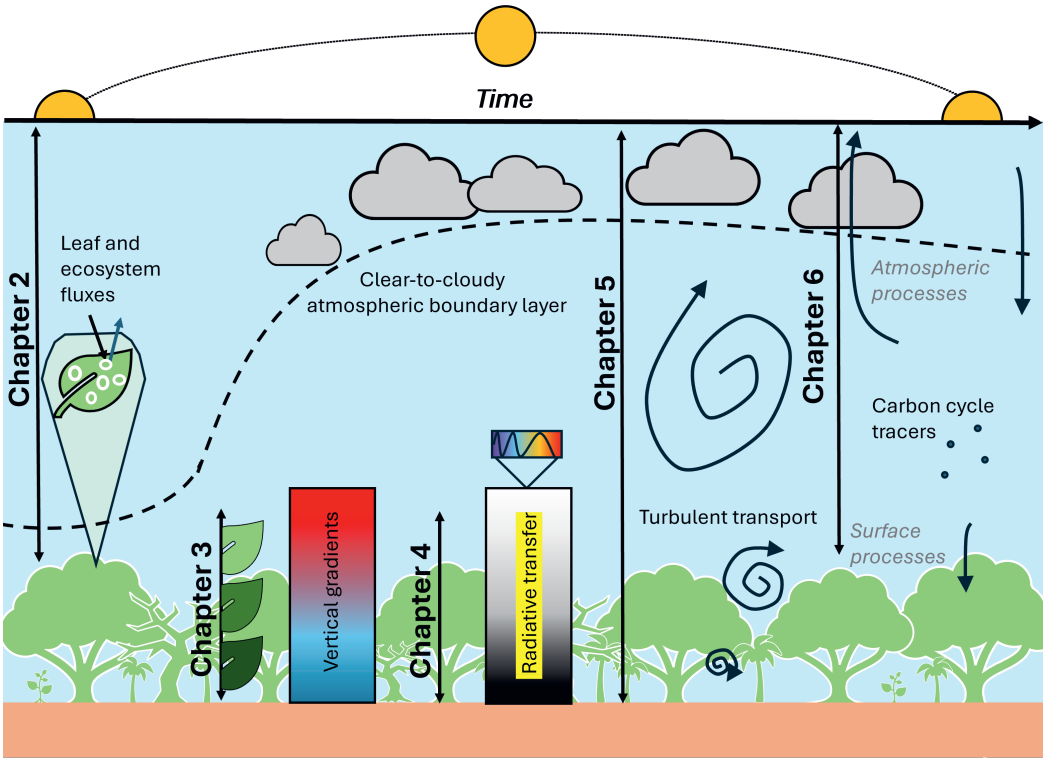



**Figure 1.5:** Conceptual figure of the main biophysical aspects covered in each of the content chapters (chapters 2, 3, 4, 5, and 6). The top x-axis represent the daytime evolution, whereas the y-axis represents the height, spanning from the soil surface to the free-troposphere. The diurnal evolution of the atmospheric boundary layer is indicated by its variation in height, indicated as a dashed black line. The atmospheric boundary layer transitions from a shallow noctural stable boundary layer to a well-mixed deeper convective boundary layer. Each chapter studies diverse fundamental biophysical processes, spanning certain vertical extent, which is indicated by the two-sided vertical black arrows near the chapter labels.

In **Chapter 3**, we address the question:

*How does canopy microclimate change with canopy depth? How does this vertical variability shape the transpiration and $CO_2$ assimilation rates?*

We address this question for a more complex canopy, a tropical rainforest. Building on the temporal perspective of Chapter 2, this chapter introduces vertical variability within the canopy as a key dimension controlling ecosystem exchange. Integrating observations with a three-layer canopy approach, we characterize how the forest microclimate and leaf traits change over canopy depth, and estimate the canopy transpiration and $CO_2$ assimilation across canopy layers.

In **Chapter 4**, we address the question:

*How is radiation transferred within canopies? How sensitive is the shortwave radiative transfer to external (atmospheric) and internal (canopy) factors?*

To address this question, we improve a canopy radiative transfer scheme in an existing atmospheric model (can-DALES model). In the improved scheme, we make the important step of accounting for the plant preferential use of radiation by resolving four shortwave spectral bands: ultraviolet radiation, photosynthetically active radiation, far-red radiation, and near infrarred radiation. We also explore how the shortwave radiative transfer varies depending on atmospheric forcings, related to the sun position and the direct and diffuse proportion of solar radiation, and on internal canopy factors, related to the leaf biomass and its distribution across the canopy.

In **Chapter 5**, we address the question:

*To what extent are turbulent resolving models able to represent the vegetation-air-cloud system? Which insights about forest-atmosphere interactions can be gained from them?*

To address this question, we use a turbulent resolving model (can-DALES) which is able to simulate turbulent flow within and above vegetation canopies while explicitly resolving low clouds. Comparing a simulation of can-DALES with observations acquired in a tropical forest, we explore the forest-atmosphere interactions across four interconnected aspects of the coupled system: forest microclimate, leaf-scale fluxes, ecosystem-scale fluxes, and the clear-to-cloudy atmospheric boundary layer transition. In doing so, we evaluate the potential of canopy-resolving LES to promote our understanding of vegetation-air-cloud dynamics.

In **Chapter 6**, we address the question:

*To what extent do surface and atmospheric processes alter the diurnal evolution of carbon cycle tracers?*

In this chapter, we move beyond the total $CO_2$ mole fractions, to also include in our study other scalars which can track the movement of carbon between the land and atmosphere. We term these scalars - which jointly are $CO_2$, $^{13}C$-$CO_2$ and $O_2$ - as carbon cycle tracers. In this study, we contribute to interpreting atmospheric signals of these carbon cycle tracers. We do so by exploring how atmospheric processes - namely entrainment, subsidence, and

cloud ventilation - and surface processes shape the diurnal evolution of the carbon cycle tracers. With this chapter, we showcase the diversity of ways in which vegetation-atmosphere interactions can be studied and understood.

Finally, in **Chapter 7**, we discuss the main research outcomes of the thesis while concisely answering the research questions mentioned above. In addition, we provide a general discussion in which we include main opportunities to further develop our understanding on vegetation-atmosphere interactions. We finalize the chapter with key concluding remarks.

# Chapter 2

# Impact of environmental variables on the diurnal dynamics of water and carbon dioxide exchange at leaf and canopy level

This chapter is based on:

González-Armas, R., Vilà-Guerau de Arellano, J., Mangan, M. R., Hartogensis, O. & de Boer, H. (2024). *Impact of canopy environmental variables on the diurnal dynamics of water and carbon dioxide exchange at leaf and canopy level*. In Biogeosciences. Copernicus GmbH. https://doi.org/10.5194/bg-21-2425-2024

# Abstract

Quantifying water vapor and carbon dioxide ($CO_2$) exchange dynamics between land and atmosphere through observations and modelling is necessary in order to reproduce and project near-surface climate in coupled land-atmosphere models. The exchange of water and $CO_2$ occurs at the leaf surface (leaf level) and in a net manner through exchanges at all the leaf surfaces composing the vegetation canopy and at the soil surface (canopy level). These exchanges depend on the meteorological forcings imposed by the overlying atmosphere (atmospheric boundary layer level). In this paper, we investigate the effect of four canopy environmental variables (photosynthetic active radiation (PAR), water vapor pressure deficit (VPD), air temperature ($T$) and atmospheric $CO_2$ concentration ($C_a$)) on the local individual leaf exchange and canopy exchange of water and $CO_2$ at hourly timescales. Additionally, we investigate the effect of atmospheric boundary layer (ABL) processes on the local exchange.

To that end, we simultaneously investigated the exchanges of water and $CO_2$ at leaf level and canopy level for an alfalfa field in northern Spain over 1 day in summer 2021. We used comprehensive observations ranging from stomatal conductance to ABL measurements collected during the Land Surface Interactions with the Atmosphere in the Iberian Semi-Arid Environment (LIAISE) experiment. To support the observational analysis, we used a coupled land-atmosphere model (CLASS model) that has representations at all levels considered. To relate how temporal changes of the four environmental variables modify the fluxes of water and $CO_2$, we studied tendency equations of the leaf gas exchange. These mathematical expressions quantify the temporal evolution of the leaf gas exchange as a function of the temporal evolution of PAR, VPD, $T$ and $C_a$. To investigate the effects of ABL processes on the local exchange, we developed three modeling experiments that impose surface radiative perturbations by a cloud passage (which perturbed PAR, $T$ and VPD), entrainment of dry air from the free troposphere (which perturbed VPD) and advection of cold air (which perturbed $T$ and VPD).

The model results and observations matched the leaf gas exchange (with $r^2$ between 0.23 and 0.67) and canopy gas exchange (with $r^2$ between 0.90 and 0.95). The tendency equations of the modeled leaf gas exchange during the study day revealed that the temporal dynamics of PAR were the main contributor to the temporal dynamics of the leaf gas exchange, with $C_a$ temporal dynamics being the least important contributor. From the three modeling experiments with ABL perturbations, the surface radiative changes induced by a cloud perturbed the $CO_2$ exchange the most, whereas all of them perturbed the water exchange to a similar extent. Second-order effects on the dynamics of the leaf gas exchange were also identified using the tendency equations. For instance, the decrease of net $CO_2$ assimilation during the cloud due to a decrease in surface radiation was further enhanced due to the decrease in air temperature also associated with the cloud. With this research we showcase that the proposed tendency equations can disentangle the effect of environmental variables on the leaf exchange of water and $CO_2$ with the atmosphere, as represented in land-surface parameter-

ization schemes. As such, this framework can become a useful tool with which to analyze these schemes in weather and climate models.

## 2.1 Introduction

The exchanges of water and carbon dioxide ($CO_2$) between land and atmosphere are essential components in constraining and understanding the water and carbon cycles. Because of the complex dynamic interactions between the soil, vegetation and atmosphere, the net surface fluxes of $CO_2$ and water vapor, known as "net ecosystem exchange" (NEE) and "evapotranspiration" (ET), remain difficult to reproduce by current land surface models (LSMs). Intercomparison studies (Henderson-Sellers et al., 1995; Chen et al., 1997; Holtslag et al., 2013; Best et al., 2015; Restrepo-Coupe et al., 2017; Renner et al., 2021) have shown systematic deviations between observed and modelled ET and NEE. Additionally, they have shown discrepancies among the different LSMs considered. For instance, Renner et al. (2021) compared the estimation of heat surface fluxes of 13 different LSMs driven by observed meteorological conditions at 20 FLUXNET sites. When assessing the performance to reproduce heat fluxes, they considered both the magnitude and a metric, called the "phase lag" (Renner et al., 2019), that indicates the asymmetry between the heat fluxes and the incoming shortwave radiation. In their study they concluded that all LSMs showed a poor representation of the evaporative fraction and phase lag. The authors also highlighted the importance of systematic evaluations of the diurnal dynamics of the fluxes in order to improve the understanding and predictive capacity of the near-surface climate.

To perform a systematic evaluation of the diurnal dynamics of ET and NEE, multiple spatial scales, ranging from the size of the stomata (10-100 $\mu$m) to the size of the atmospheric boundary layer (ABL; $\sim$ 1 km), must be considered. We have broadly divided the spatial scales into three discrete spatial levels: leaf level, canopy level and, ABL level (Fig. 2.1). The leaf and the canopy levels are two distinct levels where the exchange of water and $CO_2$ occur. They are different because at the leaf level our system comprises the leaf surface which experiences certain environmental conditions, whereas at the canopy level the system comprises the whole vegetation canopy (with changing environmental conditions experienced by a leaf depending on its location in the canopy) including the soil. The third level is the ABL level, which is confined at the lower side by the canopy. The ABL reacts to the dynamics of the canopy and imposes forcings on it. Apart from local canopy processes, the ABL state also depends on non-local processes such as entrainment of air from the free troposphere; advection of heat, moisture, and $CO_2$; and subsidence motions created by the influence of synoptic weather patterns.

At the leaf level the dynamic exchange of water and $CO_2$ is crucially influenced by in-canopy light, temperature, humidity, and $CO_2$ concentration as well as by the plant responses to these environmental conditions in terms of photosynthesis, transpiration and stomatal conductance. Several models and theories have been proposed for representing the water and $CO_2$ leaf gas fluxes. Normally, these leaf gas exchange models are composed of a leaf photosynthesis model that calculates the $CO_2$ assimilation rate and a stomatal conductance model. The most widespread leaf photosynthesis model is the one developed by Farquhar, von Caemmerer, and Berry (FvCB) (Farquhar et al., 1980). This model is generally coupled with a

stomatal conductance model such as the one proposed by Ball et al. (1987) and Collatz et al. (1991). Another leaf photosynthesis model commonly used is the one proposed by Goudriaan et al. (1985) (G85 model). This model is used as part of the photosynthesis-stomatal description called "A-$g_s$ model" developed by Jacobs (1994). The A-$g_s$ model can be found in the LSMs of several atmospheric models such as the European Centre of Medium-Range Weather Forecasts (ECMWF) (Boussetta et al., 2013), the Earth system model operated by the *Centre National de Recherches Météorologiques* (CNRM-ESM1) (Calvet et al., 1998; Masson et al., 2013; Séférian et al., 2016), the Dutch Atmospheric Large-Eddy Simulation (Vilà-Guerau de Arellano et al., 2014), and the CLASS mixed-layer model (Vilà-Guerau de Arellano et al., 2015). A recent intercomparison between FvCB and G85 model (van Diepen et al., 2022) revealed that despite fundamental differences in model structures, they have remarkable functional similarities.



The canopy level, as we have defined it, is composed by all the leaves and other phytomass that make up the plant canopy, the soil, and the air inside and directly above the canopy. To connect the leaf-level fluxes to the plant canopy level fluxes, assumptions about the vertical variability of (1) in-canopy environmental variables, (2) leaf physiology, and (3) phytomass allocation have to be made. A traditional way of representing the plant canopy is the so-called big leaf approach, in which the plant canopy is assumed to be a homogeneous, single layer of vegetation with no vertical structure. In that approach, to calculate a bulk surface stomatal conductance that represents the single "one big leaf" layer of the canopy and enables the calculation of ET and NEE, the leaf gas exchange model is integrated over leaf area assuming that radiation is the only in-canopy variable that varies vertically and which is generally assumed to decay exponentially with leaf area index (e.g., Ronda et al. 2001).

The ABL is typically defined as "that part of the troposphere that is directly influenced by the presence of the earth's surface, and responds to surface forcings with a time scale of about an hour or less" (Stull, 1988). In addition, the ABL also imposes forcings on the surface. For example, the presence of clouds alters the radiation received at the surface (Mol et al., 2023), which in turn, alters the surface fluxes of heat, water, and $CO_2$. Other ABL processes such as advection of air masses with different thermodynamic properties and the entrainment of dry air masses from the free troposphere have been reported to alter the surface turbulent fluxes (Tolk et al., 2006; Mangan et al., 2023a; van Heerwaarden et al., 2009).

The objective of this research is to provide a framework with a new analytical method proposed for analyzing the diurnal dynamics of the fluxes of water and $CO_2$. In particular, we aim to answer the following research question:

- To what extent do the diurnal dynamics of environmental variables affect the diurnal dynamics of the water and $CO_2$ exchange at the leaf and canopy levels?

Because processes interact across our three defined levels (leaf, canopy, and ABL levels) and together they shape the exchange of water and $CO_2$, the framework combines observations and an encompassing model with representations at the leaf, canopy, and ABL levels. The analytical method entails the calculation of the tendency equations of the stomatal conductance,

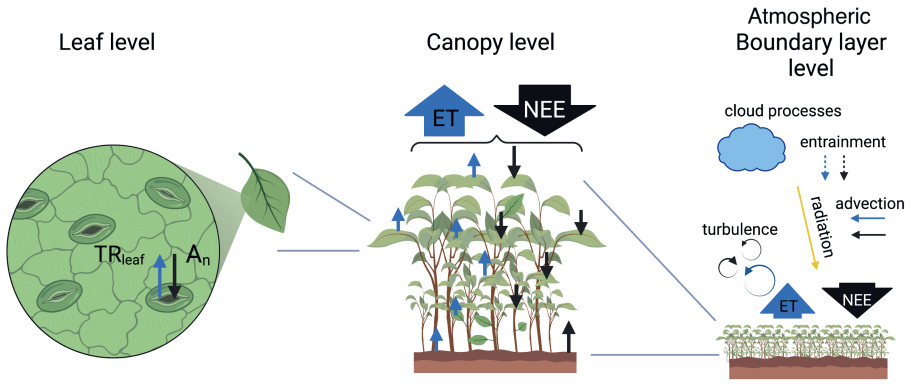



**Figure 2.1:** Scheme of the three levels considered in the study of the exchange of water (represented by blue arrows) and carbon (represented by black arrows): (1) leaf level, (2) canopy level, and (3) ABL level. The exchanges of water and $CO_2$ at leaf level are represented by the leaf transpiration ($TR_{leaf}$) and net $CO_2$ assimilation ($A_n$), respectively. At the ABL, several processes are included in the scheme such as advection of moistue and $CO_2$ and entrainment of air from the free troposphere. Advection and entrainment of moisture and $CO_2$ are indicated by solid arrows if they contribute to higher concentrations of water or $CO_2$ in the ABL and by dashed arrows if they contribute to lower concentrations. In the scheme, we represent advection of moist and $CO_2$-enriched air and entrainment of drier and $CO_2$-depleted air from the free troposphere. The scheme was created using BioRender (https://www.BioRender.com; last access: 15 April 2024).

the leaf net $CO_2$ assimilation, and the leaf transpiration. The tendency equations quantify the influence of temporal changes of four environmental variables on temporal changes of the leaf gas exchange. These four environmental variables are the photosynthetic active radiation (PAR), the air temperature ($T$), the vapor pressure deficit (VPD) and the atmospheric $CO_2$ concentration ($C_a$). The quantification of their influence on the leaf gas exchange allow us to investigate which environmental variables control the dynamics of the exchange at different moments of the day. This framework was applied to an alfalfa crop in Spain over 1 day in summer 2021. To further explore the dependencies of the water and $CO_2$ exchange on the environmental variables, three modeling experiments with ABL perturbations were analyzed.

## 2.2 Methods

### 2.2.1 LIAISE field campaign and definition of the case study

This research builds on the observations obtained as part of the field campaign Land surface Interactions with the Atmosphere over the Iberian Semi-arid Environment (LIAISE). LIAISE took place in the Ebro River basin in northeastern Spain with an special observation period (SOP) from 15 to 29 July 2021 with the overarching objective “to improve the understand-

ing of land-atmosphere-hydrology interactions in a semi-arid region characterized by strong surface heterogeneity owing to contrasts between the natural landscape and intensive agriculture" (Boone et al., 2021). Further details about the field campaign and study site can be found in Boone et al. (2019), Boone et al. (2021) and Mangan et al. (2023a).

La Cendrosa, our main study site, was one of the seven instrumented sites within the LIAISE domain. It was even considered a "supersite" since, in addition to standard energy balance and basic meteorology measurements, it also consisted of ABL measurements in the form of hourly launched radiosondes, ground based remote sensing equipment, and a blimp with turbulence measurements. The crop grown at La Cendrosa is alfalfa, which was regularly irrigated through gravity-driven flood irrigation during LIAISE (on the nights of the 10 and 23 July 2021).



Our research focused on the dynamics observed during the SOP on 17 July 2021. In this study, we express time series in coordinated universal time (UTC). In the region, local time (LT) is UTC + 2. We chose to use UTC because, in this region, UTC aligns better with solar time, with 12 UTC roughly corresponding to solar noon. During the studied day, there were no clouds present; there was light wind ($\approx$ 2 m $s^{-1}$ at 2 m height) and a maximum temperature of 32 $^{o}$C. The synoptical condition was characterized by a thermal low pressure system advecting warm and dry air to the study domain in the morning and early afternoon by light, westerly winds. In the late afternoon (after 18:00 UTC) a sea breeze front, the Marinada, came in from the east bringing cooler and moister air.

### 2.2.2 ABL level

*CLASS model*

The CLASS mixed-layer model (Vilà-Guerau de Arellano et al., 2015) was used to create the modeling numerical experiments. The CLASS model describes the ABL but it also contains a land surface scheme (Sect. 2.2.3) and a leaf gas exchange model (Sect. 2.2.4). A numerical experiment, referred to as the "control experiment", was created to represent the study day and it was compared with observations. Details about the model initialization values of the control experiment and the land surface parameters are given in the following sections. Three additional numerical experiments based on the control experiment were created to explore the effect of various ABL perturbations on the local exchange of water and $CO_2$ (Sect. 2.2.6).

Regarding how CLASS represents the ABL, CLASS is based on mixed-layer theory (summarized in Sect. 2.2 of Vilà-Guerau de Arellano et al. 2015), which states that atmospheric scalar variables are well mixed in height during the daytime, creating an atmospheric convective boundary layer (CBL). Consequently, the CBL can be described as a bulk layer, in which scalars (such as potential temperature, specific humidity, and $CO_2$ concentration) are nearly constant with height and can be described by a single mixed-layer value. The interface between the CBL and the free troposphere is described as a sharp discontinuity in the

scalars (e.g., potential temperature, humidity) normally called "scalar jump". The free troposphere is described as a layer in which scalars change linearly with height. For instance, potential temperature increases at a constant lapse rate which is initially fixed in the experiment settings. CLASS also represents the surface layer (assumed to be the lower 10 % of the CBL) with Monin-Obukhov similarity theory (Monin & Obukhov, 1954), which allows for estimations of wind, temperature, and specific humidity at different heights in the surface layer. Because with CLASS we describe a CBL, our analysis during the study day started at 05:00 UTC, when the ABL was a CBL according to vertical profiles of potential temperature measured by radiosondes. Our analysis was restricted until 15:40 UTC, when our numerical experiment indicated a transition to non-convective conditions.

*Data and model initialization*

To characterize the ABL, vertical profiles of temperature, relative humidity, and wind obtained from radiosondes were used together with wind sensors located in a tower of 50 m height (at 10, 20, and 45 m). The radiosondes were released hourly from 04:00 to 17:00 UTC from the site. Radiosondes were used to provide the initial conditions for the numerical experiments (see Table 2.1 for exact values). Estimations of the CBL height were obtained from the radiosonde profiles using the parcel method (Kaimal & Finnigan, 1994). Mixed-layer values for potential temperature and specific humidity were obtained averaging the profiles below the CBL height minus a constant entrainment zone of 50 m and excluding the surface layer assumed to be the lower 10 % of the CBL. Lapse rates were obtained by calculating the slope of a linear regression of the vertical profile from 200 m above the top of the ABL until 3000 m height. Then, the jumps were calculated as the difference between the interpolated value at the CBL height and the mixed-layer value. Because the radiosondes did not measure $CO_2$, we initialize the mixed layer value with the value provided by the $CO_2$ sensor that was part of an eddy covariance (EC) system located at 3 m height. Due to the lack of additional $CO_2$ data, the initial jump of $CO_2$ and the $CO_2$ lapse rate were chosen in order to reproduce the magnitude of the diurnal variability in atmospheric $CO_2$ measured by the EC system. Advection of heat and moisture was included based on estimations derived from a network of meteorological stations operated by the *Servei Meteorològic of Catalunya* as calculated in previous research developed by Mangan et al. (2023a). The advective terms of the control numerical experiment can be found in Appendix 2.A. Initial conditions for the CBL together with the time variables and the geographic coordinates needed for the initialization of radiation are given in Table 2.1.

### 2.2.3 Canopy level

*Land-surface scheme*

CLASS represents the plant canopy as a homogeneous single layer of phytomass without vertical structure (often referred to as the "one big leaf" approach). That layer is represented

**Table 2.1:** General settings, radiation parameters, and initial conditions of CBL variables used in the control experiment.

| Variable | Symbol | Value |
|---|---|---|
| *Time variables* | | |
| Time step | $\Delta t$ | 5 s |
| Initial time | $t_0$ | 5 UTC (7 LT) |
| Simulation duration | $t_f - t_0$ | 16 h |
| *Geographic coordinates for radiation* | | |
| Latitude | $\phi_{rad}$ | 41.69º N |
| Longitude | $\lambda_{rad}$ | 0.96º E |
| Day of the year | DOY | 198 |
| *Convective boundary layer* | | |
| Initial boundary layer height | $h_0$ | 150 m |
| Surface pressure | $P_s$ | 101300 Pa |
| Initial potential temperature | $\theta$ | 293 K |
| Initial potential temperature jump | $\Delta\theta$ | 1.5 K |
| Initial potential temperature lapse rate | $\gamma_\theta$ | 0.012 K $m^{-1}$ |
| Initial specific humidity | q | 9.5 $g_{water}$ $kg_{air}^{-1}$ |
| Initial specific humidity jump | $\Delta q$ | -2 $g_{water}$ $kg_{air}^{-1}$ |
| Initial specific humidity lapse rate | $\gamma_q$ | 0.011 $g_{water}$ $kg_{air}^{-1}$ |
| Initial $CO_2$ | $CO_2$ | 470 ppm |
| Initial $CO_2$ jump | $\Delta CO_2$ | -65 ppm |
| Initial $CO_2$ lapse rate | $\gamma_{CO_2}$ | 0 ppm $m^{-1}$ |

by a bulk surface canopy conductance to water vapor ($g_{surf}$) or by its inverse, the surface canopy resistance to water vapor ($r_{surf} = \frac{1}{g_{surf}}$). To obtain $g_{surf}$, the stomatal conductance to water vapor at leaf level ($g_s$) calculated with the leaf gas exchange model of CLASS (the A-$g_s$ model, Sect. 2.2.4) is upscaled from the leaf to the canopy level. This upscaling is carried out by integrating $g_s$ over the leaf area and assuming an exponential decay of PAR with respect to leaf area index, as developed in Ronda et al. (2001). Then, to calculate ET the Penman–Monteith equation is used:

$$ET = \frac{1}{L_v} \frac{(R_n - G)\frac{dq_{sat}}{dT} + \frac{\rho c_p}{r_a}(q_{sat} - < q >)}{\frac{dq_{sat}}{dT} + \frac{c_p}{L_v}\left(1 + \frac{r_{surf}}{r_a}\right)}, \tag{2.1}$$

where $R_n$ is the net radiation, $G$ is the soil heat flux, $q_{sat}$ is the saturated specific humidity, $< q >$ is the well-mixed specific humidity, $c_p$ is the heat capacity of air at constant pressure, $L_v$ is the latent heat flux of vaporization, $r_a$ is the areodynamic resistance, and $\rho$ is the air density.

NEE is calculated as the difference between the net $CO_2$ rate assimilated by the vegetation canopy ($A_{nc}$) and the soil respiration (Resp).

$$NEE = -A_{nc} + Resp \tag{2.2}$$

NEE is considered negative if $CO_2$ is removed from the atmosphere and positive if $CO_2$ is added to the atmosphere. Resp has the same sign convention and it is always positive because it adds $CO_2$ to the atmosphere. Unlike NEE and Resp, $A_{nc}$ is defined positive if $CO_2$ is removed from the atmosphere. $A_{nc}$ is derived with an approximation of Fick's law of diffusion, Eq. (2.3), that considers the difference between $C_a$ and the inter-cellular $CO_2$ concentration ($C_i$), the surface resistance, and the aerodynamic resistance. The $C_i$ value is calculated with the A-$g_s$ model (presented in Sect. 2.2.4).

$$A_{nc} = \frac{C_a - C_i}{r_a + 1.6 \cdot r_{surf}} \tag{2.3}$$

The factor of 1.6 accounts for the different molecular diffusivity of water vapor and $CO_2$ (Jacobs & de Bruin, 1997).

In the model, soil is represented with a two soil force–restore model as developed by Noilhan & Planton (1989) with a plant water stress function added by Combe et al. (2016). Soil respiration is parameterized as a function of soil temperature and soil moisture. The surface and soil parameters used for the control experiment are described in Table 2.2.

*Data and model initialization*

To characterize the canopy, we measured the leaf area index (LAI); the canopy height; and time series of environmental variables (PAR, $T$, specific humidity, $C_a$ and wind), of soil respiration, and of the turbulent surface fluxes of water and $CO_2$. We measured LAI with a LAI ceptometer (ACCUPAR LP-80). The instrument contains a PAR sensor to be deployed above the canopy together with a linear array of PAR sensors to be deployed inside the canopy. It calculates LAI considering the sun position and an spherical leaf angle distribution. We measured LAI between 10 and 12 times at different orientations in 12 locations at La Cendrosa site. In total, we obtained 132 measurements for the study day with an average value of 1.33 and a standard deviation of 0.58. Similarly, we determined the canopy height by measuring 20 times at random locations in the field. The average canopy height was 28.5 cm with an standard deviation of 6.3 cm. We measured soil $CO_2$ efflux with a SRC-2 soil respiration chamber connected to a EGM-5 portable $CO_2$ gas analyzer. When measuring the soil $CO_2$ efflux, we check that no alfalfa plant was inside the chamber. In that way, no above-ground plant gas exchange would occur inside the chamber. We measured the soil $CO_2$ efflux sevem times throughout the day (from 07:15 to 19:00 UTC) near the EC tower. Every time, three or four soil $CO_2$ efflux measurements were recorded. As a result, we obtain seven averaged values with their corresponding standard deviation.

Time series of environmental variables and fluxes were measured. PAR and $C_a$ were measured above the canopy (at approximately 3 m), whereas temperature and specific humidity were also measured at different heights inside and right above the canopy. The sensible heat flux ($H$), latent heat flux (LE), and net ecosystem exchange (NEE) were measured at a surface station that was composed of an EC system (at 3 m height); four-stream radiometers, which measured net radiation ($R_n$); and ground heat flux ($G$) measurements. The average energy budget non-closure was calculated as $(R_n - G - H - LE)/(R_n - G)$. For more details about the set-up of the surface station, the reader is referred to Mangan et al. (2023a).

To compare model results and observations, we calculated the square of the Pearson correlation coefficient ($r^2$), the $p$ value, and the root mean squared error (RMSE) between model and observed NEE and ET.

### 2.2.4 Leaf level

*A-$g_s$ model*

In the numerical experiments created with the CLASS model, we represented the leaf gas exchange with the A-$g_s$ model (Goudriaan et al., 1985; Jacobs, 1994). Details about the A-$g_s$ implementation used in CLASS can be found in Appendix A of Ronda et al. (2001) and in Appendix E of Vilà-Guerau de Arellano et al. (2015). The A-$g_s$ model calculates the internal $CO_2$ concentration, the net assimilation rate ($A_n$), and the stomatal conductance to water vapor ($g_s$) and to $CO_2$ ($g_{sc}$). Similar to $A_{nc}$, $A_n$ is defined positive if $CO_2$ is taken up from the

**Table 2.2:** Surface and soil parameters used in the control experiment.

| Variable | Symbol | Value |
|---|---|---|
| *Surface properties* | | |
| Vegetation cover fraction | $c_{veg}$ | 1 |
| Leaf area index | LAI | 1.33 |
| Albedo | $\alpha$ | 0.2 |
| Surface skin temperature | $T_s$ | 293 K |
| *Soil properties* | | |
| Volumetric water content top soil layer | $w_g$ | 0.21 |
| Volumetric water content deeper soil layer | $w_2$ | 0.30 |
| Soil temperature at top soil layer | $T_{soil}$ | 293 K |
| Soil temperature at deeper soil layer | $T_2$ | 289 K |
| Thermal diffusivity of the skin layer | $\lambda$ | 50 W m$^{-2}$ K$^{-1}$ |
| Respiration at 10 ºC | $R_{10}$ | 2.73 $\mu$mol CO$_2$ m$^{-2}$ s$^{-1}$ |
| Activation energy | $E_0$ | 5.33·10$^4$ kJ kmol$^{-1}$ |

atmosphere. $A_n$ is calculated with the model developed by Goudriaan et al. (1985), which captures dependencies with PAR, $T$ and $C_i$ and requires some parameters that describe the photosynthetic traits of the vegetation. $C_i$ is calculated as a function of $C_a$, $T$, and VPD. To use the A-$g_s$ scheme in CLASS, five environmental variables are needed: PAR, $T$, VPD, $C_a$ and the soil water content at the root zone ($w_2$). To represent the leaf level fluxes, we have used the PAR received above the canopy (representing a sun-lit leaf); the soil water content of the second layer of soil (deeper layer of soil from CLASS); and $C_a$, T and VPD at 0.105 m height. Finally, we have derived the leaf transpiration ($TR_{leaf}$) taking into account $g_s$ and VPD.

*Data and model initialization*

In terms of in situ plant ecophysiology observations, an LI-6400XT portable photosynthesis system was used to quantify the photosynthetic traits of the alfalfa crop and to measure the diurnal variability in $g_s$. Photosynthetic traits were derived from photosyntesis response curves to PAR and to $C_i$, known as "A-PAR and A-$C_i$ response curves". Three A-PAR curves were measured at ambient temperatures ranging from 21 ºC to 27 ºC among the three curves and a constant ambient $CO_2$ concentration of 400 ppm. The PAR approximate set points were 0, 10, 20, 40, 60, 120, 250, 500, 1000, 1200 and 1500 $\mu$mol m$^{-2}$ s$^{-1}$. Five A-$C_i$ response curves were measured at saturating light ($\approx$ 1500 $\mu$mol photons m$^{-2}$) and ambient leaf temperatures ranging from 21 ºC to 28.5 ºC with $C_i$ approximate set points of 50, 75, 100, 125, 175, 250, 400, 600, 800, 1000 and 1200 ppm. These measurements enabled the calculation of parameters that constrain the specific photosynthesis response of the alfalfa crop. The three fitted parameters, which are in the A-$g_s$ scheme, were (1) the $CO_2$ maximal primary productivity at 298 K ($A_{max,298}$), (2) the mesophyll conductance at 298 K ($g_{m,298}$) and (3) the light use efficiency at low-light conditions ($\alpha_0$). Finally, another parameter called

the "high reference temperature for mesophyll conductance" was increased to better reflect the warm growth conditions of the alfalfa crop. All the parameters of the A-$g_s$ model used in our study are indicated in Table 2.3. The observed and modelled response curves can be found in Appendix 2.A.

The second type of measurements were diurnal time series of $g_s$. We measured 221 leaves from 05:30 UTC to 20:00 UTC. To mimic the field conditions, we set PAR inside the chamber to the values measured outside. In practice, PAR values were updated in varying time steps of 15 min to 1 h to reflect the values measured by a PAR sensor located above the canopy. Based on the $g_s$ and on the in-canopy sensors present on the field, diurnal curves of $TR_{leaf}$ and $A_n$ were derived. These measurements have been termed as "post-processed observations". The processing procedure is based on (1) Fick's law of diffusion applied to the stomatal pores, (2) assuming thermal equilibrium between the air temperature measured inside the canopy and the leaves, and (3) assuming a neglegible leaf boundary layer resistance. Further details about the procedure to calculate the post-processing of observations can be found in Appendix 2.A.



Similarly to the canopy level, we calculated $r^2$, the $p$ value, and RMSE to compare model results and observations. Additionally, to facilitate the visual comparison of the time series, a simple moving average was computed by calculating an unweighted average considering the 15 previous and the 15 posterior observations for each leaf gas exchange data point.

**Table 2.3:** Parameters of the A-$g_s$ model used for the numerical experiments. Parameters shown in bold font were modified from the default values used in the CLASS model (Vilà-Guerau de Arellano et al., 2015). For these modified parameters, the default values are shown within parenthesis and in normal font.

| **Variables** | | **Values** |
|---|---|---|
| Symbol | Definition | |
| $a_d$ (kPa$^{-1}$) | Regression coefficient to calculate $C_{frac}$ | 0.07 |
| $f_0$ (-) | Maximum value of $C_{frac}$ | 0.89 |
| $g_{min}$ (m s$^{-1}$) | Cuticular conductance to water vapor | $0.25 \cdot 10^{-3}$ |
| $A_{max,298}$ ($\mu$mol m$^2$ s$^{-1}$) | **$CO_2$ maximal primary productivity at 298 K** | **68.74** (50) |
| $g_{m,298}$ (mm s$^{-1}$) | **Mesophyll conductance at 298 K** | **10.2** (7.0) |
| $\alpha_0$ (mg J$^{-1}$) | **Light use efficiency at low light conditions** | **0.0265** (0.0170) |
| $\Gamma_{298}$ (ppm) | $CO_2$ compensation concentration at 298 K | 68.5 |
| $K_x$ (m m$^{-1}$) | Extinction coefficient of PAR inside the canopy | 0.7 |
| $Q_{10,CO2}$ (-) | Temperature response coefficient for $\Gamma$ | 1.5 |
| $Q_{10,gm}$ (-) | Temperature response coefficient for $g_m$ | 2.0 |
| $Q_{10,Ammax}$ (-) | Temperature response coefficient for $A_{mmax}$ | 2.0 |
| $T_{1,gm}$ (K) | Low reference temperature for $g_m$ | 278 |
| $T_{1,Ammax}$ (K) | Low reference temperature for $A_{mmax}$ | 281 |
| $T_{2,gm}$ (K) | **High reference temperature for $g_m$** | **306** (301) |
| $T_{2,Ammax}$ (K) | High reference temperature for $A_{mmax}$ | 311 |

### 2.2.5 Tendency equations for the leaf gas exchange

We derived tendency equations for the leaf gas exchange as a method for analyzing the temporal dynamics of the water and $CO_2$ exchange. These equations describe the time evolution of the leaf gas exchange variables as a function of the time evolution of the environmental variables. Three tendency equations are proposed: (1) one for $g_s$, (2) one for $A_n$, and (3) one for $TR_{leaf}$. As a starting point to derive the tendency equations, we used the A-$g_s$ model (see González-Armas et al. (2024) for a full derivation). Therefore, the set of environmental variables used in the tendency equations is the same as that used in the A-$g_s$ model, which is: (1) PAR, (2) $C_a$, (3) VPD, (4) air $T$ and (5) $w_2$. Because, according to our formulation, these five environmental variables control the leaf gas exchange, we refer to them as "environmental drivers" (of the leaf gas exchange). Although the tendencies were calculated considering all five environmental drivers, in this research we ignore the diurnal dynamics of $w_2$ as $w_2$ can be assumed constant in time in the root zone during the case study for La Cendrosa Alfalfa field. This assumption was based on measurements of soil volumetric water content at 30 cm depth on the field, which showed a diurnal variation lower than 0.01 $m^3$ $m^{-3}$, and on the knowledge that the roots were likely to be deeper than 30 cm. The tendency equation for a leaf gas exchange variable $Y$ (i.e., $g_s$, $A_{n,l}$, or $TR_{leaf}$) has the following form:

$$\frac{dY}{dt} = \overbrace{\frac{\partial Y}{\partial PAR}\frac{dPAR}{dt}}^{\text{Radiative term}} + \overbrace{\left(\frac{\partial Y}{\partial T}\right)_{VPD}\frac{dT}{dt}}^{\text{Temperature term}} + \overbrace{\left(\frac{\partial Y}{\partial VPD}\right)_{T}\frac{dVPD}{dt}}^{\text{Vapor pressure deficit term}} + \overbrace{\frac{\partial Y}{\partial C_a}\frac{dC_a}{dt}}^{\text{Ambient } CO_2 \text{ term}} \tag{2.4}$$

The left-hand side (LHS) of equation (2.4) describes the total rate of change in time of the generic leaf gas exchange variable $Y$. Taking as an example $g_s$, this first term would indicate the rate of opening or closure of the stomatal pores. The right-hand side (RHS) of the equation is composed of four terms which quantify the rate of change of Y due to temporal changes of PAR, $T$, VPD and $C_a$. Using the same example of $Y = g_s$, the terms would quantify the contribution to the total rate of opening or closure of the stomatal pores that is attributed to the temporal changes of PAR, $T$, VPD or $C_a$. For instance, the radiative term of $g_s$ tendency equation in the morning would indicate how much of the stomatal opening is happening because radiation is increasing. Each of the terms on the RHS of the equation is the product of the partial derivative of $Y$ with respect to a particular environmental driver (which give information of the sensitivity of Y to a change in that environmental driver) multiplied by the total time derivative of the environmental driver. The sub-index notation for the $T$ term (with VPD as sub-index) and for the VPD term (with $T$ as sub-index) indicates that the partial derivative were calculated considering the variable that appears as the sub-index to be constant. This notation was inspired in the thermodynamics notation for partial derivatives, and although it may seem redundant because of the definition of partial derivatives, it is deemed necessary to indicate that we considered T and VPD as independent variables. Another choice of independent variables was also possible. For instance, specific humidity or water vapor pressure could have been used in place of VPD. This is further explored in González-Armas et al. (2024). As it is defined now, the temperature term only includes the plant physiolog-

**Table 2.4:** Numerical experiments of this study. The last three rows present the three experiments with ABL perturbations.

| Cases | Perturbation | Timing [UTC] |
|---|---|---|
| Control | None | |
| PAR-CLD | Decrease in PAR | 10:00-14:00 |
| VPD-ENT | Entrainment of drier air from the free troposphere | 06:20-15:35 |
| TEM-ADV | Advection of cold air | 11:15-15:35 |

ical processes dependent on $T$ such as the $T$ dependency of mesophyll conductance and of maximal primary productivity. The total time derivatives of the environmental drivers (e.g., $\frac{dPAR}{dt}$) were numerically derived from the modeling experiment output.



### 2.2.6 Three numerical experiments with ABL perturbations

Apart from the Control experiment, three additional numerical experiments were performed. They were created to analyze how ABL processes that perturb the environmental drivers (i.e., PAR, $T$, VPD and $C_a$) change the diurnal dynamics of water and $CO_2$ exchange at leaf and canopy level. The new experiments were inspired on ABL processes that occurred at another time during LIAISE. The three experiments are (1) PAR-CLD, which represents surface radiative changes due to a cloud passage (Mol et al., 2023); (2) VPD-ENT, which represents entrainment of dry air masses from the free troposphere to the ABL (van Heerwaarden et al., 2009); and (3) TEM-ADV which represents advection of cold air masses (Mangan et al., 2023a). Table 2.4 summarizes the type of perturbation of each experiment and the time when the perturbation was effective.

In the PAR-CLD experiment, surface PAR was reduced about 25 % of its value at midday, representing the radiative effect of a cloud casting a shadow on the surface (Fig. 2.2a). The magnitude of the reduction of PAR was based on observations during another day of the campaign (24 July 2021; Fig. 2 in González-Armas et al. (2024)) on which high clouds were present. In the VPD-ENT experiment, we imposed a drier free troposphere (compared with the control), which caused entrainment of drier air masses in the ABL (Fig. 2.2b). The magnitude of the mixing ratio in the free troposphere was 2 $g_{water}$ $kg_{air}^{-1}$ drier than the control case and represented a range similar to the one investigated by van Heerwaarden et al. (2009). Finally, in the TEM-ADV experiment, we imposed strong cold air advection (Fig. 2.2c). The magnitude of the cold air advection ($\approx$ -2.7 K $h^{-1}$ at its maximum) was based on the estimations of cold advection associated with the sea breeze that arrived in the region at 18:30 UTC during the study day (Mangan et al. (2023a); Fig. 2.A.1).

To analyze the diurnal dynamics for the three perturbed numerical experiments, we compared the perturbed experiments against the control experiment in two ways: the first was to calculate the changes in the time-averaged leaf and canopy variables, and the second was to compare the changes in the tendencies terms.

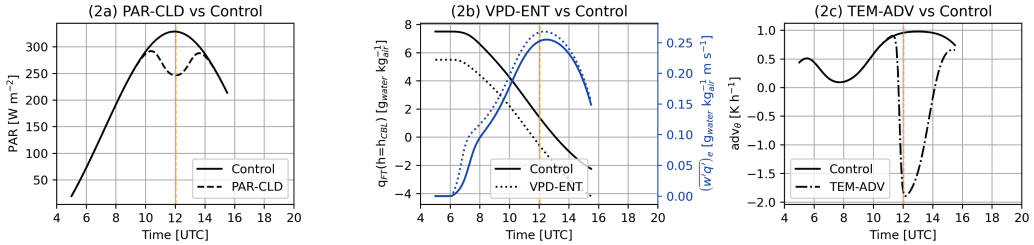



**Figure 2.2:** Atmospheric changes imposed in the three perturbed experiments compared with the control simulation. Time series of (a) PAR for the PAR-CLD and control experiments, (b) specific humidity of tropospheric air and entrainment flux of specific humidity for the VPD-ENT and control experiments, and (c) temperature advection the for TEM-ADV and control experiments. Vertical dashed orange lines indicate solar noon.

The changes in the time-averaged variables were calculated as the mean percentage change of the leaf and canopy variables considering all the simulated hours. The mean percentage change, $P_{X,exp_i}$, represents the change of variable X of the $i$th experiment (exp$_i$) compared with the control experiment. It was calculated as follows:

$$P_{X,exp_i} = \frac{\int_{t_{ini}}^{t_{fin}} X_{exp_i} dt}{\int_{t_{ini}}^{t_{fin}} X_{Control} dt} \cdot 100 = \frac{< X_{exp_i} >_t}{< X_{Control} >_t} \cdot 100, \tag{2.5}$$

where $< X >_t$ is the temporal mean of variable $X$, $t_{ini}$ for the initial time, and $t_{fin}$ for the final time. $P_{X,exp_i}$ was calculated for seven variables. The first three represented the leaf level: $g_s$, $A_n$ and $\mathrm{TR}_{\mathrm{leaf}}$. The second three were analogous variables but considering the whole canopy: the $g_{surf}$, $A_{nc}$ and ET. Lastly, we included $-$NEE to quantify the effects of the soil on the total carbon canopy flux. The negative sign applied to NEE was used to have the same sign convention as $A_{nc}$. We did not considered the canopy transpiration ($\mathrm{TR}_{\mathrm{canopy}}$) because soil evaporation was negligible in our numerical experiments. As a consequence, ET was virtually equal to $\mathrm{TR}_{\mathrm{canopy}}$.

## 2.3 Results

### 2.3.1 Control case

*Environmental drivers of water and $CO_2$ gas exchange*

During the control day, there were no clouds and PAR was symmetric around solar noon (12:02:27 UTC), with a maximum value of 500 W m$^{-2}$ ($\approx$ 2200 $\mu$mol m$^{-2}$ s$^{-1}$); Fig. 2.3a. Observed $C_a$ was 480 ppm at 04:00 UTC and decreased rapidly in the morning until 08:00 UTC when $C_a$ stabilized around a relatively constant value of approximately 390 ppm (Fig.

2.3b). Observed potential temperatures varied among the heights inside (0.105 m) and above the canopy (3 m and mixed-layer value), Fig. 2.3c. Inside the canopy, the maximum potential temperature was acquired sooner than above the canopy. VPD was found to increase with height, reaching a maximum difference of approximately 1000 Pa between 0.105 m and 3 m (Fig. 2.3d). The model captured the diurnal and height-dependent variability observed for the environmental drivers except for $C_a$. For $C_a$ the model captured the magnitude of the diurnal variability but failed to capture its dynamics. Modeled $C_a$ decreased at a lower pace than observed $C_a$. As a consequence, modeled $C_a$ was larger than observed $C_a$, particularly in the morning. To explore the implications of this mismatch in our results, we carried out an additional numerical experiment (see González-Armas et al. (2024)). Possible explanations of this mismatch are discussed in Sect. 2.4.



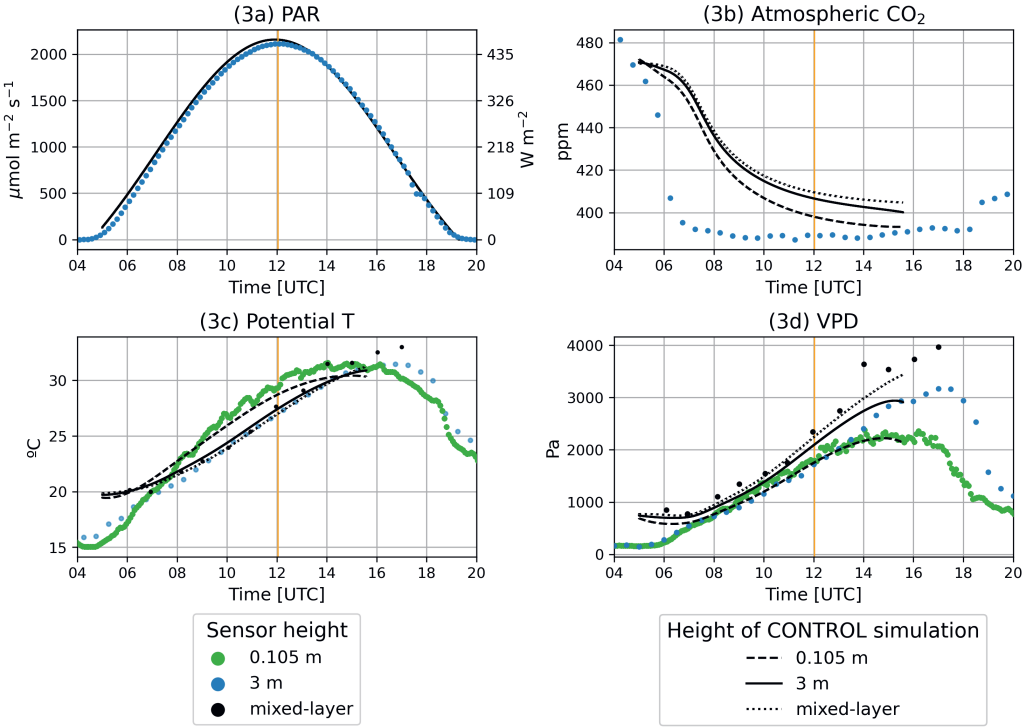



**Figure 2.3:** Diurnal time series of (a) PAR, (b) $C_a$, (c) potential temperature, and (d) VPD. Observations are depicted as dots. The sensor at 0.105 m height is located inside the canopy. Black dots shown potential T and VPD derived from radiosondes. The solid black lines correspond to the control experiment at 3 m, and the dashed line correspond to the control experiment at 0.105 m; the dotted line is the mixed-layer value. Vertical orange lines depict the solar noon. Direct and diffuse componenets of radiation can be found in González-Armas et al. (2024).

*Leaf gas exchange*

Observed $g_s$ showed the highest values in the morning, reaching a maximum value of approximately 0.020-0.030 m $s^{-1}$ ($\approx$ 1.00-1.20 mol $m^{-2}$ $s^{-1}$) at 10:00 UTC and declined afterwards until the end of the day (Fig. 2.4a). Modeled $g_s$ was at a maximum at the same time as the observed $g_s$ and showed a relatively weak but significant correlation with the observations ($r^2$ = 0.223, p ¡ 0.001). Observed and modeled $A_n$ followed closely the diurnal pattern of PAR (Fig. 2.3a), achieving maximum values approximately at solar noon between 12:00 and 13:00 UTC (Fig. 2.4b). Model results showed a significant correlation with the post-processed observations ($r^2$ = 0.383, $p$ ¡ 0.001). Finally, $TR_{leaf}$ also increased in the morning and decreased in the afternoon, with a maximum value achieved towards the afternoon between 12:45 and 14:00 UTC (Fig. 2.4c). Model results showed a significant and high correlation ($r^2$ = 0.677, $p$ ¡ 0.001) with post-processed observations, although model results overestimated maximum $TR_{leaf}$ compared to the post-processed observations. Comparing the modeled leaf gas exchange variables with the observed moving averaged variables, we noticed that the diurnal pattern is well captured, thus, suggesting that the relatively low correlations were partly due to the scatter of observations. A more elaborate comparison of the observations and model results of the leaf gas exchange can be found in González-Armas et al. (2024).

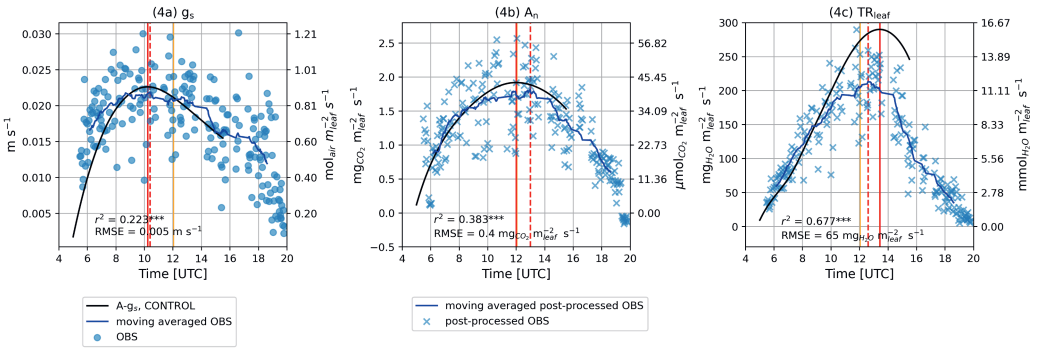



**Figure 2.4:** Diurnal time series of (a) $g_s$, (b) $A_n$, and (c) $TR_{leaf}$ for the control experiment. Direct observations are depicted by blue dots, whereas post-processed observations are depicted in blue crosses. Moving averaged observations and post-processed observations are indicated with a blue line. Model results of the control experiment are depicted by black solid lines. Vertical solid orange lines depict solar noon. The time when the maximum value of the leaf gas exchange variable at hand was achieved is depicted by vertical solid red lines for model results and vertical dash red lines for observations or post-processed observations.

*Canopy level gas exchange*

Observed NEE was positive before 06:00 UTC, indicating a net transport of $CO_2$ from the surface to the atmosphere (Fig. 2.5a), which suggests that ecosystem respiration was providing

$CO_2$ to the atmosphere. From 06:00 until 18:00 UTC, the observed flux was negative, acquiring a minimum value between 11:00 and 12:00 UTC. The diurnal negative NEE indicated a net transport of $CO_2$ from the atmosphere to the surface, suggesting that the photosynthesis of the crop was dominant over respiration processes. Modelled NEE had a strong and significant correlation with observations ($r^2$ = 0.89 and $p$ ¡ 0.001). Additionally, the time at which the minimum NEE was attained matched well between observations and model results. Observed soil respiration was between 4.5 and 9 $\mu$mol $m^{-2}$ $s^{-1}$ during the day, which coincided with the range reproduced by the model. Observed ET acquired a maximum value of 6.5 mmol $m^{-2}$ $s^{-1}$ that stayed relatively constant between 11:00 and 15:00 UTC. This plateau was not reproduced by the model, which peaked at approximately 12:45 and then declined. Similar to the observation at leaf level, modeled ET was higher than observed ET. The overestimation of modeled ET was of the same magnitude than the observed energy budget non-closure. Despite the apparent differences, modeled ET had a strong and significant correlation with observed ET ($r^2$ = 0.95 and $p$ ¡ 0.001) (Fig. 2.5).



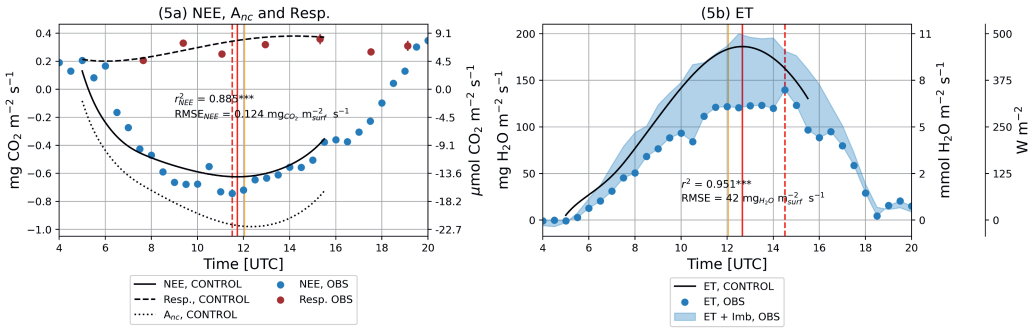



**Figure 2.5:** Diurnal time series of (a) NEE, -$A_{nc}$ and soil respiration (Resp.); and (b) ET and latent heat flux (LE). The 30 min averaged observations from the EC system are depicted in blue dots, whereas model results are depicted by different line styles. Respiration observations are depicted by red dots with an error bar that represents the standard error of the mean. The measured surface energy budget non-closure is depicted by a shaded space covering the area from the measured ET or LE value to the measured ET or LE value plus the measured surface energy budget non-closure. Vertical solid orange lines depict solar noon. The times when the maximum of NEE and ET was achieved are depicted by vertical solid red lines for model results and vertical dashed red lines for observations or post-processed observations.

*Tendencies of the leaf gas exchange*

The total tendencies of $g_s$, $A_n$ and $TR_{leaf}$ (LHS of Eq. (2.4)) described the diurnal dynamics observed in the modeled leaf gas exchange variables (Sect. 2.3.1). These dynamics consisted of an increase of the leaf gas exchange variables (positive total tendency term) until reaching a maximum (null total tendency term), which occurred in the morning for $g_s$, at noon for $A_n$, and in the afternoon for $TR_{leaf}$, followed by a decrease until the end of the simulation time

(negative total tendency term). The sum of the partial tendency terms (RHS of eq. (2.4)) matched exactly the total tendency term (LHS of eq. (2.4)) for $g_s$, $A_n$, and $TR_{leaf}$ (see the overlapping of the solid black line and the grey dashed line in Fig. 2.6a, 2.6b, and 2.6c). This verification guaranteed that the temporal evolution of $g_s$, $A_n$, and $TR_{leaf}$ was fully determined by the temporal evolution of PAR, T, VPD, and $C_a$. Focusing on the partial terms, the radiative terms (PAR terms) were found to be the primary contribution to the total terms of the leaf gas exchange variables, especially for $g_s$ and $A_n$. The temporal changes in PAR tended to increase the leaf gas exchange variables before noon (positive PAR terms) and to decrease it after noon (negative PAR terms). The $T$, VPD, and $C_a$ terms added secondary temporal dynamics to the contribution of the PAR terms.

For $g_s$ (Fig 2.6a), the VPD term was negative from 07:00 to 15:00 UTC, indicating that the diurnal increase in VPD (Fig. 2.3d) led to smaller $g_s$ values. This effect was partially compensated by the $T$ and $C_a$ terms which were both positive. Therefore, both the increase in $T$ due to the diurnal warming of the atmosphere (Fig. 2.3c) and the decrease in $C_a$ due to the entrainment of $CO_2$-depleted air from the free troposphere (Fig. 2.3b) contributed to increase $g_s$. The net effect of these opposing terms resulted in the maximum of $g_s$ being achieved 2 h before solar noon. For $A_n$ (Fig. 2.6b), the diurnal increase in $T$ favored higher $A_n$ values, increasing the $A_n$ rate specially in the morning (positive $T$ term). Both the VPD and $C_a$ terms were relatively small compared to the PAR and $T$ terms, which suggested that the diurnal dynamics of $A_n$ were relatively insensitive to diurnal changes in VPD and $C_a$. Finally, for $TR_{leaf}$ (Fig. 2.6c), the $T$, VPD and $C_a$ terms tended to further increase $TR_{leaf}$ values. The $T$ and VPD terms were found comparable and greater that the PAR term for several hours in the morning and early afternoon. The combined effect of the $T$, VPD and $C_a$ terms was responsible of delaying the maximum $TR_{leaf}$ from occurring at solar noon (if the model would be sensitive only to PAR temporal changes) to 13:30 UTC. The results of the partial tendency terms highlighted that diurnal temporal changes in PAR primarily forced the net diurnal dynamics of the leaf gas exchange variables, whereas diurnal temporal changes in $C_a$ were found to be the least important factor for describing the leaf gas exchange dynamics.

### 2.3.2 Three experiments with ABL perturbations

*Environmental drivers of water and $CO_2$ gas exchange*

The three experiments with ABL perturbations (PAR-CLD, VPD-ENT, and TEM-ADV) modified the environmental drivers of the water and $CO_2$ exchange compared with the control simulation, except for $C_a$, which remained almost equal to the control for all the perturbed experiments (Fig. 2.7a). The PAR-CLD experiment described a cloud passage which reduced surface PAR (Fig. 2.2a). The cloud passage also modified the surface energy balance during and after the cloud shade. As a consequence, $T$ and VPD were reduced up to 1 K and 250 Pa, respectively (Fig. 2.7b and c). The VPD-ENT experiment, which described a drier free troposphere than the control experiment, only modified VPD which increased up to 250 Pa (Fig. 2.7c). Lastly, the TEM-ADV experiment, which described strong cold air advection, reduced

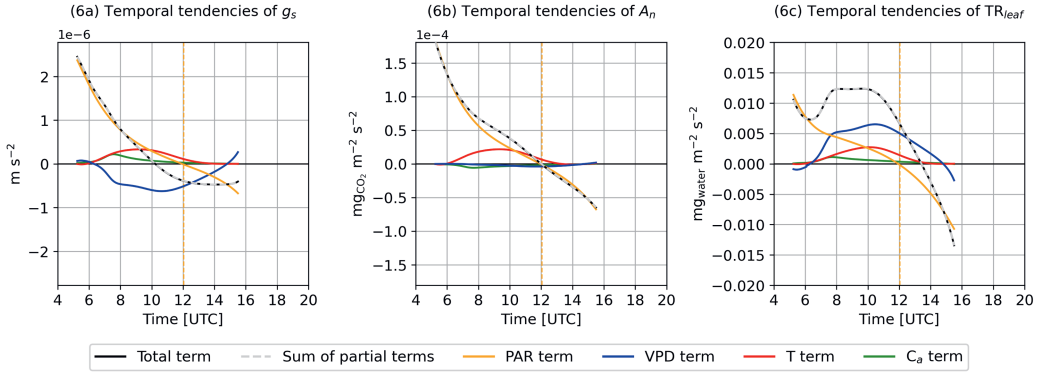



**Figure 2.6:** Temporal evolution of the tendencies of (a) $g_s$, (b) $A_n$, and (c) $TR_{leaf}$. Black lines depict the total tendency terms, dashed grey lines depict the sum of the partial terms, and the other solid colored lines depict the partial tendency terms due to temporal changes of PAR (orange lines), VPD (blue lines), $T$ (red lines), and $C_a$ (green lines). The vertical dashed orange lines depict solar noon.

not only $T$ by up to 4 K but VPD by up to 1000 Pa (Fig. 2.7b and c).

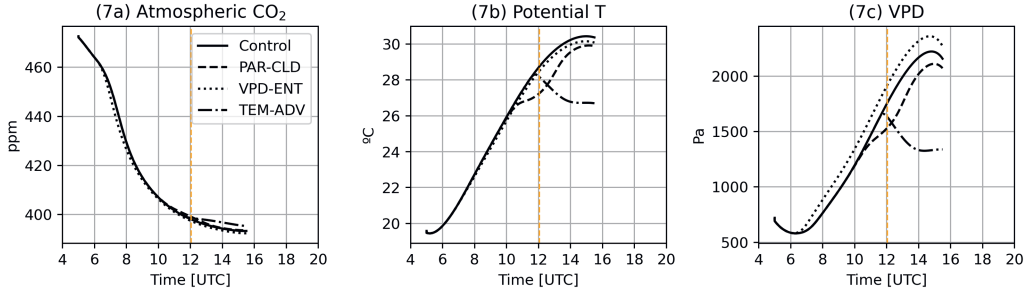



**Figure 2.7:** Temporal evolution of (a) $C_a$, (b) potential T, and (c) VPD at 0.105 m for the four experiments. The solid black line corresponds to the control experiment, dashed black line to the PAR-CLD experiment, the dotted black line to the VPD-ENT experiment, and the dashed-dotted black line to the TEM-ADV experiment. Vertical dashed orange lines depict solar noon.

*Leaf and canopy gas exchange*

Compared with the control experiment, the changes in the environmental drivers led to changes in the leaf and canopy variables that describe the water and $CO_2$ exchange. The mean values of the exchange variables changed by up to 11 % compared with the control experiment (Fig. 2.8). For PAR-CLD, there was a slight reduction of stomatal conductance and surface conductance ($P_{g_s}$, $P_{g_{surf}} >$ -3 %), a moderate reduction of the assimilated $CO_2$ by the vegetation ($P_{A_n}$, $P_{A_{nc}} <$ - 3 %), and a strong reduction in the water exchange at leaf and

canopy levels ($P_{TR_{leaf}}$, $P_{ET} <$ -5 %). For VPD-ENT, a moderate reduction in stomata and surface conductance was reported ($P_{g_s}$, $P_{g_{surf}} \approx$ -3 %), whereas $TR_{leaf}$ and ET were moderately increased ($P_{TR_{leaf}}$, $P_{ET} >$ 3 %). $A_n$ and $A_{nc}$ barely changed compared to Control experiment ($|P_{A_n}|$, $|P_{A_{nc}}| <$ 2 %). Lastly, for TEM-ADV there was a strong increase in stomatal conductance and surface conductance ($P_{g_s}$, $P_{g_{surf}} >$ 7.5 %), a strong decrease in $TR_{leaf}$ ($P_{TR_{leaf}} <$ -5 %), and a moderate decrease in ET ($P_{ET} <$ -3 %). Similar to the VPD-ENT experiment, $A_n$ and $A_{nc}$ barely changed in comparison with the control experiment ($|P_{A_n}|$, $|P_{A_{nc}}| <$ 2 %).

When comparing the experiments, all of them modified moderately or strongly $TR_{leaf}$ and ET, whereas only PAR-CLD experiment modified moderately $A_n$ and $A_{nc}$. Comparing the trends between leaf and canopy level for each experiment ($g_s$ versus $g_{surf}$, $A_n$ versus $A_{nc}$, and $TR_{leaf}$ versus ET), we generally observed similar patterns in the magnitude and sign of the change between the leaf- and canopy-level variables, with two remarkable exceptions. The first exception was the small decrease in $A_n$ at leaf level opposed to a small increase in $A_{nc}$ at canopy level for the VPD-ENT experiment compared with the control. Further analysis revealed that the decrease in VPD for VPD-ENT was leading to a reduced $C_i$ which affected the $CO_2$ exchange differently at the leaf level and canopy level. At leaf level, the decrease in $C_i$ implied lower maximum rates of photosynthesis because less $CO_2$ was available to perform photosynthesis, which finally lead to a smaller net assimilation rate. However, at canopy level, the decrease in $C_i$ was accounted for with a diffusion type of equation (equation 2.3), which resulted in a higher $A_{nc}$ due to a higher $CO_2$ gradient ($C_a - C_i$). The second unexpected result was the large decrease in $TR_{leaf}$ at leaf level compared to the moderate decrease in ET at canopy level for TEM-ADV. Further exploration revealed that the change in magnitude was partially attributed to the effect of the wind in the exchange which was only accounted for at canopy level. Although horizontal wind was equal for all experiments, the vertical component was greater for TEM-ADV than for the control, which implied a smaller aerodynamic resistance and favourable conditions for the exchange of water for TEM-ADV with respect to the control. This effect was partially responsible of a smaller decrease on ET than on $TR_{leaf}$.

*Tendencies of the leaf gas exchange*

Analyzing the tendency terms of the three perturbed ABL experiments showed clear separation between the effects of the environmental drivers on $A_n$ and $TR_{leaf}$ (Fig. 2.9). The reduction in $A_n$ for the PAR-CLD experiment (Fig. 2.9a) followed closely the shape of the decrease in PAR which occurred roughly between 10:00 and 14:00 UTC (Fig. 2.2a). Accordingly, the difference of the net total tendency terms between PAR-CLD and control followed closely the difference of the radiative terms (Fig. 2.9b). This suggests that the dip in $A_n$ was mostly attributed to the radiative changes. As a second-order effect, the difference in the temperature terms indicated that the temperature variability during the cloud also contributed to reducing $A_n$. For VPD-ENT and TEM-ADV, the $A_n$ diurnal dynamics remained quite similar to those of the control, and hence the difference of the tendencies terms were much smaller that those of PAR-CLD.

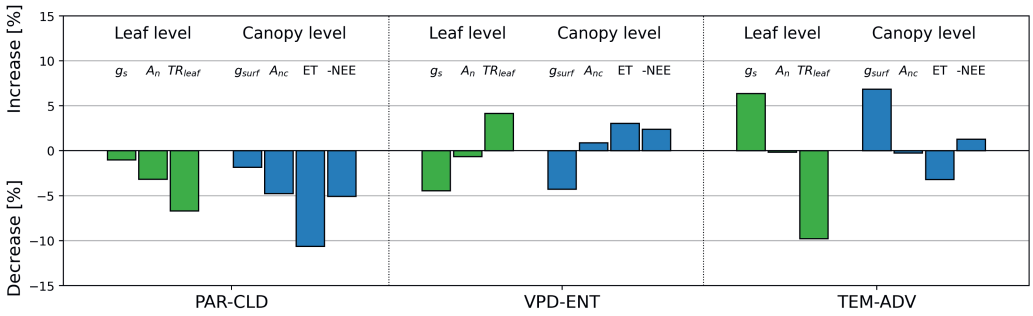



**Figure 2.8:** Bar plot of the mean percentage change of seven leaf and canopy variables of the perturbed experiments with respect to the control experiment. The set of variables is composed of three leaf gas exchange variables ($g_s$, $A_n$, and $TR_{leaf}$), indicated by green bars, and of four canopy gas exchange variables ($g_{surf}$, $A_{nc}$, ET, and -NEE) in blue bars.

Similarly to the reduction of $A_n$ for PAR-CLD, the reduction in $TR_{leaf}$ for the PAR-CLD (Fig. 2.9e) experiment was strongly influenced by the reduction in radiation (Fig. 2.9f). However, in this case both the temporal dynamics of temperature and VPD during the cloud contributed to the reduction in $TR_{leaf}$ (Fig. 2.9f). For the VPD-ENT experiment, $TR_{leaf}$ was higher than in the control between 06:00-07:00 UTC and the end of the simulation. The difference in the total tendency term was very similar to the difference in the VPD term, indicating that the VPD diurnal variability was responsible of the increase $TR_{leaf}$ (Fig. 2.9g). Lastly, $TR_{leaf}$ for the TEM-ADV experiment was strongly reduced compared with the control experiment after the advection started (Fig 2.9e). This reduction resulted from the contribution of the reduction both in VPD and $T$, with the dynamics of VPD being roughly 3 times more important than the dynamics of temperature (Fig 2.9h). Interestingly, our tendencies showed that PAR contributed positively to $A_n$ and $TR_{leaf}$ during the advection of cold air (Fig. 2.9d and h), even though PAR diurnal variability remained unchanged compared the control experiment. The positive value of the difference in PAR tendency terms for $TR_{leaf}$ indicated that temporal changes in radiation were contributing less to the decrease of $TR_{leaf}$ in TEM-ADV compared with the control. This effect was related to the lower contribution of radiative variability to the changes in stomatal conductance, which were predominantly influenced by the drop in VPD.

## 2.4 Discussion

The framework proposed in this research was constituted by observations and a coupled model with descriptions at leaf, canopy, and ABL levels and by tendency equations of the modeled leaf gas exchange (for net assimilation rate, stomatal conductance, and leaf transpiration). Our research strategy resembled that of Vilà-Guerau de Arellano et al. (2020) and Mangan et al. (2023a), in that a range of spatial scales were integrated to investigate

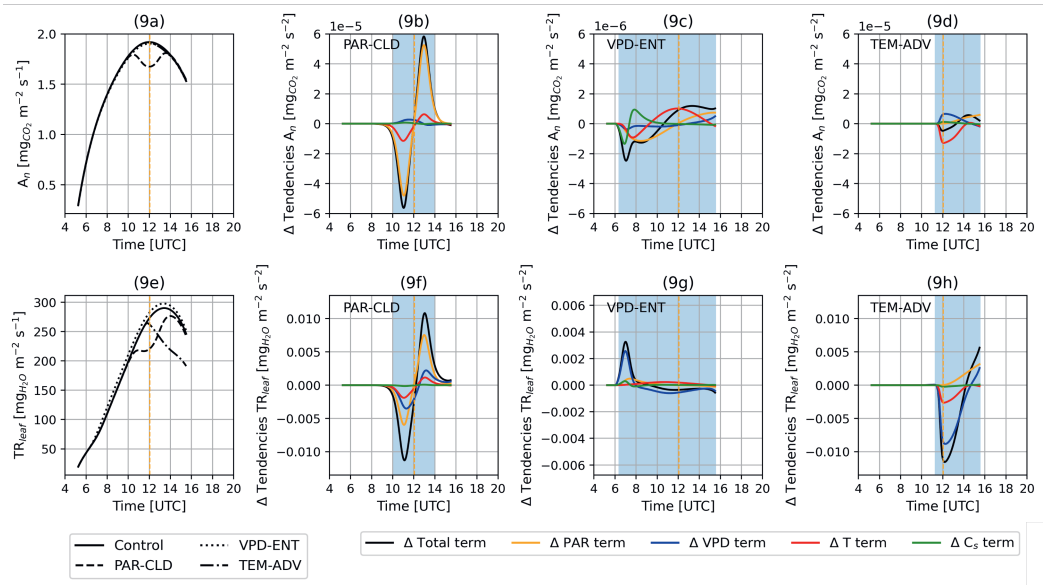



**Figure 2.9:** Diurnal evolution of (a) $A_n$ and (e) $TR_{leaf}$ for the control (solid black line), PAR-CLD (dashed black line), VPD-ENT (dotted black line), and TEM-ADV (dash-dotted black line) experiments. Diurnal evolution of the difference in $A_n$ tendencies terms of each perturbed experiment against the control experiment is shown in (b) for PAR-CLD, (c) for VPD-ENT, and (d) for TEM-ADV. The diurnal evolution of the difference in $TR_{leaf}$ tendencies terms between each perturbed experiment against the control experiment is shown in (f) for PAR-CLD, (g) for VPD-ENT, and (h) for TEM-ADV. Notice that the difference in the tendencies terms for VPD-ENT experiment is smaller than for PAR-CLD and TEM-ADV experiments. Because of that, the y axis of (c) is 10 times smaller than the y axis in (b) and (c), and the y axis of (g) is half the y axis in (f) and (h). Solar noon is indicated with a vertical dashed orange line. Time periods when the ABL perturbations were effective are shown as blue shades in panels (b), (c), (d), (f), (g) and (h).

the diurnal variability of turbulent fluxes. Additionally, a key element of the study is the comprehensiveness of the measurements (leaf gas exchange observations, surface turbulent fluxes, and ABL observations), which is considered suitable to progress in the investigation of the vegetation/ecosystem response to meteorological conditions and the effect of ecosystem responses on the atmospheric dynamics (land-atmosphere bi-directional feedbacks) (Helbig et al., 2021).

In this study, the coupled model CLASS was able to reproduce the observed diurnal variability of the environmental drivers for the study day excepting for the variability of $C_a$ (Fig. 2.3b). Unlike for VPD and $T$, $C_a$ measurements were only available at 3 m, and we did not have information about its vertical variability. The CLASS model assumes that $C_a$ is well mixed from the start of the numerical experiment. However, $C_a$ vertical profiles can depict strong vertical gradients during and after the morning transition from a stable ABL to an unstable and well-mixed ABL, as it has been previously observed over grass (Casso-Torralba et al., 2008). As a consequence, the initial observed $C_a$ values may not be representative of the initial convective ABL. To explore the impact that the mismatch between modeled and observed $C_a$ had on our results, we performed an additional numerical experiment in which modeled $C_a$ resembled closely observed $C_a$ (see González-Armas et al. (2024)). We found that the leaf gas exchange tendencies retained their main features, and they led to the same conclusions of the study.



Regarding the leaf level, observations of stomatal conductance were scattered, which led to scatter in the post-processed observations of net assimilation and leaf transpiration (Sect. 2.3.1). This showed that randomly picked leaves within the alfalfa canopy at a same moment of the day gave values of stomatal conductance that differ from each other. We attribute this spread to the different environmental conditions experienced by each leaf (e.g., sunlit and shaded leaves) and to differences in leaf properties (e.g., age or damage of leaves). Similar dependencies of leaf gas exchange on the sun or shade preconditioning of leaves and on the age of the leaves have been previously reported for a cotton crop by Echer & Rosolem (2015). Our modeled results did not represent this variability, as they were based on a single combination of the modelled PAR, atmospheric $CO_2$, T and VPD per time during the day and the same photosynthetic traits for all leaves. Despite the scatter, the moving averaged observations presented a magnitude and diurnal characteristics that were consistent with the model results such as the time of occurrence of maximum values.

Based on the modeled leaf gas exchange, tendency equations were used to quantify the effect of the diurnal dynamics of the environmental drivers on the dynamics of the leaf gas exchange. In that regard, the tendency terms informed about the modeled leaf gas exchange and are bounded by the assumptions of the same. An addition that could be made to the A-$g_s$ scheme is the temporal adaptation of the stomata to instantaneous changes in environmental conditions (Sellers et al., 1996; Vico et al., 2011; Sikma et al., 2018). Adaptation of the stomata could be important specially for fast radiative perturbations as those that have been observed and modeled in previous research (Kivalov & Fitzjarrald, 2018; Mol et al., 2023). Another feature that was not accounted for in the numerical experiments was the partition-

ing of shortwave radiation between its direct and diffuse components. This partitioning can be important because diffuse light is considered to increase the vegetative canopy that is receiving illumination, and therefore it can increase the net $CO_2$ assimilated by the canopy (Niyogi et al., 2004; Knohl & Baldocchi, 2008). During the LIAISE field campaign, direct and diffuse components of shortwave radiation were measured at La Cendrosa (Fig. 1 and Fig. 2 in González-Armas et al. (2024)). During the study day, the ratio of diffuse radiation to net radiation was approximately 15 %, categorized as a low diffusive regime according to Niyogi et al. (2004). Therefore, we anticipate minimal impact of the partitioning of the direct and diffuse components for the control experiment, on which we based the largest part of our conclusions. For the VPD-ENT and TEM-ADV numerical experiments, the partitioning of radiation remains consistent, suggesting a minor impact on our results. However, for the PAR-CLD numerical experiment, the ratio of diffuse radiation to net radiation could substantially change compared with the control because of the cloud. On a cloudy day during the campaign, the ratio of diffuse radiation to net radiation oscillated between 35 % and 100 %, with values larger than 60 % being categorized as high diffusive according to Niyogi et al. (2004), Fig.2 in González-Armas et al. (2024). Such cloud-induced changes in direct and diffuse partitioning could influence the $CO_2$ exchange, potentially leading to larger canopy $CO_2$ uptake in PAR-CLD compared with our results. For instance, Pedruzo-Bagazgoitia et al. (2017) found greater (up to 9 %) net assimilaton of $CO_2$ under thin clouds (with a cloud optical depth smaller than 3) than under clear sky in large-eddy simulations. We emphasize that the direct and diffuse partitioning is relevant for understanding the vertical profiles of light within the canopy, and therefore it is considered when upscaling the fluxes from the leaf level to the canopy level. However, the leaf tendencies as they have been presented here could still be coupled with a model that accounts for direct and diffuse components of radiation.

Tendency equations, similar to the ones presented here, have been proposed in the past for leaf transpiration (Jarvis & McNaughton, 1986), evapotranspiration (van Heerwaarden et al., 2010), and net ecosystem exchange (Pedruzo-Bagazgoitia et al., 2017) but with substantial differences with respect to our study. Jarvis & McNaughton (1986) used a similar approach to investigate the dependency of transpiration on stomatal conductance for scales ranging from $10^{-5}$ to $10^{5}$ m. The approach was different because it was not intended to analyze the temporal dynamics of the fluxes but to investigate the sensitivity of transpiration on stomatal conductance at different scales. Because of that, Jarvis & McNaughton (1986) used differential equations but not with respect to time. Additionally, the $CO_2$ fluxes were not investigated, and to the authors' knowledge, this is the first time that the tendencies have been calculated simultaneously for stomatal conductance, leaf transpiration, and net assimilation, providing a complete view of the leaf gas exchange. On the other hand, van Heerwaarden et al. (2010) calculated tendency equations for the canopy evapotranspiration and Pedruzo-Bagazgoitia et al. (2017) for the net canopy $CO_2$ assimilation. Both groups applied the approach to investigate diurnal dynamics in realistic field conditions. The approach of van Heerwaarden et al. (2010) was based on the Penman–Monteith equation combined with mixed-layer theory for CBL, whereas Pedruzo-Bagazgoitia et al. (2017) was based on the upscaled $CO_2$ flux given by the A-$g_s$ model (Eq. (2.3)). The main difference between those approaches and the one pre-

sented here is that we calculated the terms as a function of state primary variables, whereas van Heerwaarden et al. (2010) and Pedruzo-Bagazgoitia et al. (2017) did so for intermediate variables. For example, a term of the equation proposed by Pedruzo-Bagazgoitia et al. (2017) contained the temporal derivative of $C_i$, which may be more difficult to interpret and relate to environmental processes than changes in PAR, $T$, VPD, and $C_a$. We acknowledge that for certain research questions it may be relevant to use a different subset of independent variables. However, the choice of another subset is also possible within the proposed framework. Finally, we would like to comment on the possibility of combining tendency equations and observations. Whereas the previous cited research calculated tendencies with modeled results, Mangan et al. (2023b) calculated the LE tendencies derived by van Heerwaarden et al. (2010) and applied them to the coupled model CLASS but also to observations. By doing so, they could explore whether the model and observations agreed that certain processes impact LE in the same manner. In principle, a similar approach could be developed for the tendencies introduced in the current manuscript. Although observations will introduce a large scatter to the tendencies, a comparison between tendencies of the leaf gas exchange applied to modeled results and observations could provide an additional tool to assess the performance of the A-gs scheme apart from directly comparing leaf fluxes.



Returning to the initial research question (*To what extent do the diurnal dynamics of environmental drivers affect the diurnal dynamics of the water and $CO_2$ exchange at leaf and canopy level?*), we observed that the dynamics of stomatal conductance and net assimilation rate were primarily forced by the diurnal dynamics of radiation. As a second-order effect, the dynamics of net assimilation rate were affected by those of $T$ and the dynamics of stomatal conductance by those of $T$ and VPD. Leaf transpiration was affected to a similar extent by the dynamics of PAR, $T$, and VPD, with PAR dynamics being the most important factor in the early morning and late afternoon. The leaf gas exchange dynamics were less sensitive to dynamics of atmospheric $CO_2$ concentration than to the dynamics of PAR, $T$, and VPD. These results indicates that radiative perturbations (as those created by clouds shade) strongly affect the diurnal evolution of the assimilation rate, a fact that was further explored by PAR-CLD experiment. In fact, from all experiments, PAR-CLD was the one that modified most the net $CO_2$ assimilation rate, suggesting that the representation and understanding of clouds and their effects on the surface are a crucial factor to understand and represent diurnal variability of $CO_2$ fluxes (Vilà-Guerau de Arellano et al., 2023). Additionally, the PAR-CLD experiment showed that not only radiative changes but also associated temperature changes produced by a cloud shade can further reduced the net assimilation rate. Although the other experiments which represented entrainment of drier air and advection of cold air (VPD-ENT and TEM-ADV) did not significantly modified the net assimilation rate and gross primary productivity, they did modify the stomatal conductance, surface conductance, leaf transpiration, and evapotranspiration. Similar to what was reported by van Heerwaarden et al. (2009), entrainment of dry air under non-stressed soil water availability (VPD-ENT experiment) enhanced the water surface exchange. Lastly, the cold air advection experiment (TEM-ADV experiment) suggested that heat advection modifies leaf transpiration not only because the temperature changes but also due to the associated VPD changes.

To close the discussion, we mention some possible avenues for future work. We envision that the tendency equations can help to identify errors and shortcomings and to investigate limiting factors of the water and $CO_2$ exchange, represented in global models that explicitly include vegetation (Doutriaux-Boucher et al., 2009), in standard weather and climate land-surface models (Renner et al., 2021), and/or in new generation models such as land-surface models with multi-layer canopy (Bonan et al., 2021). One possible application of the method is to investigate the dependency of the temporal dynamics of the leaf gas exchange on soil moisture during a dry spell (Combe et al., 2016) or during and after a precipitation event. Soil moisture tendencies were not investigated in this manuscript because the alfalfa crop leaf gas exchange was not limited by its root soil water content. However, our modeling framework enables the calculation of the soil water content tendency. In principle, the tendency equations can be applied to timescales larger than 1 day such as weekly or monthly scale. Another application of the tendencies could be to analyze how the relations between the environmental drivers and the leaf gas exchange vary vertically inside a canopy. For instance, this analysis could help in understanding the causes of the different magnitude of the fluxes in the layers of a forest (e.g., understory versus top of the canopy). For this, the method could be applied to different layers within a multi-layer canopy (Bonan et al. 2021; Pedruzo-Bagazgoitia et al. 2023). Lastly, we would like to comment that the tendencies can be calculated with the output of models if the needed variables have been saved. Because of that, this interpretative tool is not computationally expensive once the model has been run.

## 2.5 Conclusions

In this research, we investigated the leaf and canopy exchange of water and $CO_2$ and its relationship with the diurnal dynamics of four environmental variables – photosynthetic active radiation (PAR), air temperature ($T$), vapor pressure deficit (VPD), and atmospheric $CO_2$ concentration ($C_a$) – for an irrigated alfalfa field. We based the research on 1 day during the field campaign Land Surface Interactions with the Atmosphere in the Iberian Semi-Arid Environment (LIAISE). We created a numerical control experiment based on the study day with a mixed-layer model (CLASS model; Vilà-Guerau de Arellano et al. 2015) that represents the convective atmospheric boundary layer (ABL) level, the canopy level, and the leaf level (with the A-$g_s$ model; Goudriaan et al. 1985; Jacobs 1994). In terms of observations, the leaf gas exchange was characterized with observations carried out with an LI-6400XT portable photosynthesis system. The canopy gas exchange was characterized with 30 minute averaged Eddy Covariance (EC) measurements and soil respiration measurements. To quantify the contributions of the diurnal dynamics of the environmental variables (PAR, $T$, VPD, and $C_a$) to the water and $CO_2$ exchange, we derived three tendency equations for stomatal conductance, net assimilation rate, and leaf transpiration. To investigate the effects of ABL processes on the local exchange, we created three additional numerical experiments with three ABL perturbations: (1) a reduction in surface radiation due to a cloud shade, (2) entrainment of drier air

masses from the free troposphere, and (3) a strong cold air advection.

We ascertain that the partial tendency terms of the leaf gas exchange fully accounted for the diurnal dynamics of the leaf gas exchange. An important finding was that PAR diurnal dynamics strongly influenced the diurnal dynamics of stomatal conductance and assimilated $CO_2$. When investigating the water and $CO_2$ exchange under the three perturbed experiments, we found that all experiments modified to a similar extent the exchange of water, whereas only the experiment of the decrease in surface radiation due to a cloud shade modified significantly the $CO_2$ exchange. The analysis with the tendency equations revealed first-order effects (e.g., radiation reduction due to a cloud shade diminishes net $CO_2$ assimilated) and second-order effects (e.g., the reduction in air temperature due to the cloud shade enhances the decrease in assimilated $CO_2$ due to less surface radiation) of the ABL perturbations on the exchange. We envision multiple applications of the proposed tendency equations, all of them orientated toward supporting the interpretation of model results of the exchange of water and $CO_2$ between the vegetation and the atmosphere, and toward investigating limiting and controlling factors of the exchange.

# 2.A Supplementary Information for Chapter 2

## 2.A.1 Heat and moisture advection

As mentioned in the paper, advection was estimated with measurements of wind, temperature, and specific humidity from an atmospheric weather station network operated by the *Servei Meteorològic of Catalunya*. More details on how the advection was calculated can be found in Sect. 4.2 "Mixed layer data: Model initialization & advection" and in Appendix B of the article by Mangan et al. (2023a). The unique differences between the cited article and the present study are that we used the daily advection estimation of the 17 July 2021 instead of the monthly average and that we smoothed the advection term by fitting the estimations to a continuous function. We smoothed the estimated advection to ensure that the temporal evolution of the environmental variables would be differentiable. This was desired to facilitate the interpretation of the tendency terms. The continuous function we used was:

$$adv_Y(t) = \sum_{i=1}^{i=2} A_{Y,i} \left( \frac{1}{1 + e^{-2k_{1,Y,i}(t - t_{ini,i})}} - \frac{1}{1 + e^{-2k_{2,Y,i}(t - t_{fin,i})}} \right) \quad ; \tag{2.A.1}$$

where $Y = \theta and q$, and $i$ represents the different advection regimes. In our case there were two regimes: (1) the warm and very dry regime from 05:00 to 08:00 UTC and (2) the very warm and slightly dry regime from 09:00 till 18:00 UTC. Coefficients $A_{Y,i}$, $t_{ini,i}$, $t_{fin,i}$, $k_{1,Y,i}$, and $k_{2,Y,i}$ represent the amplitude of the advection, the initial and final time when advection occurs, and the rate of change from no advection to advection and vice versa. Note that the sea breeze (advection of cold and wet air from 18:00 UTC onwards) was not imposed as a boundary condition in the experiments because at this time the atmosphere was not well-mixed and therefore we did not study that period. However, the smooth function of the sea breeze advection was also calculated for the temperature (not shown here), as it was imposed for TEM-ADV experiment.

The estimations of heat and moisture advection together with the smoothed advection terms used as boundary conditions in the control experiment are shown in Fig. 2.A.1 and Fig. 2.A.2.

## 2.A.2 Leaf level: photosynthesis response curves

Figures 2.A.3a and Fig. 2.A.3b show the observed and modeled net $CO_2$ assimilation curves to $C_i$ and PAR.

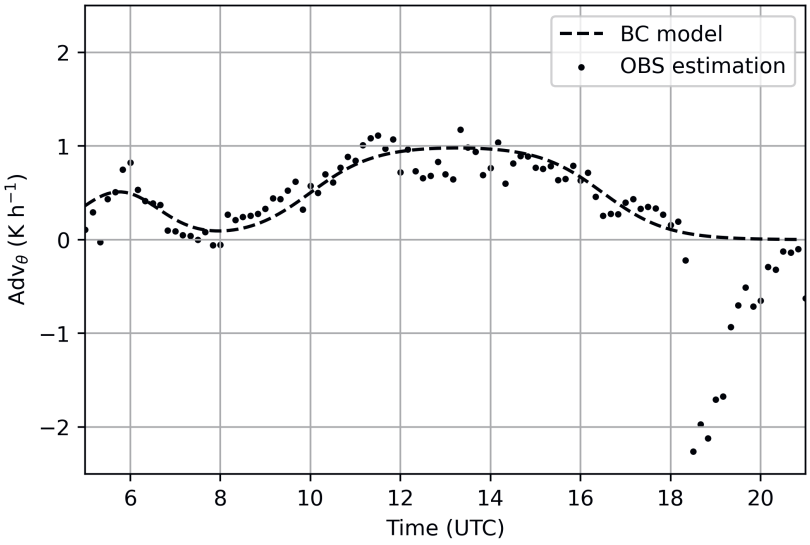



**Figure 2.A.1:** Temporal evolution of the temperature advection. Black dots indicate the estimations from the network of atmospheric weather stations and the dashed line shows the smoothed advection of temperature that was added as a boundary condition (BC) to the control experiment.

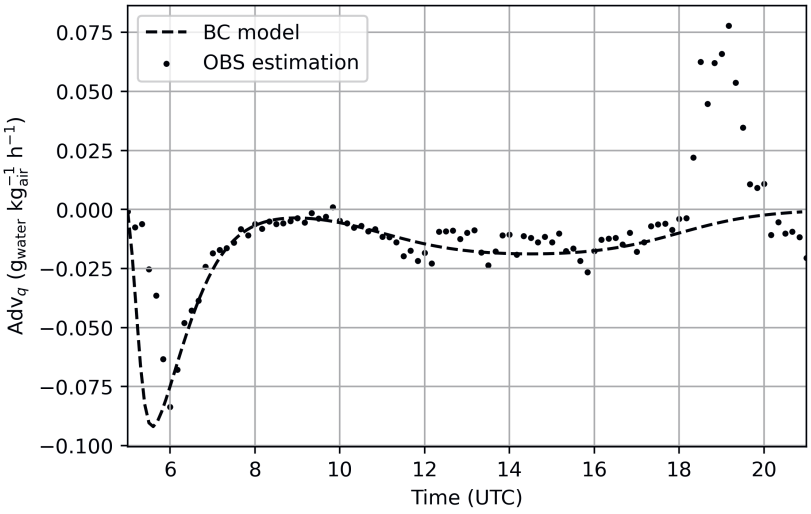



**Figure 2.A.2:** Same as 2.A.1 but for specific humidity advection.

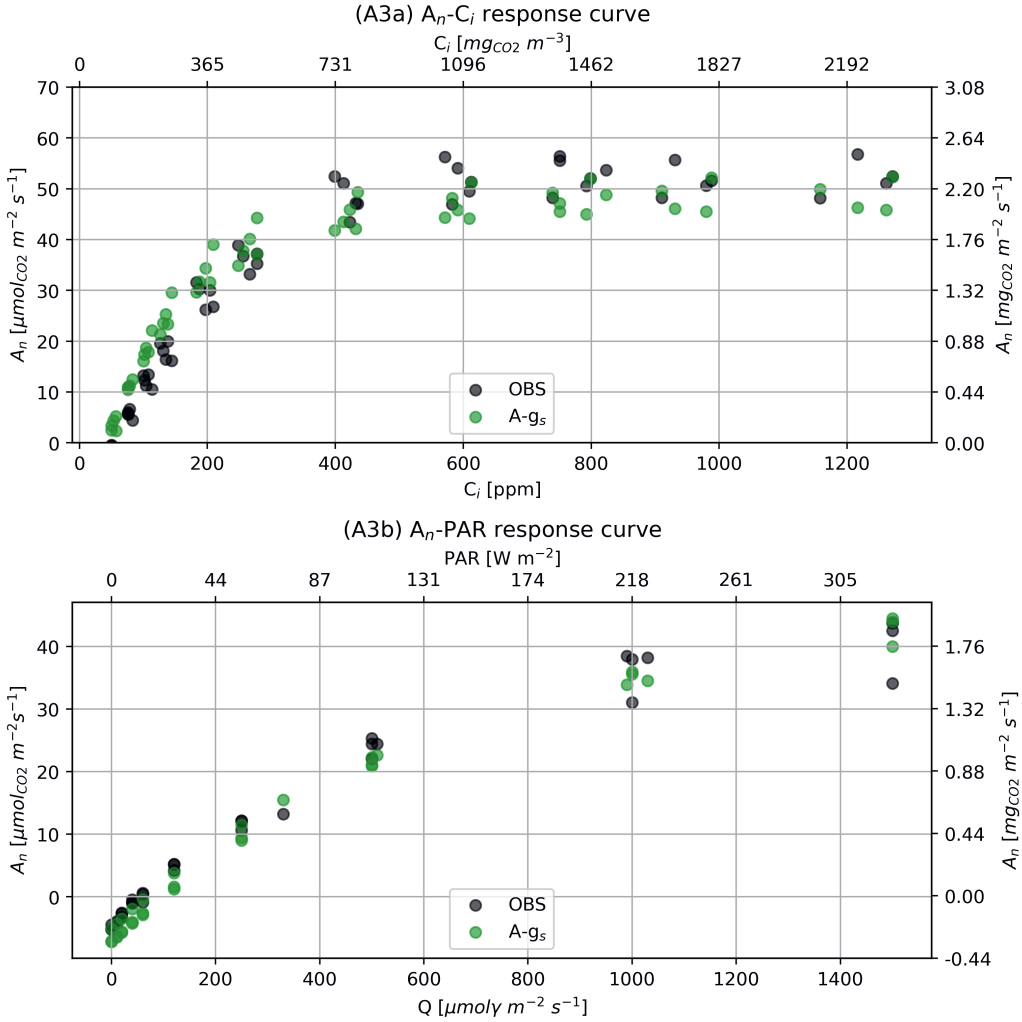



**Figure 2.A.3:** Response curves of net $CO_2$ assimilation rate to (a) $C_i$ and (b) PAR or molar flux of photons (Q). Black dots are the observations and green dots are A-$g_s$ modeled results. A-$g_s$ predictions were made using the environmental conditions set in the leaf chamber (same temperature, radiation, and $CO_2$ concentration) and the optimized parameters shown in Table 2.3.

### 2.A.3 Leaf level: procedure to calculate net $CO_2$ assimilation rate and leaf transpiration

In this section we detail how we estimated the net assimilation rate and leaf transpiration based on observations. We have called these estimations "post-processed observations" because they combine observations of the closed chamber portable photosynthesis system (LiCOR 6400-XT) and of the in-canopy and above-canopy sensors of T, PAR, specific humidity, and $C_a$. Although the post-processed observations are not direct observations and they have certain limitations due to the assumptions made, we used them as a way of visualizing the essential diurnal variability of leaf fluxes. To study the leaf gas exchange in greater detail, another procedure should be used in combination. We do so, by complementing the observations with models of the leaf gas exchange.



The net assimilation rate and the leaf transpiration have been calculated using the following equations:

$$A_n = \frac{g_{s,w}}{\mu}\left(C_a - C_i\right) \tag{2.A.2}$$

$$TR = g_{s,w} q_{sat}(T)\left(1 - RH\right)\frac{m_{air}}{m_{H2O}} \tag{2.A.3}$$

where $\mu$ is the ratio of molecular diffusivities of water vapor and $CO_2$, $m_{air}$ is the molecular mass of air, $m_{H2O}$ is the molecular mass of water, and RH is the relative humidity of the air. $T$, RH, and $C_a$ were taken from sensors inside the canopy ($T$ and RH at 0.105 m) and above the canopy ($C_a$ at 3 m). $C_i$ was calculated using the ratio of internal to external $CO_2$ concentration measured inside the closed chamber of the portable photosynthesis system and the $C_a$ measured above the canopy.

# Chapter 3

# Daytime water and carbon dioxide exchange within and above the Amazon rainforest

This chapter is based on:

González-Armas, R., Rikkers, D., Hartogensis, O., Dias-Júnior, C. Q., Komiya S., Pugliese, G., Williams, J., van Asperen, H., Vilà-Guerau de Arellano J. & de Boer, H. J. (2025). *Daytime water and $CO_2$ exchange within and above the Amazon rainforest* In Agricultural and Forest Meteorology. https://doi.org/10.1016/j.agrformet.2025.110621

## Abstract

We studied the sub-hourly variability of water and $CO_2$ fluxes within and above the Amazon tropical forest during the dry season. Our aim was to investigate how forest layers contribute to the net ecosystem exchange (NEE) and evapotranspiration (ET) by accounting for the existing vertical profiles of leaf traits and microclimate, and the presence of clouds. To this end, we estimated NEE and ET with a 3-layer land-surface model driven by vertical profiles observed at the Amazon Tall Tower Observatory (ATTO) site during CloudRoots-Amazon22 field campaign. Our analysis focused on a typical "shallow-convective" day, composed of 6 individual days with similar conditions. The observed vertical profiles characterized microclimatic variables (photosyntethic active radiation, air temperature, humidity, $CO_2$, wind, and turbulence) as well as leaf traits (maximum carboxylation rate, $\mathrm{V_{cmax}}$; maximum electron transport, $\mathrm{J_{max}}$; and $^{13}$C leaf isotopic composition, $\delta^{13}\mathrm{C_p}$) across three layers that represented the understory, the mid-canopy, and the forest top-crown. The modeled NEE and ET were subsequently compared with eddy-covariance (EC) fluxes observed above the canopy.

We found distinctive vertical profiles of leaf traits and microclimate that were maintained during most of the day. In particular, we observed a persistent inversion of temperature within the canopy which hindered air mixing between the top-crown and the lower layers. Modeled NEE and ET fluxes were comparable in magnitude to the EC-measured fluxes, with flux dynamics dominated by the exchange of the top-crown layer. However, differences between observed and modeled NEE emerged during the morning transition (from 07:30 to 09:00 LT), when $CO_2$ stored within the canopy overnight was released. We conclude that tropical forests exhibit complex, distinctive vertical profiles of microclimate and leaf traits that influence the water and $CO_2$ vegetation exchange and the transport of air within the canopy.

## 3.1 Introduction

Forests interact with the atmosphere through exchanges of water, $CO_2$, energy, and momentum, setting up a characteristic microclimate inside and above the vegetation layer (Finnigan et al., 2009; Belcher et al., 2012). Properly accounting for these forest-atmospheric interactions is vital to understand and quantify the biospheric compound of the terrestrial carbon and water cycles (Gentine et al., 2019). This can be particularly relevant in tropical regions because of their importance to the global hydrological and carbon cycles (Anav et al., 2015), because of the current uncertainty in their response to climate change (Friedlingstein et al., 2006; Davidson et al., 2012), and because tropical forests are dense and with large complex vertical variability (Shuttleworth et al., 1989). Traditionally, land-surface parameterizations have simplified the vertical extension of forests by representing them as a single vegetation layer (known as big leaf approaches) or, at most, as a single layer with sun-lit and shaded portions (known as two big leaf approaches) (Raupach & Finnigan, 1988; Bonan et al., 2021). In the past, these simplifications have been instrumental for advancing our understanding of land-atmosphere interactions. Nowadays, increasing model capabilities and availability of within-canopy observational datasets is enabling a more detailed description of the within-canopy microclimate, leaf traits, and forest canopy architecture, thereby fostering an improved understanding of forest-atmospheric interactions (Bonan et al., 2021).



Exchanges and interactions between the forest and the atmosphere are governed by processes that operate at the subdiurnal timescale (Seo & Dirmeyer, 2022). Some of them are the solar diurnal irradiance pattern, the growth of the convective boundary layer, the distinct turbulence regimes, the entrainment of air from the free troposphere into the atmospheric boundary layer (ABL), and the presence of clouds (such as shallow-cumulus clouds) which are coupled to the ABL state. A realistic characterization of the subdiurnal timescale is also important for atmospheric inversion models and remote sensing applications, for example, for relating remote sensing measurements of sun-induced fluorescence to canopy photosynthesis (Sun et al., 2015).

A large body of research has focused on characterizing particular subdiurnal features of microclimate (Shuttleworth, 1984, 1985; Wofsy et al., 1988; Shuttleworth et al., 1989; Culf et al., 1997; Malhi et al., 1998; Kruijt et al., 2000; Santana et al., 2017; Parker et al., 2019), subdiurnal features of leaf and ecosystem gas exchange (Fitzjarrald et al., 1990; Dolman et al., 1991; Grace et al., 1995; Araújo et al., 2002), and the vertical gradients of leaf traits (Carswell et al., 2000; Lloyd et al., 2010) in the Amazon forest. However, few field-campaigns have measured them simultaneously and for multiple forest layers. A comprehensive study that combined observations of microclimate above the canopy, leaf gas exchange, and leaf traits with a land-surface parameterization is that of Lloyd et al. (1995). They used a big-leaf approach, driven by the observed microclimate and leaf traits, to simulate the gross primary productivity (GPP) of an Amazonian forest, and they discussed the validity of the big-leaf approach in tropical forests.

In this study, we used a similar approach to that of Lloyd et al. (1995). However, key dis-

tinctions are the breakdown of the canopy into three forest layers, the use of microclimate observations measured within the canopy, and the calculation of both $CO_2$ and water fluxes. Our objective is not to compare big-leaf and multi-layer approaches. We consider that this topic has been extensively covered by, for instance, Raupach & Finnigan (1988) and recently by Bonan et al. (2021). Instead, we aim to derive water and $CO_2$ fluxes in three forest layers and to investigate the different vegetation-atmospheric dynamics at play in each layer, taking into account the fast cloud and canopy radiative perturbations at the subdiurnal scale. To this end, we analyzed and extended the comprehensive observational dataset measured at the Amazon Tall Tower Observatory (ATTO) during CloudRoots-Amazon22 field campaign (Vilà-Guerau de Arellano et al., 2024). In this manuscript, we first present a characterization of the observed microclimate and leaf traits during a typical "shallow-convective" day, composed of 6 individual days with similar conditions. Subsequently, we analyzed in depth the results of a three-layer model that is driven by the observed profiles of microclimate and leaf traits. Finally, we compare and discuss the ecosystem fluxes of the observational-driven three layer-model with respect to those observed by an eddy-covariance (EC) system located above the forest.

## 3.2 Methods

### 3.2.1 Study site and CloudRoots-Amazon22 Field Campaign

Observations used in this study were acquired at ATTO (2° 8' 45" S, 59° 0' 19" W; Andreae et al., 2015) during the CloudRoots-Amazon22 field campaign (Vilà-Guerau de Arellano et al., 2024). The CloudRoots project explores the interactions between vegetation and atmosphere, and the role of clouds therein. The project adopts a bottom-up approach that integrates biophysical process understanding and observations from the leaf surfaces up to the ABL, or even the regional atmospheric scale (Vilà-Guerau de Arellano et al., 2023). CloudRoots-Amazon22 extends the general project approach to a tropical forest. The campaign added dedicated observations which, together with the continuous observations regularly acquired at the ATTO facility, allowed the characterization of the land-atmosphere system from the stomata (size of 10 to 100 $\mu$m) to the depth of the ABL (ca. 1 km). CloudRoots-Amazon22 campaign took place from August 8 to 21, 2022 (Southern Hemisphere Amazon dry season) at and around the measurement sites of ATTO and a nearby observatory called Campina (2° 10' 55" S, 59° 1' 18" W). For more details about the campaign, see Vilà-Guerau de Arellano et al. (2024).

An extensive documentation about ATTO research facility can be found in Andreae et al. (2015). Here, we summarize some relevant features of the site. The ATTO site is located 150 km northeast of Manaus (Brazil) and approximately 1000 km inland and downwind from the Atlantic Ocean. It is located at 120 m.a.s.l. on a plateau of terra firme (i.e., non-flooded upland) pristine forest. The mean tree height is 20.7 $\pm$ 0.4 m but the tallest trees reach up to 36-40 m. The ATTO facility consists of three towers: ATTO tall tower (ca. 323

m), a triangular tower (ca. 100 m), and the Instant tower (ca. 80 m). Sensors placed at the towers continuously monitor key atmospheric variables (e.g., radiation, temperature, humidity, wind), trace gases (e.g., $CO_2$, $CH_4$), chemically reactive species, and turbulent fluxes. In this study, we exclusively used data from the Instant tower because that tower was densely surrounded by vegetation, being fully integrated into the forest structure, and it had several radiation sensors within and above the canopy.

During CloudRoots-Amazon22, all days were characterized by shallow-cumulus clouds, which appeared at approximately 09:00-10:00 LT. Shallow-cumulus clouds are ubiquitous in the Amazon rainforest (Giangrande et al., 2017). Their onset is related to the transition of the nocturnal stable atmospheric boundary layer into a convective boundary layer (Henkes et al., 2021), which normally occurs between 08:00-09:00 and 11:00 LT. To organize the CloudRoots-Amazon22 days, we followed the regime classification developed by Henkes et al. (2021) which distinguishes between (1) shallow-convective days and (2) shallow-to-deep convective days. This classification was already used for the CloudRoots-Amazon22 field campaign in Vilà-Guerau de Arellano et al. (2024) (see Table 2 therein for details). In this study, we focused exclusively on the shallow-convective days. These days were August 9, 10, 11, 15, 17 and 18, 2022. We present results for a composite "shallow-convective" day created by averaging each variable across the 6 individual shallow-convective days.



### 3.2.2 Observations

*Microclimate*

The microclimate inside and above the canopy was characterized by vertical profiles and temporal series of photosynthetic active radiation (PAR), air temperature (T), relative humidity (RH), vapor pressure deficit (VPD), atmospheric $CO_2$ concentration ($C_a$), horizontal wind-speed (U), and turbulence kinetic energy (TKE). Additionally, observed long-wave outgoing radiation ($LW_{out}$) was use to derive the surface skin temperature based on Stephan-Boltzman equation for an emissivity of $\varepsilon = 1$. Table 3.1 indicates the instruments that measured each variable together with the time frequency of the sensor and the heights where the sensors were deployed.

In the vertical profiles, we indicated the aerodynamic height of the canopy. The aerodynamic height ($h_a$) was calculated as the inflection point on the vertical wind profile using a similar procedure as Thomas & Foken (2007). To obtain a smooth wind vertical profile, we fitted a piecewise cubic polynomial that was twice continuously differentiable to the wind vertical profile.

To have a reference of clear-sky radiation, we used the McClear version 4.6 product (Lefèvre et al., 2019) from the Copernicus Atmosphere Monitoring Service (CAMS). CAMS McClear includes corrections based on atmospheric composition from re-analysis data, such as aerosol concentration and total column atmospheric water vapour. This estimation allowed us to describe the above-canopy radiative perturbations caused solely by clouds. The only further

processing applied to the CAMS McClear product was the conversion from global horizontal irradiance (GHI) to PAR. To derive this conversion, we use GHI and PAR observed by a spectroradiometer (FROST instrument; Heusinkveld et al., 2023) above the canopy (at 63 m). The observations indicated a conversion of PAR $= 0.4400 \cdot$GHI, Fig. 3.A.1.

*Leaf traits and leaf gas exchange*

To characterize the vertical variability of leaf traits, we divided our measurements over three roughly equally spaced canopy layers: understory (0-10 m), mid-canopy (10-20 m), and top-crown (20-30 m). To characterize the leaf traits of each layer, we carried out two type of measurements: photosynthesis response curves to internal $CO_2$ concentration (known as "A-$C_i$ response curves") and $^{13}C$ carbon isotope analysis. A-$C_i$ response curves were measured with an LI-6400 XT portable photosynthesis system (Licor Inc., Lincoln, NA, USA). We measured A-$C_i$ curves on randomly chosen leaves from trees and understory vegetation surrounding the Instant tower. Once the tree was selected, a professional tree climber climbed to the desired height, cut a branch of approximately 1 m in length and let it fall to the forest floor. Then, we measured the A-$C_i$ response curves at saturating light ($\approx$ 2000 $\mu$mol m$^{-2}$ s$^{-1}$) following Evans & Santiago (2014). In total, we measured 8 A-$C_i$ response curves in the understory, 9 in the mid-canopy, and 9 in the top-crown (Fig. 3.A.3).

For each of the curves, we derived model parameters according to two leaf gas exchange models. The first model was the Farquhar, von Caemmerer and Berry model (Farquhar et al., 1980) from which we estimated the maximum velocity of carboxylase ($V_{c,max}$) and the maximum rate of electron transport ($J_{max}$). The second model was the A-$g_s$ model (Jacobs, 1994) and we estimated the maximum leaf photosynthetic capacity at 298 K ($A_{mmax298}$) and the mesophyll conductance at 298 K ($g_{m298}$). Both models proved capable of representing the measured response curves, which is consistent with a thorough comparison between the two models (van Diepen et al., 2022) that reports that both models simulate similar photosynthetic response curves.

In addition to the A-$C_i$ response curves, stomatal conductance was measured using the LI-6400XT system in five periods centered around solar noon (06:00-07:30 LT, 08:30-10:00 LT, 11:15-12:45 LT, 14:00-15:30 LT, and 16:30-18:00 LT), during two consecutive days (August 11 and 12, 2022). We measured 6 leaves (when possible 3 sun-lit and 3 shaded) per layer and time period. For these measurements, we measured leaves that were accessible from the Instant tower or from the ground. Once a tree was selected, we cut small branches (of approximately 30 cm), let them fall to the forest floor, and immediately performed the measurements at the ground level of the forest where we had our instrumental set-up. The chamber head of the LI-6400XT system was closed, so we had to set the environmental conditions inside the chamber. To set a realistic radiation, we measured radiation with a LAI ceptometer (ACCUPAR LP-80, Meter) that is composed by a linear array of PAR sensors. For each forest layer, we measured radiation according to two light treatments: shaded and sun-lit spots, and we measured 8 times for each treatment at several horizontal orientations.

**Table 3.1:** Microclimatic variables within and above the forest. The heights of the observations used as input for the 3-layer land-surface model appear in **bold** font. RH and VPD at 4 m was calculated from the measurements of $H_2O$ concentration (Picarro L2140-i), air temperature, and air pressure. The $H_2O$ concentration measurements at 4 m were only available for a subset of the composite days (August 17 and 18). The G2401 system measures $CO_2$ concentration over a buffer system (Winderlich et al., 2010; Botía et al., 2020)

| Variable | Instrument | Time frecuency | Height |
|---|---|---|---|
| PAR (incoming) | Quantum sensor (PAR LITE, Kipp & Zonen, The Netherlands) | 1 min | **5**, **15**, **25**, 35, 50, 81 m |
| PAR (incoming) | FROST[a] (Heusinkveld et al., 2023) | 1 s | 0.5, 5, 15, 23, 63 m |
| Air T and RH | Thermohygrometer (IAKM, Galltec, Germany) | 1 min | **26**, 36, 55, 73, 81 m |
| Air T | Thermometer (Hmt337, Vaisala, Finland) | 1 min | **4**, **12** m |
| $H_2O$ concentration | Picarro (L2140-i, Picarro Inc., Santa Clara, CA, USA) | $\approx$ 24 min | **4** m |
| $CO_2$ concentration | Picarro (G2401, Picarro Inc., Santa Clara, CA, USA) | 30 min | **4**, **24**, 38, 53, 79 m |
| U and TKE | 3D Ultrasonic Anemometer (CSAT-3b, Campbell Scientific Instrument Inc., USA) | 30 min | 5, 25, 50, 81 m |
| U and TKE | 3D Ultrasonic Anemometer (THIES, Germany) | 30 min | 15, 35 m |
| $LW_{out}$ | Pyrgeometer (CGR4, Kip & Zonen, Netherlands) | 10 min | 75 m |

[a]It should be noted that the FROST instruments are not part of the continuous ATTO observation network; they were brought exclusively for the field campaign.

Lastly, the (sun-lit or shaded) averaged measured radiation was set in the closed chamber to measure the stomatal conductance of a (sun-lit or shaded) leaf.

The second type of observations that characterized the leaf traits were $^{13}$C isotope analysis. First, we sampled the leaves in which we measured the A-$C_i$ curves and some additional leaves that were selected in the same manner as the leaves for the A-$C_i$ curves. In total, we sampled 56 leaves (19 in the understory, 18 in the mid-canopy, and 19 in the top-crown). After collection, the leaves were first dried in an oven at 60 °C for the following 48 h and then stored in sealed bags to keep them dry. A few days later, leaves were manually ground at the National Institute of Amazonian Research (INPA) and stored in plastic centrifugal tubes for export. After re-drying them at 60 °C for 12 h at the GeoLab in Utrecht University, fine grinding was performed using a Mixer Mill for 120 s per sample. Then, we prepared the fine ground samples for the isotope analysis by placing 1000-1500 $\mu$g of leaf material in tiny aluminum cups. Finally, the isotope measurements were performed with a EA-IRMS (Elemental Analyzer – Isotope Ratio Mass Spectrometer) instrument with IAEA-CH-7 as the $^{13}$C reference standard.

Based on the $^{13}$C isotopic measurements, we estimated the ratio of internal sub-stomatal $CO_2$ ($C_i$) to atmospheric $CO_2$ mixing ratios ($C_a$). To that aim, we employed the following expression in accordance to Farquhar et al. (1989):

$$\frac{C_i}{C_a} = \frac{\Delta^{13}C - a}{b - a} \tag{3.1}$$

where $a$ (4.4 ‰) and $b$ (28 ‰) are constants representing the fractionation due to diffusion and carboxylation, respectively, (Farquhar et al., 1982), and $\Delta^{13}$C is the carbon discrimination calculated following Farquhar et al. (1989) as:

$$\Delta^{13}C = \frac{\delta_a^{13}C - \delta_p^{13}C}{1 + \delta_p^{13}C} \tag{3.2}$$

where $\delta_a^{13}$C and $\delta_p^{13}$C are the $^{13}$C isotopic composition of the atmospheric $CO_2$ and of the carbon in the leaf material with respect to the Vienna Peedee Belemnite (VPDB) isotope reference. The atmospheric isotopic composition, $\delta_a^{13}$C, was measured during CloudRoots-Amazon22 field campaign. Measurements were available right above the canopy (38 and 42 m), at the top-crown (24 m), and in the understory (4 m) (for details about the instruments, see Vilà-Guerau de Arellano et al., 2024). To use a unique diurnal value per layer, we averaged the observations during the days with shallow-convection, which are presented in Vilà-Guerau de Arellano et al. (2024) (Fig. 4 therein). For the top-crown layer we used the observations from 24 and 38 m, for the mid-canopy we used the values from 4 and 24 m, and for the understory we used the values from 4 m. The values for the top-crown, mid-canopy, and understory were respectively -9.14 ‰ , -9.69 ‰, and -10.23 ‰.

*Ecosystem fluxes*

An eddy covariance system was used to calculate the surface turbulent fluxes of water and $CO_2$ ($F_{H_2O}$ and $F_{CO_2}$) above the forest (at 50 m.a.g.l $\approx 1.5\ \ h_a$) for 30 min intervals. Three-dimensional wind and temperature fluctuations were measured by a sonic anemometer (instrument details in Table 3.1). $CO_2$ and $H_2O$ fluctuations were measured by three fast response closed-path $CO_2$/$H_2O$ infrared gas analyzers (IRGA LI-7200) installed at a lateral distance of about 10 cm from the sonic path. The high-frequency signals were recorded at 10 Hz by CR1000X data logger. The raw data was processed applying the software EddyPro Biosciences L (2019). Fluxes, means, and variances were calculated for half-hourly intervals. The vertical turbulent transport measured by the EC-system does not necessarily equal the ecosystem exchange (defined as the sum of emissions and/or uptake by the vegetation and soil) because water and $CO_2$ can be stored in the air layer below the sensor (Foken et al., 2012). This effect was quantified by the storage flux term, $F_{stor,\chi}$, with $\chi$ being water vapor or $CO_2$. The storage terms were calculated as:



$$F_{stor,\chi} = \int_0^h \frac{\rho_d}{M_d} \frac{\partial \chi}{\partial t} dz, \tag{3.3}$$

with $h$ being the height of the EC-system where turbulent fluxes are observed, $\rho_d$ the dry air density, and $M_d$ the molecular weight of dry air. To estimate the integral in height, we used 4 sensors that measured humidity (at 4, 26, 36, and 55 m) and $CO_2$ concentration (at 4, 24, 38, and 53 m). Finally, the observed ecosystem fluxes – the net ecosystem exchange ($NEE_{obs}$) and evapotranspiration ($ET_{obs}$) – were estimated as the sum of the surface turbulent fluxes and the storage fluxes:

$$NEE_{obs} = F_{CO_2} + F_{stor,CO_2} \tag{3.4}$$

$$ET_{obs} = F_{H_2O} + F_{stor,q} \tag{3.5}$$

Soil respiration ($CO_2$ emission flux) was also measured close to the ATTO tall tower using an automated closed dynamic soil flux measuring system (Licor Inc., Lincoln, NA, USA). The system consisted of an infrared gas analyzer (LI-870), a 8-port multiplexer (LI-8250), and 3 dynamic long-term chambers with opaque lids (LI 8200-104). The flux measurements of each chamber consisted of: 1.5 min of pre-purge during which the chamber lid was opened and lines flushed with ambient air, 4 min of closure time, and 1 min of post-purge. The three chambers measured consecutively, and the soil $CO_2$ flux was calculated by applying an exponential model to the $CO_2$ concentration during the chamber closure period (Pugliese et al., 2023). The three chambers were placed on PVC-collars (Ø: 19.4 cm) installed on three types of surfaces: bare organic soil, bare clay soil, and clay soil with litter. To characterize the diurnal surface respiration we averaged the measurements over the three surface types.

Additionally, observed friction velocity ($u_*$) and sensible heat flux (H) at 50 m were used to define a morning transition from the nocturnal ABL to a well-mixed ABL, Fig. 3.A.5. The morning transition was defined as the period between the time when the sensible heat flux became positive and the time when the friction velocity stabilized (Dupont et al., 2024).

### 3.2.3 Three-layer model

At each layer (understory, mid-canopy, and top-crown), we represented the leaf gas exchange (stomatal conductance, net $CO_2$ leaf assimilation, leaf transpiration, and $C_i$) with the A-$g_s$ model (Goudriaan et al., 1985; Jacobs, 1994). The model described the observed leaf traits since it included the measured vertical profiles of mesophyll conductance and maximum assimilation rate at 298 K. Furthermore, the model used as input the observed vertical profiles and time series of PAR, T, VPD, and $CO_2$. Because no observations of VPD and $CO_2$ were available at the mid-canopy, VPD and $CO_2$ were linearly interpolated at 15 m from the available observations in the understory and top-crown. Additionally, $CO_2$ observations were linearly interpolated in time to match the 1 min resolution of the other observations.

To up-scale from leaf fluxes to canopy fluxes, we used the 3-point Gaussian quadrature approach (Goudriaan, 1986). Details about the approach can be found in 3.A.5. In that approach, we considered a leaf area index (LAI) of 5.32 $m^2$ $m^{-2}$ in accordance to the value reported by Gomes Alves et al. (2023) for the ATTO site. By up-scaling the fluxes, we estimated the $CO_2$ assimilation ($A_n$) and transpiration (TR) of the individual forest layers and of the whole vegetation canopy. Apart from the vegetation fluxes, we calculated the water use efficiency (WUE) defined as the ratio between $A_n$ (defined as positive if $CO_2$ is taken up by the plant) and TR. Finally, the up-scaled fluxes were compared with those observed (eq. 3.4 and eq. 3.5). To be able to compare them, we needed to include the soil contribution to the up-scaled fluxes. We did so by including the observed soil respiration to the up-scaled net $CO_2$ assimilation and assuming negligible soil evaporation.

## 3.3 Results

### 3.3.1 Vertical profiles of microclimate and leaf traits

*Radiation*

Incoming PAR above the canopy followed a diurnal pattern that was perturbed by the presence of shallow-cumulus clouds (Fig. 3.1a). The shallow-cumulus clouds were present from approximately 09:45 LT and their net diurnal effect was to diminish incoming radiation compared to clear sky values by 6.2 $\pm$ 2.3%. During 40 % of the day we observed cloud shadows (Fig. 3.A.2), which reduced radiation by approximately 14 % on average. During 13 % of

the time, we observed enhancement of radiation due to the increased diffuse radiation from nearby clouds edges, which increased radiation by approximately 4 % on average.

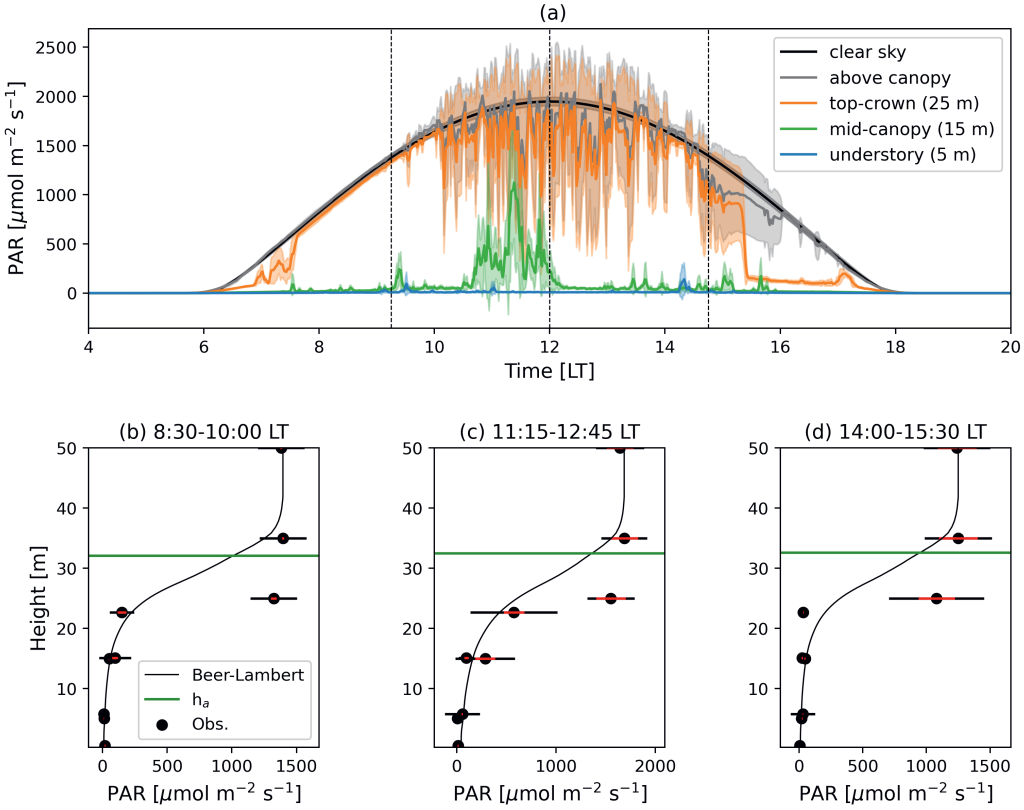



**Figure 3.1:** Panel (a) depicts the time series of observed PAR (above the canopy, at 25 m, 15 m, and 5 m) and a clear-sky reference for the composite day. The solid lines represent the mean value whereas the shaded region indicates the range within one standard deviation. Panels (b), (c), and (d) are vertical profiles of observed PAR. Two standard deviations of the observations are shown, the black error bars show the standard deviation during the time periods whereas red error bars show the standard deviation across the individual days that constitute the composite. Additionally, panels (b), (c), and (d) show the Beer-Lambert extinction profile of $K_x = 0.65$, LAI $= 5.32$ m$^2$ m$^{-2}$ and leaf area density as indicated in Fig. 3.A.7. Aerodynamic canopy height is indicated as a green horizontal line.

PAR measured inside the top-crown layer of the canopy was slightly reduced but still highly correlated with PAR above the canopy ($r^2 = 0.95$). Consequently, the cloud-induced radiative perturbations affected the photosynthesis in the top-crown leaves. From 06:00 to 07:30 LT and from 15:30 to 18:00 LT, PAR measured at the top-crown was significantly lower than that measured above the canopy, most probably due to the high solar zenith angle. When the solar zenith angle is high, the direct light beam travels longer until reaching a certain height

within the canopy, increasing the chances for light to encounter obstacles such as leaves and branches. Additionally, the anisotropy of the plant material around the radiation sensor can create shades at particular moments of the day. For instance, between 15:30 and 17:00 LT, the top-crown sensor was likely shaded by some big opaque object such as a trunk because it registered the same values across the 6 days (showing a small standard deviation across days). In the mid-canopy, radiation was reduced to, on average, 7 % of the above canopy radiation. Most of the mid-canopy radiation was received close to noon (between 10:30 and 12:00 LT). The higher radiation received at noon is likely related to the creation of a small clearing when the solar zenith angle is low. In the understory, radiation was minimal; only 0.7 % of the above canopy radiation reached the sensor located at 5 m height.

Observed PAR attenuated inside of the canopy abruptly between 25 and 15 m and moderately below 15 m (Fig. 3.1b, c, and d). The variability of the observed PAR intensity during the 1.5 h time periods (black error bars) was higher than the day-to-day variability (red error bars). This indicates that the observed PAR intensity varied more due to the diurnal cycle of radiation than due to the differences between individual days. The observed PAR vertical profiles seemed generally consistent with the exponential Beer-Lambert law of light extinction of a fitted extinction coefficient $K_x = 0.65$ and LAI $= 5.32$ m$^2$ m$^{-2}$ (leaf area density in Fig. 3.A.7), although the observed profile showed a steeper radiative attenuation between 25 m and 15 m at all time intervals.

*Temperature, humidity, and $CO_2$*

Vertical profiles of air temperature (Fig. 3.2a) indicated the presence of a stable layer within the canopy during daytime. This stable layer was characterized by a temperature maximum above the canopy (from 06:00 to 7:30 LT and from 16:30 to 18:00 LT) or at the top-crown layer (from 8:30 to 15:30 LT), and decreasing temperatures with canopy depth. The temperature inversion was generally slightly stronger in the understory than in the mid-canopy. The temperature range within the canopy was approximately 2 °C at the beginning of the day and 3-4 °C during the rest of the day. The highest air temperatures found at the top-crown canopy (from 08:30 to 15:30 LT) are associated with the outgoing sensible heat flux from the warm sun-lit leaf surfaces of the top-crown layer. The skin temperature derived from the terrestrial long-wave radiation was generally higher than the temperature at the top-crown (by up to 1 °C), suggesting higher leaf temperatures than atmospheric temperatures at this canopy layer. The day-to-day air temperature variability was similar to the variability during the 1.5 h intervals, and generally smaller than the vertical variability. The largest day-to-day air temperature variability occurred from 06:00 to 7:30 LT, suggesting the influence of individual nighttime conditions on the early morning vertical profiles of air temperature.

We observed a clear separation in VPD and RH between the understory and the top-crown layer (Fig. 3.2b) from 08:30 LT. Comparing the understory with the top-crown and above canopy sensors, we observed a difference of approximately 500-750 Pa in VPD and of approximately 5%-15% in RH. Despite the differences, both top-crown and understory sensors

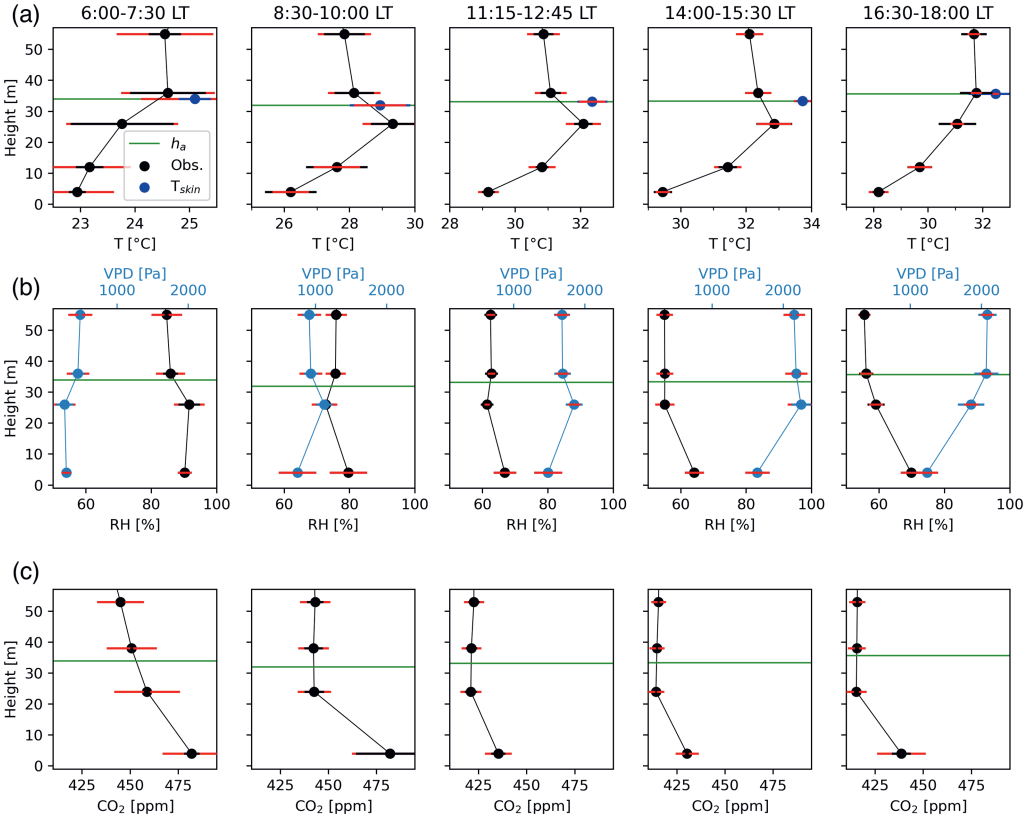



**Figure 3.2:** Vertical profiles of observed: air temperature (a), vapor pressure deficit and relative humidity (b), and atmospheric carbon dioxide (c). Profiles are shown for the composite day for 5 time intervals: from 06:00 to 7:30 LT, from 08:30 to 10:00 LT, from 11:15 to 12:45 LT, from 14:00 to 15:30 LT, and from 16:30 to 18:00 LT. Black (or blue for skin temperature and VPD) error bars show the standard deviation during the interval time for the average observation whereas red error bars show the standard deviation across the individual days that constitute the composite. Aerodynamic canopy height is indicated as a green horizontal line.

depicted a diurnal cycle in which VPD increased until reaching a maximum at 14:00-15:30 LT and then decreased until sunset. The opposite occurred for RH, which decreased until reaching a minimum at 14:00-15:30 LT and then increased until sunset.

Atmospheric $CO_2$ showed a vertical profile with $CO_2$ maxima near the forest floor during all time intervals (Fig. 3.2c). In the understory, the highest $CO_2$ values were observed during the two early time intervals (from 06:00 to 10:00 LT). During these moments, differences between understory and above canopy $CO_2$ were approximately 30-40 ppm. From 11:15 to 15:30 LT the difference in $CO_2$ between understory and above canopy air was smaller (approximately 20 ppm) but it increased again (to approximately 30 ppm) in the late afternoon (from 16:30 to 18:00 LT). Similar to air temperature, the day-to-day variability was largest from 06:00 to 7:30 LT, suggesting the influence of individual nighttime conditions on the early morning vertical profiles of $CO_2$.

*Wind and turbulence*

Atmospheric variables related to the mixing of air also changed with height and time (Fig. 3.3). Wind attenuated near and within the canopy following the widespread assumption of a logarithmic decay above the canopy and an exponential decay within the canopy (Fig. 3.3a). The aerodynamic height, defined as the inflection point of the wind speed vertical profile, was 33.7 m $\pm$ 1.2 m. The turbulent kinetic energy varied throughout the day, showing the highest values between 11:15 and 15:50 (Fig. 3.3b). Similar to the wind profile, its decay inside the canopy resembled an exponential function with great attenuation in the upper half of the canopy.

*Leaf traits*

Leaf traits showed distinct vertical gradients within the canopy, Fig. 3.4 and Table 3.A.1. Observed $V_{c,max}$ and $J_{max}$ increased with height from the understory to the top-crown canopy by 20 $\mu$mol m$^{-2}$ s$^{-1}$ and 50 $\mu$mol m$^{-2}$ s$^{-1}$ respectively, Fig. 3.4a and b. The leaf $^{13}$C isotopic composition, $(\delta_p^{13}\mathrm{C})_{\mathrm{VPDB}}$, increased with height with a difference of 3.75 ‰ between understory and top-crown canopy, Fig. 3.4c. The $C_i/C_a$ ratios derived from the $\delta_p^{13}$C observations exhibited an opposite vertical profile with lower ratios higher in the canopy, Fig. 3.4d. These ratios suggest greater $CO_2$ leaf assimilation rates higher in the canopy. This is in line with the greater radiation (Fig. 3.1), $V_{c,max}$ (Fig. 3.4a), and $J_{max}$ (Fig. 3.4b) observed at the top-crown canopy.

### 3.3.2 Modeled and observed leaf gas exchange

Observed and modeled $C_i/C_a$ ratios showed a diurnal cycle (Fig. 3.5a) with a marked vertical gradient during daytime (Fig. 3.5b). The gradient, depicting lower $C_i/C_a$ ratios higher in the canopy, was milder for the modeled results than for the two observational sets: the

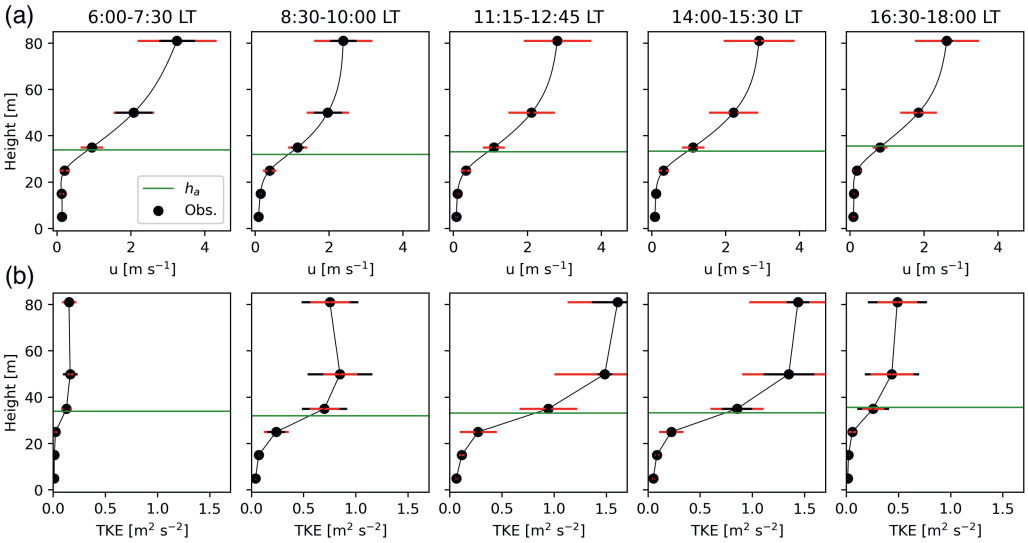



**Figure 3.3:** Vertical profiles of observed: wind speed (a) and turbulent kinetic energy (b). Profiles are shown for 5 different times of the composite day: from 06:00 to 7:30 LT, from 08:30 to 10:00 LT, from 11:15 to 12:45 LT, from 14:00 to 15:30 LT, and from 16:30 to 18:00 LT. Black error bars show the standard deviation during the time interval for the composite vertical profile whereas red error bars show the standard deviation across the individual days that constitute the composite. Aerodynamic canopy height is indicated as a green horizontal line.

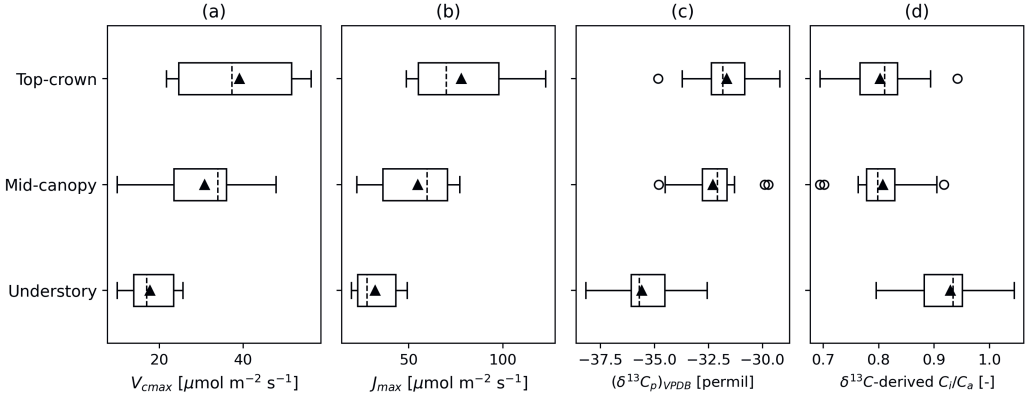



**Figure 3.4:** Vertical profiles of: $V_{c,max}$ (a), $J_{max}$ (b), leaf $^{13}C$ isotopic composition, $(\delta_p^{13}C)_{VPDB}$, (c), and $\delta^{13}C$-derived $C_i/C_a$ ratio (d). Black triangles depict mean values whereas dashed black lines depict the median.

$\delta^{13}$C-derived measurements and the leaf gas exchange measurements. The observed and modeled diurnal cycle of $C_i/C_a$ (Fig. 3.5a) was characterized by a decline until achieving minimum values between 14:00 and 16:00 LT, followed by an increase until sunset. The $C_i/C_a$ ratio showed an opposite diurnal cycle than VPD, with lower $C_i/C_a$ ratios with higher VPD (Fig. 3.2b). Model results and observations differed most around sunrise and sunset, when observed ratios were larger than modeled results.

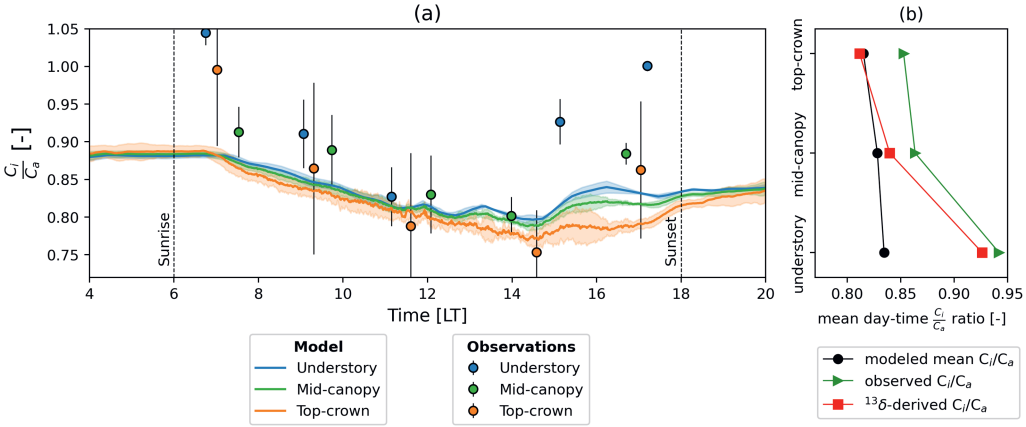



**Figure 3.5:** Time series of $C_i/C_a$ ratio (a), and vertical profiles of mean daytime $C_i/C_a$ ratio (b). In panel (a), leaf gas exchange observations are shown with large circles with a black outline and an inner color that is: blue for the understory, green for mid-canopy, and orange for top-crown. Leaf gas exchange observations have a vertical error bar that corresponds with the standard deviation. Model results are shown as lines with the same colors for each layer as the observations (blue, green and orange). The shaded area represents the range within one standard deviation of the modeled $C_i/C_a$ ratio across the 6 individual shallow convective days. In panel (b), three vertical profiles are shown: the modeled profile (black line and circles), the profile observed through leaf gas exchange measurements (green line and triangles), and the profile derived from the $\delta^{13}$C observations (red line and squares).

Stomatal conductance (Fig. 3.6) also showed a diurnal cycle with a strong vertical gradient, indicating larger stomatal conductance higher in the canopy. For both model and observations, stomatal conductance was larger at all moments in the top-crown that in the mid-canopy and understory. In the top-crown layer, the modeled results depicted a steep stomatal aperture at 07:00 LT that continued at a slower rate until reaching maximum values of 0.4 mol $m^{-2}$ $s^{-1}$ at 10:00 LT. Afterwards, the modeled stomatal conductance fluctuated due to the radiative cloud perturbations. The modeled top-crown stomatal conductance corresponded well with the maximum sun-lit observations performed at that layer. The mean top-crown observations were smaller (approximately 0.2 mol $m^{-2}$ $s^{-1}$) and had a large standard deviation (of approximately 0.1 mol $m^{-2}$ $s^{-1}$). This highlights the large variability in observed stomatal conductance that occurs within the top-crown. The modeled and observed mid-canopy stomatal conductance had similar values. Modeled mid-canopy stomatal conductance highly fluctuated in synchrony with the radiation perturbations experienced in that

layer (Fig. 3.1a), which are the result of the diurnal PAR cycle, the light extinction, the cloud radiative perturbations, and the canopy shading. In the understory, the modeled stomatal conductance underestimated the observed one. Modeled stomatal conductance in the understory was modest and only increased with occasional sun flecks.

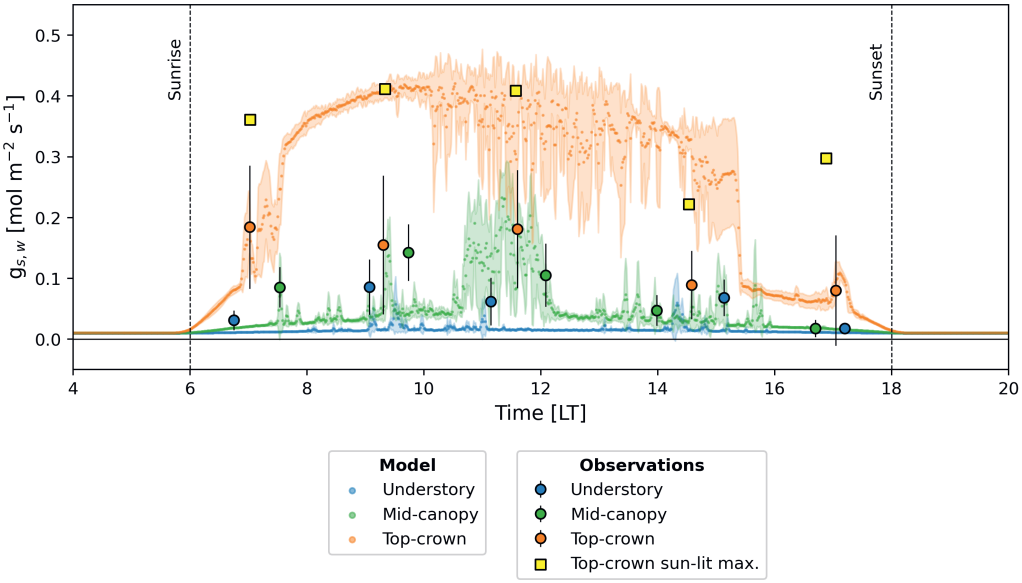



**Figure 3.6:** Time series of stomatal conductance to water vapor. Leaf gas exchange observations are shown in circles with a black circumference and an inner color that is: blue for the understory, green for mid-canopy, and orange for top-crown. Leaf gas exchange observations for each layer have a vertical error bar that corresponds to the standard deviation. Additionally, observed maximum stomatal conductance for the sun-lit leaves at the top-crown layer are shown in yellow squares. Model results are shown in smaller dots with the same colors per layer as the observations (blue, green and orange). The shaded area represents the range within one standard deviation of the modeled stomatal conductance across the 6 individual shallow convective days.

### 3.3.3 Modeled and observed ecosystem fluxes

Similar to stomatal conductance, modeled $A_n$ and TR showed a diurnal cycle that was most pronounced in the top-crown canopy, Fig. 3.7a and b. Time series of $A_n$ and TR depicted temporal variability similar to that of the observed radiation (Fig. 3.1a). $A_n$ was more symmetric around solar noon than TR because TR was importantly affected by the time series of VPD (Fig. 3.2b), which indicated higher VPD in the afternoon than in the morning.

Comparing the contributions of the different canopy layers, we observe that the top-crown layer dominated the whole vegetative canopy exchange (Fig. 3.7, Table 3.2). The mid-canopy layer had a lesser contribution, contributing 3 % of the total vegetative canopy up-take and 19

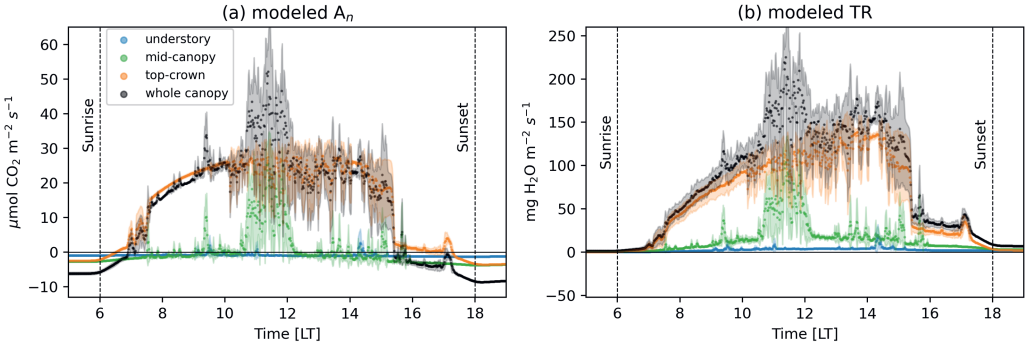



**Figure 3.7:** Time series of modeled: canopy net assimilation of $CO_2$ (a) and canopy transpiration (b). In each panel the total canopy flux appear in black dots whereas the contribution of each canopy layer to the net flux appear in: orange for top-crown, green for mid-canopy, and blue for understory. The shaded area indicates the range within one standard deviation of the mean across the individual shallow convective days.

% of the total vegetative canopy transpiration (Table 3.2). But, even though the top-crown layer dominated the net daytime forest fluxes, the mid-canopy occasionally exchanged as much as the top-crown, especially when direct radiation penetrated deeper inside the canopy. This can be observed between 10:30 and 12:00 LT when both $A_n$ and TR peaked (Fig. 3.7) at the same time that mid-canopy radiation was maximum (Fig. 3.1a). The understory had the lowest contribution to the total daytime vegetative canopy transpiration (3 %). However, it contributed more than the mid-canopy to the total daytime $CO_2$ exchange. In contrast to the mid-canopy contribution, the modeled understory was a net diurnal source of $CO_2$ due to respiration processes, which accounted for 6 % of the total diurnal $CO_2$ exchange in the vegetative canopy.

The water use efficiency (WUE), calculated as the ratio of the cumulative daytime $A_n$ and the cumulative daytime TR, increased with height. Modeled WUE was large at the top-crown (9.99 g $CO_2$ $kg^{-1}$ $H_2O$), low at the mid-canopy (1.11 g $CO_2$ $kg^{-1}$ $H_2O$), and even negative for the understory (-13.66 g $CO_2$ $kg^{-1}$ $H_2O$).

Considering soil respiration and assuming zero soil evaporation, we could obtain modeled NEE and ET. Modeled NEE and ET compared well with the observed NEE and ET in terms of the magnitude and diurnal pattern, particularly for ET, Fig. 3.8. Modeled and observed ET followed a similar diurnal pattern which grew quickly from about 1 h after sunrise, acquired maximum values between 11:00 and 15:00 LT, and declined afterwards until sunset, Fig. 3.8b. Modeled and observed ET correlated well and significantly ($r^2 = 0.95$ and $p < 0.001$), and had similar cumulative evaporated water during daytime (Table 3.A.2). Noticeable differences between modeled and observed NEE and ET occurred in two periods: midday (between 10:30 and 12:00 LT), and afternoon (between 15:30 and 17:00 LT). At midday, model results depicted an enhanced net $CO_2$ assimilation and transpiration compared to observations. The enhanced modeled fluxes are related to the local high radiation available in the

**Table 3.2:** Modeled cumulative $CO_2$ and water vegetation exchange per unit area during daytime for: the whole canopy, the top-crown, the mid-canopy, and the understory. Between brackets it appears the percentage of the contribution of each layer to the total vegetation exchange. The percentage is negative for the understory contribution to the net canopy assimilation because the modeled understory was respiring $CO_2$ instead of assimilating it.

| Variable | Units | Whole canopy (vegetation) | Top-crown | Mid-canopy | Understory |
|---|---|---|---|---|---|
| $\int_{sunrise}^{sunset} A_n \, dt$ | g $CO_2$ $m^{-2}$ | 28.25 (100 %) | 29.15 (103 %) | 0.81 (3 %) | -1.71 (-6 %) |
| $\int_{sunrise}^{sunset} TR \, dt$ | kg $H_2O$ $m^{-2}$ | 3.77 (100%) | 2.92 (78 %) | 0.72 (19 %) | 0.13 (3 %) |
| WUE | g $CO_2$ $kg^{-1}$ $H_2O$ | 7.50 | 9.99 | 1.11 | -13.66 |

mid-canopy at that moment (Fig. 3.1). The fluxes during this period reflect potential ecosystem exchanges, which may happen when radiation is able to penetrate further the canopy. In the afternoon, modeled results depict a dominance of respiration over assimilation (Fig. 3.8a) and a reduced evapotranspiration (Fig. 3.8b), which contrasts with the $CO_2$ assimilation and larger evapotranspiration suggested by the observations. The discrepancy is due to the reduced observed radiation at the top-crown layer (Fig. 3.1a) due to a shade by a large opaque object and it also reflects highly local conditions. As a consequence, during that periods modeled fluxes may not be representative of the whole canopy and should not be overemphasized.

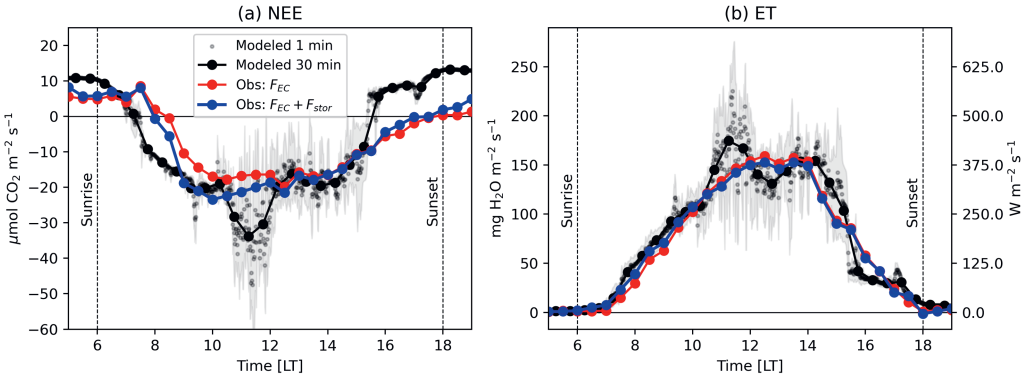



**Figure 3.8:** Time series of: NEE (a) and ET (b) for the 6-day composite. 1-min modeled NEE and ET appear in grey small dots with a shade area that represents the range within one standard deviation across the 6 shallow convective days. 30-min modeled NEE and ET appear as black dots connected by a solid line. The 50 m observed NEE and ET appear as blue dots connected by a solid line. Observed NEE and ET are the sum of the surface turbulent fluxes measured by the EC system ($F_{EC}$) and the storage terms ($F_{stor}$). $F_{EC}$ also appear in the figure as red dots connected by a solid line.

Modeled and observed NEE showed a similar magnitude of maximum $CO_2$ up-take and a similar diurnal pattern. They correlated well and significantly ($r^2 = 0.75$ and $p < 0.001$). The diurnal cycle was characterized by positive values at nighttime (between 0 and 10 $\mu$mol $CO_2$ $m^{-2}$ $s^{-1}$) corresponding with respiration processes and negative fluxes during daytime (of approximately 20 $\mu$mol $CO_2$ $m^{-2}$ $s^{-1}$ at noon) corresponding with a net assimilation of $CO_2$. Unlike for ET, a difference between modeled and observed results occurred in the early morning (between 07:30 and 09:00 LT). At 07:30, modeled NEE indicated a transition from the ecosystem being a net source of $CO_2$ (by respiring) to a sink (by assimilating). This transition was indicated by observations at 08:00 LT, half an hour later. Additionally, modeled results indicated larger assimilation rates from 07:30 until 09:00 LT. The effect of the storage term on the observations was noticeable, particularly in the morning (from 07:30 to 12:00 LT). By including the storage term, the respiration-assimilation transition shifted from 08:30 to 08:00 LT, getting closer to the modeled respiration-assimilation transition (07:30 LT). The morning, when we observed large observed-modeled NEE differences, is an interest-

ing period. At that time, high $CO_2$ concentrations that were accumulated overnight within the canopy can be released by intense turbulent motions (Fig 3.3), which occasionally penetrate the canopy. The resulting upward turbulent transport of enriched $CO_2$ air could offset the instantaneous net ecosystem uptake (what our model predicts) and result in a net positive turbulent flux (what the EC system measures). Remarkably, air transport seemed to play a lesser role for the water fluxes (Fig. 3.8b).

## 3.4 Discussion

The objective of this study was to investigate the vertical and subdiurnal variability of ET and NEE in the Amazon rainforest. Our discussion is structured in four sections. In the first section, we compare the observed microclimate and leaf traits with what has been reported by literature for dense tropical rainforests. In the second, we discuss how the within canopy horizontal heterogeneity of microclimate, particularly of radiation, affects modeled NEE and ET. In the third section, we comment on the contributions of each forest layer to the ecosystem fluxes, placing emphasis on the understory dynamics. In the final section, we discuss the modeled and observed ecosystem fluxes, focusing particularly on an intriguing period: the morning transition.



### 3.4.1 Microclimate and leaf traits

We found large vertical variability in microclimate and leaf traits within the canopy. The observed vertical profiles coincided with what has been previously reported in different studies for the region. In addition, the day-to-day variability of microclimatic variables was generally small, indicating robust and distinct vertical profiles. Radiation reaching the understory was found 0.7 % of the above canopy radiation which is similar to the 1 % reported by Shuttleworth (1984) for the forest floor of another Amazonian site. Temperature was found maximum at the canopy top and it decreased within canopy depth as reported by other studies (Shuttleworth, 1985; Kruijt et al., 2000). The temperature inversion within the canopy is indicative of an stable air layer. Such stable layers have been reported previously for the Amazon forest (Santana et al., 2018). In terms of relative humidity, we found higher relative humidity closer to the ground in agreement with a previous study (Shuttleworth, 1985). $CO_2$ mixing ratios were maximum at all times in the understory due to soil respiration which agrees with previous research (Wofsy et al., 1988). Turbulence attenuated sharply in the upper half of the canopy where it coexisted with the temperature inversion associated with an stable air layer. This characterization of turbulence shows similarities with previous studies by Kruijt et al. (2000) and Santana et al. (2018). The temperature inversion and low turbulence intensity at mid-canopy suggest a decoupling of the air from the lower half of the canopy with the air above, with turbulent motions unable to break the temperature gradients that hinder the within canopy air mixing during daytime (Vilà-Guerau de Arellano et al., 2023). Additionally, turbulence could not eliminate the gradients of other scalars such as

$CO_2$ (Fig. 3.2), potentially affecting their residence times within the canopy during these days characterized by shallow convection.

Regarding the leaf traits, both $V_{cmax}$ and $J_{max}$ increased with height within the canopy. $V_{cmax}$ at the top-crown was roughly two times that at the understory and $J_{max}$ at the top-crown was roughly about three times that at the understory. These gradients coincided with those reported by Carswell et al. (2000) who estimated the gradients measuring two different tree species at four different heights in a nearby site. These vertical gradients in photosynthetic biochemistry likely reflect optimality in the investment of nitrogen and rubisco as a function of light intensity (Stocker et al., 2020; Harrison et al., 2021). Although the gradients corresponded well, we found slightly lower values than those reported by Carswell et al. (2000). Finally, we also found similar $C_i/C_a$ ratios to Carswell et al. (2000), which often exceeded 0.8 (Fig. 3.4d and Fig. 3.5).

### 3.4.2 Horizontal heterogeneity

Our study covered key controlling variables of the water and $CO_2$ exchange at multiple heights within and above the canopy. Ecosystem fluxes were modeled using vertical profiles derived from in-canopy measurements collected at a single tower, assuming that these profiles are representative of the forest canopy. Although this assumption is likely valid for variables such as $CO_2$, VPD, and temperature, which exhibit limited horizontal variation, radiation has significant horizontal heterogeneity (Anhuf & Rollenbeck, 2001; Parker et al., 2019). Rapid and intense fluctuations in radiation within the canopy were observed, driven by factors such as cloud passages, leaf flutter, and branch sway, which vary with sensor placement. In addition, at certain times of the day, the sensors were consistently shaded by opaque objects (top-crown from 15:30 to 17:00 LT in Fig. 3.1a) or consistently illuminated by the alignment of the sun and a forest clearing (mid-canopy from 11:00 to 12:00 LT in Fig. 3.1a).

The in-canopy horizontal heterogeneity in radiation is related to the forest canopy architecture. Old growth forests, such as the pristine tropical rainforest present at ATTO, are characterized by high rugosity, which is defined as the standard deviation of the canopy height (Parker & Russ, 2004; Parker et al., 2019). The high forest rugosity is thought to relate with the horizontal variability in light transmissivity (Parker et al., 2019). Anhuf & Rollenbeck (2001) measured 36 vertical profiles of light transmissivity on a tropical rainforest. Their individual vertical profiles differed in the height and steepness where the largest light attenuation occurs. Comparing the individual vertical profiles with the average profile, it is noticeable that the individual profiles depict a more abrupt light attenuation than the average profile. This feature is also visible in our results, when we compare our individual PAR profile and the Beer-Lambert's (average) derived profile, Fig. 3.1b, c and d.

Because NEE and ET heavily depend on radiation, the not captured horizontal heterogeneity of radiation introduces uncertainty in our flux estimations. Because of that, modeled NEE and ET should be interpreted as indicative of a potential range of exchange across vertical layers, with the understanding that the underlying radiation measurements are highly local.

We still regard our estimations valuable since they represent typical radiative perturbations that a single leaf experiences. However, in Sect. 3.A.7, we provide a more conservative estimation of the ecosystem fluxes by using in-canopy radiation derived from Beer-Lambert's law (Fig. 3.A.8), which results in ecosystem fluxes with smoother diurnal cycles (Fig. 3.A.9 and Fig. 3.A.10).

### 3.4.3 Modeled fluxes per layer

The transpiration and the net $CO_2$ assimilation was dominated by the top-crown layer (fig. 3.7). Water use efficiency, calculated as the ratio between the $CO_2$ assimilated during daytime and the water transpired, increased with height (Table 3.A.2), meaning that the $CO_2$ assimilation had greater vertical gradients than the transpiration. During nighttime, the understory respired less $CO_2$ than the mid-canopy and top-crown (Fig. 3.7a) likely because the understory leaves had to maintain less photosynthetic-related biochemical systems.



Despite producing reasonable results, the model may not fully capture some understory dynamics of the $CO_2$ exchange. The cumulative daytime $CO_2$ exchanged in the understory corresponded to a respiration of 1.71 g $CO_2$ $m^{-2}$ (Table 3.2), indicating that those leaves were not being productive for the understory vegetation. Several factors could influence this outcome. Firstly, the understory PAR sensor may have been positioned in a particularly shaded area, potentially leading to an overestimation of the low light conditions in the 0–10 m layer. Secondly, the understory vegetation might exhibit greater photosynthetic activity under low light conditions than assumed in the model. Due to the lack of measured photosynthetic response curves to PAR, the same photosynthetic response to low light was applied across all canopy levels. However, understory vegetation often demonstrates higher tolerance to low light environments, being able to assimilate $CO_2$ at lower light intensities compared to mid-layer or top-crown vegetation (Sterck et al., 2013). Thirdly, the spectrum of light could also play a role in the understory $CO_2$ assimilation (Zhen et al., 2022; Jans et al., 2025; Wang et al., 2024). Within a forest, trees and plants primarily absorb radiation from the PAR wavelength (400-700 nm) and they transmit relatively enriched far-red light (700-750 nm). These far-red light can be used by plants for photosynthesis, particularly, when supplemented with radiation from the PAR wavelength spectrum (Zhen et al., 2022). The consideration of the far-red light for vegetation productivity is most important for shaded vegetation (Zhen et al., 2022) such as the understory represented in our study.

### 3.4.4 Ecosystem exchanges and the morning transition

Modeled and observed ecosystem fluxes (NEE and ET) showed strong agreement, exhibiting similar diurnal cycles and cumulative exchanges. This gives confidence on the ability of a three-layer model initialized by observations to reproduce forest fluxes. However, discrepancies were observed for NEE during the night and during some parts of the morning (from 07:30 to 09:00 LT), midday (from 10:30 to 12:00 LT), and afternoon (from 15:30 to 18 LT).

During midday, the mid-canopy sensor measured persistent (local) illumination that probably overestimated the light condition of the layer, resulting in an overestimation of modeled NEE and ET. During the afternoon, modeled NEE could not be well studied due to a persistent (local) shade at the top-crown sensor. At night, discrepancies may stem from factors such as those identified by Aubinet et al. (2012), including the potential influence of advection terms, which may no longer be negligible.

During the morning, we observed differences particularly from 07:30 LT when the sensible heat flux became positive (Fig. 3.A.5b) until 09:00 LT. This period is part of the morning transition. During the morning transition the nocturnal stable ABL shifts towards a well-mixed ABL. Convective turbulence during this phase entrains air from the nocturnal residual layer and free troposphere while flushing air stored within the canopy. These processes have been observed in Amazon rainforest studies (e.g., Culf et al., 1997; Araújo et al., 2002) and modeled by Dupont et al. (2024) (low wind case, Fig. 2c therein). The storage terms, which corrects observed turbulent fluxes to estimate ecosystem fluxes, played a different role for $CO_2$ and water. While the storage term for water (Fig. 3.A.6b) had a minimal contribution to the total evapotranspiration, the storage term for $CO_2$ (Figure 3.A.6a) had a great impact on NEE during the morning. The magnitude and diurnal cycle of the $CO_2$ storage term align with prior estimates (Malhi et al., 1998; Araújo et al., 2002), peaking at approximate -10 $\mu$mol $CO_2$ $m^{-2}$ $s^{-1}$ in the morning and becoming smaller and positive in the afternoon. However, these estimates are subject to uncertainties, such as sampling limitations, where reducing the number of sensors can introduce a root mean square error of up to 20% (Xu et al., 2019).

Despite the inclusion of the storage terms, modeled and observed NEE differed in the morning transition, particularly regarding the timing of the shift from net ecosystem respiration to net assimilation of $CO_2$. Previous studies (Malhi et al., 1998; Araújo et al., 2002) found that adding the storage term advanced this transition by 1–2 h. Similarly, Dupont et al. (2024) reported a 2 h anticipation for the top layer of their default canopy under low wind conditions (Fig. 9f). By contrast, in our study, the inclusion only advanced the transition by 0.5 h. This mismatch underscores the complex dynamics of the morning transition, where flushing events, entrainment of air with varying $CO_2$ mixing ratios, and turbulence dependent on wind regimes all interact (Dupont et al., 2024).

## 3.5 Conclusions

In this research, we investigated the sub-diurnal variability of water and $CO_2$ fluxes across three canopy layers in a tropical rainforest during days characterized by shallow convection. We used and extended the continuous ATTO observational network during CloudRoots-Amazon22 field Camapign in the Amazonian dry season. These observations enable a detailed characterization of the microclimate (photosynthetic active radiation, temperature, vapor pressure deficit, $CO_2$ mixing ratios, wind, and turbulence), leaf traits (maximum car-

boxylation rate, maximum electron transport, and $^{13}C$ leaf isotopic composition), leaf gas exchange (stomatal conductance and sub-stomatal to atmospheric $CO_2$ mixing ratio), and above canopy ecosystem fluxes (turbulent fluxes and storage terms). The high temporal resolution of these observations allowed us to capture dynamic events, such as cloud-induced radiative perturbations and light penetration variability within the canopy. In this sudy, we first characterized the observed microclimate and leaf traits and then used the observed vertical profiles to drive a three-layer land-surface model which estimated ecosystem fluxes. The modeled ecosystem fluxes (NEE and ET) were then compared to fluxes observed above the canopy.

Our results revealed distinctive vertical profiles of microclimate and leaf traits that influenced the vegetation exchange of water and $CO_2$ and the air transport within the canopy. For instance, we observed a persistent daytime inversion of temperature within the canopy that hindered the air mixing between the mid-canopy and understory with the top-crown layer and the air aloft. In examining the contributions of different canopy layers to the ecosystem fluxes, we found that the top-crown layer played a dominant role in the diurnal patterns of NEE and ET. The mid-canopy layer contributed significantly to NEE and ET only when sufficient radiation penetrated the canopy, while the understory's contributions were generally modest. Overall, the modeled ecosystem fluxes, particularly ET, were in good agreement with those observed above the canopy. However, differences between observed and modeled NEE emerged at specific times: at night when $CO_2$ accumulated within the canopy, and during the morning transition (from 07:30 to 10:30 LT) when some of the accumulated $CO_2$ was released. These discrepancies underscore the importance of accurately representing $CO_2$ storage and release within the canopy, along with the associated ABL transient dynamics.

We believe that multi-layer canopy large-eddy simulations (LES) represent a powerful tool for investigating exchange dynamics across forest layers and for analyzing turbulent transport both above and within the canopy. LES offer high temporal resolution and effectively model the most energetic aspects of turbulence. Our findings emphasize the complexity of vertical gradients within forest canopies, including a variety of microclimatic variables, leaf traits, and canopy fluxes. These results provide a basis for comparison with multi-layer canopy LES and highlight the potential for future research incorporating vertical variability in forest microclimate and leaf traits.

# 3.A Supplementary Information for Chapter 3

### 3.A.1 Correlation between GHI and PAR above the canopy

To convert the clear sky global horizontal irradiance (GHI) reference to a clear sky PAR, a conversion factor was needed. To calculate it, we used observations from a spectroradiometer (FROST; Heusinkveld et al., 2023) located above the forest (at 63 m). This sensor measured different wavelengths and it was able to measure both GHI and PAR. The correlation between both quantities was high, Fig. 3.A.1. By performing a linear regression with null intercept, we found the conversion equation: $PAR = 0.44 \cdot GHI$.

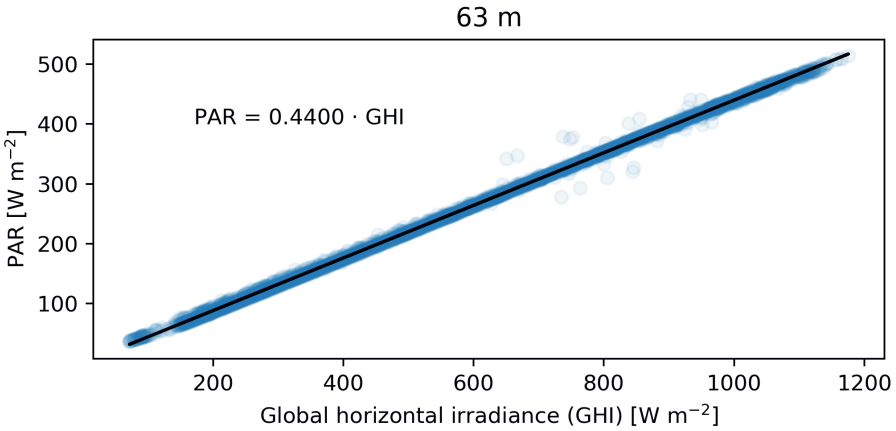



**Figure 3.A.1:** Scatterplot of observed PAR versus observed global horizontal irradiance between 07:00 and 17:00 LT. The radiation sensor was located at 63 m height. A linear fit with null intercept was performed to the observations to calculate a conversion factor between global solar irradiance (GHI) and PAR.

### 3.A.2 Radiative perturbations by clouds

During the selected days, shallow cumulus clouds were present. These clouds perturbed the incoming surface radiation by either casting shadows over the surface or by enhancing the incoming radiation due to scattering of nearby cloud edges. We classified the radiative effect of clouds in three categories: shade, no effect, and enhancement, Fig. 3.A.2. To identify the effect, we calculated the difference between the clear sky PAR reference and the value measured above the canopy. Whenever the difference was larger than 25 $\mu$mol m$^{-2}$ s$^{-1}$, we identified it as a cloud enhancement. On the contrary, if the difference was smaller than $-25$ $\mu$mol m$^{-2}$ s$^{-1}$, we identified it as cloud shade. If none of the previous conditions was met, we classified it as "no effect". "No effect" category can occur because there are not clouds or because they are not altering in a net manner the surface radiation.

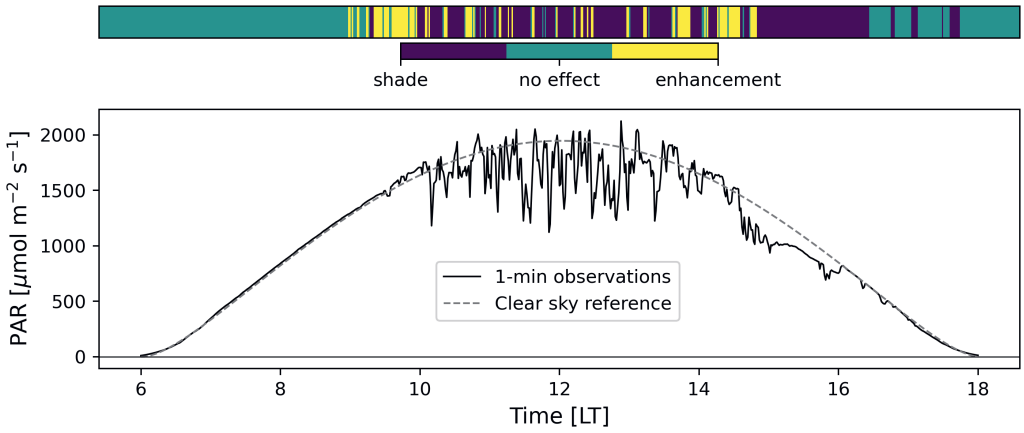



**Figure 3.A.2:** The bottom panel depicts time series of clear sky PAR reference (dashed grey line) and the observed above canopy PAR (solid black line). The upper panel indicates when the cloud is producing a shade (purple), an enhancement (yellow), or no effect (blue).



**Table 3.A.1:** Mean observed A-$g_s$ parameters for the three canopy layers.

| Forest layer | $A_{mmax298}$ [$\mu$mol $m^{-2}$ $s^{-1}$] | $g_{m298}$ [mm $s^{-1}$] |
|---|---|---|
| Top-crown | 17.6 | 2.63 |
| Mid-canopy | 11.9 | 2.25 |
| Understory | 6.8 | 1.46 |

### 3.A.3 Leaf traits

Photosynthesis response curves to sub-stomatal $CO_2$ concentration (Fig. 3.A.3) were used to calculate parameters for the A-$g_s$ leaf gas exchange model. The two calculated parameters were the maximum leaf photosynthetic capacity at 298 K ($A_{mmax298}$) and the mesophyll conductance at 298 K ($g_{m298}$). The fitted parameters can be found in Table 3.A.1.

### 3.A.4 Observed ecosystem fluxes

Soil respiration was measured during CloudRoots-Amazon22 in ATTO. Mean soil respiration efflux had a mild diurnal cycle with values between 4.5 $\mu$mol $CO_2$ $m^{-2}$ $s^{-1}$ and 5 $\mu$mol $CO_2$ $m^{-2}$ $s^{-1}$, Fig. 3.A.4. Fig. 3.A.5 shows time series of the friction velocity ($u_*$) and sensible heat flux (H). These two quantities enabled the determination of the morning transition, defined as the period when the sensible heat flux becomes positive until the time when the friction velocity stabilizes. Finally, in this section we show the time series of the storage fluxes of water and $CO_2$, Fig. 3.A.6.

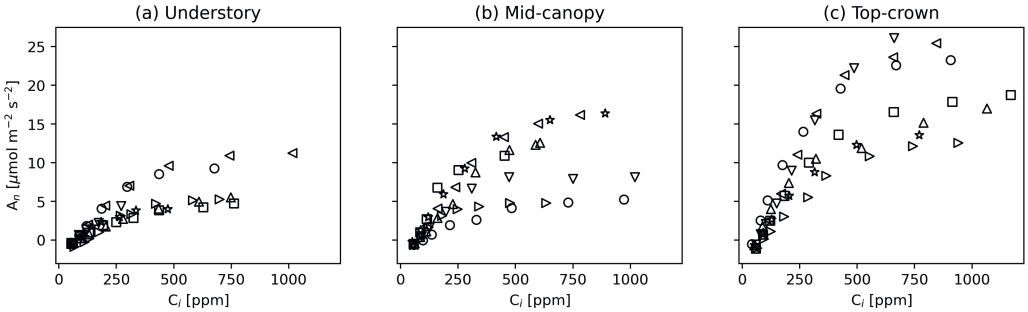



**Figure 3.A.3:** Measured A-$C_i$ response curves for the understory (a), mid-canopy (b), and top-crown (c) forest layers. The symbols depict the individual curves, each performed on a different leaf.

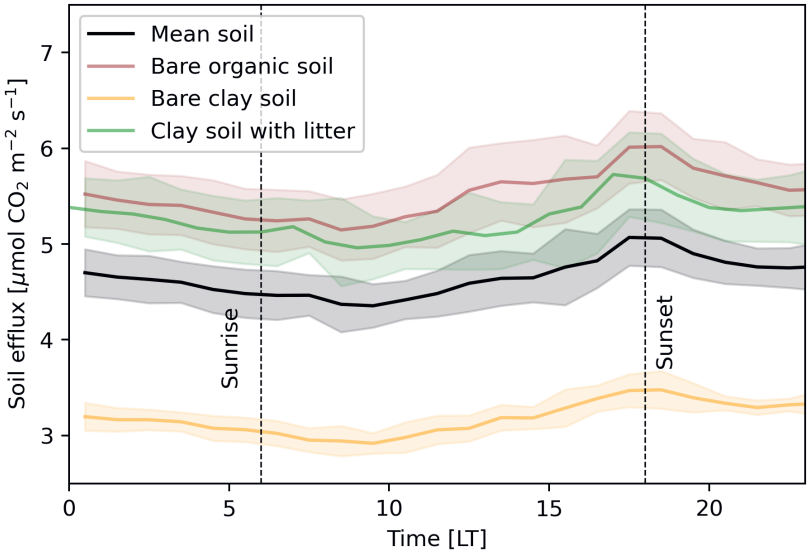



**Figure 3.A.4:** Time series of observed soil respiration efflux. The lines represent the measured soil respiration efflux for the 6-day composite in bare organic soil (red), bare clay soil (yellow), clay soil with litter (green), and the average of the three soil types (black). The shaded region indicates the range within one standard deviation of the mean and represents the variability across the individual days of the 6-day composite.

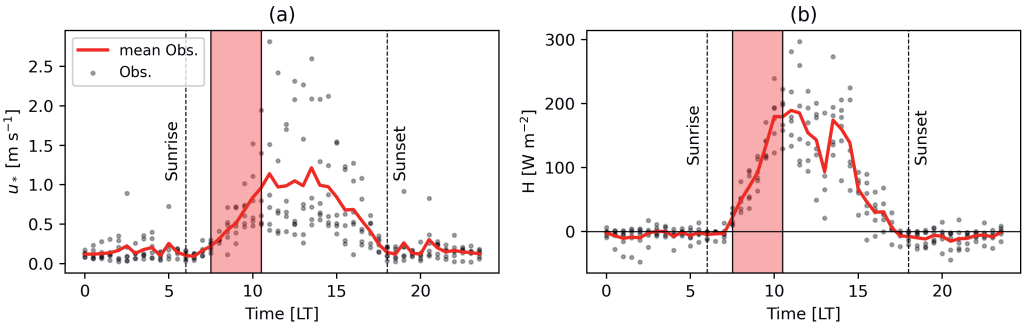



**Figure 3.A.5:** Time series of observed friction velocity, $u_*$, (a); and sensible heat flux, H, (b) at 50 m. Individual observations for the 6 shallow convective days are shown in grey points whereas the mean values are shown as a red line. H only accounts for the turbulent heat flux and it does not include a storage estimation. The red area indicates the morning transition defined to start when H becomes positive (07:30 LT) until when $u_*$ stabilizes (10:30 LT).

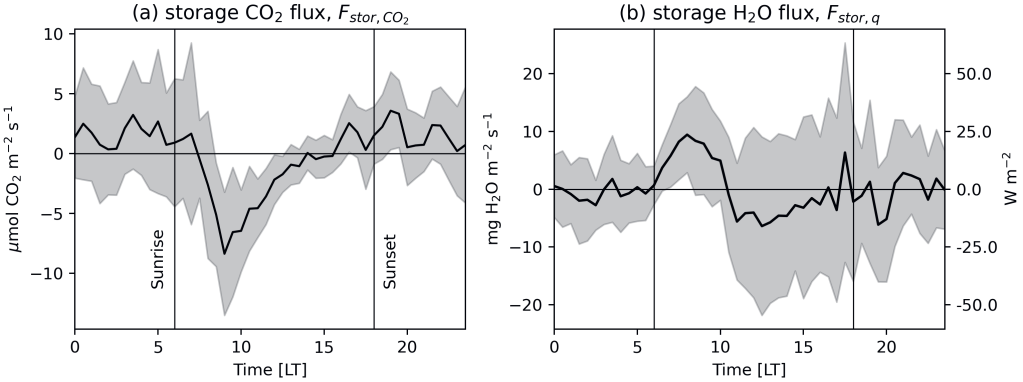



**Figure 3.A.6:** Time series of storage fluxes of $CO_2$ (a) and water (b) at 50 m. The solid line represents the mean value while the shaded region indicates the range within one standard deviation of the mean.

### 3.A.5 Up-scaling leaf fluxes to vegetation canopy fluxes

To calculate vegetation canopy fluxes from leaf fluxes, we need to account for the quantity of leaves that compose the canopy. We do so by integrating the leaf fluxes (leaf transpiration and leaf net $CO_2$ assimilation) over the cumulative leaf area index ($L$), Eq. 3.A.1. We assumed the vertical profile of leaf area density (LAD) and LAI (= 5.32 $m^2$ $m^{-2}$) reported by Gomes Alves et al. (2023) for the ATTO site, Fig. 3.A.7. The observations were carried out with a ground light detection and ranging sensor in October 2015 (details in Section 2.4 of Gomes Alves et al., 2023). The up-scaling from leaf fluxes to vegetation canopy fluxes was performed using the 3-point Gaussian quadrature method (Goudriaan, 1986). The Gaussian quadrature method was constructed to yield exact integration calculation for polynomials. In the case of the 3-point Gaussian quadrature, it is able to exactly integrate polynomials of degree 5 and lower. In the 3-point Gaussian quadrature, the function we aim to integrate, $f(L) = A_n(L)$ or $TR(L)$, is calculated as a weighted sum of the function evaluated at three points ($L_1$, $L_2$ and $L_3$), Eq. 3.A.2.

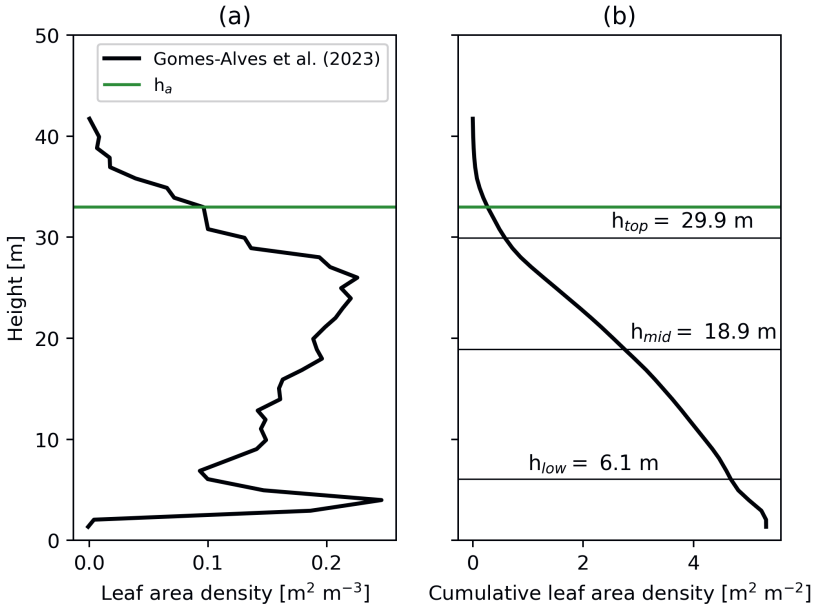



**Figure 3.A.7:** Leaf area density (a) and cumulative leaf area index (b) for terra firme upland rainforest. Values are based on Gomes Alves et al. (2023) study. The vertical lines in panel (b) indicate the heights ($h_{top}$, $h_{mid}$, $h_{low}$) where the leaf fluxes are evaluated to up-scale to canopy fluxes using the 3-point Gaussian quadrature method.

$$A_{n,canopy} = \int_0^{LAI} A_n(L)dL \quad ; \quad TR_{canopy} = \int_0^{LAI} TR(L)\, dL \tag{3.A.1}$$

$$\int_0^{LAI} f(L)dL \approx \frac{LAI}{3.6} \sum_{i=1}^{3} w_i \cdot f(L_i) \tag{3.A.2}$$

with weights: $w_1 = w_3 = 1$ and $w_2 = 1.6$, and points: $L_1 = (0.5 - \sqrt{0.15})LAI$, $L_2 = 0.5 \cdot LAI$ and $L_3 = (0.5 + \sqrt{0.15})LAI$

Given the assumed LAI and cumulative LAD profiles (Fig. 3.A.7b), we can find the three heights where the functions ($A_n(L)$ and $TR(L)$) must be known. These quadrature heights are: 29.9 m for the top-crown, 18.9 m for the mid-canopy, and 6.1 m for the understory. These heights do not directly correspond with the heights where the sensors were positioned. In general, the sensors were located slightly lower (1-5 m) than the quadrature heights. We decided not to interpolate our observations over height to match the quadrature heights. Our reasoning was two-fold. First, a height interpolation would modify the measured temporal variability of the observed microclimate, maybe in ways that are not realistic, particularly for radiation. Second, the local canopy architecture surrounding the sensors may be different than that depicted by the mean LAD profile, introducing uncertainty to the quadrature heights estimation.



Finally, with the 3-point Gaussian quadrature approach, we decompose the ecosystem fluxes into the contributions of the understory, mid-canopy, and top-crown. We do so by attributing $\frac{LAI}{3.6} w_1 \cdot f(L_1)$ to the understory, $\frac{LAI}{3.6} w_2 \cdot f(L_2)$ to the mid-canopy, and $\frac{LAI}{3.6} w_3 \cdot f(L_3)$ to the top-crown.

### 3.A.6 Cumulative daytime NEE and ET (observations and modeled results)

To compare observed and model ecosystem fluxes, we calculated the cumulative daytime NEE and ET for both observations and model results, Table 3.A.2. This quantity reflects the water and $CO_2$ exchanged per unit area from sunrise until sunset. To quantify the effect of the storage term, we also calculated the cumulative of the surface turbulent fluxes and compare it with the cumulative of the observed ecosystem fluxes which accounted for the storage.

### 3.A.7 Calculation of the ecosystem fluxes with averaged in-canopy radiative fluctuations

Within the canopy, radiation measurements are sensitive to the position of the sensor. Because we used a PAR profile measured in a single tower, our leaf stomatal conductance (Fig. 3.6), canopy fluxes (Fig. 3.7), and ecosystem fluxes (Fig. 3.8) are sensitive to the local radiation fluctuations. Our estimated ecosystem fluxes (Fig. 3.7 and Fig. 3.8) represent the variability that an ecosystem would experience if subject to the strongly varying light environment that a leaf experiences.

**Table 3.A.2:** Cumulative ecosystem water and $CO_2$ exchange per area during daytime. The table shows the cumulative for modeled NEE and ET, observed NEE and ET, and observed surface turbulent fluxes of water and $CO_2$ ($F_{CO_2}$ and $F_{H_2O}$).

| Variable | Units | Whole ecosystem (vegetation + soil) |
|---|---|---|
| $-\int_{sunrise}^{sunset} NEE_{modeled}\, dt$ | g $CO_2$ $m^{-2}$ | 19.41 |
| $-\int_{sunrise}^{sunset} NEE_{observed}\, dt$ | g $CO_2$ $m^{-2}$ | 19.16 |
| $-\int_{sunrise}^{sunset} F_{CO_2,observed}\, dt$ | g $CO_2$ $m^{-2}$ | 16.03 |
| $\int_{sunrise}^{sunset} ET_{modeled}\, dt$ | kg $H_2O$ $m^{-2}$ | 3.76 |
| $\int_{sunrise}^{sunset} ET_{observed}\, dt$ | kg $H_2O$ $m^{-2}$ | 3.55 |
| $\int_{sunrise}^{sunset} F_{H_2O,observed}\, dt$ | kg $H_2O$ $m^{-2}$ | 3.53 |

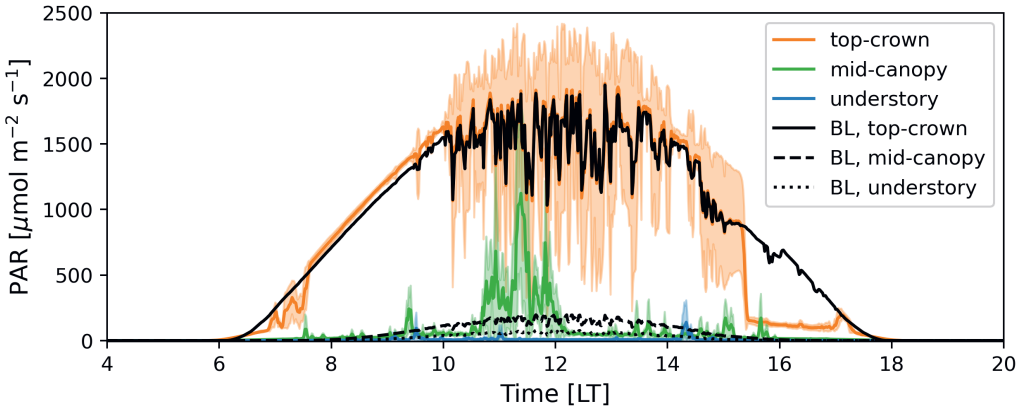



**Figure 3.A.8:** Time series of observed PAR as in Fig. 3.1 and Beer-Lambert's (BL) law estimation of PAR for the three canopy layers (shown in black lines).

As a sensitivity study, we have recalculated the fluxes using Beer-Lambert law estimations of radiation in the three layers (Fig. 3.A.8). In doing so, we also eliminated the observed opaque shadow in the top-crown layer between 15:30 and 17:00 LT.

As expected, the resulting fluxes per layer have a smoother diurnal cycle (Fig. 3.A.9) at all levels than when using the observed PAR profile (Fig. 3.7). In the mid-canopy and understory, the diurnal cycles of $A_{nc}$ and TR are particularly symmetric around solar noon, indicating the maximum rates at midday. The modeled and observed ecosystem fluxes remain similar (Fig. 3.A.10). The afternoon transition of the ecosystem from being a $CO_2$ sink into a source occurs at approximately 16:30 LT for both model and observations.

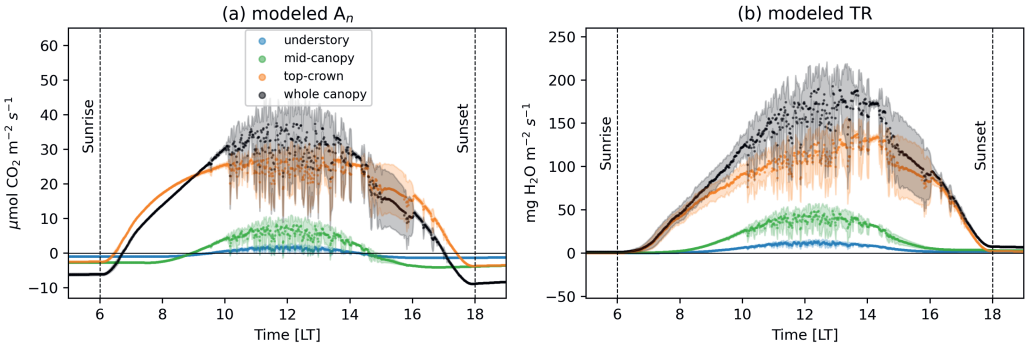



**Figure 3.A.9:** Same as Fig. 3.7 but for the modeled results using averaged in-canopy radiation.

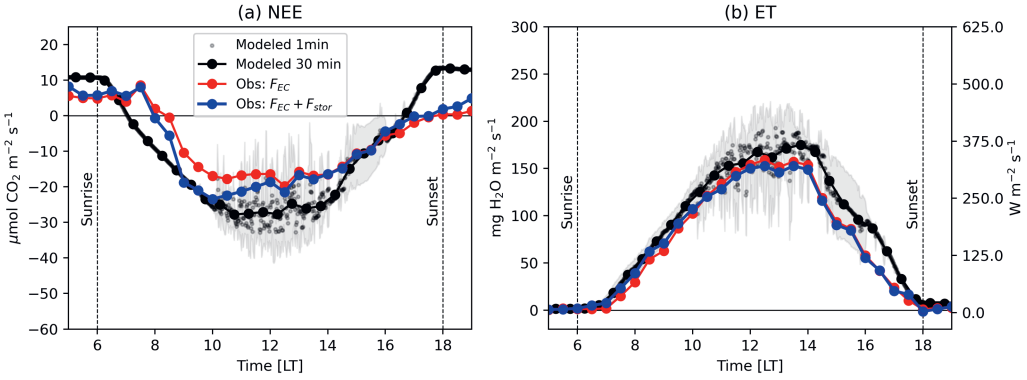



**Figure 3.A.10:** Same as Fig. 3.8 but for the modeled results using averaged in-canopy radiation.

# Chapter 4

# Radiative transfer within vegetation canopies

This chapter is based on:

González-Armas R., Vilà-Guerau de Arellano J., de Boer, H. J., Pedruzo-Bagazgoitia X. & Veerman M. A. *Development and Evaluation of a Multi-Spectral Canopy Radiation Transfer Scheme in a Canopy-Resolving Large Eddy Simulation* (In Preparation)

## Abstract

Radiation is a key driver of land-atmosphere interactions. Solar shortwave radiation provides the energy needed to evaporate and transpire water, and to warm the surface and the adjacent air, initiating the convective mixing of the atmosphere during daytime. Part of that radiation, the photosynthetically active radiation (PAR), provides the energy plants need to photosynthesize. The longwave radiation emitted by the vegetation canopy, soil and sky also plays a major role in the surface energy balance, influencing canopy and near-surface air temperatures as well as air stability and turbulent air flow.

In this study, we revised the one-dimensional canopy radiative transfer scheme of the multi-layer canopy large-eddy simulation model, can-DALES. The updated scheme simulates shortwave and longwave radiation, and now resolves four shortwave spectral bands, representing an advancement over the previous broadband formulation. Specifically, it distinguishes ultraviolet (UV; 280-400 nm), PAR (400-700 nm), far-red (700-750 nm), and near infrared (NIR; 750-4000 nm), which are transferred independently through the canopy. We also reformulated several components of the shortwave and longwave transfer scheme, yielding a more consistent and robust representation aligned with established approaches.

We analyzed the sensitivity of the shortwave radiative transfer to external atmospheric forcings (i.e., the diffuse radiative flux fraction and the solar zenith angle) and internal canopy factors (i.e., leaf area density and leaf area index). Furthermore, we validated the model against radiation measurements from the Amazon rainforest. The revised scheme accurately reproduced (i) the stronger attenuation of UV and PAR relative to far-red and NIR, (ii) the spectral differences in shortwave and PAR reflectance, and (iii) the observed diurnal patterns. These improvements build confidence on the capabilities of the canopy radiative transfer scheme of can-DALES, which now enable to study the impact of UV and far-red spectral bands on photosynthesis and surface energy balance. Some model limitations remain, the most important being the absence of explicit woody biomass and of canopy heat storage in can-DALES.

## 4.1 Introduction

Radiation is a primary driver of land-atmosphere interactions, governing both ecosystem functioning and the dynamics of the atmospheric boundary layer. From the vegetation perspective, the solar radiation pertaining to the photosynthetically active range (PAR; 400-700 nm) is used by plants to perform photosynthesis and thereby, uptake $CO_2$ from the atmosphere (McCree, 1981). Additionally, the vertical and spectral distribution of radiation within plant canopies determines where photosynthesis is most active (Monsi & Saeki, 2005; Goudriaan, 1977), and drives structural adaptations of the vegetation to these light gradients through adjustments in leaf morphology, leaf nitrogen distribution, and crown architecture (Horn, 1971; Niinemets, 2010; Hikosaka, 2014; Valladares & Niinemets, 2007). From the atmospheric perspective, the solar radiation controls the development of the atmospheric boundary layer (e.g., Sarma et al., 2022), by modulating surface turbulent heat fluxes (Best et al., 2015), evapotranspiration (Pieruschka et al., 2010; Best et al., 2015, and Chapter 2) and near-surface atmospheric stability (Oke, 1987; Stull, 1988; Garratt, 1992; Monteith & Unsworth, 2013). Longwave radiation (LW; 3-100 $\mu$m; Monteith & Unsworth, 2013) emitted by the soil, vegetation, clouds and atmospheric gases also plays a role in land-atmosphere interactions, as it redistributes energy, and modulates canopy temperatures and air stability (Schilperoort et al., 2020; Froelich et al., 2011; Mahrt, 1999).



The transfer of radiation through a vegetation canopy depends on both external forcings and internal canopy factors. External factors include incoming downward radiation intensity, its partitioning between direct and diffuse components, and the solar zenith angle. Diffuse light is particularly important because it redistributes light more evenly within the canopy, increasing net $CO_2$ assimilation in a phenomenon known as the diffuse fertilization effect (Gu et al., 2002; Mercado et al., 2009; Wang et al., 2018; Gu et al., 2003; van Diepen et al., 2025). On top of the increase in $CO_2$ assimilation rates, diffuse light is also thought to increase evapotranspiration (Wang et al., 2022a). The diffuse fertilization effect varies diurnally, seasonally, and across ecosystems as solar zenith angles and atmospheric conditions change (Wang et al., 2022b), acquiring different significance for diverse ecosystems.

Internally, canopy architecture and the leaf optical properties regulate the radiative transfer (Bonan, 2019). The quantity and vertical distribution of plant material, typically expressed as the plant area density (PAD) and plant area index (PAI), control how much radiation is absorbed by the canopy. Since forest types can exhibit markedly different PAD and PAI (Asner et al., 2003; Tang et al., 2016; Béland & Kobayashi, 2021), the radiation transmissivity through diverse canopies also varies. Beyond the vertical structure, radiation transfer is also dependent on the three-dimensional distribution of foliage and the leaf angle distribution. At the leaf scale, optical properties vary strongly with wavelength, with different scattering characteristics for ultraviolet radiation (UV), photosynthetic active radiation (PAR), far-red radiation (Far-Red), and near infrared radiation (NIR). As a result, the vertical attenuation of radiation exhibits distinct profiles for each spectral band (de Castro, 2000; Wang et al., 2024).

Several one-dimensional modeling approaches have been developed to describe the radiative transfer within canopies and the above mentioned mechanisms. Some widespread radiative schemes are the numerical solution proposed by Norman (1979), the analytical solution proposed by Goudriaan & Van Laar (1994), and the 2-stream numerical approximation developed by Dickinson (1983) and Sellers (1985). These three approaches treat the canopy as a horizontally homogeneous layer and focus on the vertical variation of radiation, only describing upward and downward radiative fluxes. To account to some extent for spatial foliage aggregation, they tend to include the clumping index, a factor which indicates the degree of clustering of leaves across stems and tree crowns. More sophisticated three-dimensional radiative schemes enable the description of detailed canopy structure (e.g., North, 1996; Kobayashi et al., 2012; Liu et al., 2022; Oshio & Asawa, 2023), but they are computationally expensive, limiting their application to specific study cases.

The multi-layer canopy Dutch Atmospheric Large Eddy Simulation (hereinafter referred to as can-DALES model; Pedruzo-Bagazgoitia et al., 2023) is an land-atmosphere model that is able to resolve canopy and atmospheric boundary layer - scale turbulence, enabling the study of forest-air-cloud interactions. Given the importance of radiation in controlling photosynthesis, evapotranspiration, and buoyancy, we report and analyze in this chapter a revised version of the canopy radiative transfer scheme used in can-DALES. The radiative scheme was and it is still based on the approach of Goudriaan & Van Laar (1994) for shortwave radiation, but it has now been extended to model separately four shortwave spectral bands: UV, PAR, far-red and NIR. Additionally, more accurate canopy reflectance parameterizations have been included. The longwave radiative scheme has also been revised and updated, and it is now based on the solution reported by Bonan (2019) but with some simplifications which enable a less computationally expensive non-iterative solution.

In this chapter, we first introduce the updated canopy radiative transfer scheme in Sect. 4.2. We then use the radiative transfer scheme in Sect. 4.3.1 and Sect. 4.3.2 as a proof of concept for exploring how the radiative transfer varies vertically and for the different shortwave spectral bands. In those sections, we also explore how the canopy radiative transfer changes due to external and internal canopy factors. Regarding the external factors, we explore how the radiative transfer changes with respect to the solar zenith angle, and the direct and diffuse partitioning of top of the canopy radiation, exploring the diffuse fertilization effect. Regarding the internal canopy factors, we explore how the radiative transfer is altered for different ecosystems using typical leaf area index (LAI) and leaf area density (LAD) values for a tropical forest (ATTO site, Brazil), a temperate forest (Loobos site, The Netherlands), and a Boreal forest (Hyytiälä site, Finland). Finally, in Sect. 4.3.3, we validate the radiative transfer against observations acquired at the Amazon tropical rainforest (ATTO site) during CloudRoots-Amazon22 Field Campaign.

## 4.2 Model formulation

### 4.2.1 Can-DALES model

Can-DALES was initially developed and documented by Pedruzo-Bagazgoitia et al. (2023). The canopy representation in can-DALES builds upon three crucial aspects: (1) the drag and dynamical effects of the canopy (Ouwersloot et al., 2017), (2) a 2 big-leaf scheme which allows the distinction between sunlit and shaded leaves per vertical level and that represents stomatal conductance, leaf photosynthesis, and transpiration (Pedruzo-Bagazgoitia et al., 2017), and (3) the canopy radiative transfer scheme. In the following sections, Sect. 4.2.2 and Sect. 4.2.3, we document the updated canopy radiative transfer scheme.

### 4.2.2 Shortwave radiative transfer scheme

The shortwave radiative transfer scheme is based on the analytical approach reported by Goudriaan (1977) and Goudriaan & Van Laar (1994). The main difference with respect to Goudriaan (1977) and Goudriaan & Van Laar (1994) is that we now distinguish four optical bands (UV, PAR, far-red, and NIR) on the shortwave broadband spectrum instead of two (PAR and NIR). We have also performed some additional modifications which are detailed in Appendix 4.A.1. In this section, we first detail the spectral band separation of the shortwave broadband in Sect. 4.2.2, and then, we detail how a generic shortwave band is transferred through the canopy in Sect. 4.2.2.



*Spectral separation*

The canopy radiative transfer of shortwave radiation depends on two spectral-specific factors: (1) the downward irradiance at canopy top, and (2) the leaf scattering coefficients. These two factors must be specified for each spectral band, and they can be modified in the settings file of can-DALES.

In this study, we used the factors indicated in Table 4.1. The spectral fractions of downward irradiance at canopy top were estimated using the Simple Model of the Atmospheric Radiative Transfer of Sunshine (SMARTS V2.9.5; Gueymard et al., 1995) for a standard tropical atmosphere. The standard tropical atmosphere was characterized by an aerosol optical depth at 500 nm of 0.1.The estimated solar spectral irradiance at canopy top is shown in Fig. 4.1 (red line, right y-axis). The downward shortwave irradiance at canopy top was primarily constituted of PAR (45.0 %), and NIR (36.7 %), and contained smaller contributions of UV (12.8 %) and Far-Red (5.5 %), Table 4.1. The band-specific leaf scattering coefficients were derived from measurements of leaf transmittances and reflectances acquired at tropical forests in Puerto Rico (Serbin et al., 2019) and Panamá (Lamour et al., 2020), Fig. 4.1 (solid and dotted black lines, left y-axis). The leaf scattering coefficient ($\sigma$) quantifies the proportion of

incident light over the leaf surface that is redirected outward, being either reflected or transmitted. Thus, the leaf scattering coefficient is estimated as the sum of the leaf reflectance and transmittance, Table 4.1.

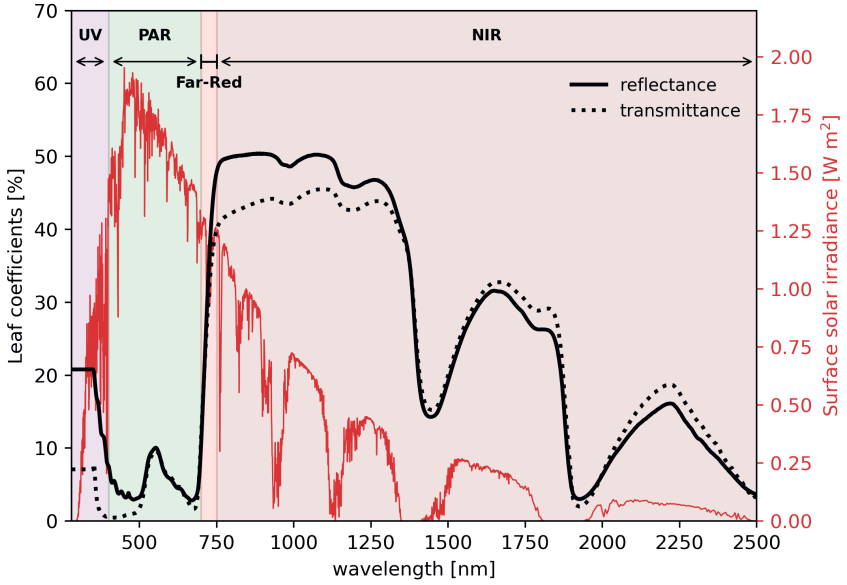



**Figure 4.1:** On the left y-axis, spectral leaf coefficients: transmittance (dotted black line) and reflectance (solid black line) for tropical forests. The spectral leaf optical coefficients average observations from two datasets, one acquired in several tropical forest sites in Puerto Rico during 2017 (Serbin et al., 2019) and the other in San Lorenzo forest site in Panamá during 2020 (Lamour et al., 2020). The four shortwave spectral bands used in the radiative transfer scheme are indicated in purple shading for UV, in green for PAR, in red for far-red, and in brown for NIR. On the right y-axis, surface solar spectral irradiance is indicated in red line as estimated from SMARTS V2.9.5 model (Gueymard et al., 1995).

*Radiative transfer of shortwave spectral bands*

To calculate the radiative transfer of a generic shortwave spectral band, specific internal canopy parameters and external boundary conditions are needed. To characterize the vegetated canopy and soil, the canopy radiative transfer scheme uses: the accumulated leaf area index starting from canopy top ($L$), the leaf scattering coefficient ($\sigma$), the clumping index ($\Omega$), and the soil reflectivity ($\rho_s$). The accumulated leaf area index $L$ is used as vertical coordinate, ranging from 0 at the top of the canopy to the leaf area index ($LAI$) at the soil surface.

**Table 4.1:** Leaf optical properties of tropical leaves based on observations performed at Puerto Rico and Panamá (Serbin et al., 2019; Lamour et al., 2020). The leaf optical properties are written as the average value ± the standard deviation. The scattering coefficients used in the present chapter are indicated between parenthesis and in bold font. The PAR and NIR scattering coefficients do not exactly correspond to the averaged value, because they have been modified to better represent the observed canopy reflectance at the ATTO site. The rightmost column indicates the percentage of surface shortwave irradiance belonging to each of the spectral bands.

| Band | Leaf optical properties [-] | | | Spectral fraction of irradiance [%] |
|---|---|---|---|---|
| | Reflectance ($\rho$) | Transmittance ($\tau$) | Scattering coefficient ($\sigma = \rho + \tau$) | |
| UV | $0.135 \pm 0.070$ | $0.022 \pm 0.014$ | $0.157 \pm 0.085$ (**0.157**) | 12.8 % |
| PAR | $0.052 \pm 0.020$ | $0.040 \pm 0.032$ | $0.092 \pm 0.052$ (**0.130**) | 45.0 % |
| Far-Red | $0.330 \pm 0.051$ | $0.293 \pm 0.068$ | $0.622 \pm 0.119$ (**0.622**) | 5.5 % |
| NIR | $0.455 \pm 0.044$ | $0.408 \pm 0.057$ | $0.863 \pm 0.101$ (**0.750**) | 36.7 % |
| SW broadband | $0.230 \pm 0.026$ | $0.194 \pm 0.038$ | $0.424 \pm 0.064$ | 100.0 % |



The boundary conditions are the downwelling radiation at the top of the canopy ($L = 0$) and the solar zenith angle ($\theta_z$). The downwelling shortwave radiation at canopy top ($\phi^{\downarrow}(0)$) has a direct component, which follows $\theta_z$, and a diffuse component, which is assumed isotropic:

$$\phi^{\downarrow}(0) = \phi^{\downarrow}_{dir}(0) + \phi^{\downarrow}_{dif}(0) \tag{4.1}$$

At a given canopy depth $L$, the downward and upward shortwave radiation follows the analytical solution proposed by Goudriaan (1977) and Goudriaan & Van Laar (1994), being expressed as the sum of two exponential profiles. We apply these solutions separately to simulate the transfer of direct and diffuse top of the canopy irradiances. The transfer of the top of the canopy direct radiation is calculated as:

$$\phi^{\downarrow}_{dir}(L) = \phi^{\downarrow}_{1,dir} \exp\left(-K_{dir} L\right) + \phi^{\downarrow}_{2,dir} \exp\left(K_{dif} L\right) \tag{4.2}$$

$$\phi^{\uparrow}_{dir}(L) = \phi^{\uparrow}_{1,dir} \exp\left(-K_{dir} L\right) + \phi^{\uparrow}_{2,dir} \exp\left(K_{dif} L\right) \tag{4.3}$$

whereas the transfer of top of the canopy diffuse radiation is calculated as:

$$\phi^{\downarrow}_{dif}(L) = \phi^{\downarrow}_{1,dif} \exp\left(-K_{dif} L\right) + \phi^{\downarrow}_{2,dif} \exp\left(K_{dif} L\right) \tag{4.4}$$

$$\phi^{\uparrow}_{dif}(L) = \phi^{\uparrow}_{1,dif} \exp\left(-K_{dif} L\right) + \phi^{\uparrow}_{2,dif} \exp\left(K_{dif} L\right) \tag{4.5}$$

where $\phi^{\downarrow}_{1,dir}$, $\phi^{\downarrow}_{2,dir}$, $\phi^{\uparrow}_{1,dir}$, $\phi^{\uparrow}_{2,dir}$, $\phi^{\downarrow}_{1,dif}$, $\phi^{\downarrow}_{2,dif}$, $\phi^{\uparrow}_{1,dif}$ and $\phi^{\uparrow}_{2,dif}$ are radiative fluxes whose functional form is detailed in the Appendix (eq. (4.A.1)-(4.A.8)), and $K_{dir}$ and $K_{dif}$ are the direct and diffuse extinction coefficients which are estimated as follows:

$$K_{dir} = \frac{\overbrace{0.5\Omega}^{K_{dir,bl}}}{cos\theta_z}\sqrt{1-\sigma} \tag{4.6}$$

$$K_{dif} = \Omega \cdot \overbrace{0.8}^{K_{dif,bl}}\sqrt{1-\sigma} \tag{4.7}$$

with $K_{dir,bl}$ and $K_{dif,bl}$ representing the extinction coefficients of black (non-scattering) leaves.

### 4.2.3 Longwave radiative transfer scheme

The canopy radiative transfer scheme for longwave radiation is based on the numerical solution described in Bonan (2019). With this approximation we calculate the downwelling and upwelling longwave fluxes at a level interface, $i$, as the sum of four terms which represent: (1) the transmitted LW radiation through open canopy holes, (2) the forward-scattered LW radiation due to the interaction with leaves, (3) the back-scattered (reflected) longwave radiation due to the interaction with leaves, and (4) the radiation emitted by the leaves.

$$LW^{\downarrow}_i = \overbrace{LW^{\downarrow}_{i+1}\tau_{d,i+0.5}}^{\text{Transmission through canopy holes}} + \overbrace{LW^{\downarrow}_{i+1}\left(1-\tau_{d,i+0.5}\right)\tau_{l,i+0.5}}^{\text{Forward-scattering by leaves}} + \overbrace{LW^{\uparrow}_i\left[(1-\tau_{d,i+0.5})\rho_{l,i+0.5}\right]}^{\text{Back-scattering by leaves}} + \overbrace{\epsilon_{l,i+0.5}\sigma_{SB}\left[T^4_{shaded,i+0.5}(1-f_{sun,i+0.5}) + T^4_{sun,i+0.5}f_{sun,i+0.5}\right]\left(1-\tau_{d,i+0.5}\right)}^{\text{Emission by leaves}} \tag{4.8}$$

$$LW^{\uparrow}_{i+1} = \overbrace{LW^{\uparrow}_i\tau_{d,i+0.5}}^{\text{Transmission through canopy holes}} + \overbrace{LW^{\uparrow}_i\left(1-\tau_{d,i+0.5}\right)\tau_{l,i+0.5}}^{\text{Forward-scattering by leaves}} + \overbrace{LW^{\downarrow}_i\left[(1-\tau_{d,i+0.5})\rho_{l,i+0.5}\right]}^{\text{Back-scattering by leaves}} + \overbrace{\epsilon_{l,i+0.5}\sigma_{SB}\left[T^4_{shaded,i+0.5}(1-f_{sun,i+0.5}) + T^4_{sun,i+0.5}f_{sun,i+0.5}\right]\left(1-\tau_{d,i+0.5}\right)}^{\text{Emission by leaves}} \tag{4.9}$$

in these equations the integer indices $i$ and $i+1$ refer to the interfaces of layers (half levels) where the radiative fluxes are defined, whereas $i+0.5$ refer to the layers (full levels) where the canopy properties, and sources and sinks are defined. $\tau_{d,i+0.5}$ is the diffuse transmittance through the canopy layer $i+0.5$, whereas $\tau_{l,i+0.5}$, $\rho_{l,i+0.5}$ and $\epsilon_{l,i+0.5}$ are the longwave leaf

transmittance, reflectance and emissivity corresponding to the canopy layer $i + 0.5$. $\sigma_{SB}$ represents the Stephan-Boltzmann constant. $T_{sun}$ and $T_{shade}$ represent the temperatures of sun-lit and shaded leaves whereas the fractional area of sun-lit leaves of the canopy layer $i + 0.5$ is represented by $f_{sun,i+0.5}$, which ranges from 0 (all leaves are shaded) to 1 (all leaves are receiving direct sunlight).

In can-DALES we solve eq. (4.8) and (4.9) at each time step with two loops: one for downwelling longwave radiation which starts at canopy top and finishes at the forest floor, and another for upwelling longwave radiation which starts at the forest floor and finishes at canopy top. While doing so, we have neglected the back-scattering component in eq. (4.8) and (4.9) ($\rho_l = 0$) as a first approximation. To estimate $\tau_d$, we followed the approximation by (Goudriaan, 1988) for spherical leaf angle distribution, and used three leaf angle classes (0-30°, 30-60 °, and 60-90°). Finally, in this chapter, we use a leaf emissivity $\epsilon_l = 0.98$ and a leaf transmissivity $\tau_l = 0.02$ for all canopy layers.

### 4.2.4 Sensitivity analysis to external and internal factors, and validation dataset

To evaluate the radiative transfer scheme, we performed (1) a sensitivity analysis of shortwave radiative transfer to external and internal canopy factors, and (2) a validation against observations for a tropical rainforest site (ATTO site; 2° 8' 45" S, 59 ° 0' 19" W; Andreae et al., 2015). For the sensitivity analysis, we used cases based on the tropical rainforest site and two additional sites: a temperate forest at Loobos site (The Netherlands Zhao et al., 2025), and a boreal forest at Hyytiälä site (Finland). For the sensitivity to external factors, we estimated the solar zenith angle during daytime for the three locations, whereas for the sensitivity to internal canopy factors, we used reported LAI values. The LAI values used for each site were: 5.3 $m^2$ $m^{-2}$ (Gomes Alves et al., 2023) for ATTO site, 3.3 $m^2$ $m^{-2}$ for Hyytiälä site (Lindroth et al., 2008), and 1.8 $m^2$ $m^{-2}$ for Loobos site (Zhao et al., 2025). We also used leaf area density values to represent each forest type. For the tropical rainforest, we used values measured at ATTO site with a ground-based light detection and ranging (LiDAR) sensor in October 2015 (Gomes Alves et al., 2023). For the temperate and boreal forest, we lacked observational profiles and thus, we used a LAD parameterization based on a beta distribution (Meyers et al., 1998; Wu et al., 2003). The LAD profile we associated to the temperate forest indicated that leaves were distributed across a wide vertical span with maximum leaf allocation at approximately $2/3$ of canopy height, whereas the LAD profile we associated to the boreal forest contained the majority of the leaves clustered in the upper half of the canopy and the maximum leaf allocation at approximately $3/4$ of the canopy height. These LAD profiles are not intended to faithfully represent the specific sites but to capture a realistic range of possible LAD configurations.

For the validation, we compared the canopy radiative transfer model results against observations acquired at ATTO tropical site during CloudRoots-Amazon22 field campaign. Details about the field campaign and observational dataset have been previously reported by Vilà-Guerau de Arellano et al. (2024). Here, we briefly detail the observations used for the canopy

radiative transfer validation. At 75 m, downwelling and upwelling longwave and shortwave radiation were measured with a Pyrgeometer (CGR4, Kip Zonen, Netherlands) and a Pyranometer (CMP21, Kipp Zonen, Netherlands) respectively (Andreae et al., 2015). Downwelling and upwelling PAR was measured with a Quantum sensor (PAR LITE, Kipp Zonen, Netherlands) at 5, 15, 25, 35, 50 and 81 m (Andreae et al., 2015). Additionally, downwelling PAR and shortwave radiation were measured with another instrument (FROST; Heusinkveld et al. (2023)) at 0.5, 5, 15, 23 and 63 m (Vilà-Guerau de Arellano et al., 2024).

### 4.2.5 Numerical settings

The canopy radiative transfer model was run with various settings for the sensitivity analysis of the shortwave transfer. The specific settings are detailed in the captions of each figure presented in Sect. 4.3.1. For the results of longwave transfer and the validation, we conducted a can-DALES simulation which is also used in Chapter 5 to explore the canopy-atmosphere interactions. Here, we explain only the details about the simulation which are relevant for the canopy radiative transfer. For additional details related to the simulation, the reader is referred to Chapter 5.

The can-DALES simulation represented the daytime period of a composite day during CloudRoots-Amazon22, which took place during the dry season. The composite day characterizes shallow-convective conditions with shallow-cumulus clouds appearing at approximately 09-10 LT and dissipating at approximately 16-17 LT. The simulation covers a domain of $12096 \times 12096 \times 5855$ m$^3$ with a resolution of $12 \times 12 \times 3$ m$^3$ within the canopy and up to 200 m on the vertical. The simulated canopy consisted of 12 canopy layers and its canopy top was located at 36 m. As mentioned above, the assumed leaf area density (LAD) profile was based on observations acquired by Gomes Alves et al. (2023). For the radiative transfer above the canopy we use the Rapid Radiative Transfer Model for General Circulation Models (RRTMG) scheme (Iacono et al., 2008). The downward fluxes calculated by the RRTMG scheme at canopy top (36 m) are subsequently used as boundary conditions for the canopy radiative transfer model.

## 4.3 Results

### 4.3.1 Shortwave radiative transfer

*Spectral wavelength dependency*

The updated scheme describes the distinct spectral-band-specific radiative transfer as shown in Fig. 4.2 for typical midday conditions at ATTO tropical site during CloudRoots-Amazon22. The downward and upward radiative fluxes, and the radiation absorbed by the leaves follow closely an exponential function whose extinction coefficient varies with the spectral band

considered, Fig. 4.2 (b-e). Downward PAR and UV are attenuated more strongly with canopy depth compared to Far-Red and NIR (Fig. 4.2b), which are transmitted deeper into the lower canopy layers and the soil surface due to the the higher scattering coefficients (Table 4.1). The downward top of the canopy shortwave radiation is richer in PAR compared to the other spectral bands (Fig. 4.2c), but due to the high PAR absorption (Fig. 4.2e), the NIR dominates the downward shortwave fluxes from certain canopy depth (ca. 5 m for Fig. 4.2c). The upward radiative fluxes are mild for all spectral bands but NIR, because its larger soil reflectance and the smaller light attenuation within canopy, Fig. 4.2d.

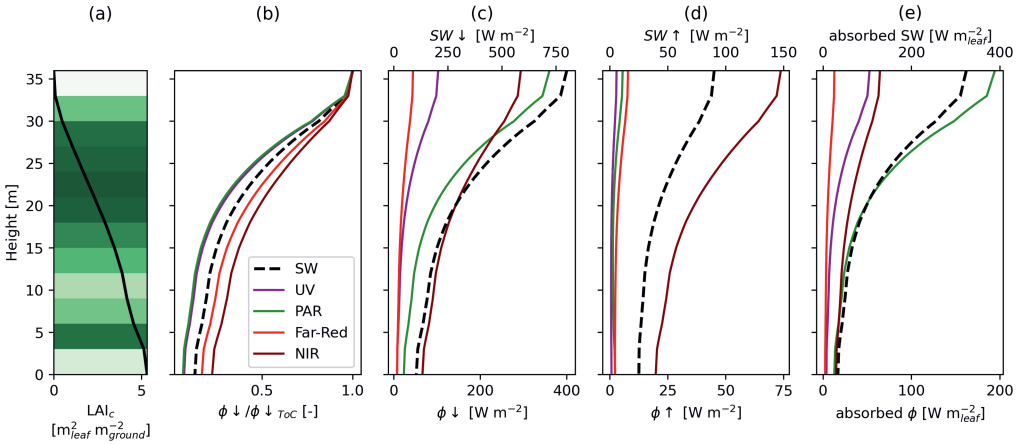



**Figure 4.2:** Vertical profiles of cumulative leaf area index (a), and radiation fluxes (b-e). Panel (a) depicts in solid black line the cumulative leaf area index whereas the leaf area density is indicated by green shades, with darker colors indicating higher values. The radiative transfer has been estimated based on a soil reflectivity ($\rho_s$) of 0.1 for UV and PAR spectral bands, and of 0.3 for Far-Red and NIR spectral bands. The clumping index ($\Omega$) was set to 1 (no clumping), the solar zenith angle to 0°, and the top of the canopy radiation to 800 W m$^{-2}$ (with 600 W m$^{-2}$ being direct radiation and 200 W m$^{-2}$ being diffuse radiation). Panel (b) shows the normalized downward component of shortwave broadband radiation (in dashed black line), and of the four shortwave spectral bands (in purple for UV, green for PAR, red for far-red, and brown for NIR). Panel (c) shows the absolute downward component of shortwave broadband and the four shortwave bands, whereas Panel (d) and (e) show the upward radiation flux and the absorbed radiation respectively.

*External controls of the radiative transfer*

The proportion of light reflected by a canopy, and thus the proportion of leftover light available for the canopy and soil, depends on the radiation wavelength, the diffuse radiative flux fraction, and the solar zenith angle. To explore these dependencies, Fig. 4.3 depicts the canopy reflectivity for direct (eq. (4.A.12)) and diffuse light (eq. (4.A.11)) as a function of the solar zenith angle. We use the term canopy reflectivity instead of canopy reflectance (eq. (4.A.9) and (4.A.10)) as the former does not weigh the influence of the soil, the reflectivity

being an intrinsic feature of the vegetation canopy. The canopy reflectivity approaches the canopy reflectance for thick vegetation canopies.

Canopy reflectivity differs per wavelength, being substantially lower for PAR (ca. 0.01-0.04) than for SW broadband radiation (ca. 0.12-0.23), Fig. 4.3. This translates in a higher proportion of available PAR radiation for the canopy and soil surface compared to SW broadband radiation.

The modeled canopy reflectivity of diffuse light is independent of solar zenith angle, and therefore of the time of the day and geographical location, Fig. 4.3. Conversely, canopy reflectivity of direct light has a clear dependency on the solar zenith angle, Fig. 4.3, and thus, on the time of the day and geographic location. Direct light can penetrate further into the canopy when the sun is overhead (low zenith angles), and is more reflected for grazing solar angles (large solar zenith angles). Two regimes can be defined based on the solar zenith angle: a direct-favored and a diffuse-favored regime. The direct-favored regime occurs at low solar zenith angles, and it indicates that the direct light can pentetrate deeper into the canopy than diffuse light. On the contrary, the diffuse-favored regime occurs at high solar zenith angles, and it indicates that diffuse light can penetrate deeper into the canopy than the direct beams. The threshold solar zenith ($\theta_{z,threshold}$) which demarks the switch between regimes, can be defined as the angle at which the extinction coefficient for the direct beam (eq. (4.6)) equals the extinction coefficient for diffuse radiation (eq. (4.7)). Solving this equivalence based on the shortwave radiative transfer scheme presented here, we obtain the following threshold solar zenith angle:

$$\theta_{z,threshold} = \arccos\left(\frac{0.5}{0.8}\right) \approx 51.32° \tag{4.10}$$

During a day, solar zenith angles are 90° at sunrise and sunset, and they reach a minimum value at solar noon. This minimum midday value depends on the time of the year and the geographic location (see Fig. 4.A.1 for midday solar zenith angle variability). In Fig. 4.3, we indicate the diurnal solar zenith angle ranges for three sites: ATTO site (tropical rainforest), Loobos site (temperate forest), and Hyytiälä site (boreal forest). Both the temperate and boreal forest have solar zenith angles corresponding to the diffuse-favored regime, and only occasionally, may experience the direct-favored regime. The tropical rainforest, on the contrary, experiences frequently both regimes, the diffuse-favored regime in the early morning and afternoon, and the direct-favored regime at and near midday. It is also relevant to notice that the differences between direct and diffuse reflectivity are larger in the diffuse-favored regime. Because differences between direct and diffuse reflectivity are largest in the diffuse-favored regime, and all locations experience this regime for all or most of their daytime (Fig. 4.A.2), this regime is dominant for canopy radiative transfer.

The diffuse-favored regime relates to the diffuse fertilization effect. Nonetheless, to understand the diffuse fertilization effect adequately we need to account not only for the total quantity of light received by the soil and canopy, but also for the vertical distribution of the

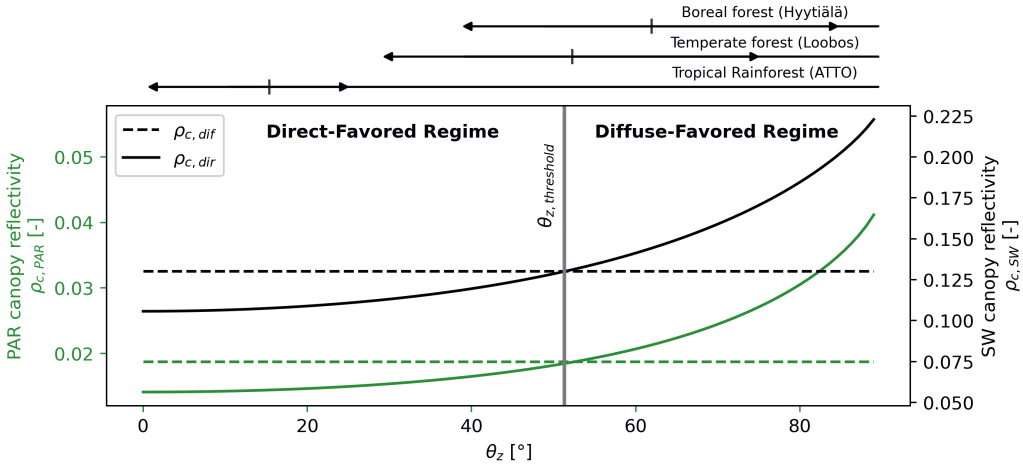



**Figure 4.3:** Direct and diffuse canopy reflectivity for PAR (green lines) and shortwave radiation (black lines). Direct canopy reflectivities are shown in solid lines whereas diffuse canopy reflectivities are shown in dashed lines. The vertical solid grey line indicates the threshold solar zenith angle ($\theta_{z,threshold}$) which distinguishes two regimes: the Direct-Favored Regime and the Diffuse-Favored Regime. Above the figure, we indicate the typical solar zenith angles for three forests: a tropical forest (ATTO site), a temperate forest (Loobos site), and a boreal forest (Hyytiälä site). The pointers and vertical line of the arrows indicate the midday solar zenith angle averaged over the year 2025 for each of the sites. The midday solar zenith angle varies throughout the year, because of that we indicate the yearly minimum solar zenith angle (left arrow pointer), the yearly mean (vertical line), and the yearly maximum (right arrow pointer). The complete yearly variability of the midday solar zenith angle for the three sites is shown in Fig. 4.A.1.

absorptance and for the distribution of radiation among leaves. These aspects are visualized in the canopy radiative budget presented in Fig. 4.4.

Fig. 4.4 quantifies the proportion of available downward PAR that is reflected at the canopy top and the proportions that are absorbed by the top third of the canopy, the middle third of the canopy, the low third of the canopy and by the soil. The budget is calculated for the tropical rainforest located at ATTO site. The budget is shown as a function of the diffuse radiative flux, with 0 and 1 values indicating that all downward radiation at the canopy top is direct and diffuse respectively. Additionally, the budget is shown for three solar zenith angles (Fig. 4.4a, b and c): (a) $\theta_z = 0°$ representing the sun at its zenith, typical at midday in tropical rainforests, and corresponding to a direct-favored regime (Fig. 4.A.1); (b) $\theta_z \approx \theta_{z,threshold}$ indicating the transition between regimes; and (c) $\theta_z = 80°$ which represents a grazing angle that occurs for tropical, temperate and boreal ecosystems, and that corresponds to a diffuse-favored regime.

The two regimes affect the vertical distribution of absorbed radiation, Fig. 4.4. In the direct-favored regime, Fig. 4.4a, direct radiation (DRF = 0) is transmitted more efficiently, being able to penetrate further into the canopy and soil compared to diffuse radiation (DRF = 1). In this case, the direct beam transmissivity is so efficient that approximately 7 % of the above canopy downward radiation is absorbed by the soil, not being accessible for the vegetative canopy. In the threshold solar zenith angle, Fig. 4.4b, the absorptance per vegetation layer and soil surface is independent of the DRF. In turn, in the diffuse-favored regime, Fig. 4.4c, diffuse radiation is able to penetrate further into the canopy being more equally shared among the forest layers. In the diffuse-favored regime, the surface absorptance under very diffuse skies (DRF = 1), although it slightly larger compared to less diffusive skies (DRF = 0), it remains small, allowing the majority of the radiation to stay within the vegetation canopy.

A noticeably effect of the DRF under all solar zenith angles is its impact on the distribution of radiation across leaves. Diffusive skies (DRF towards 1) tend to share radiation more evenly across leaves. This effect can be noticed in Fig. 4.4 by looking at the absorbed radiation for sunlit and shaded leaves in conjunction to the sunlit leaf fraction. For instance, in Fig. 4.4a, under clear skies (DRF = 0), 75 % of top-canopy leaves (the sunlit leaves) absorbed nearly all the radiation at that layer, while the remaining 25 % (shaded leaves) barely absorbed radiation, being consequently unable to photosynthesize. In turn, under diffusive skies (DRF = 1), all leaves absorbed similar radiation rates, enabling more leaves to photsynthesize. Due to the non-linear photosynthesis response to light, canopies are able to assimilate more $CO_2$ when radiation is homogeneously distributed with the leaf area instead of when the same radiation is concentrated over a few very productive leaves.

In this section, we have studied how external factors, namely the solar zenith angle and the diffuse radiative flux fraction, affect the wavelength-dependent radiative transfer within canopies. The dependence of radiative transmission on the solar zenith angle enables the definition of two regimes, the direct-favored regime and the diffuse-favored regime. This regime categorization is independent on the wavelength of radiation. Even though direct ra-

diation can occasionally be transferred more efficiently than diffuse radiation (direct-favored regime), diffuse radiation always enables more leaf area to photosynthesize, which promotes a diffuse fertilization effect on forests. The extent of the diffuse fertilization effect as well as the radiative transfer in general also depends on internal canopy factors, topic we briefly cover in the next section.

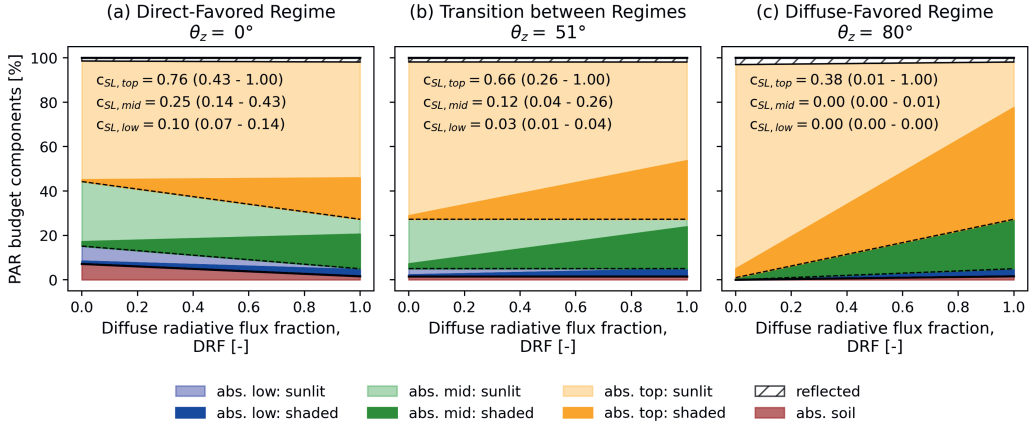



**Figure 4.4:** The budget of radiation for a forest as a function of the diffuse radiative flux fraction (DRF) for three solar zenith angles: 0° (a), 45° (b), and 80° (c). The budget of radiation indicates from top to bottom the proportion of: reflected PAR (white area with diagonal black lines), the absorbed PAR by the upper third of the canopy for sunlit leaves (light yellow area) and shaded leaves (dark yellow area), the absorbed PAR by the middle third of the canopy for sunlit leaves (light green area) and shaded leaves (dark green area), the absorbed PAR by the lower third of the canopy for sunlit leaves (light blue area) and shaded leaves (dark blue area), and the absorbed PAR by the soil (brown area). The vertically averaged fraction of sunlit leaves is annotated inside the panels for each of the vegetation canopy layers (upper, middle, and lower), while the minimum and maximum fractions are annotated in between parenthesis. We assumed a soil reflectivity of 0.1 for UV and PAR spectral bands, and of 0.3 for far-red and NIR spectral bands. Clumping index was set to 1 (no clumping).

*Internal controls of the radiative transfer*

The canopy radiative transfer depends on the forest biomass as well as its vertical allocation. In Fig. 4.5, we show a sensitivity of the radiative transfer for three different type of forests, a tropical, temperate, and boreal forest, located at the sites above described. The tropical forest consisted of a densely populated canopy (LAI $= 5.3$ m$^2$ m$^{-2}$) with maximum leaf allocation at the top-crown and understory, Fig. 4.5. The temperate forest was sparsely populated by leaves (LAI $= 1.8$ m$^2$ m$^{-2}$), consisting of a vertical extendend top-crown characteristic of deciduous and spruce-like vegetation, Fig. 4.5. The boreal forest was moderately populated by leaves (LAI $= 3.3$ m$^2$ m$^{-2}$) and consisted of a narrower top-crown leaf allocation characteristic of pine forests with no understory vegetation, Fig. 4.5.

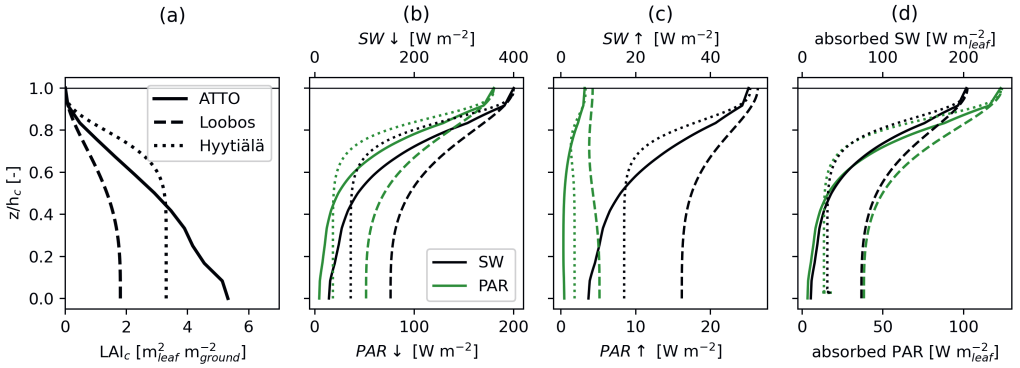



**Figure 4.5:** Vertical profiles of cumulative leaf area index (a), downward PAR and SW fluxes (b), upward PAR and SW fluxes (c), and absorbed PAR and SW fluxes per area of leaf (d). Results are shown for three different types of forest: a tropical forest located at ATTO site (solid lines), a temperate forest located at Loobos site (dashed lines), and a boreal forest located at Hyytiälä site (dotted lines). PAR fluxes are shown in green lines whereas SW fluxes are shown in black lines. To generate these profiles, we assumed no clumping ($\Omega = 1$), a solar zenith angle of 45, and a top of the canopy downward shortwave radiation of 400 W m$^{-2}$, with 100 W m$^{-2}$ being diffuse radiation and 300 W m$^{-2}$ being direct radiation.

The three forest types depict exponential-like vertical profile in radiative fluxes, but they reveal differences regarding the total and the vertical distribution of light attenuation, Fig. 4.5. As expected, denser forests result in lower forest-floor transmissivity (see downward radiative fluxes in Fig. 4.5b), and lower forest floor refectance (see upward radiative flux at z = 0, Fig. 4.5c) The extinction of light with canopy depth is controlled by the cumulative leaf area index, with denser top-crowns (such as the boreal forest case) damping radiation more effectively. The upward PAR flux sometimes depicts a non-monotonic dependency over height, with both maxima at the canopy top and forest floor (see the temperate forest case in Fig. 4.5c). This characteristic upward PAR flux occurs when significant downward PAR is reflected on the forest floor, and can be absorbed in its upward trajectory through the canopy. This effect would be larger for relatively open forest with high radiative reflectance, such as forest floors covered by snow but with still active vegetation cover.

Other internal canopy factors which vary among ecosystems, such as the clumping of leaves, the leaf optical properties, and the wood to leaf ratio, also affect radiative transfer. Their effects are discussed in Sect. 4.4.

### 4.3.2 Longwave radiative transfer

To examine longwave radiation transfer within forest canopies, Fig. 4.6 presents the modeled downward, upward, and absorbed longwave radiation for a tropical rainforest representative of the ATTO site. Vertical profiles of longwave fluxes have a shape which remains similar

during most of daytime. Fig. 4.6a. Downward longwave is minimum at canopy top and rapidly increases with canopy depth until a height approximately corresponding to the lower end of the canopy crown. This rapid increase reflects the downward longwave emission by the leaves located at the canopy top which are being warmed up by the solar shortwave radiation. The increase in longwave radiation is largest at midday, where radiation is the strongest and it is penetrating further into the canopy (direct-favored regime). At a height around mid-canopy, downward longwave stabilizes or starts to slightly decrease with canopy depth. On the other hand, the upward longwave flux increases over canopy height, excepting in the lower part of the canopy (below 10 m), where it can occasionally decrease. At canopy top, upward longwave radiation surpasses the downward component by 40-70 W $m^{-2}$, indicating a warmer canopy than the overlying atmosphere.

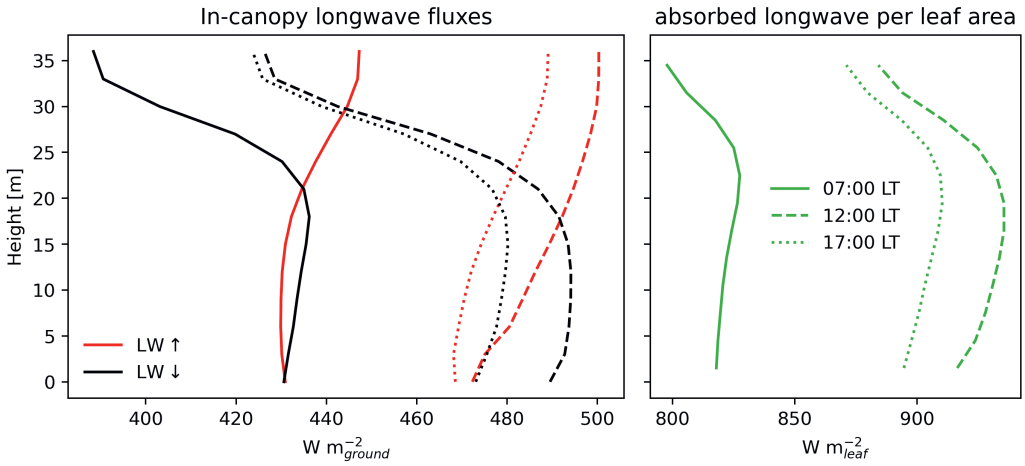



**Figure 4.6:** Modeled within canopy vertical profiles of upward and downward longwave fluxes (a), and absorbed longwave radiation per two-sided leaf area (b), for three times during the day: 07:00 LT (solid lines), 12:00 LT (dashed lines), and 17:00 LT (dotted lines) at ATTO site.

The absorbed longwave radiation by the leaves acquires a minimum at the canopy top, as these leaves are exposed on the upward hemisphere to the lower sky radiation and only on the lower hemisphere to the warmer canopy. Similarly to the downward longwave radiation, the absorbed longwave radiation increases with canopy depth up to a specific height, after which it begins to decrease slightly. Absorbed, upward, and downward longwave radiative fluxes are largest at midday. Additionally, they are greater in the afternoon than in the morning, reflecting the asymmetric diurnal cycle of air and leaf temperatures around solar noon.

### 4.3.3 Validation using data from a tropical rainforest site

Can-DALES accurately reproduced the observed downward and upward shortwave radiation, demonstrating its ability to represent both atmospheric and canopy radiative transfer, Fig.

4.7a. In both simulation and observations, downward shortwave radiation varied due to the presence of clouds, from their onset at approximately 10:00 LT until their dissipation at approximately 15:30-16:00 LT, although simulated variability was damped due to horizontal averaging. The observed canopy shortwave reflectance (albedo) and the PAR canopy reflectance showed a diurnal cycle, with larger values near sunrise and sunset, and a minimum reflectance at midday, Fig. 4.8. This diurnal cycle, which is driven by the solar zenith angle variability (Fig. 4.3), was accurately represented by can-DALES. Consequently, the model could reproduce the transient aspect of canopy reflectances, a process often neglected in land-surface parameterizations such as in one or two big-leaf models.

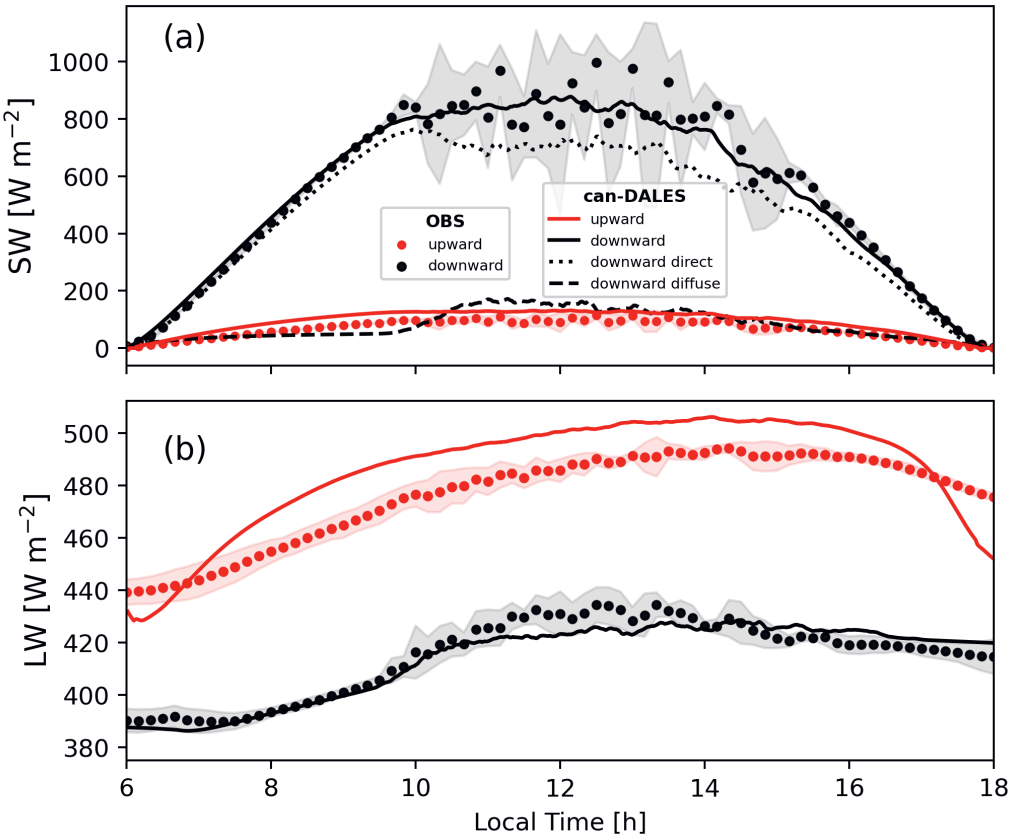



**Figure 4.7:** Diurnal time series of radiative fluxes for shortwave (a), and longwave (b) at 75 m. Observations are shown in dots whereas simulated value are shown in lines. Upward fluxes are shown in red whereas downward fluxes are shown in black. The shaded regions indicate the area within one stardard deviation from observations. The standard deviation was calculated from the individual days that were part of the shallow-convective composite day.

Although direct and diffuse radiation components were not measured during CloudRoots-Amazon22, the simulation provides some insights of the direct and diffuse partitioning on

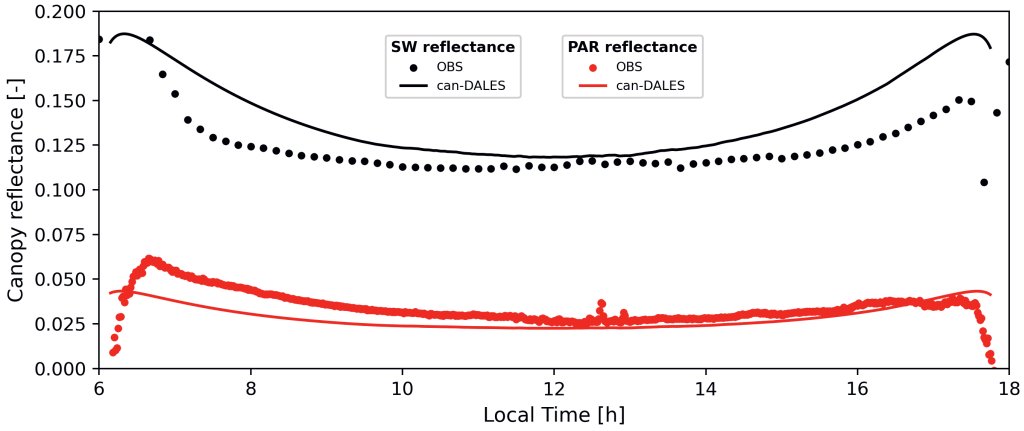



**Figure 4.8:** Diurnal time series of simulated and observed canopy reflectance for shortwave broadband radiation (shown in black dots for observed values and a black line for simulated values), and PAR (shown in red dots for observed values and a red line for simulated values). Observed reflectance are calculated with upward and downward fluxes measured at 75 m height.

skies characterized by shallow-cumulus. Whereas direct radiation was reduced after the onset of shallow-cumulus clouds, diffuse radiation increased by up to 100 W $m^{-2}$, Fig. 4.7a. The cloud-induced decrease in total downward shortwave radiation tends to reduce forest net assimilation whereas the also cloud-induced increase in DRF can amplify net assimilation by spreading the radiation more evenly across leaves (Fig. 4.4). Can-DALES reproduces the interplay of these compensating factors, enabling the study of radiative forest-cloud interactions.

Observed vertical profiles of PAR were accurately represented by can-DALES for both the downward and upward components. Above the canopy, observed downward PAR was approximately 44 % of downward broadband SW radiation as previously reported in Chapter 3. Similar to modeled results, observations depicted an exponential decay with canopy depth for both upward and downward fluxes, excepting at 08:30-10:00 LT when upward PAR had a maximum within canopy. This maximum is related to the canopy architecture around the sensors, which may see occasionally forest clearings at certain times in the day. Overall, can-DALES proved capable of representing the within canopy ranges and gradients of both upward and downward PAR fluxes.

Finally, the diurnal evolution of longwave radiation was also accurately represented in the simulation. Above canopy downward longwave radiation agreed to a large extent with observed values, indicating a satisfactory representation of longwave atmospheric radiative transfer of can-DALES, which accounts for greenhouse gas composition and for the presence of clouds. The above canopy upwelling longwave component reflected the radiation emitted by the canopy, and its diurnal evolution agreed to a large extent for simulation and observations, particularly between 07:00 and 17:00 LT. Nonetheless, the simulated upward

longwave flux had a positive bias from 07:00 to 17:00 LT, suggesting higher canopy temperatures in the simulation compared to observations. Additionally, simulation results and observations disagreed during the first and last hour of the daytime, when the transition from stable to unstable conditions (or viceversa) takes place. This discrepancy suggests that the canopy thermal inertia is underestimated in can-DALES, which could result in abrupt stable-to-unstable (or viceversa) transitions.

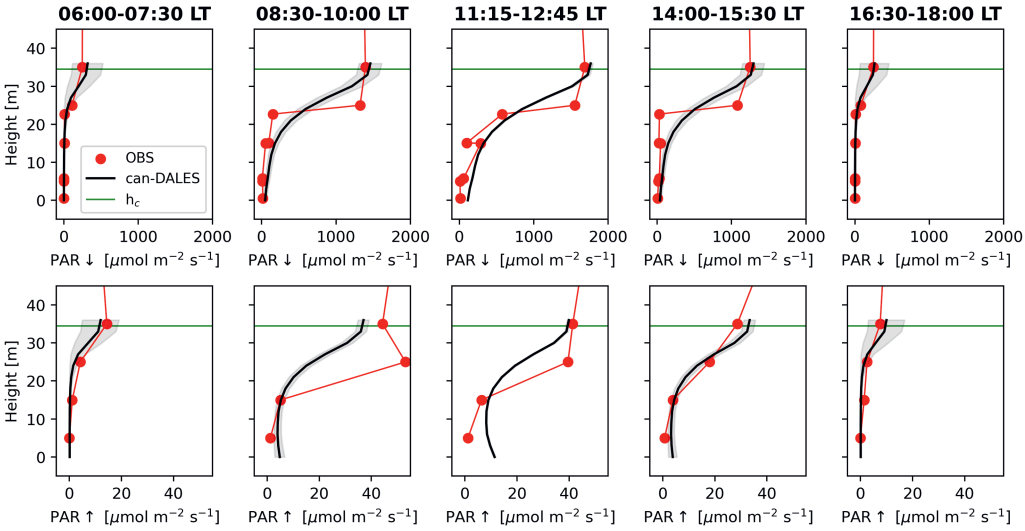



**Figure 4.9:** Modeled and observed within canopy vertical profiles of downward PAR fluxes (upper row), and downward PAR fluxes (lower row) for five time intervals: from 06:00 to 07:30 LT, from 08:30 to 10:00 LT, from 11:15 to 12:45 LT, from 14:00 to 15:30 LT, and from 16:30 to 17:00 LT. Observed values are shown in red dots connected by thin red lines, whereas simulated values are shown in solid black lines. The grey shaded area indicates the region within one standard deviation from the simulated value. The standard deviation was calculated with regard to the interval time.

## 4.4 Discussion

The revised radiative transfer scheme reproduced key features of canopy radiative environments, giving confidence in its applicability for coupled canopy-atmosphere simulations. The scheme captured (1) the vertical distribution of shortwave and longwave radiation, (2) the diurnal cycle of radiative fluxes and reflectances, and (3) the expected sensitivity to external (solar zenith angle, diffuse radiative flux fraction) and internal canopy (leaf area index and leaf area density) factors. Comparisons against observations in a tropical rainforest showed good agreement for upward and downward shortwave and longwave fluxes above the canopy (Fig. 4.7), canopy PAR and broadband shortwave reflectance (Fig. 4.8), and PAR attenuation through the canopy (Fig. 4.9). These results indicate that the scheme provides a realistic ba-

sis for investigating coupled radiative, bio-physiological, and micrometeorological processes in forest canopies.

Beyond bulk shortwave fluxes, the scheme reproduced distinct vertical profiles across UV, PAR, far-red and NIR spectral bands, which are consistent with modeled results by Wang et al. (2024). In their study, Wang et al. (2024) highlighted the importance of UV and Far-Red radiation for surface albedo and canopy photosynthesis. With the revised spectral-band formulation, can-DALES can now explicitly represent these radiative components and their vertical gradients, thereby enabling analyses of their influence on net ecosystem exchange and the surface energy budget. In particular, the model can be used to study the Far-Red contribution to photosynthesis in shade-tolerant understory vegetation, a process of growing interest (Zhen et al., 2022). Using narrow spectral bands (655–665 nm and 725–735 nm), the model reproduced realistic Red:Far-Red ratios (Fig. 4.A.5c), ranging from 1.33 at the canopy top to 0.37 near the forest floor, matching classical observations by de Castro (2000). A complete assessment of far-red effects on canopy assimilation in forests will require extending the leaf gas exchange scheme to include far-red supplementation on photosynthesis, using formulations similar to Wang et al. (2024) and Jans et al. (2025).

A key advantage of the multilayer structure of can-DALES is its ability to capture the diurnal variability of canopy reflectance, in contrast to one-big-leaf or two-big-leaf approaches that typically impose static reflectance properties. The observed asymmetry on reflectance, with higher reflectance during morning and evening, and lower values around noon, affects surface heating rates and, consequently, can potentially alter the evolution of the atmospheric boundary layer. Thus, representing this diurnal pattern is desirable when examining land-atmosphere coupling at fine temporal scales. The model also represented the interplay between solar zenith angle and the diffuse radiative flux fraction, both of which modulate the diffuse fertilization effect (e.g., Fig. 4.3 and Fig. 4.4). The diffuse radiative flux fraction varies diurnally and seasonally based on the meteorological conditions such as clouds presence and aerosol loading (e.g., Butt et al., 2010). Can-DALES is able to represent these diurnally varying meteorological conditions and provides a useful framework to investigate how diffuse light availability modifies canopy photosynthesis and radiative transfer across different forests sites and times of day.

Despite these strengths, several limitations remain. They can be grouped into (1) limitations of the current model formulation, and (2) uncertainties in the specification of input parameters. The most important structural limitation is the absence of explicit woody biomass. Branches and stems are not represented separately from the plant area, and no dedicated optical properties or temperatures are assigned to woody elements. As a result, leaf area density is implicitly treated as plant area density, which can bias light attenuation and vertical radiative profiles in forests with substantial woody biomass. Using lidar observations and a 3D ray-tracing model, Béland (2025) showed that wood absorbs roughly 10% of canopy-absorbed PAR and up to 30% of canopy-absorbed NIR, highlighting the potential magnitude of this bias.

The exclusion of woody material also affects longwave fluxes and the surface energy balance.

Forest biomass, and woody material in particular, stores and releases heat. The biomass heat storage flux is non-negligible in forest ecosystems and has been proposed as one contributor to the observed surface energy imbalance (Haverd et al., 2007; Leuning et al., 2012). Observed biomass heat storage acquire maximum values which range between 20 and 50 W $m^{-2}$, which is comparable to or exceeding the air heat storage maximum (Moore & Fisch, 1986; dos Santos Michiles & Gielow, 2008; Lindroth et al., 2010). Because can-DALES does not yet include biomass heat storage, trunk and branch temperatures are omitted, and all canopy longwave emission is currently assigned to leaves. This simplification likely contributes to the overly rapid morning and evening transitions in simulated longwave emission (Fig. 4.7b). Adding biomass heat storage in can-DALES would likely improve the representation of canopy temperature dynamics, particularly at night (as documented by Swenson et al., 2019) and during transition periods when the biomass heat storage can dampen the air warming and cooling, potentially affecting canopy air stability.

Uncertainties in input parameters present a second source of limitations. Parameters such as leaf and wood optical properties, LAD and PAD profiles, and clumping indices can vary widely within and across sites, and can be challenging to constrain. Nevertheless, observational datasets for these parameters are increasingly available across forest types, and they already allow for realistic representation of the dominant radiative processes. The current radiatve transfer implementation focuses on vertical radiative processes, following the standard practice in canopy radiative transfer modeling. However, recent advances in ground-based lidar now enable detailed three-dimensional reconstructions of canopy structure. Given the spatial resolution of can-DALES (grid cells on the order of $12 \times 12 \times 3$ m), integrating three-dimensional canopy structure into the model would allow simulation of spatially heterogeneous forests with crown-scale variation in radiative and structural properties. Achieving this will require balancing physical realism with computational cost, but ongoing developments in remote sensing, high-performance computing, and radiative transfer modelling make such advances increasingly feasible.

## 4.5 Conclusions

In this chapter, we revised the canopy radiative transfer of can-DALES, a large eddy simulation model with a multi-layer canopy approach. The revised scheme separates shortwave radiation into four spectral bands: UV, PAR, far-red and NIR. Additionally, the longwave radiative transfer scheme was modified following Bonan (2019). The simulation results compared well with observations acquired at the ATTO tropical rainforest site, providing confidence in the model's applicability for coupled canopy-atmosphere simulations. Furthermore, the radiative transfer scheme exhibits the expected sensitivity to external drivers (solar zenith angle and diffuse radiative flux fraction), and internal canopy properties (leaf area index and leaf area density).

Overall, the model adequately captures the biophysical processes of a forest canopy, although

the model still retains some limitations. A current limitation is the absence of a biomass heat storage and an explicit representation of the radiative effects of woody biomass. The omission of these processes constrains the analysis of nighttime conditions and may lead to overly abrupt morning and nighttime transitions. Therefore, the inclusion of biomass heat storage and radiative properties of woody biomass is recommended for future model development.

# 4.A Supplementary Information for Chapter 4

### 4.A.1 Supplementary equations of the shortwave radiative transfer

Following the analytical solution introduced by Goudriaan (1977) and Goudriaan & Van Laar (1994), the radiative fluxes used in eq. (4.2)-(4.5) are calculated as follows:

$$\phi^{\downarrow}_{1,dir} = \frac{\phi^{\downarrow}_{dir}(0)}{1 + \eta_{dir} \exp\left(-(K_{dif} + K_{dir}) \cdot LAI\right)} \tag{4.A.1}$$

$$\phi^{\downarrow}_{2,dir} = \frac{\phi^{\downarrow}_{dir}(0) \cdot \eta_{dir} \cdot \exp\left(-(K_{dif} + K_{dir}) \cdot LAI\right)}{1 + \eta_{dir} \exp\left(-(K_{dif} + K_{dir}) \cdot LAI\right)} \tag{4.A.2}$$

$$\phi^{\uparrow}_{1,dir} = \frac{\phi^{\downarrow}_{dir}(0) \cdot \rho_{c,dir}}{1 + \eta_{dir} \exp\left(-(K_{dif} + K_{dir}) \cdot LAI\right)} \tag{4.A.3}$$

$$\phi^{\uparrow}_{2,dr} = \frac{\phi^{\downarrow}_{dir}(0) \cdot \eta_{dir} \cdot \exp\left(-(K_{dif} + K_{dir}) \cdot LAI\right)}{\rho_{c,dir}(1 + \eta_{dir} \exp\left(-(K_{dif} + K_{dir}) \cdot LAI\right))} \tag{4.A.4}$$

$$\phi^{\downarrow}_{1,dif} = \frac{\phi^{\downarrow}_{dif}(0)}{1 + \eta_{dif} \exp\left(-2K_{dif} \cdot LAI\right)} \tag{4.A.5}$$

$$\phi^{\downarrow}_{2,dif} = \frac{\phi^{\downarrow}_{dif}(0) \cdot \eta_{dif} \cdot \exp\left(-2K_{dif} \cdot LAI\right)}{1 + \eta_{dif} \exp\left(-2K_{dif} \cdot LAI\right)} \tag{4.A.6}$$

$$\phi^{\uparrow}_{1,dif} = \frac{\phi^{\downarrow}_{dif}(0) \cdot \rho_{c,dif}}{1 + \eta_{dif} \exp\left(-2K_{dif} \cdot LAI\right)} \tag{4.A.7}$$

$$\phi^{\uparrow}_{2,dif} = \frac{\phi^{\downarrow}_{dif}(0) \cdot \eta_{dif} \cdot \exp\left(-2K_{dif} \cdot LAI\right)}{\rho_{c,dif}(1 + \eta_{dif} \exp\left(-2K_{dif} \cdot LAI\right))} \tag{4.A.8}$$

where $\eta_{dir}$ and $\eta_{dif}$ are a function of the canopy reflectivity ($\rho_{c,dir}$ and $\rho_{c,dif}$), and the soil reflectivity.

$$\eta_{dir} = \frac{\rho_{c,dir} - \rho_s}{\rho_s - \frac{1}{\rho_{c,dir}}} \tag{4.A.9}$$

$$\eta_{dif} = \frac{\rho_{c,dif} - \rho_s}{\rho_s - \frac{1}{\rho_{c,dif}}} \tag{4.A.10}$$

The canopy reflectivities, $\rho_{c,dir}$ and $\rho_{c,dif}$, have been fitted, using the iterative canopy radiative transfer developed by Goudriaan (1977) as reference. The reason to update $\rho_{c,dif}$ was

that the original $\rho_{c,dif}$ expression (Goudriaan & Van Laar (1994); eq. 6.19) was derived for horizontal leaves, whereas we are assuming a spherical leaf distribution. For $\rho_{c,dir}$, we simply update the fitting as the original mathematical expression was an approximation, and we find higher accuracy for the new fitting when compared to the iterative canopy radiative transfer (Goudriaan, 1977).

$\rho_{c,dif}$ has been fitted as a function of the leaf scattering coefficient $\sigma$ as follows:

$$\rho_{c,dif} = 4.636239 \cdot 10^{-3} e^{\left(19.707778 \cdot \sigma - 57.752878 \cdot \sigma^2 + 100.713885 \cdot \sigma^3 - 88.256337 \cdot \sigma^4 + 30.761673 \cdot \sigma^5\right)} \tag{4.A.11}$$

whereas $\rho_{c,dir}$ has been fited as a function of $\rho_{c,dir}$ and of the solar zenith angle $\theta_z$ as follows:

$$\rho_{c,dir} = \rho_{c,dif} \cdot \left(A \cdot \exp\left(-B \cdot (\cos\theta_z)^C\right) + 0.4\right) \tag{4.A.12}$$

with A, B and C coefficients calculated as:

$$A = 1.677900 \cdot \exp\left(-1.804072 \cdot (\rho_{c,dif})^{0.935482}\right) + 0.347942 \tag{4.A.13}$$

$$B = 4.206250 \exp\left(-0.534006 \cdot (\rho_{c,dif})^{0.955533}\right) - 2.443320 \tag{4.A.14}$$

$$C = -0.366804 \cdot \exp\left(-0.676143 \cdot (\rho_{c,dif})^{0.983803}\right) + 1.107502 \tag{4.A.15}$$

### 4.A.2 Ecosystem variability of solar zenith angle

Fig. 4.A.1 shows the yearly variability in midday (minimum) solar zenith angle for ATTO site, Loobos site, and Hyytiälä site. Fig. 4.A.2 shows a daytime series of the yearly averaged solar zenith angle.

### 4.A.3 Radiation budget for shortwave broadband radiation and Far-Red

Fig. 4.A.3 and Fig. 4.A.4 depict the radiation budget for SW broadband and Far-Red spectral band. By examining these figures, we can observe spectral variation in the way radiation is redistributed over the canopy and soil.

### 4.A.4 Simulated Red:Far-Red ratio in the tropical rainforest (ATTO site)

To examine further the Far-Red (FR) distribution over the canopy, we calculated PAR:FR and Red:FR ratios for the ATTO site case, Fig. 4.A.5.

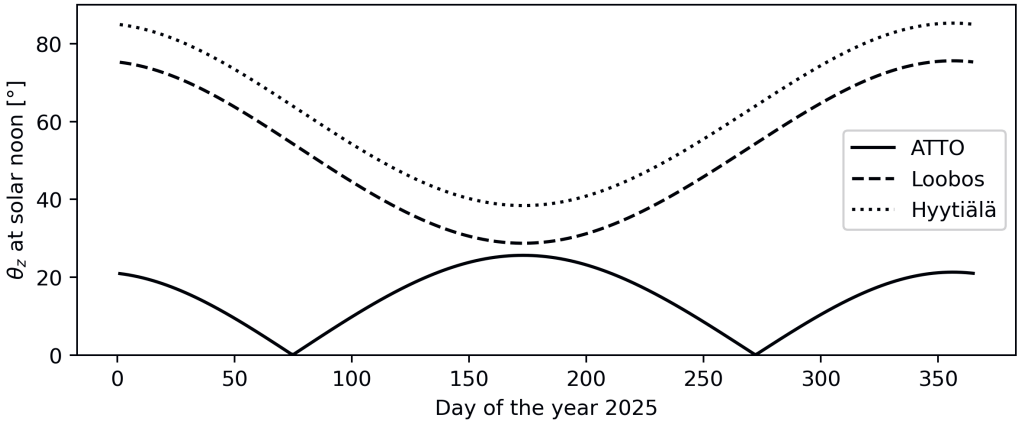



**Figure 4.A.1:** Time series of midday solar zenith angle across 2025 for three sites: ATTO site (tropical forest, shown in solid black line), Loobos site (temperate forest, shown in dashed black line), and Hyytiälä site (boreal forest, shown in dotted black line).

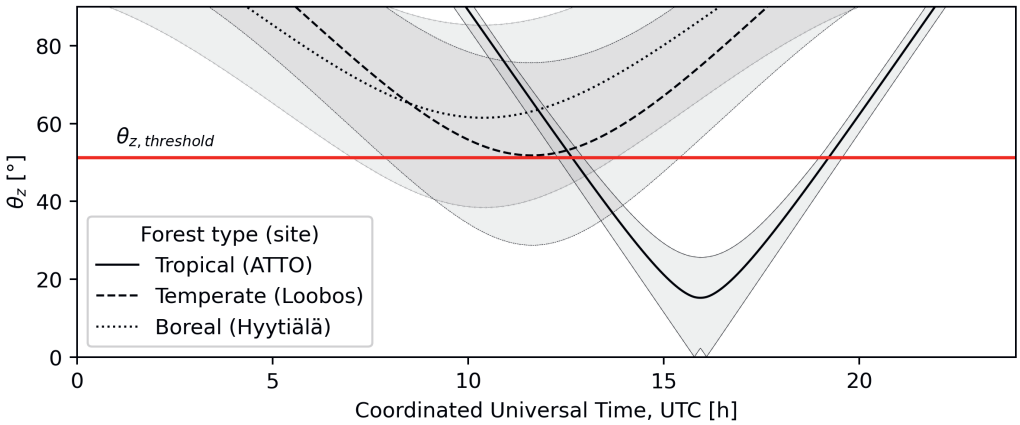



**Figure 4.A.2:** Time series of daytime zenith angle for three sites: ATTO site (tropical forest, shown in solid black line), Loobos site (temperate forest, shown in dashed black line), and Hyytiälä site (boreal forest, shown in dotted black line). The lines represent the yearly average of the daytime solar zenith angle, while the shaded areas represent its yearly variability between the minimum and maximum yearly values.

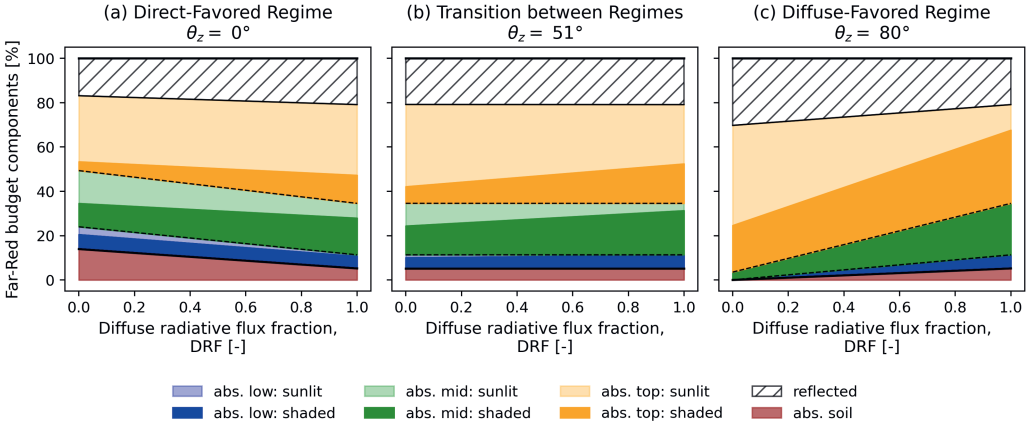



**Figure 4.A.3:** Same as Fig. 4.4 but for Far-Red radiation.



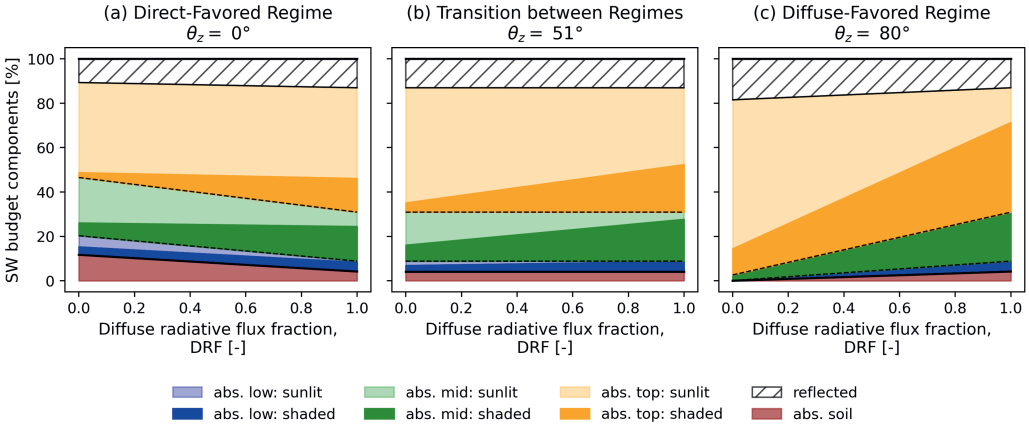



**Figure 4.A.4:** Same as Fig. 4.4 but for SW broadband radiation.

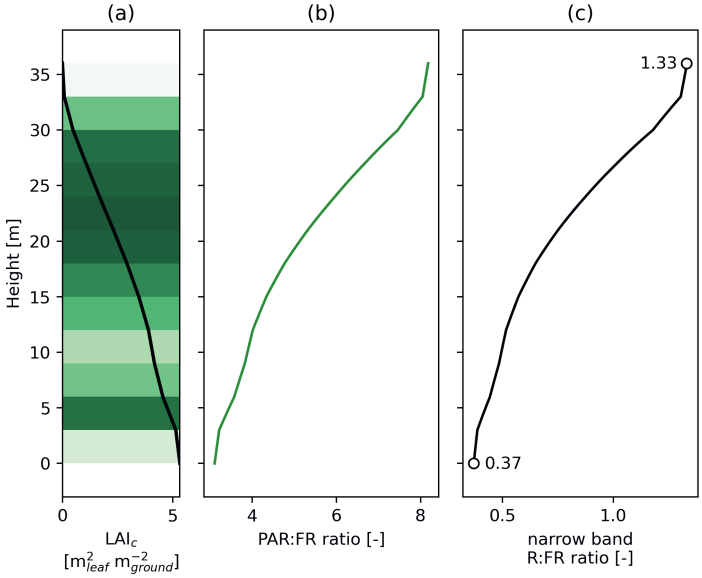



**Figure 4.A.5:** Vertical profiles of: cumulative leaf area index (a), PAR to Far-Red ratio (PAR:FR) (b), and narrow band Red to Far-Red ratio (R:FR) (c). The R:FR ratio was calculated from the canopy radiative transfer of the Red and Far-Red narrow-bands (655-665 nm and 725-735 nm). The respective scattering coefficients were 0.055 (R) and 0.728 (FR) and were estimated from the spectral leaf optical coefficients presented in Fig. 4.1. The narrow-bands made up 1.2 % (R) and 0.9 % (FR) of the incident top of the canopy shortwave broadband radiation.

# Chapter 5

# Forest-atmosphere coupling in cloudy conditions revealed by canopy-resolving large eddy simulations and observations

This chapter is based on:

González-Armas R., Pedruzo-Bagazgoitia X., de Boer, H. J., de Feiter V., Veerman M. A., Hartogensis, O., Dias-Júnior, C. Q., & Vilà-Guerau de Arellano J. *Forest-Atmosphere Coupling and Boundary-Layer Processes Revealed by Canopy-Resolving Large Eddy Simulations and Observations* (In Preparation)

## Abstract

Large eddy simulations (LES) coupled with a multi-layer canopy scheme are a promising and novel modeling technique to investigate land-atmosphere interactions. These simulations explicitly resolve the dominant canopy- and boundary-layer-scale turbulence, as well as the onset and evolution of low clouds.

Validating canopy-resolving LES against comprehensive observational datasets is an essential step before these models can be used to investigate canopy-cloud interactions in diverse environments. This study benchmarks a one-day multi-layer canopy LES using high-quality Amazon observations, providing insight into how well such models capture forest-atmosphere exchange processes. To our knowledge, this is the first study that includes a canopy-resolving LES case and shallow cumulus clouds.

By identifying agreements and discrepancies between canopy LES and observations, this study outlines the present strengths and limitations of canopy-resolving LES. In particular, we systematically analyzed four interconnected aspects of the land-atmosphere system: (i) the forest microclimate, (ii) the leaf gas exchange and energy balance, (iii) the ecosystem and surface fluxes, and (iv) the clear-to-cloudy atmospheric boundary layer. The canopy LES successfully captured complex biophysical processes, such as the stable air layer in the lower third of the canopy, which is linked to plant ecophysiology, canopy wind drag, and canopy radiative transfer. The level of mechanistic processes included in the LES allows for realistic representation of within-canopy air storage and ventilation events. Overall, the study underscores the value of using canopy LES as a tool to explore forest-air-cloud interactions.

## 5.1 Introduction

Forests interact with the atmosphere in complex ways by regulating the surface radiative and energy balance, modifying turbulent structures near and within the canopy, regulating the water and carbon cycles, and altering the atmospheric chemical state. Despite the importance of forest-atmosphere interactions in the weather and climate system, land surface models have historically relied on overly simplified representations of forest canopies, limiting our ability to accurately describe and understand these processes. A common simplified representation of canopies are the so-called "big-leaf" approaches, which neglect or strongly simplify the vertical structure of forests, thereby overlooking key within-canopy gradients and exchanges (Raupach & Finnigan, 1988; Bonan et al., 2021). While big-leaf schemes played a crucial role in the early development of atmospheric models by providing effective boundary conditions for surface fluxes, they are increasingly recognized as insufficient for capturing the complexity of forest-atmosphere coupling (Bonan et al., 2021, 2026). Consequently, multi-layer canopy models have emerged as a promising alternative (Bonan et al., 2021), as they explicitly represent the vertical structure of the canopy and the air space within it. By resolving within-canopy microclimate and transport processes, these models foster a more faithful representation of forest microclimate and its coupling to ecophysiological processes (Bonan et al., 2026), thereby enabling a stronger connection between the biosphere and the atmosphere.



Large Eddy Simulations (LES) with multi-layer canopy representations are a type of multi-layer canopy model, which is able to explicitly solve the most energetic part of the turbulence transport (Patton et al., 2016). By accounting for multiple vertical layers inside the canopy, canopy-resolving LES enable detailed investigations of momentum, heat, water vapor, and scalar transport across the forest-atmosphere interface. Canopy-resolving LES have achieved several milestones in the past, particularly in advancing our understanding of canopy-scale turbulent structures. Under neutral conditions, LES studies (Shaw & Schumann, 1992; Dupont & Brunet, 2008; Finnigan et al., 2009) confirmed the presence of canopy-scale coherent turbulent structures that had previously been hypothesized (Raupach et al., 1996). Under unstable conditions, a recent canopy LES study (Dupont et al., 2024) revealed the inprint of atmospheric bounday layer-scale motions on the canopy-scale turbulent structures, particularly under low wind conditions.

Despite these advances, important forest-atmosphere interactions remain largely unexplored with canopy-resolving LES. In particular, to our knowledge, no previous LES studies with explicit canopy representations have included boundary-layer clouds, despite their ubiquity in many forest ecosystems (Giangrande et al., 2017). Shallow clouds can substantially modify the surface radiation balance, with documented impacts on net ecosystem exchange (NEE) and evapotranspiration (ET) (Knohl & Baldocchi, 2008; Pedruzo-Bagazgoitia et al., 2017), and are therefore likely to influence canopy microclimate and turbulent exchange processes. The lack of canopy-resolving LES studies that explicitly address cloud-canopy interactions represents a key gap in our understanding of forest-atmosphere coupling.

In this chapter, we pursue two main objectives. First, we evaluate the ability of a canopy-resolving LES to realistically reproduce the key biophysical processes governing the forest-atmosphere boundary layer system. Second, building on a detailed comparison between simulations and observations, we use the model to gain process-level insight into forest-atmosphere interactions and to identify research opportunities enabled by LES with explicit canopy representations in the context of land-atmosphere coupling.

To address these objectives, we employ the Dutch Atmospheric Large Eddy Simulation model (DALES; Chapter 4) to simulate a daytime cycle over the Amazon basin during the dry season and under shallow-convective conditions. The simulation results are systematically evaluated against comprehensive observations collected at the Amazon Tall Tower Observatory (ATTO) during the CloudRoots-Amazon22 field campaign (Vilà-Guerau de Arellano et al., 2024). The canopy-resolving configuration of DALES, hereinafter referred to as can-DALES, is assessed along four interconnected themes introduced in the following section (Fig. 5.1, upper panels). Together, these themes encompass the dominant biophysical processes linking forests and the atmosphere (Fig. 5.1, lower panel) and provide the organizational framework for the remainder of this chapter.

## 5.2 Conceptual framework

Our analysis is structured around four distinct themes: (1) the forest microclimate, (2) the physiological responses of leaves the this microclimate (leaf gas exchange and energy balance), (3) the integrated ecosystem response that forces the atmosphere (ecosystem and surface fluxes), and (4) the resulting atmospheric state (clouds and atmospheric boundary layer).

The forest microclimate is primarily governed by the canopy radiative transfer (a topic extensively cover in Chapter 4). In this Chapter, we focus on the other drivers of the vegetation response (temperature, specific humidity, $CO_2$, and wind; Chapter 2) as well as on turbulent state variables (turbulent kinetic energy, TKE; buoyancy; and shear). These variables exhibit strong vertical gradients (Chapter 3), which are often neglected or oversimplified in land-surface schemes, but which affect the ecosystem fluxes and the coupling between within canopy air and above canopy air.

The leaf gas exchange and energy balance theme addresses how individual leaves respond to the microclimate through adjustments in leaf temperature, photosynthetic uptake, and transpiration. These processes are mediated by stomata regulation and are modulated by the leaf boundary layer, which affects the near leaf surface environment depending on leaf features as well as on wind and air stability.

The ecosystem and surface fluxes theme integrates the responses of individual leaves and soil to describe the net forcing exerted by the forest on the atmosphere. Here, we distinguish between ecosystem fluxes, representing exchanges between vegetation and within-canopy

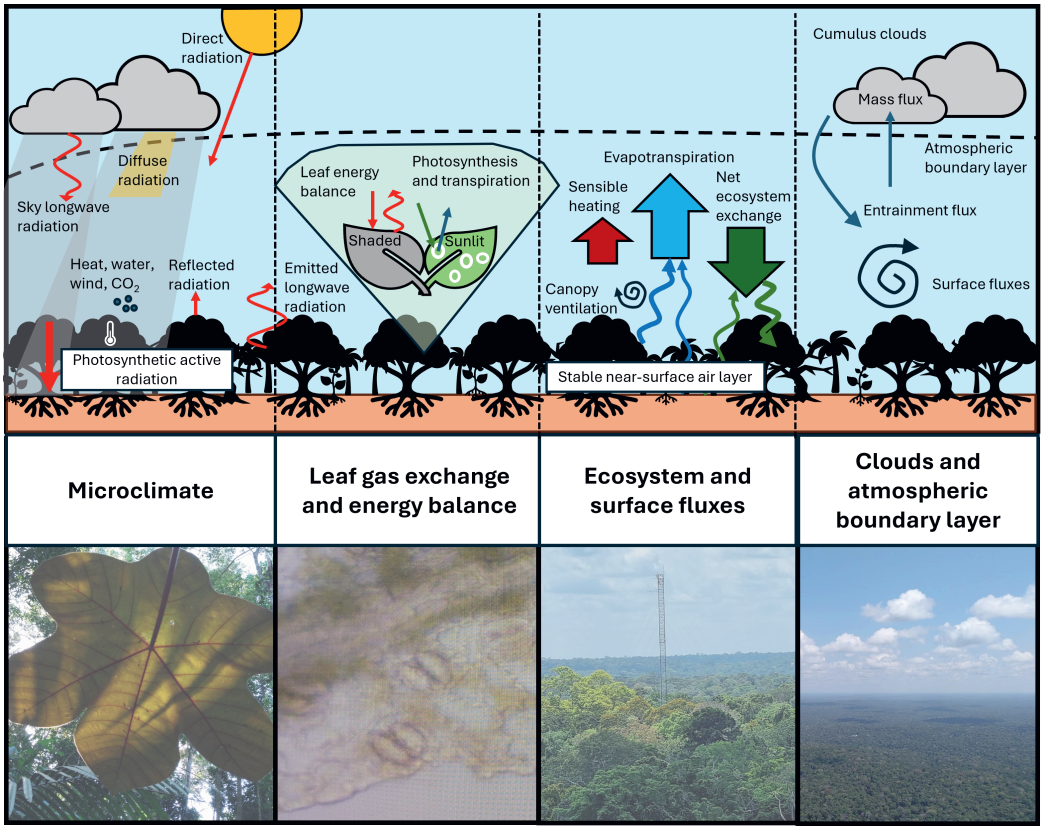



**Figure 5.1:** Conceptual overview of the four themes explored in this study and their role in forest-atmosphere interactions. From left to right, the figure illustrates (1) the forest microclimate shaped by radiative and turbulent processes, (2) the leaf gas exchange and energy balance, (3) the ecosystem and surface fluxes that force the overlying atmosphere, and (4) the atmospheric boundary layer and shallow cumulus clouds responding to surface, entrainment and mass-flux processes.

air, and surface fluxes, which act as boundary conditions for the atmospheric boundary layer. These two fluxes can become decoupled at specific times of the day due to within-canopy air storage, stable near-surface layers, and ventilation events. Such decoupling processes are commonly overlooked in land-surface models but emerge naturally in multi-layer canopy representations coupled with explicit turbulent transport.

Finally, the fourth interconnected theme addresses the evolution of the atmospheric boundary layer and the shallow cumulus clouds as a response to surface forcings and non-local processes such as entrainment from the free troposphere, and cloud mass-flux transport outside of the atmospheric boundary layer.

## 5.3 Methods

### 5.3.1 Study site and CloudRoots-Amazon22 Field Campaign

Similar to Chapter 3, the observations used in this study were acquired at the ATTO site (2° 8' 45" S, 59° 0' 19" W; Andreae et al., 2015) and at the Campina sites (2° 10' 55" S, 59° 1' 18" W), during the CloudRoots-Amazon22 field campaign (Vilà-Guerau de Arellano et al., 2024). The CloudRoots-Amazon22 campaign took place from 8 to 21 August 2022, during the Amazon dry season, at and around these measurement sites. For more details about the campaign, see Vilà-Guerau de Arellano et al. (2024). In this chapter, we extended the observations used in Chapter 3. The included observational dataset is detailed in Sect. 5.3.3.

An extensive documentation of the ATTO research facility can be found in Andreae et al. (2015), while a brief summary of the site features is provided in Chapter 3. The ATTO site is located approximately 150 km northeast of Manaus (Brazil), at 120 m.a.s.l. on a plateau of pristine terra firme (i.e., non-flooded upland) forest. The mean tree height is 20.7 $\pm$ 0.4 m but the tallest trees reach up to 36-40 m. During the study period, we reported an aerodynamic canopy height of 33.7 $\pm$ 1.2 m (Chapter 3).

Our study characterizes a typical shallow-convective day during CloudRoots-Amazon22 field campaign. During the campaign, five days were classified as shallow-convective: 9, 10, 11, 15, 17, and 18 August 2022, (Vilà-Guerau de Arellano et al., 2024). These days were characterized by the appearance of shallow-cumulus clouds around 09-10 LT and their dissipation around 16-17 LT. Based on the observations acquired during these five days, a shallow-convective composite case was created as reported in previous research (Chapter 3 and de Feiter et al., 2025). In this chapter, we extended the modeling effort reported in Chapter 3 by explicitly solving turbulent transport, increasing the number of canopy layers, including a detailed radiative transfer within the canopy (Chapter 4), and explicitly simulating atmospheric dynamics such as boundary layer growth, entrainment, and shallow-cumulus clouds.

### 5.3.2 Can-DALES model and numerical experiment

We used the Dutch Atmospheric Large Eddy Simulation (DALES) model with a multi-layer canopy representation based on the version developed and documented by Pedruzo-Bagazgoitia et al. (2023), which was greatly influenced by the model implementation reported by Patton et al. (2016). The only difference in the model framework compared to Pedruzo-Bagazgoitia et al. (2023) is the canopy radiative transfer scheme, which is reported in Chapter 4. The multi-layer canopy scheme consists of three main components: (1) the drag and dynamical effects of the canopy (Ouwersloot et al., 2017), (2) a shortwave and longwave radiative transfer model (Chapter 4), and (3) a two-big-leaf scheme that distinguishes between sunlit and shaded leaves at each vertical level (Pedruzo-Bagazgoitia et al., 2017).

Our numerical simulation complements and expands upon the one reported by Pedruzo-Bagazgoitia et al. (2023). Similarly to Pedruzo-Bagazgoitia et al. (2023), we conducted a numerical experiment on the Amazon basin during the dry season albeit at a different site and in another time period. In this study, we extend the validation provided by Pedruzo-Bagazgoitia et al. (2023) thanks to the comprehensive observations acquired during CloudRoots-Amazon22 (Vilà-Guerau de Arellano et al., 2024), and we make the important step of resolving shallow-cumulus clouds, and thus, moving beyond clear-sky cases. In the following paragraphs, we summarize the numerical settings and initial profiles of the simulation, highlighting the differences with respect to the numerical experiment reported by Pedruzo-Bagazgoitia et al. (2023).



The simulation covered a domain of 12096 $\times$ 12096 $\times$ 5855 $m^3$ with a resolution of 12 $\times$ 12 $\times$ 3 $m^3$ up to 100 m height. Above 100 m, the vertical spacing stretches by a factor of 1.5 % ($\Delta z_i = \Delta z_{i-1} \cdot 1.015$), with the uppermost level having a vertical resolution of 89 m. The simulation starts at sunrise (06:00 LT (UTC$-$4)) and ends at sunset (18:00 LT (UTC$-$4)), covering the whole daytime cycle, and simulating the complete morning transition and partially the afternoon transition to nighttime conditions. The duration of the simulation already extends the validation provided by Pedruzo-Bagazgoitia et al. (2023) who simulated only partially the diurnal cycle, covering from 08:00 to 16:00 LT. Addditionally, we modified the sub-grid parameterization scheme compared to Pedruzo-Bagazgoitia et al. (2023). In our simulation, we activated a surface-limited mixing length formulation (Mason, 1989), which reduces the subgrid mixing length scale close to the forest ground.

At 06:00 LT, coinciding with sunrise, we initialized the simulation with observed vertical profiles of potential temperature, humidity, wind, and $CO_2$ concentration acquired by radiosondes and sensors deployed at the ATTO towers, Fig. 5.A.1. More details regarding the initialization can be found in Sect. 5.A.1.

In the numerical simulation, the canopy top was located at 36 m, which is comparable to the observed aerodynamic canopy height of approximately 34 m. The simulated canopy consisted of 12 canopy layers, and the prescribed leaf area density (LAD) profile was based on observations acquired with a ground-based light detection and ranging (LiDAR) system at ATTO

in October 2015 (Gomes Alves et al., 2023), Fig. 5.A.2. The main difference between the observation-based LAD profile and the one prescribed by Pedruzo-Bagazgoitia et al. (2023) is that the observed LAD profile is bimodal rather than unimodal. The bimodal distribution indicates maximum leaf allocation both in the upper canopy layer and in the understory (approximately at 3-6 m height), a feature that is captured in our simulation.

In the Results section (Sect. 5.4), we compare simulated horizontally averaged variables with observations. Horizontally averaged simulated values (slab averages) are the most representative of the ecosystem, and are, thus, the most appropiate for an initial comparison. Nonetheless, can-DALES also allows the exploration of horizontal heterogeneity through the visualization and analysis of three-dimensional output fields. Horizontal heterogeneity in forest-air-cloud interactions is beyond the scope of this Chapter, but it will be addressed on the Sect. 5.5.

### 5.3.3 Observational Dataset

The observations used in this study were acquired during CloudRoots-Amazon22 field campaign and they are described in detail by Vilà-Guerau de Arellano et al. (2024) and in Chapter 3. In this chapter, we continue using the observational dataset introduced in Chapter 3. This dataset includes in-canopy and above canopy vertical profiles of potential temperature, specific humidity, $CO_2$, photosynthetically active radiation (PAR), TKE, and wind; upward longwave radiation at 75 m; vertical profiles of stomatal conductance and of the ratio of intercellular to external $CO_2$ concentration ($C_i/C_a$); 30-min eddy covariance measurements of turbulent fluxes at 50 m; vertical profiles of leaf area density; and air storage fluxes at 50 m of specific humidity and $CO_2$.

In addition to these measurements, the present chapter also uses: downward longwave radiation at 75 m; air storage flux of sensible heat at 50 m; turbulent fluxes measured by additional eddy-covariance systems deployed at multiple heights; atmospheric boundary layer vertical profiles of $CO_2$ (acquired by sensors onboard an aircraft); atmospheric boundary layer vertical profiles of temperature, specific humidity, and wind (acquired by radisonde measurements); and cloud remote sensing measurements acquired at the Campina site. In the following paragraphs, we detail the sensors and procedures used to measure the new introduced variables compared to Chapter 3.

Similar to upward longwave radiation, downward longwave radiation was measured at 75 m with a pyrgeometer system (CGR4, Kip Zonen, The Netherlands) and with a temporal resolution of 10 min.

The air storage flux of sensible heat ($F_{stor,H}$) at height $h$ was estimated every 30 min using an expression analogous to that used for the storage fluxes of specific humidity and $CO_2$ (Eq. 3.3 in Chapter 3):

$$F_{stor,H} = \int_0^h \rho_d \cdot C_p \cdot \frac{\partial T}{\partial t} \cdot dz, \tag{5.1}$$

where $\rho_d$ is the dry air density, $C_p$ is the specific heat capacity of dry air at constant pressure, and $T$ is the air temperature. To estimate the integral over height, we used air temperature measurements from four sensors located at 4, 26, 36, and 55 m.

In addition to the turbulent fluxes measured at 50 m, we used flux measurements from eddy-covariance systems deployed at the following heights: 5, 15, 25, 35, 81, 100, 127, 151, 172, 196, 223, 247, 298, and 316 m. At these levels, momentum and sensible heat fluxes were available, while latent heat and $CO_2$ fluxes were measured only at 5, 25, 50, 81, 196, and 316 m.

On 18 August 2022, vertical profiles of $CO_2$ up to 5 km altitude were acquired by an aircraft during two flights: a morning flight (from 09:06 LT to 10:47 LT), and an afternoon flight (from 12:50 to 14:27 LT). Onboard the aircraft, $CO_2$ values were measured using a Picarro gas analyzer.

To characterize the atmospheric boundary layer height and clouds properties, we followed the observational analysis reported by de Feiter et al. (2025). Boundary layer height was estimated using two independent approaches. The first estimate was derived from backscatter observations obtained by a permanently installed ceilometer at the Campina site. The second estimate was inferred from vertical profiles measured by radiosondes. To characterize the clouds, we compared the simulated clouds against the cloud base and top retrieved from a MIRA Doppler cloud radar.



## 5.4 Results

### 5.4.1 Microclimate

*Air temperature, humidity and $CO_2$*

Can-DALES was able to represent, to a large extent, the observed potential temperature, humidity and $CO_2$ mole fractions, Fig. 5.2. The simulation results were characterized by within-canopy potential temperature differences of 2-4 K, which are similar to the observed ranges (Fig. 5.2, upper row). Potential temperature gradients were also well captured by the simulation, giving confidence in the ability of can-DALES to represent realistic canopy thermal stratification.

The representation of humidity, however, showed larger discrepancies (Fig. 5.2, middle row). During most of the day, simulated specific humidty profiles were quasi well mixed within the canopy but for the lowest 5 m where a stable air layer caused a steep specific humidity gradi-

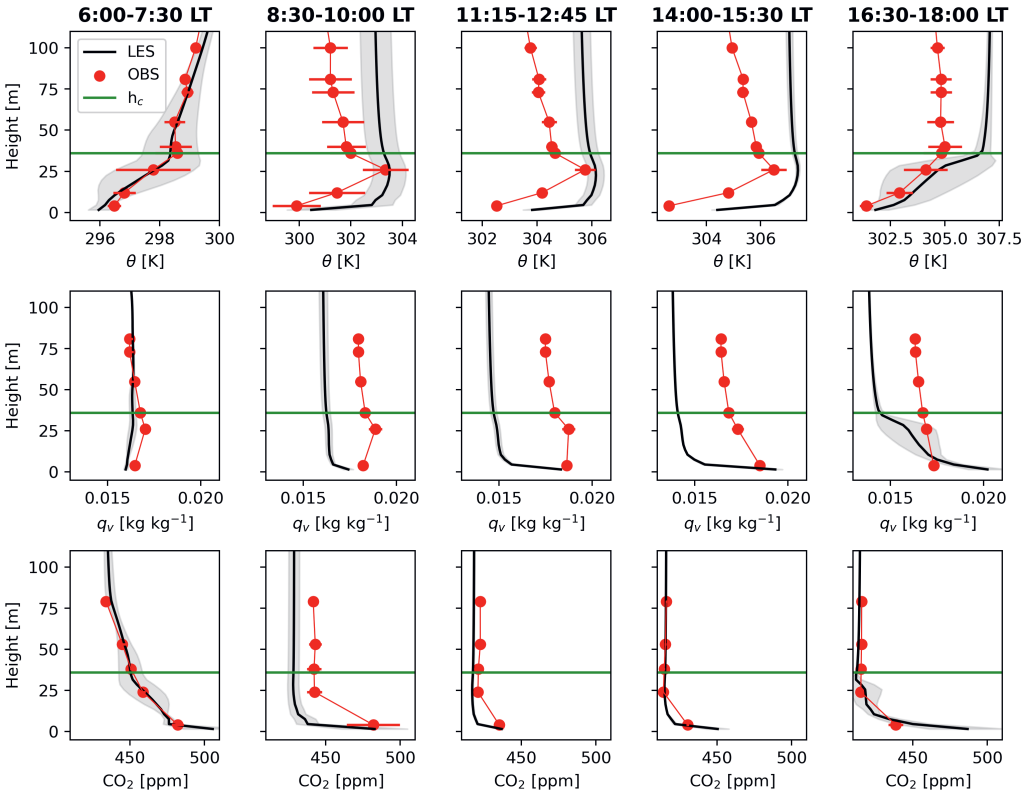



**Figure 5.2:** Vertical profiles within and above the canopy of potential temperature (upper row), specifc humidity (middle row), and $CO_2$ mole fractions (lower row) at several time intervals. Simulated results are shown as black solid lines whereas observations are depicted as red dots connected by red lines. The grey area depicts the range within one stardard deviation of the simulated slab-averaged values, and, as such, the area shows the simulated temporal variability within the considered time interval. The red error bars quantify the observed standard deviation across 1.5 h time interval. Green horizontal lines indicate canopy height.

ent. The discrepancy of the specific humidity gradient between simulation and observations can be partially explained by an enhanced soil evaporation source in can-DALES.

Simulated and observed $CO_2$ mole fractions aligned well overall (Fig. 5.2, lower row). Can-DALES reproduced the observed vertical variability, which ranged up to 40 ppm. This agreement with observations provides further confidence in the model's ability to capture the thermal stratification and its effect on atmospheric gas distributions.

Taken together, this comparison shows that can-DALES reproduces the within-canopy microclimate satisfactorily, realistically representing vertical gradients. The microclimate validation outperforms that reported by Pedruzo-Bagazgoitia et al. (2023), which did not show such a strong and realistic thermal stratification. The improved performance is partially explained by changes in the subgrid-scale parameterization, which in our simulation reduced subgrid-scale diffusivity close to the ground, allowing for a more realistic representation of near-surface shear and turbulence.

Nonetheless, certain biases remained on the simulation. Above canopy air was warmer (up to 1.5 K), drier (approximately 0.0025 kg $kg^{-1}$; also within the canopy), and $CO_2$-depleted (the latter only during the morning transition). We interpret these biases as interconnected, likely resulting from a stronger and earlier entrainment flux in the simulation compared to observations. Accordingly, we attribute these biases to a somewhat faster and earlier morning transition and boundary layer growth in the simulation. Variables and arguments supporting this hypothesis are developed throughout the following sections.



*Wind and turbulence*

Wind speed and TKE agreed closely between the observations and simulation results in terms of shape and magnitude. In the simulation, winds were slightly weaker (approximately 0.5 m $s^{-1}$), particularly in the afternoon, while TKE values were similar between simulation and observations excepting during the morning and nighttime transitions above the canopy.

During the morning transition (from 08:30 to 12:45 LT), simulated TKE exceeded observed values. This excess of simulated TKE is likely linked to a faster growth of the ABL, and to an earlier and stronger entrainment flux, which is consistent with the warm and dry biases reported in the previous section, Fig. 5.2 (upper and middle rows). The lack of simulated TKE during the nighttime transition (from 16:30 to 18:00 LT) indicates a suppression of turbulence above the canopy, suggesting a faster nighttime transition in the simulation than in the observations. The abrupt simulated nighttime transition is related to the rapid decrease in simulated longwave radiation emitted by the canopy at the end of the day (Fig. 4.7 in Chapter 4), which reveals remaining limitations of can-DALES longwave canopy radiative scheme.

The can-DALES simulation explicitly represented large-scale eddies in the flow while parameterizing small-scale eddies. Subgrid-scale parameterized TKE accounted for less than 20

% of the total TKE (Table 5.A.1), reaching this fraction only near to the simulated canopy top.

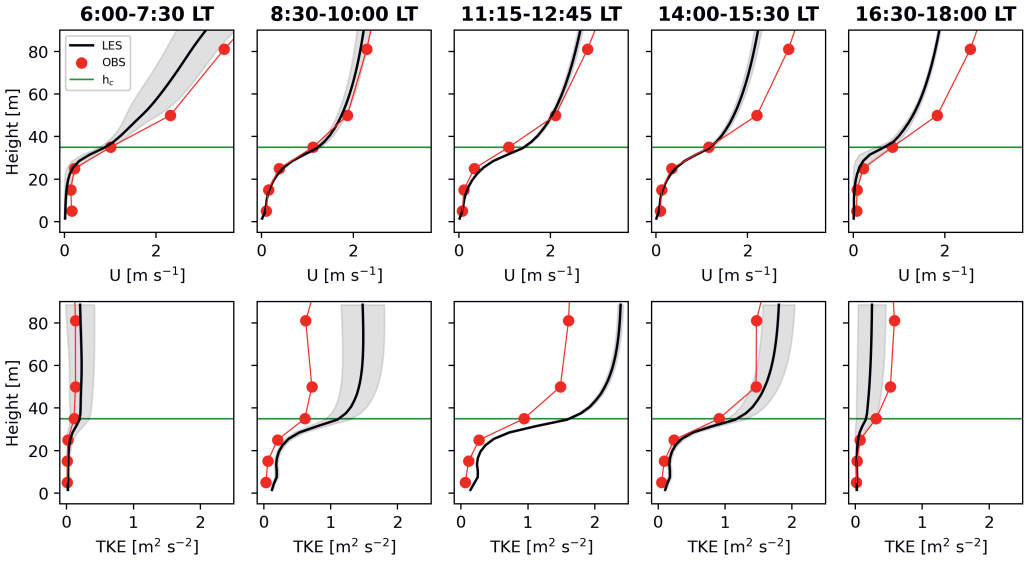



**Figure 5.3:** Vertical profiles within and above the canopy of wind speed (upper row), and turbulent kinetic energy (lower row) at several time intervals. Simulated results are shown as black solid lines whereas observations are depicted as red dots connected by red lines. The grey area depicts the range within one stardard deviation of the simulated slab-averaged values, and, as such, the area shows the simulated temporal variability within the considered time interval. Green horizontal lines indicate canopy height.

The simulated shear and buoyancy terms revealed distinct features of canopy turbulence dynamics, Fig. 5.4. At the beginning and end of the day (from 06:00 to 07:30 LT and from 16:30 to 18:00 LT), air located near the canopy top (between 20 and 30 m) was slightly negatively buoyant in both observations and simulated results due to radiative cooling, indicating a mild local tendency for air parcels to sink (Fig. 5.4, upper row). This feature can promote well-mixed profiles within the canopy, such as those observed for potential temperature and $CO_2$ during nighttime (Huitema et al., 2026).

During the remainder of the day, air in the lower simulated canopy was negatively buoyant, while the upper canopy air was postively buoyant. These features, together with the absence of shear and the minimal turbulent kinetic energy in the lower canopy, highlights the presence of a stable air layer that decouples air mixing within the canopy (Chapter 3; Santana et al., 2018). The simulated stable layer varied in depth over the course of the day, Fig. 5.5. It acquired maximum depths (of approximately 0.5 $h_c$) in the early morning and late afternoon, and minimum depths (of approximately 0.25 $h_c$) at midday, when direct solar radiation beams penetrated the canopy more effectively (Chapter 4).

The simulated above-canopy buoyancy flux compared well with observations in both mag-

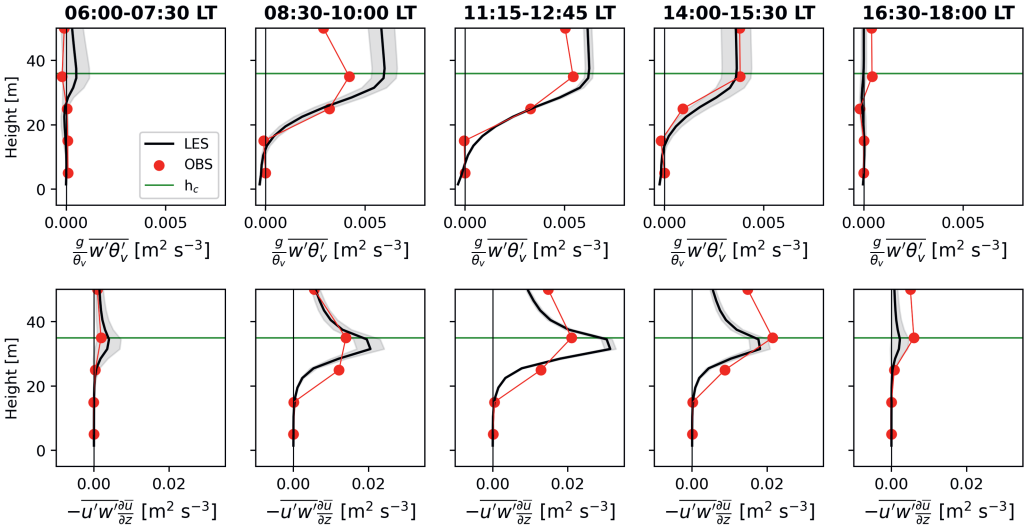



**Figure 5.4:** Vertical profiles of the buoyancy production/loss term (upper row), and the shear production term (lower row) at several time intervals near and within the canopy. Simulated results are shown as black solid lines whereas observations are depicted as red dots connected by red lines. The grey area depicts the range within one stardard deviation of the simulated slab-averaged values, and, as such, the area shows the simulated temporal variability within the considered time interval. Green horizontal lines indicate canopy height. An extended vertical profile of the shear and buoyancy terms which covers up to 300 m can be found in Fig. 5.A.5.

nitude and shape, excepting for a few discrepancies which align with our previous findings. During the early morning (from 06:00 to 07:30 LT), simulated above-canopy buoyancy was positive indicating the onset of convective turbulent movements due to the surface warming caused by solar irradiance. Observations, however, suggested a delay in the onset or at least in the strength of these convective movements, probably caused by biomass heat storage or other buffering processes not yet fully captured by the canopy radiative transfer model (Chapter 4). Similarly, near the end of the day (from 16:30 to 18:00 LT) simulated buoyancy approached zero, while observations still indicated weak positive buoyancy, again suggesting missing heat buffering processes. During the morning transition (from 08:30 to 12:45 LT), the simulation exhibited stronger positive buoyancy than observed, supporting the hypothesis of enhanced entrainment flux and boundary layer growth.

Shear also compared well between simulation and observations (Fig 5.4, lower row). Shear peaked at canopy top and exhibited a clear diurnal cycle, with larger values from 08:30 to 15:30 LT in both observations and simulated results. Overall, can-DALES represented buoyancy and shear processes within and above the canopy realistically, capturing the presence a within-canopy stable air layer that may alter gas residence times within the canopy.

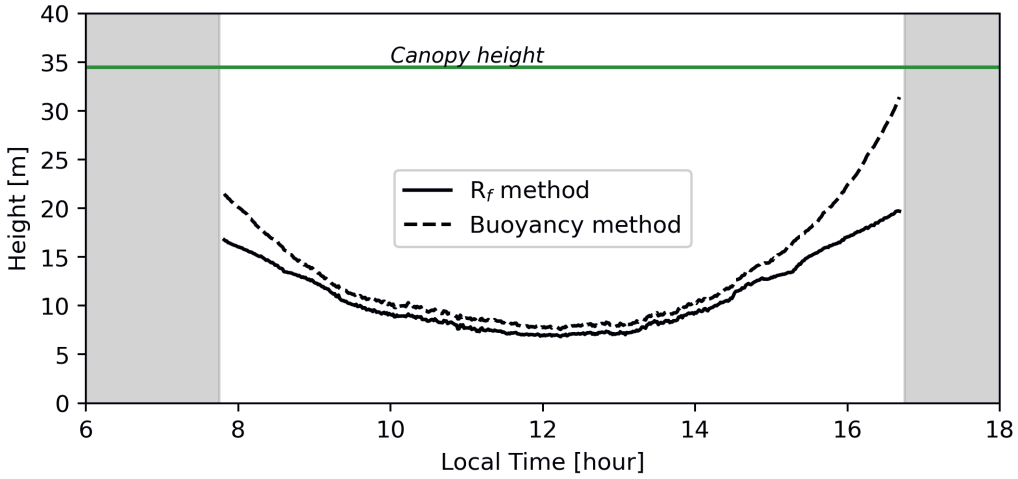



**Figure 5.5:** Simulated daytime series of the top of the stable layer that is located within the canopy. The height of the top of the stable layer has been estimated through two methods: (1) as the minimum height when buoyancy becomes positive (buoyancy method), and (2) as the minimum height where the flux Richardson number acquires the threshold value of 1, indicating a transition from stable to unstable and turbulent conditions ($R_f$ method). Grey areas denotes the time periods when the stable layer is not well-defined.

### 5.4.2 Leaf gas exchange

*Leaf temperatures*

Simulated leaf temperatures differed markedly among sunlit and shaded leaves. Temperatures of shaded leaves were relatively similar to air temperatures, with differences of approximate 1 K across canopy depth, whereas temperatures of sunlit leaves showed much larger departures, reaching differences of up to 5 K. These differences were particularly pronounced in the lower canopy, where air temperatures were the lowest (Fig. 5.6, upper row).

By weighting sunlit and shaded leaf temperatures by their fractional area at each vertical layer, we derived a mean leaf temperature representative of each horizontal level. Differences between mean leaf and air temperatures were largest at the canopy top (approximately 1.7-2.5 K), where most solar radiation was absorbed, and decreased with canopy depth.

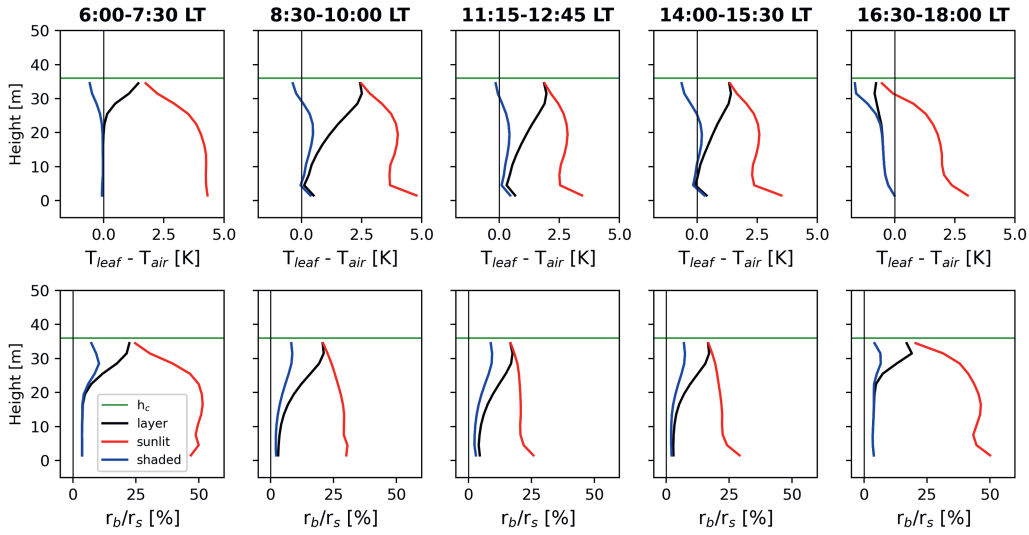



**Figure 5.6:** Vertical profiles of simulated leaf to air temperature (upper row) and of the ratio of leaf boundary layer resistance to heat ($r_b$) and stomatal resistance to water vapor ($r_s$) for five time intervals. Each panel depicts the variables for: sunlit leaves (red line), shaded leaf (blue line), and for the mean vertical layer (black line). The mean vertical layer accounts for the sunlit and shaded proportion at the corresponding vertical level. Horizontal green lines indicate the canopy height.

*Leaf boundary layer*

The simulated leaf boundary layer resistance ($r_b$) was consistently smaller than the stomatal resistance ($r_s$), with $r_b$ ranging between approximately 0.05 and 0.5 $r_s$. This result confirms than simulated leaf-scale fluxes of water and $CO_2$ were primarily controlled by stomatal

behavior rather than aerodynamic limitations (see Eq. (5.A.1), (5.A.2) and (5.A.3) for the functional dependency of leaf-scale fluxes on $r_b$ and $r_s$).

According to the simulation results (not shown), the leaf boundary layer resistance was nearly identical for sunlit and shaded leaves. At the canopy top, $r_b$ acquired values of approximately 100 s m$^{-1}$, which increased with canopy depth by about 30–50 s m$^{-1}$. This increase reflects calmer wind conditions deeper in the canopy, which enhance the thickness of the leaf boundary layer and thereby hinder leaf-scale fluxes.

*Stomatal conductance and internal to atmospheric $CO_2$ concentrations*

Observed and simulated internal-to-atmospheric $CO_2$ concentration ratios ($C_i/C_a$) and stomatal conductance ($g_s$) exhibited similar magnitudes and diurnal cycles. Simulated $C_i/C_a$ ratios slightly underestimated observed values, whereas simulated $g_s$ generally fell within the observed range.

Simulated sunlit leaves absorbed large amounts of radiation (approximately 1000 $\mu$mol m$^{-2}$ s$^{-1}$) from shortly after sunrise until just before sunset. High absorbed PAR values occurred throughout the canopy, including the mid and lower layers, due to the penetration of direct solar beams. On average, sunlit leaves absorbed about 75 % of the direct normal PAR (i.e., PAR received from the sun on a surface perpendicular to the solar rays). Shaded leaves absorbed less than 500 $\mu$mol m$^{-2}$ s$^{-1}$ of PAR, with absorption decreasing with canopy depth.

Stomatal conductance differed markedly between sunlit and shaded leaves, being consistently higher for sunlit leaves. In general, $g_s$ increased toward the upper canopy, although some exceptions occurred. For example, during the afternoon, $g_s$ of sunlit understory leaves exceeded that of top-canopy leaves when radiation was no longer a limiting factor and vapor pressure deficit became the dominant control factor.

### 5.4.3 Ecosystem and surface fluxes

The turbulent fluxes of sensible heat, latent heat and $CO_2$ at 50 m agreed remarkably well between observations and simulation results, particularly for $CO_2$ fluxes (Fig 5.8). In addition, can-DALES reproduced realistic air storage fluxes (Fig. 5.A.3) and vertical profiles of the turbulent fluxes across the surface layer, Fig. 5.A.4.

In the morning, the simulated and observed sensible heat fluxes at 50 m became positive at the same time, suggesting good agreement in the onset of unstable atmospheric conditions. Nonetheless, the simulated sensible heat flux increased more rapidly, exceeding observed values by approximately 50-75 W m$^{-2}$ during the morning transition. This overestimation is consistent with the excessive simulated TKE and buoyancy production, as well as with the warm and dry biases discussed previously.

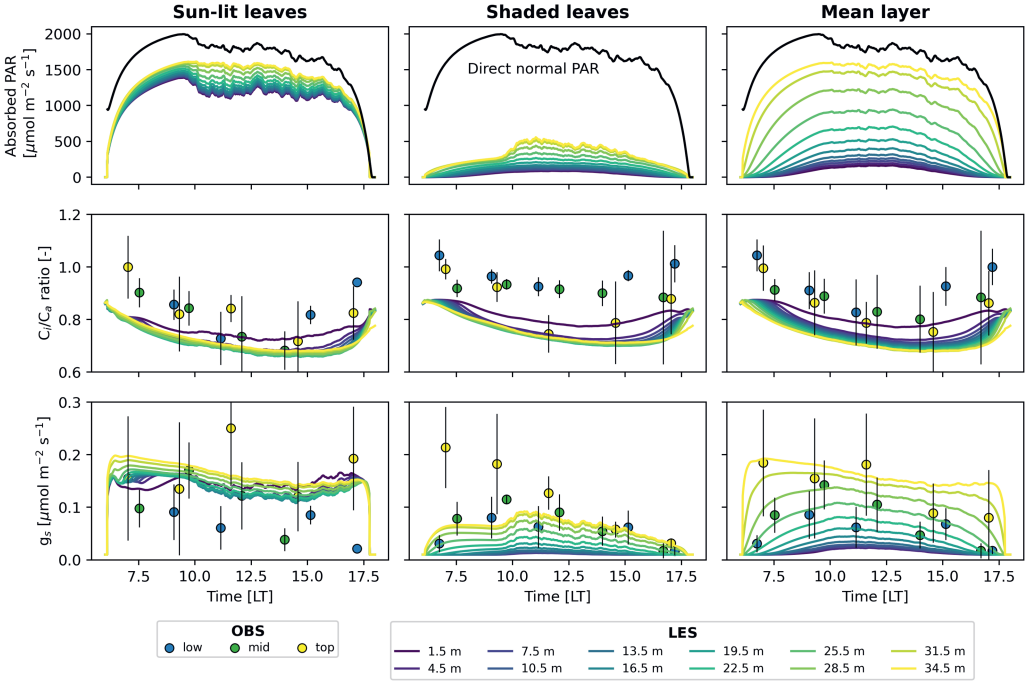



**Figure 5.7:** Time series of absorbed PAR (upper row), internal to atmospheric $CO_2$ concentration ($C_i/C_a$; middle row), and stomatal conductance to water vapor ($g_s$; lower row) for various canopy heights. Simulated results are shown with solid lines while observations are depicted in circles with an error bar representing the standard deviation across leaf samples. Upper canopy layers are shown with lighter colours whereas lower layers are shown in darker colors. Results are shown for sunlit leaves (left column), shaded leaves (center column), and a mean leaf representative of the vertical level (right column). The simulated time series direct normal PAR at 50 m is shown in solid black lines.

The ecosystem sensible heat flux, which represents the exchange between the forest and the air within the canopy, was similar to the turbulent flux measured at 50 m, differing only during the early morning and late afternoon. During these periods, the ecosystem response (i.e., ecosystem exchange) and the surface forcing exerted on the atmosphere (i.e., surface flux) were partially decoupled.

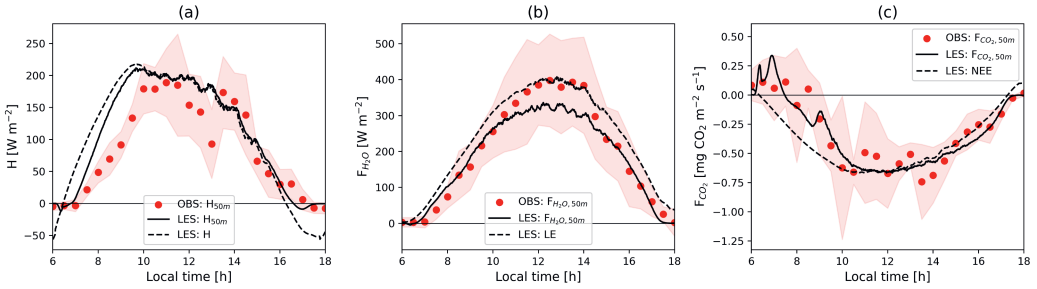



**Figure 5.8:** Time series of sensible heat flux (a), latent heat flux (b), and $CO_2$ turbulent flux (c) at 50 m height. The simulated turbulent fluxes are shown in solid black lines whereas observations are shown as red circles. The red area depicts the range within one stardard deviation of the observed turbulent fluxes. Addditionally, the simulated ecosystem fluxes are shown as dashed black lines.

The simulated latent heat flux at 50 m closely matched the observed diurnal shape and magnitude, although it was underestimated at midday (from 10:00 to 15:00 LT) by up to 100 W m$^{-2}$. In contrast, the simulated ecosystem latent heat flux exceeded the turbulent flux at 50 m by up to 100 W m$^{-2}$ throughout the day. This discrepancy can be explained by simulated soil evaporation, which reached values of up to 100 W m$^{-2}$ at midday but which was unable to ventilate out of the canopy due to a strongly stable air layer located in the lowest model level. The simulated soil evaporation was likely overestimated, as soil evaporation in dense tropical forests is typically reported to be close to zero (Chapter 3). This suggests that can-DALES underestimated vegetation transpiration to some extent, with ecosystem evapotranspiration being compensated by the overestimated soil fluxes.

The simulated turbulent $CO_2$ flux at 50 m agreed remarkably well with observations. The simulation accurately reproduced the transition from nighttime positive $CO_2$ fluxes to daytime negative fluxes, which occurred at approximately 08:00 LT. At the beginning of the simulation, can-DALES captured near-zero turbulent $CO_2$ fluxes, followed by a pronounced peak associated with the ventilation of $CO_2$ accumulated overnight within the canopy. During the morning transition, the net ecosystem exchange (NEE) differed from the turbulent flux at 50 m due to the same release of $CO_2$-enriched air stored within the canopy.

Air storage fluxes were consistent between observations and simulations, both in sign and diurnal pattern (Fig. 5.A.3). This agreement indicates that can-DALES captures realistic within-canopy airflow dynamics and is able to distinguish ecosystem responses from the subsequent surface forcings exerted on the atmosphere. Surface fluxes also compared well at other heights within the canopy and across the surface layer (Fig. 5.A.4), with simulation

results reproducing the observed vertical variability, although observations suggested larger fluxes near the forest top.

### 5.4.4 Atmospheric boundary layer and cloud dynamics

*Boundary layer height and cloud properties*

Boundary layer height, $z_i$, increased from sunrise until approximately 16:00 LT, when it started decreasing, Fig. 5.9. The simulated $z_i$ reached values of up to 1800 m, approximately 250 m higher than the observed $z_i$. In addition, the simulated $z_i$ increased more rapidly during the morning transition, when it was at times 400 m higher than the observed $z_i$.

The enhanced simulated boundary layer growth is mainly the result of the larger sensible heat flux during the morning transition (Fig. 5.8a). Despite these differences, shallow cumulus clouds developed in both the simulation and the observations, starting at approximately 9:30-10:00 LT. Cloud bases were located near the top of the corresponding $z_i$ and thus, cloud bases for the simulation were higher than those observed. Similarly, cloud tops were higher in the simulated results than in the observations. Overall, simulated clouds were slighlty deeper than observed clouds, likely as a result of stronger simulated thermals.



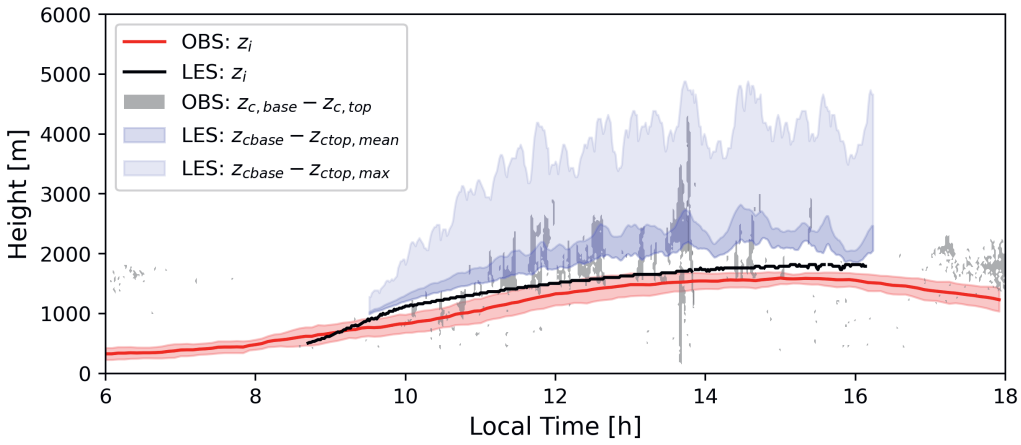



**Figure 5.9:** Time series of boundary layer height, cloud base, and cloud top for both observations and simulation results.

*Atmospheric boundary layer vertical profiles*

The simulated vertical profiles of potential temperature, specific humidity and wind speed closely resembled the observed profiles at 09:00, 11:00, 15:00, and 18:00 LT, Fig. 5.10, indi-

cating that the simulated atmospheric boundary layer state was realistic overall. Nonetheless, three differences between observations and simulated results can be identified.

First, the cloud layer was more strongly influenced by the atmospheric boundary layer development in the simulation than in the observations. This feature is evident in the vertical profiles of potential temperature and specific humidity at 15:00 and 18:00 LT, which exhibit a colder and moister cloud layer (approximately between 1800 m and 4000 m, Fig. 5.9) and, conversely, a warmer and drier boundary layer relative to observations. Second, the simulation produced a more well-mixed atmospheric boundary layer profiles of specific humidity than suggested by observations. Both of these features are consistent with more vigorous thermals and enhanced vertical mass fluxes driven by thicker and deeper clouds in the simulation. Finally, simulated winds speeds were weaker than those observed.

Simulated vertical profiles of $CO_2$ across the ABL also also compared well with observations, Fig. 5.11, but simulated $CO_2$ concentrations were slighlty lower than observed values during the afternoon. The slightly $CO_2$-depleted ABL is likely linked to a stronger entrainment flux at the boundary layer top, which is consistent with the enhanced boundary layer growth and the deeper cloud development discussed above.

Overall, the consistency between simulated and observed boundary layer evolution, cloud properties, and scalar transport indicates that can-DALES captures the key feedbacks linking forest surface processes and shallow convective dynamics under cloudy conditions.

## 5.5 Discussion

### 5.5.1 Overview of key findings

In this chapter, we assessed the ability of can-DALES to reproduce and investigate land-atmosphere interactions over the Amazon Basin during a day characterized by shallow-cumulus clouds. Can-DALES proved capable of capturing the coupled evolution of canopy microclimate, atmospheric turbulence, surface fluxes, and shallow-cumulus clouds development, while also revealing some systematic biases. The simulation constitutes a LES study with unprecedent realism, due to the simultaneous representation of a detailed multi-layer canopy and boundary-layer clouds.

Can-DALES captured exceptionally well the $CO_2$ dynamics, reproducing observed vertical profiles of $CO_2$ mole fractions and surface fluxes (Fig. 5.2 lower row, and Fig. 5.8c). Can-DALES was able capture the $CO_2$ dynamics well because it realistically represented leaf ecophysiology (Fig. 5.7) and within-canopy turbulent structure (Fig. 5.3 and Fig. 5.4). The simulation captured $CO_2$ ventilation events, the $CO_2$ storage flux (Fig. 5.A.3), and a stable air layer within the canopy (Fig. 5.5). The depth of the stable layer is consistent with previous literature (Santana et al., 2018), which estimated an extent from the forest floor to approximately 0.5 $h_c$. The simulation allowed us to further explore its depth, revealing a diurnal variability

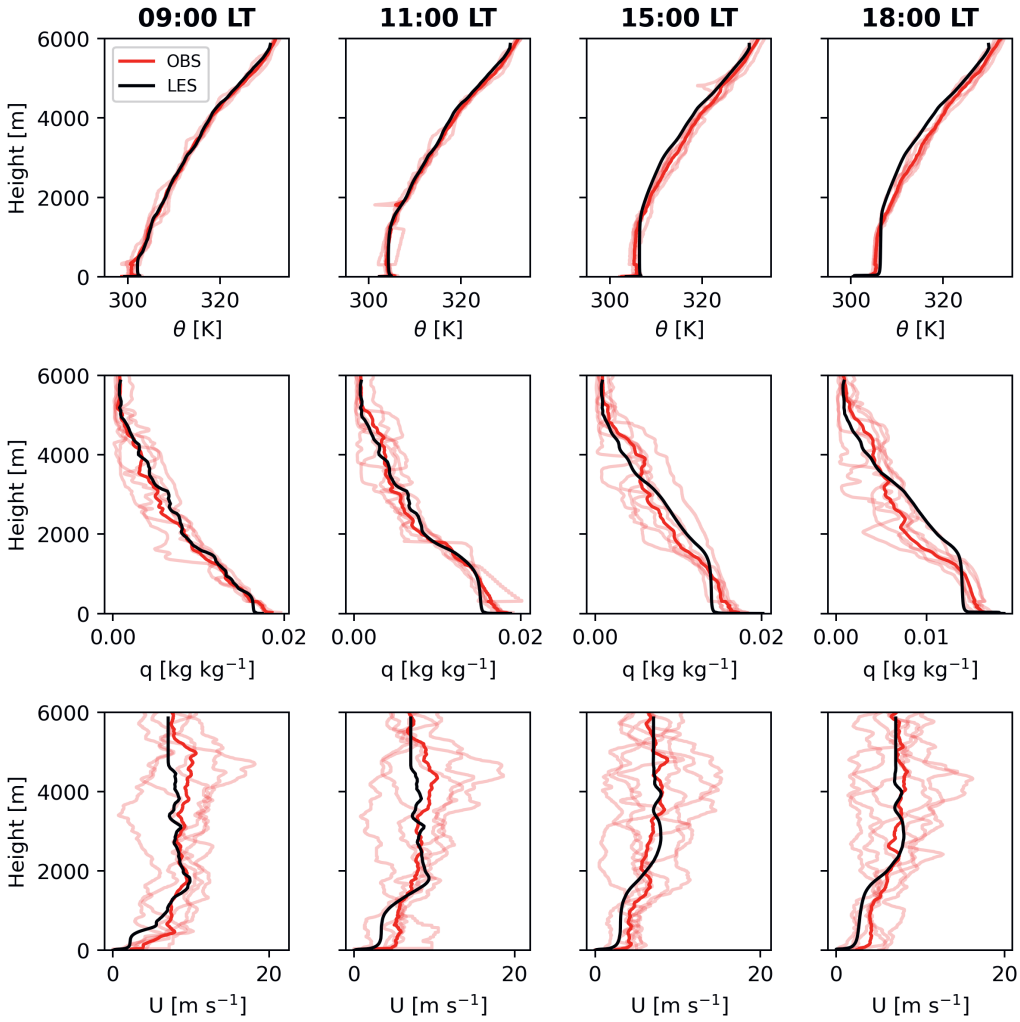



**Figure 5.10:** Vertical profiles of potential temperature (upper row), specific humdity (middle row), and wind speed (lower row) for both observations (darker red line) and LES results (black line). Light red lines depict the individual radiosonde profiles across the six shallow-convective days.

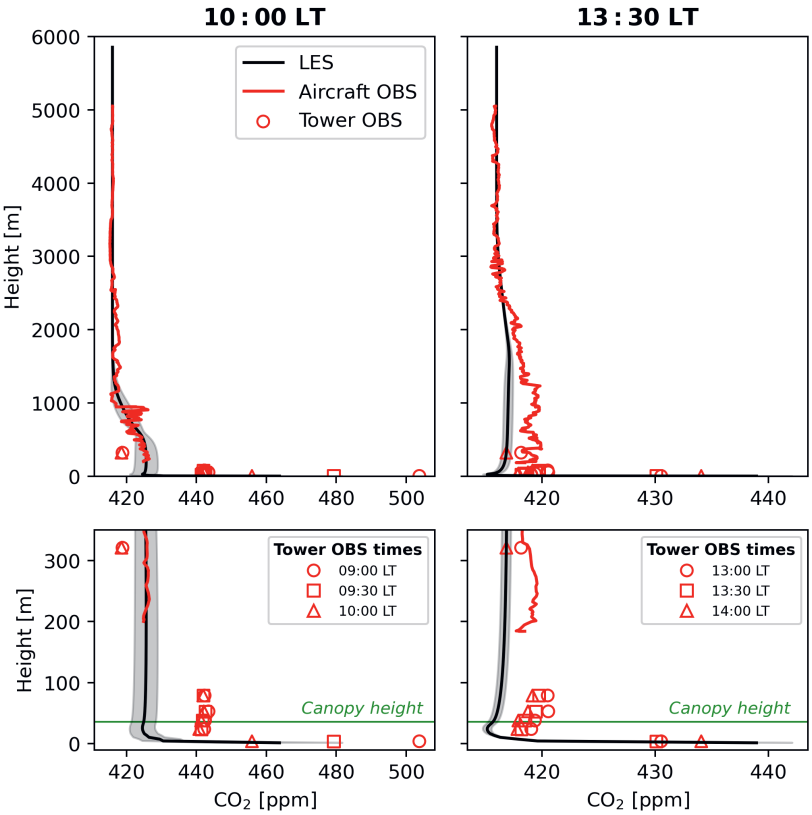



**Figure 5.11:** Vertical profiles of observed and simulated $CO_2$ mole fractions duing two time intervals when aircraft measurements were acquired: from 09:06 LT to 10:47 LT (left column), and from 12:50 to 14:27 LT (right column). The upper row shows profiles spanning up to 6 km height, while the lower row focuses on the near-canopy region. Aircraft measurements are shown as red lines, tower observations as red-outlined markers with different shapes indicating local time, and LES results as black solid lines with grey shading representing one standard deviation of the slab-averaged simulated profiles.

that depended on the canopy radiative transfer.

The simulation represented a realistic atmospheric boundary layer state and shallow-cumulus field. The differences between simulated results and observations were consistent, indicating expected forest-atmosphere dynamics and also highlighting some model limitations, which are discussed later. Compared to observations, the simulation exhibited larger sensible heat fluxes, TKE, and buoyancy during the morning, which caused an earlier growth of the atmospheric boundary layer and larger entrainment fluxes. As a result, the simulated atmospheric boundary layer was deeper and the shallow-cumulus clouds were thicker. Consequently, the clouds ventilated air more efficiently out of the atmospheric boundary layer, altering the state of the lower free-troposphere. While these dynamics vary in strength from those observed, they remain physically sound and within the plausible range for shallow-convective conditions over the Amazon forest.

### 5.5.2 Canopy thermal air stratification and forest-atmosphere coupling

Air stable layers within canopies are relevant when studying land-atmosphere interactions, as they can, partially or totally, decouple air mixing within and right above the forest. Within-canopy air stable layers are not exclusive of tropical forests and they occur in other forest ecosystem during both nighttime and daytime (e.g., Alekseychik et al., 2013; Schilperoort et al., 2020). Representing them well in land-surface schemes is challenging, as they require realistic vertical profiles of buoyancy and shear at high spatial resolution, but which can be achieved in canopy LES. Representing within-canopy air stable layers is relevant to disentangle surface turbulent fluxes from ecosystem exchanges, and thus, to properly attribute microclimatic changes to subsequent ecosystem responses. When not represented well, stable air canopy layers can confound ecosytems response with surface fluxes, particularly during transient periods such as the morning transition (Chapter 3). The use of canopy LES to represent air stable layers within canopies has diverse applications. For instance, it can be applied in studies related to atmospheric chemistry, such as ozone deposition studies over forests (Wang et al., 2025), when realistic residence times of gases, as well as realistic vertical gradients of mole fractions and turbulent transport, are required.



### 5.5.3 Canopy processes and the clear-to-cloudy transition

This study simulated realistic leaf ecophysiology, canopy radiative transfer, turbulent structures and shallow-cumulus clouds, making it suitable to investigate forest-atmosphere interactions in clear-to-cloudy conditions. Previous studies have shown the radiative impact of shallow-cumulus clouds on surface fluxes, but always considering simplified canopy representations (e.g., Vilà-Guerau de Arellano et al., 2020). By realistically representing both the canopy and the boundary-layer clouds, we can now resolve the buffering between radiative-driven ecosystem responses and the surface forcing to the atmosphere. This buffering could also alter the diurnal evolution of shallow cumulus clouds. While beyond the scope of this

study, can-DALES offers the possibility of exploring three-dimensional airflow fields, which can help disentangle radiative and turbulent feedbacks between the forest and boundary-layer clouds.

### 5.5.4 Missing processes

While the simulated results presented in this study were realistic, the simulation still simplified or neglected processes known to play a role in forest-atmosphere dynamics, resulting in certain biases.

In particular, atmospheric water dynamics were less well reproduced compared to $CO_2$ dynamics. Simulated soil evaporation was larger than expected for dense tropical forests, while the simulated atmospheric boundary layer was more well-mixed and drier than suggested by observations. We attribute these biases to several factors. In first instance, the soil scheme may need certain adaptation to account for the litter layer present over the forest floor, which could act as an insulating layer that reduces soil evaporation rates (Park et al., 1998). Additionally, the strong entrainment fluxes caused by excessive simulated buoyancy during the morning transition, were reponsible for the drying of the atmospheric boundary layer and partially for the overly well-mixed conditions.

Several hydrological processes relevant to forest ecosystems could still be explored and revisited in can-DALES. Dew formation is known to occur in the Amazon forest during both the dry and wet season (Binks et al., 2021), with dew dissipating at approximately 06:30-07:00 LT during the dry season. In can-DALES, water can condensate within the canopy, and in the simulation it dissipated during the first simulated hour. While the simulation was not significantly affected by dew dissipation, we recommend future revisions of the representation of dew and fog formation within the canopy in can-DALES to ensure consistency between dew formation, canopy radiative transfer, and the ecophysiological processes.

In this study, the simulation comprised flat terrain with horizontally homogeneous canopy. Topographic variations, present around the ATTO site, have been shown to modify the surface atmospheric layer compared to idealized flat terrain (Chamecki et al., 2020). Consequently, topography could influence the development of shallow-cumulus. Similarly, the assumption of a horizontally homogeneous canopy, differs from real canopies, which exhibit local variations in canopy top and leaf area density (Parker & Russ, 2004; Parker et al., 2019; Anhuf & Rollenbeck, 2001). This simplification could also influence the surface layer and the forest-atmosphere coupling. Horizontal heterogeneity in the forest structure is likely to explain part of the deviations between the highly local observations and the horizontal homogeneous simulated results. Future canopy LES studies could focus on the horizontal variations in canopy microclimate and turbulent structure to determine whether they interact with transport changes induced by shallow-cumulus clouds (de Feiter et al., 2025).

Finally, as mentioned in Chapter 4, heat storage in the forest biomass, particularly in the woody material, could modify surface turbulent fluxes, thereby altering the evolution of

shallow-cumulus clouds. The implementation of these processes in can-DALES could further strengthen the realism and physical fidelity of the simulated forest-atmosphere interactions.

## 5.6 Conclusions

This chapter assessed the ability of a multi-layer canopy LES to reproduce land-atmosphere interactions during the transition from clear sky to shallow cumulus dominated conditions. We used the can-DALES model to simulate a daytime cycle over the Amazon Basin, which we contrasted with a comprehensive observational dataset acquired at and around the ATTO site during CloudRoots-Amazon22 field campaign. To explore the land-atmosphere interactions, we analyzed four interconnected aspects of the land-atmosphere system: the forest microclimate, the leaf gas exchange and energy balance, the ecosystem and surface fluxes, and the clear-to-cloudy atmospheric boundary layer.

The simulation validated well against observations for the four themes, satisfactorily representing within and above canopy gradients, and diurnal variability. Regarding the forest microclimate, the simulation reproduced a stable air layer within the canopy, which expanded and shrunk following a diurnal cycle. Regarding the leaf-scale fluxes, the simulation exhibited realistic vertical profiles and daytime evolution of leaf temperatures, stomatal conductance and internal to atmospheric $CO_2$ concentrations; which validated well against observations acquired in the forest. Regarding the ecosystem-scale fluxes, the simulation represented the measured surface fluxes whose temporal dynamics were affected by ventilation and storage of within canopy air, which were linked with the presence of the within-canopy stable air layer. Regarding the clear-to-cloudy atmospheric boundary layer, the simulation captured the transition to a shallow-cumulus regime while resolving canopy-scale turbulence that modulated the surface forcing. While the simulated atmospheric boundary layer dynamics varied somewhat in strength from those observed, they remained physically sound and within the plausible range for shallow-convective conditions over the Amazon forest. Overall, this study underscores the potential of canopy-resolving LES to bridge ecosystem-scale processes and atmospheric dynamics.

# 5.A Supplementary Information for Chapter 5

## 5.A.1 Initialization and model settings

*Initial atmospheric boundary layer profiles*

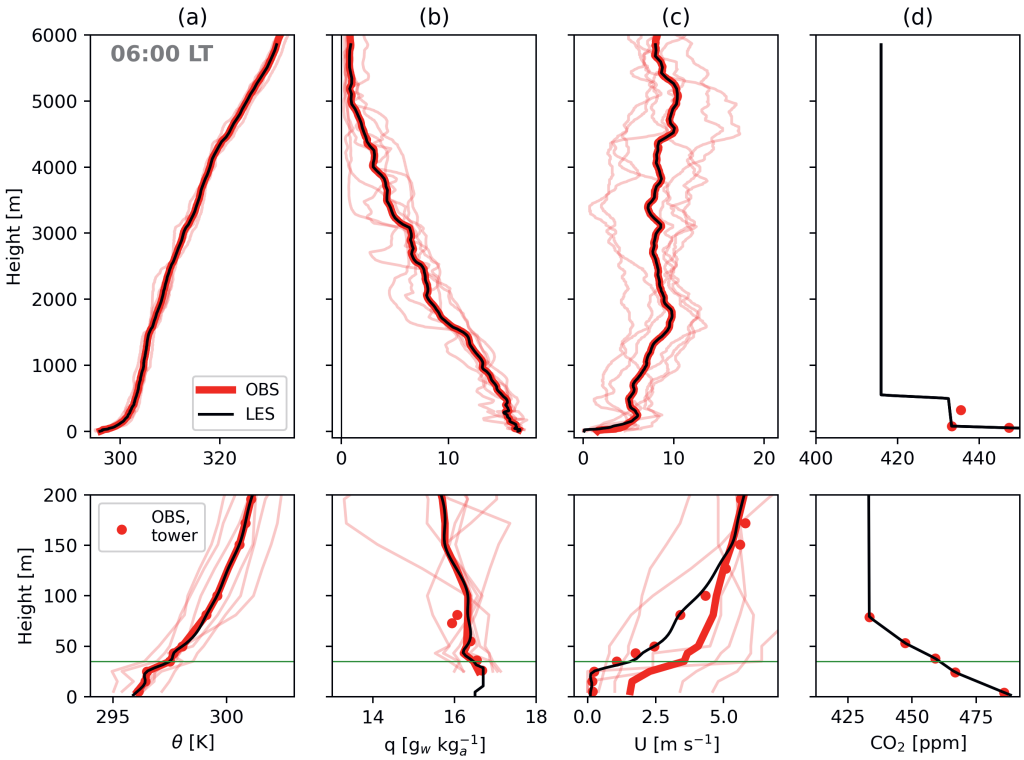



**Figure 5.A.1:** Vertical profiles of observations from radiosondes and model initialization, at 6 LT. The lowest row show the same profiles but near the canopy. Can-DALES initial profiles are shown in a black solid line whereas radiosondes observed vertical profiles are shown in a red solid lines. Observations acquired by sensors located at the ATTO towers are shown as red dots. The canopy height is indicated as a horizontal green line.

To initialize the simulation at 06:00 LT, we used vertical profiles of potential temperature, humidity, and wind acquired by radiosondes as well as by the sensors within and close to the canopy, Fig. 5.A.1a, b, and c. Compared to temperature, humidity, and wind, the $CO_2$ observations at 06:00 LT were scarcer; six $CO_2$ sensors were deployed below 330 m (at 4, 24, 38, 53, 79, and 321 m) but none above. Nonetheless, $CO_2$ vertical profiles were measured by an aircraft during two later flights on August 18, 2022. These measurements confirmed a steady free-tropospheric $CO_2$ concentration of 416 ppm, which enable us to characterize

the free tropospheric values. For the remaining vertical profile, we assumed an initial $CO_2$ vertical profile that was consistent with the surface tower $CO_2$ data, and which had a well-mixed residual layer from 80 m to approximately 500 m. Above 500 m, $CO_2$ attained the observed free-tropospheric value (416 ppm), Fig. 5.A.1d.

*Leaf area density and leaf area index*

Leaf area index and leaf area density were based on observations acquired at and around the ATTO site in October 2015 by Gomes Alves et al. (2023). Fig. 5.A.2 shows the prescribed vertical profiles for the simulation presented in this study.

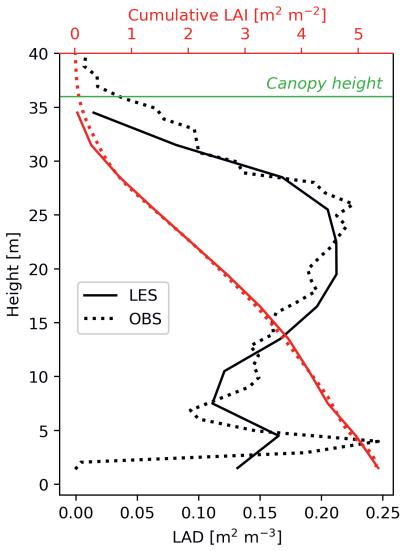



**Figure 5.A.2:** Vertical profile of leaf area density (black lines) and cumulative leaf area index (red lines). Solid lines indicate the vertical profiles prescribed in can-DALES simulation whereas dotted lines indicate the observations as reported by Gomes Alves et al. (2023).

## 5.A.2 Parameterized and resolved turbulence

The can-DALES simulation solved the turbulent transport of some eddies while it still parameterizing the effect of smaller eddies. To quantify the relative proportion of paramterized motions to resolved ones, we estimated the ratio of subgrid-scale parameterized turbulent kinetic energy ($TKE_s$) and the total turbulent kinetic energy ($TKE_t$), Table 5.A.1. This ratio was estimated as the daytime average of $TKE_s$ divided by the daytime average of $TKE_t$.

**Table 5.A.1:** Daytime average of the ratio of subgrid-scale parameterized turbulent kinetic energy ($TKE_s$) and the total turbulent kinetic energy ($TKE_t$).

| Height [m] | $TKE_s/TKE_t$ [%] |
|---|---|
| 1.5 | 5.7 |
| 4.5 | 2.7 |
| 10.5 | 5.3 |
| 16.5 | 10.5 |
| 22.5 | 15.7 |
| 28.5 | 18.0 |
| 34.5 | 11.6 |
| 40.5 | 9.3 |
| 49.5 | 8.1 |
| 58.5 | 7.5 |
| 70.5 | 7.0 |
| 82.5 | 6.7 |

### 5.A.3 Leaf boundary layer effect on leaf-scale fluxes

In can-DALES, the effect of the leaf boundary layer on the leaf gas exchange fluxes is quantified as a resistance, the leaf boundary layer resistance to heat, $r_b$. The leaf boundary layer resistance to heat relates to the leaf fluxes as follows:

$$F_{H,leaf} \propto \frac{1}{r_b} \tag{5.A.1}$$

$$F_{H_2O,leaf} \propto \frac{1}{r_s + \frac{1}{1.075} \cdot r_b} \tag{5.A.2}$$

$$F_{CO_2,leaf} \propto \frac{1}{1.6 \cdot r_s + \frac{1.4}{1.075} \cdot r_b} \tag{5.A.3}$$

where $r_s$ is the stomatal resistance to water vapor, which is the inverse of the stomatal conductance to water vapor, and $F_{H,leaf}$, $F_{CO_2,leaf}$ and $F_{H_2O,leaf}$ are the leaf fluxes of sensible heat, $CO_2$ and water vapor.

### 5.A.4 Air storage and turbulent fluxes

Air storage terms of sensible heat flux, latent heat flux and $CO_2$ flux were estimated for the can-DALES simulation and contrasted to observed values, Fig. 5.A.3. The simulated storage terms compared well with the obserations, with larger differences found at the beginning and end of the daytime period.

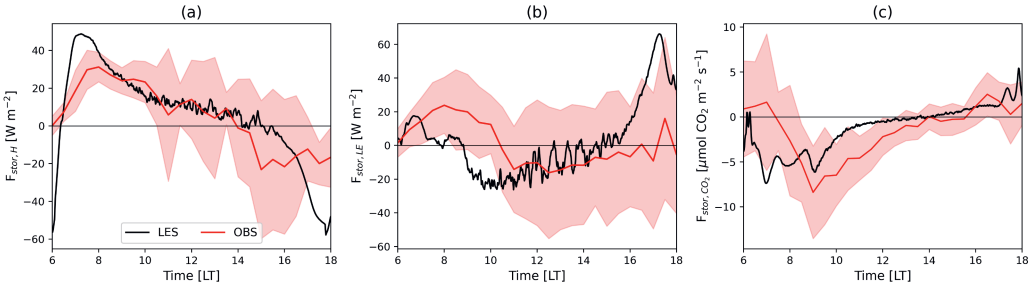



**Figure 5.A.3:** Simulated and observed time series of air storage of sensible heat flux (a), latent heat flux (b), and $CO_2$ turbulent flux (c).

Vertical profiles of latent heat flux, sensible heat flux, $CO_2$ fluxes, and shear and buoyancy terms, were also compared for can-DALES results and observations across the surface layer, Fig. 5.A.4 Fig. 5.A.5

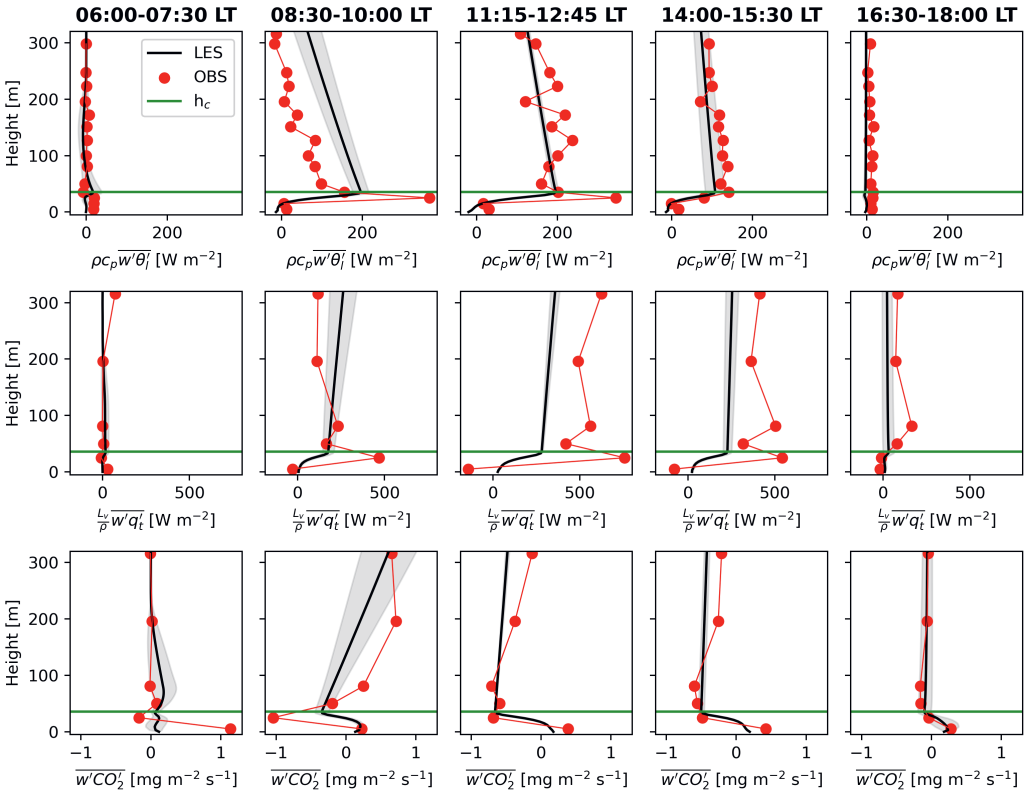



**Figure 5.A.4:** Vertical profiles of the sensible heat flux (upper row), latent heat flux (middle row), and $CO_2$ turbulent flux (lower row) at several time intervals and across the surface layer. Simulated results are shown as black solid lines whereas observations are depicted as red dots connected by red lines. The grey area depicts the range within one stardard deviation of the simulated slab-averaged values, and, as such, the area shows the simulated temporal variability within the considered time interval. Green horizontal lines indicate canopy height.

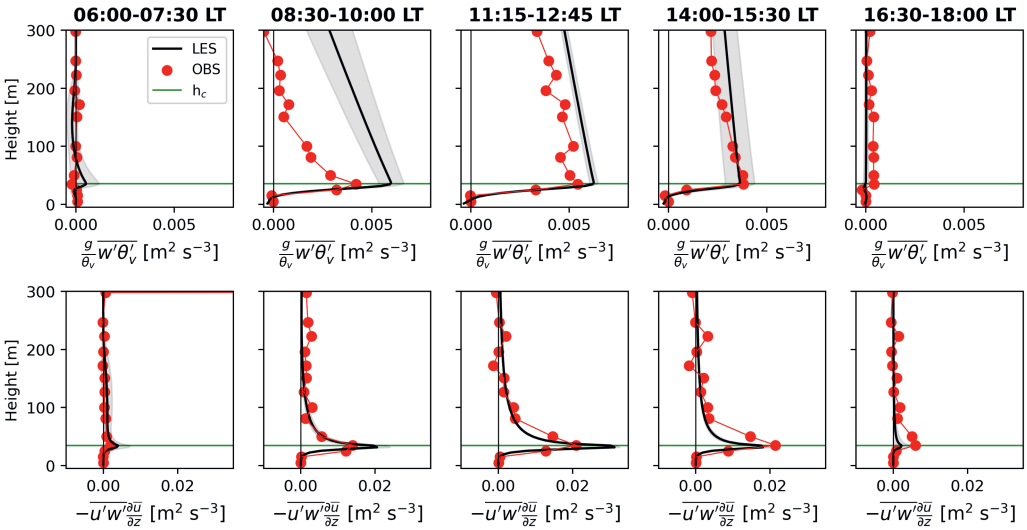



**Figure 5.A.5:** Same as Fig. 5.4 but extending the height, and using all the available eddy-covariance measurement systems.

# Chapter 6

# Tracing diurnal variations of atmospheric $CO_2$, $O_2$ and $\delta^{13}CO_2$ over a tropical and a temperate forest

This chapter is based on:

Faassen, K. A. P., González-Armas, R., Koren, G., Adnew, A., van Asperen, H., de Boer, H. J., Botía, S., de Feiter, V. S., Hartogensis, O., Heusinkveld, B. G., Hulsman, L. M., Hutjes, R. W. A., Jones, S. P., Kers, B. A. M., Komiya, S., Machado, L. A. T., Martins, G., Miller, J. B., Mol, W., van der Molen, M., Moonen, R., Dias-Junior, C., Röckmann, T., Snellen, H., Luijkx, I. T., & Vilà-Guerau de Arellano, J. (2025). *Tracing diurnal variations of atmospheric $CO_2$, $O_2$ and $\delta^{13}CO_2$ over a tropical and a temperate rainforest*. In Geophysical Research Letters. American Geophysical Union (AGU). https://agupubs.onlinelibrary.wiley.com/doi/full/10.1029/2025GL118016

## Abstract

We analyze the diurnal variability of atmospheric $CO_2$, $O_2$ and $\delta^{13}CO_2$ above the canopies of two contrasting ecosystems: the Amazon tropical forest and the Loobos temperate forest. Using a coupled forest-atmosphere model constrained by tower-based and aircraft observations, we quantify the role of atmospheric processes - including entrainment, subsidence, and cloud ventilation - in shaping the amplitude, or diurnal range (DR), of carbon-cycle tracers. Our results show that atmospheric processes can contribute more than twice as much as surface processes to DR. Misrepresenting these influences leads to substantial errors in interpreting observations and modeling tracer variability. We propose using DR as a metric to evaluate atmospheric tracer transport models and to compare site-level measurements. We present a roadmap to identify which atmospheric or surface processes are poorly represented when modeled and observed DR diverge.



## Plain Language Summary

Increasing atmospheric carbon dioxide ($CO_2$) concentrations causes climate change. Atmospheric measurements of $CO_2$ alone lack enough information on the origin of the $CO_2$ signal. Atmospheric carbon tracers can help disentangle the atmospheric $CO_2$ signal into different contributing sources. Here, we focus on the biosphere-atmosphere exchange of $CO_2$ in two contrasting ecosystems: a temperate forest in Europe and a tropical forest in the Amazon. Combining observations and model results, we study the difference between daily maximum and minimum tracer concentrations (diurnal tracer range). Our findings show that for these ecosystems, both surface and atmospheric processes influence the daytime signals of carbon-cycle tracers. Atmospheric processes, such as exchange with higher atmospheric layers and within clouds, are important to consider when analysing daytime signals. Misrepresentations of the interplay of these processes can lead to misrepresenting tracer diurnal variations in models. We recommend using the diurnal range of carbon-cycle tracers to validate models because it integrates surface and atmospheric processes.

## 6.1 Introduction

Advancing our understanding of the terrestrial carbon cycle is critical for reducing uncertainties in the global carbon budget (e.g., Friedlingstein et al., 2024; Piao et al., 2020). Measuring and modeling terrestrial carbon cycle exchange processes is complex due to the integration of multiple processes and scales. Carbon cycle tracers disentangle and quantify these processes. Here, we focus on atmospheric carbon dioxide ($CO_2$), oxygen ($O_2$), and the isotope composition of $CO_2$ ($\delta^{13}CO_2$). The $O_2/CO_2$ exchange ratios and the $\delta^{13}CO_2$ value have been used in previous studies to partition terrestrial carbon cycle processes (Ishidoya et al., 2015; Faassen et al., 2023; Seibt et al., 2008; Wehr et al., 2016).

Understanding the diurnal cycles of carbon cycle tracers is essential to apply partitioning methods (Yi et al., 2004; Kretschmer et al., 2014) and to accurately represent them in high-resolution atmospheric models (Bonan et al., 2024). These diurnal cycles are shaped by both surface and atmospheric processes. For $CO_2$, previous studies (e.g., Denning et al., 1996; Larson & Volkmer, 2008; Pino et al., 2012; Williams et al., 2011; Schuh & Jacobson, 2023) quantified the influence of atmospheric processes (such as entrainment, subsidence, and cloud interactions) on the diurnal variability. Atmospheric tracer transport models and $CO_2$ inversions, as used in, for example, Friedlingstein et al. (2024), typically use only afternoon observations because the models represent these well-mixed conditions better. As models advance toward higher spatiotemporal resolution, resolving atmospheric processes and their interactions becomes increasingly important for capturing sub-diurnal tracer variability. For $O_2$ and $\delta^{13}CO_2$, the influence of atmospheric processes on the diurnal cycles has been acknowledged (Bowling et al., 2005; Faassen et al., 2023), but not yet quantified, due to a lack of observations within and above the boundary layer.



In this paper, we combine observations and conceptual modeling to identify common patterns in the diurnal cycles of $CO_2$, $O_2$, and $\delta^{13}CO_2$ across two contrasting ecosystems. We analyze the simultaneous effects of surface exchange, entrainment, subsidence, and cloud ventilation. We present two comprehensive datasets of atmospheric $CO_2$, $O_2$, and $\delta^{13}CO_2$, along with extensive micrometeorological, radiosonde, and aircraft measurements, for a temperate needle leaf forest (Loobos, The Netherlands; Dolman et al. (2002)) and a tropical forest (Amazon, Brazil; Andreae et al. (2015)). To characterize diurnal variability, we introduce the "Diurnal Range" (DR), defined as the daily amplitude or difference between the daily maximum and minimum value of tracers. We use the coupled Chemistry Land-surface Atmosphere Soil Slab model (CLASS; Vilà-Guerau de Arellano et al., 2015) to identify drivers of DR. DR complements the Diurnal Temperature Range (DTR), which is widely used to assess climate variability and model skill in reproducing diurnal variability (e.g., Qu et al., 2014; Lindvall & Svensson, 2015; Adekanmbi & Sizmur, 2022; Huang et al., 2023). DR also serves as a metric for evaluating modeled diurnal cycles in atmospheric tracer transport models and complements existing metrics like the carbon uptake period (Gonsamo et al., 2012; Kariyathan et al., 2024) and seasonal amplitude (e.g., Piao et al., 2018).

## 6.2 Methods

Our analysis is based on our comprehensive observations from a temperate (Loobos, the Netherlands, 52.1664° N, 5.7436° E) and a tropical (Amazon Tall Tower Observatory: ATTO, Brazil, 2.1819° S, 59.0217° W) forest. Meteorological variables, including radiation, surface energy, $CO_2$ fluxes, and $CO_2$ mole fractions were continuously measured at both sites, on a 36-m tower at the Loobos site (Dolman et al., 2002; Elbers et al., 2011) (https://maq-observations.nl/) and on a 321-m tower at the ATTO site (Andreae et al., 2015; Botía et al., 2022; Vilà-Guerau de Arellano et al., 2024). In 2022, we conducted additional measurement campaigns at both sites, including flask sampling on the towers and vertical profiles of meteorological variables and $CO_2$, from radiosondes and aircraft at different times of the day. At Loobos, additional flasks from aircraft below above the boundary layer height (BLH) were taken (Sect. 6.A.4; Vellinga et al., 2013). At ATTO, additional $\delta^{13}CO_2$ flux measurements were taken (Moonen et al., 2023). Flasks were measured for $CO_2$, $O_2$, and $\delta^{13}CO_2$ (see Sect. 6.A.6 for details). Atmospheric $O_2$ was measured as $\delta(O_2/N_2)$ on the Scripps Institution of Oceanography 2017 scale, and converted to ppm equivalents (ppmEq) (Tohjima et al., 2005; Kozlova & Manning, 2009). $\delta^{13}CO_2$ was measured on the VPDB scale (Coplen, 2011; Wehr et al., 2013). Sect. 6.A.1, 6.A.2 and 6.A.4 provide a complete description of these campaigns. Our two datasets are unique as they simultaneously include observations of carbon cycle tracers, meteorological surface data, and aircraft measurements at different heights for both carbon cycle tracers and meteorological variables above forests ecosystems, including vertical profiles of $CO_2$ flux. As such, they offer a novel opportunity to quantify the interaction between atmospheric and surface processes in relation to the diurnal range (DR).

DR is influenced by both surface and atmospheric processes. Our analysis integrates both, leveraging the uniqueness of our campaigns. Assuming well-mixed conditions and no horizontal advection of the carbon cycle tracers, the atmospheric exchange flux ($F_a$) between the atmospheric boundary layer (ABL) and free troposphere (FT) is given by:

$$F(\phi)_a = F(\phi)_e + F(\phi)_M = -w_e \cdot \Delta_{(ft-bl)\phi} + F(\phi)_M = \\ -\left(\frac{dh}{dt} - w_s\right) \cdot \Delta_{(ft-bl)\phi} + M \cdot (\phi_{cc} - \overline{\phi}(h^+)). \tag{6.1}$$

Here, $\phi$ represents a generic carbon cycle tracer, $F(\phi)_e$ is the entrainment flux, $F(\phi)_M$ is the cloud mass flux, $w_e$ is the entrainment velocity, $\Delta_{(ft-bl)\phi}$ is the "jump" in the mole fractions between FT and ABL, $dh/dt$ is the ABL growth rate, $w_s$ is the subsidence velocity, $M$ is the cloud mass flux, $\phi_{cc}$ is the cloud core mole fraction, and $\overline{\phi}(h^+)$ is the sub-cloud mole fraction. When clouds are absent ($F_M = 0$), the entrainment flux ($F_e$) provides a first estimate of $F_a$ (see Sect. 6.A.4). When shallow-cumulus clouds are present, $F_M \neq 0$ and the clouds enhance the transport between the ABL and cloud layer atop. A full derivation of Eq. 6.1 is provided in Sect. 6.A.7. Vertical profile measurements of carbon cycle tracers and meteorological variables enable the estimation of $F_e$, a proxy of the atmospheric influence. This flux, rarely

measured and often crudely modeled, mixes air from the FT or residual layer into the ABL. The "jump" in the mole fractions between the FT and ABL, $\Delta_{(ft-bl)} = \phi_{ft} - \phi_{bl}$, allows for an estimation of $F_e$ (Tennekes & Driedonks, 1981). Other atmospheric processes, such as the cloud mass flux ($F_M$, note that this does not include rain), subsidence, and horizontal advection, also affect tracer variability but are more difficult to observe.

To study the DR of carbon cycle tracers, we calculate the different components of Eq. 6.1, using the governing equations of the ABL in the CLASS model (van Stratum et al., 2014; Vilà-Guerau de Arellano et al., 2015). CLASS assumes that under convective conditions, meteorological and carbon tracers are well-mixed within the ABL, with constant mole fractions with height (Lilly, 1968; Tennekes, 1973). This assumption holds for $CO_2$, $O_2$, and $\delta^{13}CO_2$ (Vilà-Guerau de Arellano et al., 2019; Faassen et al., 2024), and it reproduces their diurnal variability well across sites, including the Harvard Forest (USA; Vilà-Guerau de Arellano et al., 2019) and Hyytiälä (Finland; Ouwersloot et al., 2012; Faassen et al., 2024). CLASS is thus well-suited to disentangle the processes controlling DR. We performed two case studies: one for Loobos (18 May 2022), featuring subsidence and cold-air advection, and one for ATTO (15 August 2022), with shallow boundary-layer clouds during the dry season. While both case studies show similar DR patterns, distinct atmospheric processes contribute, allowing us to test the processes that determine DR. Model initialization, parameters, and validation are detailed in Sect. 6.A.3.

The diurnal range of carbon cycle tracers is influenced by surface processes ($F_s$), atmospheric contributions ($F_a$, Eq. 6.1), and boundary layer growth. We quantify these contributions using:

$$DR = \overbrace{\int_{t_{min}}^{t_{max}} \frac{F_s(t)}{h(t)} dt}^{\text{Surface contribution}} - \overbrace{\int_{t_{min}}^{t_{max}} \frac{F_a(t)}{h(t)} dt}^{\text{Atmospheric contribution}} \tag{6.2}$$

Where $t_{min}$ and $t_{max}$ are the times of the day with the minimum and maximum tracer mole fraction values, and $h$ is the ABL height. Text S7 includes the derivation of this equation. Additionally, we define $\beta$ to quantify the relative importance of atmospheric processes versus surface processes:

$$\beta = -\frac{F_a}{F_s} \tag{6.3}$$

Previous studies defined $\beta$ as the ratio of $F_e$ and $F_s$ (Vilà-Guerau de Arellano et al., 2004), and here we extend it to include $F_M$. To understand the diurnal variability, $\beta$ is calculated for three periods during daytime based on ABL growth regimes (Martin et al., 1988) (see Sect. 6.A.3). In the first period (P1), the ABL is shallow; in the second period (P2), the ABL grows rapidly due to high surface buoyancy; and in the third period (P3), the ABL reaches its highest altitude and stagnates due to the decrease of the surface buoyancy flux.

## 6.3 Results

### 6.3.1 Diurnal ranges for $CO_2$, $O_2$, and $\delta^{13}CO_2$

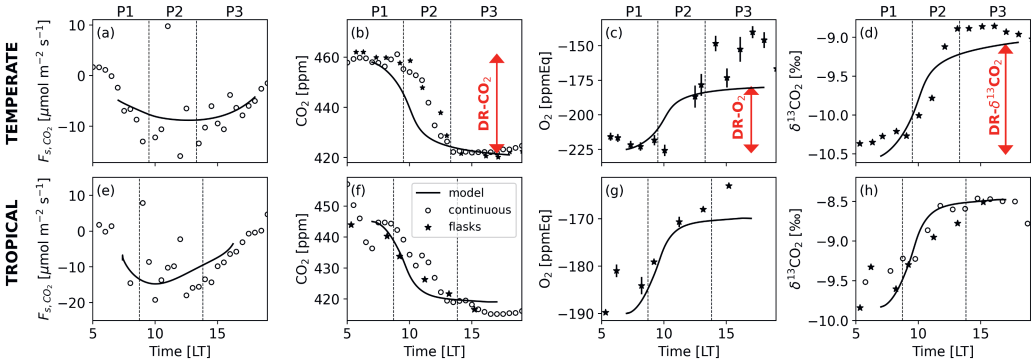



**Figure 6.1:** Observed diurnal cycles of $CO_2$ surface flux ($F_{s,CO_2}$), $CO_2$, $O_2$ and $\delta^{13}CO_2$ for the temperate forest (a-d) and for the tropical forest (e-h) in comparison to Chemistry Land-surface Atmosphere Soil Slab (CLASS) model simulations. The vertical lines indicate the three periods as defined in Sect. 6.2. Measurements were made at 38 m for the temperate forest, and for the tropical forest at: 50 m ($F_{s,CO_2}$), 53 m (continuous $CO_2$), 60 m (flask samples), and 42 m (continuous $\delta^{13}CO_2$). Time is reported as Local Time (LT) (winter time for the temperate forest).

Both flask and continuous observations of $CO_2$, $O_2$, and $\delta^{13}CO_2$ showed similar diurnal variability for the temperate and the tropical site (Fig. 6.1). For all three tracers, the rate of change was highest during P2 and decreased significantly in P3. This behavior cannot be explained by the diurnal pattern of the surface flux alone (Figures 6.1a and 6.1e), which showed the largest negative values during both P2 and P3, showing that DR of the carbon cycle tracers is not only driven by surface exchange, but also by atmospheric processes. The contribution of atmospheric processes of $CO_2$ ($\beta_{co2}$) can directly be quantified with vertical $CO_2$ flux turbulent measurements (Fig. 6.A.5), showing a $\beta_{CO_2}$ for the temperate site of -0.38 at 08:00 LT and 0.05 at 14:00 LT. Unfortunately, these measurements are not available for $O_2$ and $\delta^{13}CO_2$.

In absence of direct observations of $O_2$ and $\delta^{13}CO_2$ atmospheric fluxes, we represent them by combining the observed jumps ($\Delta_{(ft-bl)}$) with the entrainment velocity as defined in Eq. 6.1 (see Sect. 6.A.4 for an elaborate explanation). The satisfactory agreement between our continuous and flask observations of $CO_2$ (Fig. 6.2a and 6.2d) shows that our flask sampling strategy allows for an accurate representation of $\Delta_{(ft-bl)}$. At both sites, we found a decreasing $\Delta_{(ft-bl)}$ throughout the day, indicating a decreasing entrainment flux. The early morning $\Delta_{(ft-bl)}$ of $CO_2$, $O_2$, and $\delta^{13}CO_2$ in the tropical forest was two times smaller compared to the temperate forest, suggesting weaker entrainment in the tropical case compared to the temperate case. The observed $\Delta_{(ft-bl)}$ provides a unique opportunity to prescribe observed FT initial conditions in the CLASS model, enabling accurate reproduction of entrainment

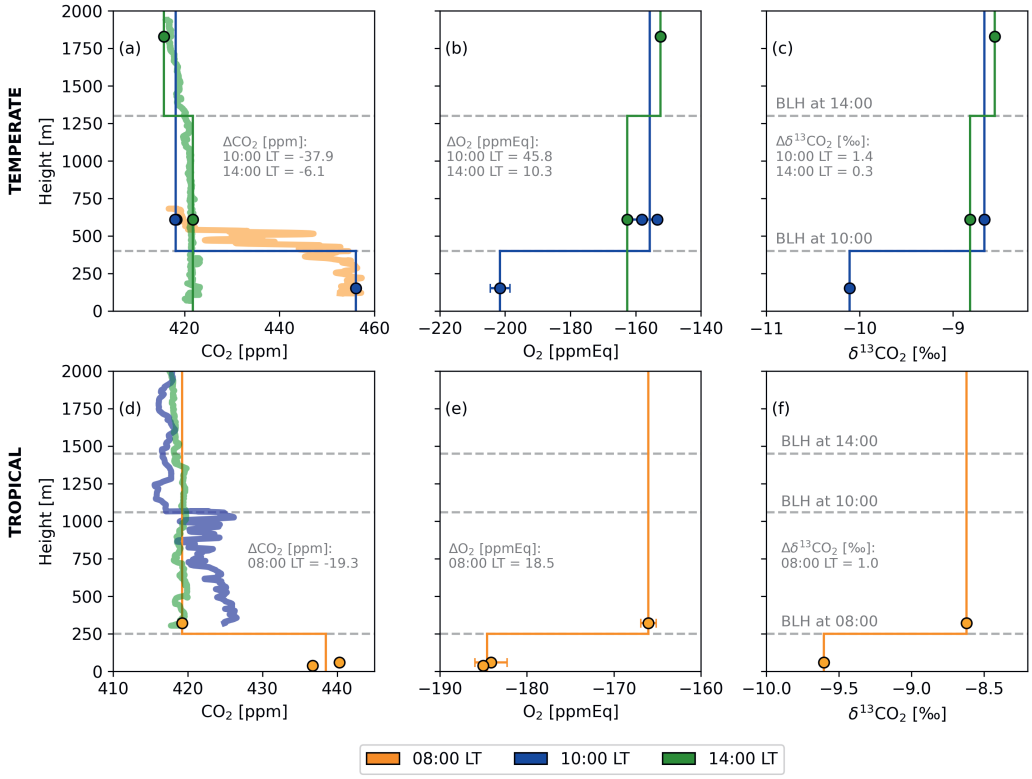



**Figure 6.2:** Observed vertical profiles of $CO_2$ (a, d), $O_2$ (b, e), and $\delta^{13}CO_2$ (c, f) for the temperate and the tropical forest cases at 08:00 LT (orange), 10:00 LT (blue) and 14:00 LT (green). Continuous $CO_2$ measurements from aircraft are shown as bold transparent lines (a, d). Flask measurements are shown as circles, and the flask-derived jump between the free troposphere and the boundary layer values ($\Delta$) is written in grey. The dashed gray horizontal lines show the boundary layer height derived from the radiosondes measurements.

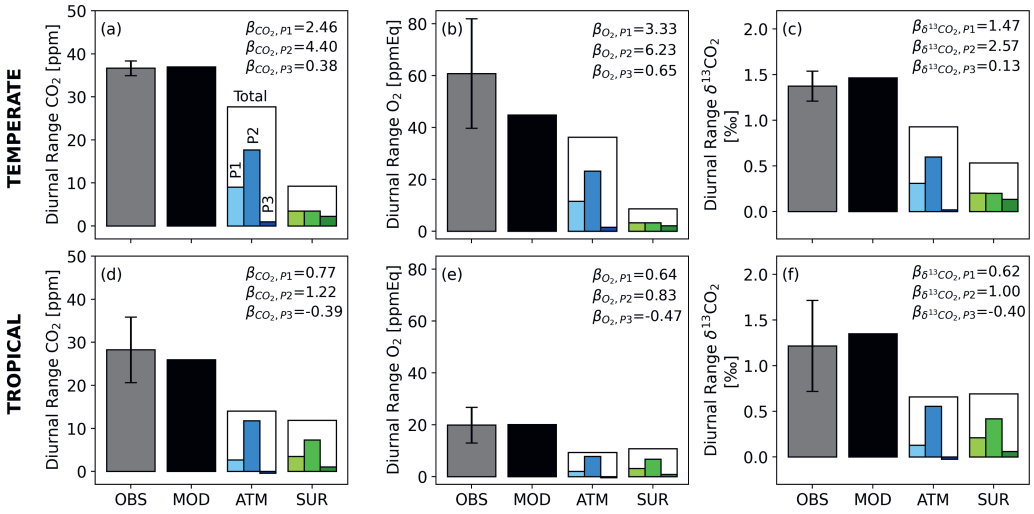



**Figure 6.3:** The diurnal ranges of observed (OBS) and modeled (MOD) $CO_2$ (a, d), $O_2$ (b, e), and $\delta^{13}CO_2$ (c, f); and the respective contributions from atmospheric processes (ATM) and surface processes (SUR) to the modeled diurnal range, for the temperate (a-c) and tropical (d-f) forest cases. The colored bars indicate three periods during the day based on atmospheric boundary layer growth regimes (Fig. 6.1). The contribution of the atmospheric and surface processes to the diurnal range is based on Eq. 6.2. The ratios between the atmospheric and surface processes ($\beta$) are given per period in the upper-right corner of each subfigure.

fluxes, surface fluxes, and DR and the quantification of the contributions of the surface and the atmosphere to the DR for all carbon cycle tracers across both ecosystems (Fig. 6.1). Additionally, we were also able to validate the model entrainment fluxes and $\beta$ values (Fig. 6.A.4 and Sect. 6.A.4).

Our modeled results shows that atmospheric processes significantly contributed to the DR of carbon cycle tracers at both sites, with $\beta$ values exceeding 1 (Fig. 6.3), particularly for the temperate forest. The $\beta$ values followed a similar diurnal pattern for each tracer, with the strongest atmospheric influence in P1 and P2, where $\beta_{P1}$ and $\beta_{P2}$ ranged from 1.47 to 6.23 for the temperate forest and from 0.62 to 1.22 for the tropical forest. In P3, the $\beta$ values decreased below 0.65 at both locations, indicating that the surface processes had a larger impact on the rate of change of the tracers than the atmospheric processes. In contrast to the $\beta$ values for the carbon cycle tracers, $\beta$ values for temperature and specific humidity were overall much lower (Fig. 6.A.9).

Variations in the morning jumps, controlled by the surface exchange during the night, caused differences in the contributions of atmospheric processes between the tropical and temperate forest site and between the individual carbon cycle tracers. As shown in Eq. 6.1, the atmospheric processes depend on several factors (including entrainment, subsidence, and cloud ventilation). We focus on the components that form the entrainment flux $F_e$ (see Eq. (6.A.6))

in Eq. 6.1 to explain the difference in atmospheric influence between the two sites. While the entrainment velocities ($w_e$) were similar between the two locations (Fig. 6.A.3), the jumps differed significantly (Fig. 6.2), with smaller jumps for the tropical case (Fig. 6.2). This resulted in a less dominant entrainment flux in the tropical forest, shown by lower $\beta$ and smaller DR values compared to the temperate forest (Fig. 6.1).

The dominance of atmospheric processes also varied between carbon cycle tracers. For the temperate forest, $\beta$ values differed widely per period, with the highest values found for $O_2$ (P1: 3.33, P2: 6.23, P3: 0.65) and the lowest for $\delta^{13}CO_2$ (P1: 1.47, P2: 2.57, P3: 0.13). The $\delta^{13}CO_2$ jump was relatively small, while the $O_2$ jump was relatively large compared to their total abundance (Fig. 6.1), leading to different entrainment fluxes. The observed jumps, and therefore the entrainment flux, cannot explain all the behavior in the $\beta$ values because other atmospheric processes are also involved (Eq. (6.1)).

Depending on the case and time of the day, different atmospheric processes, ranging from entrainment to subsidence and cloud ventilation, contributed to $F_a$ shown in Fig. 6.3. Boundary layer growth had the largest influence on the atmospheric processes and DR for both cases (Fig. 6.A.8). At the temperate forest site, the subsidence velocity was significant, due to the influence of a high-pressure system during the campaign. The subsidence velocity limited boundary layer growth but increased entrainment velocity (Eq. (6.A.9)). The influence of subsidence on DR was of similar magnitude as the surface flux. For the tropical forest case, cloud ventilation was significant because boundary layer clouds were formed in the morning and persisted into the late afternoon. Cloud ventilation transports air out of the well-mixed boundary layer, limiting ABL growth but adding an extra ventilation flux for the carbon cycle tracers (Eq. (6.A.3) and (6.A.9)) (van Stratum et al., 2014; Vilà-Guerau de Arellano et al., 2020). Cloud ventilation was especially important during P2, becoming as important as boundary layer dynamics during this period.



### 6.3.2 Impact of large-scale forcings on the diurnal range

The diurnal range is a result of the combination of surface, boundary layer, synoptic, and cloud processes (Fig. 6.4a). These processes should be calculated simultaneously to understand the coupling between the ABL and the synoptic processes, and their combined effect on the DR and $\beta$. We analyzed the influence of high-pressure systems on DR as a representative example of typical synoptic events (see Sect. 6.A.5). This enables us to understand the coupling between high pressure systems and DR. High pressure systems are characterized by high values of (a) the divergence of the mean wind (DivU), resulting in a high subsidence velocity, also called vertical advection (Williams et al., 2011), ($w_s$, Eq. (6.A.10)); and (2) the potential temperature lapse rate ($\gamma_\theta$), which quantifies the FT stability (Pino et al., 2012).

$\gamma_\theta$ and $w_s$ independently affect DR and $\beta$ throughout the day (Fig. 6.4 for $CO_2$ and Fig. 6.A.7 for $O_2$ and $\delta^{13}CO_2$). Larger values of $\gamma_\theta$ (orange colors) lead to reduced boundary layer growth (Fig. 6.4b) and entrainment velocity ($w_e$, Fig. 6.4d), and, as a result, decreased both DR (Fig. 6.4e) and $\beta$ (Fig. 6.4g). In turn, higher values of $w_s$ (black colors) also limited

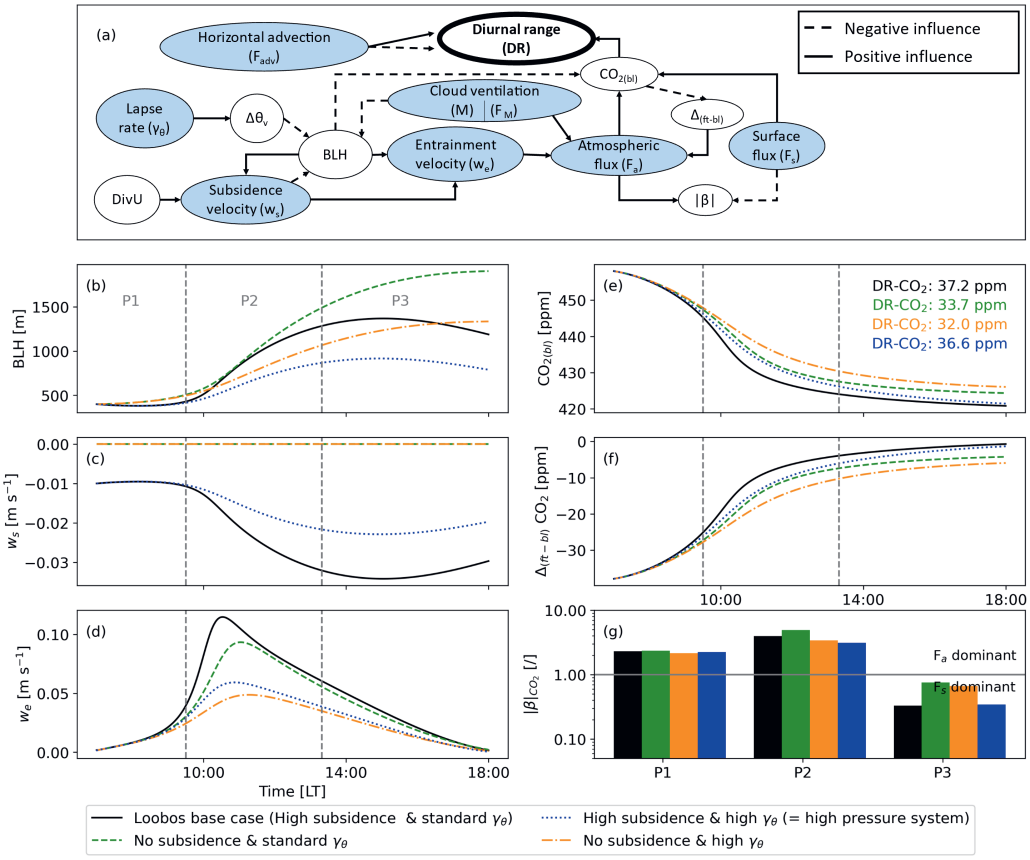



**Figure 6.4:** Schematic overview of the cause-effect relationships influencing the diurnal range (DR) for $CO_2$ (a), and results of our sensitivity analysis for the temperate forest case (b-g). Four model runs were included with either high or no subsidence (through high or null horizontal wind divergence, DivU), and high or standard lapse rate ($\gamma_\theta$, related to the free troposphere stability). Results are shown for the boundary layer height (b), the subsidence velocity ($w_s$) (c), the entrainment velocity ($w_e$) (d), the boundary layer mole fraction ($CO_2(bl)$) (e), the jump ($\Delta_{(bl-ft)}$) (f), and $\beta$ (the ratio between the atmospheric flux ($F_a$) and the surface flux ($F_s$)) (g).

boundary layer growth but increased $w_e$ (Eq. 6.1). The increased $w_e$ caused a high DR and therefore a low jump ($\Delta_{(ft-bl)}$, Fig. 6.4f), resulting in a decreased $\beta$. In situations characterized by high pressure systems, such as heatwaves, high values for both $\gamma_\theta$ and $w_s$ (blue colors) increased DR because of an extremely shallow boundary layer height (Fig. 6.4b). The $\beta$ decreased because of a low $w_e$ (Fig. 6.4d) and a low $\Delta_{(ft-bl)}$ (Fig. 6.4f). In turn, cloud ventilation, which occurred in the tropical forest case, would also increase DR and decrease $\beta$, because it has the same feedbacks as subsidence (Fig. 6.4a). Our analysis shows that atmospheric processes (entrainment, subsidence and cloud ventilation) highly influence DR. Fig. 6.4a shows the interrelations of surface and atmospheric processes controlling DR.

## 6.4 Discussion

We propose using DR of carbon cycle tracers ($CO_2$, $O_2$, and $\delta^{13}CO_2$), similar to the widely-used DTR, as a metric to evaluate atmospheric tracer transport models and analyze observations, as it integrates surface and atmospheric processes. DR of carbon cycle tracers is more complex to interpret compared to DTR due to individual exchange processes associated to each tracer, but it still is a valuable constraint for observations and models because of the simplicity of its calculation. When models fail to capture DR, the next step is to identify processes that are misrepresented by the model. We recommend to first evaluate the surface fluxes, and when these are in agreement between model and observations, the atmospheric processes can be analyzed using Fig. 6.4a as a road map to determine which processes should be improved. In a similar way, Fig. 6.4a can be used to interpret DR from observations.



As models advance to finer spatial and temporal resolutions like those in the 6th Coupled Model Intercomparison Project (Park et al., 2021; Martín-Gómez et al., 2023), it becomes increasingly important to capture DR correctly. This is especially true for carbon cycle tracers because they show higher $\beta$ values and variability compared to meteorological variables, revealing the significantly larger role of atmospheric processes on their DR, which was also found in previous studies (Davis et al., 1997; Vilà-Guerau de Arellano et al., 2004; Gibert et al., 2007; Casso-Torralba et al., 2008). Thus, adding DR of individual carbon cycle tracers as an additional metric to validate atmospheric tracer transport models would be highly beneficial.

Given the short duration of our campaigns, our ecosystem specific findings cannot be generalized for diurnal variability or differences between ecosystems, because surface dynamics and vertical profiles of the carbon cycle tracers vary daily (Ouwersloot et al., 2013). Further research should explore the drivers of DR between ecosystems and over time, by investigating DR variations from weekly to seasonal and yearly trends (Graven et al., 2013). Additionally, the effect of rain (Machado et al., 2024) and horizontal advection of and carbon cycle tracers on the DR should be further explored. To establish DR as a reliable metric, high-quality surface and upper-atmospheric observations are essential, and long term DR measurements are needed to detect trends.

Our unique data set is a clear example of which observations are essential to analyze DR. The observations presented in this study made it possible to introduce DR as a metric and to quantify the atmospheric and surface contributions to DR of carbon cycle tracers. Especially the addition of vertical atmospheric measurements from (tall) towers, radiosondes, and aircraft for different carbon cycle tracers at the same time was unique in our campaign. Additional observations would have further strengthened our campaigns, including surface flux measurements for all the tracers ($O_2$ in both locations and $\delta^{13}CO_2$ in the temperate forest), and vertical flux profile measurements during P2 to capture the high entrainment fluxes and subsequently the $\beta$ values. Furthermore, a better location-specific representation of the exchange ratio for $O_2$ and the process-specific fractionation coefficients for $\delta^{13}CO_2$ would have better constrained the surface processes (Ishidoya et al., 2015; Wehr et al., 2016). Consequently, we call for more of these comprehensive campaigns that also have the ability to measure long-term. We advocate for more experimental "super sites" with measurements at various heights, including upper atmospheric measurements from tall towers or aircraft. These super sites significantly enhance future research on vegetation dynamics in a changing climate (Yi et al., 2004; Bonan et al., 2021, 2024).

## 6.5 Conclusion

For a tropical (dry season) and a temperate forest (summer), we show the need to simultaneously resolve atmospheric processes – such as entrainment, subsidence, and cloud ventilation – and surface processes to understand the diurnal range of carbon cycle tracers (DR). We combined unique observations with a coupled forest-atmosphere model to reproduce and interpret the $CO_2$, $O_2$, and $\delta^{13}CO_2$ diurnal variability. Using aircraft, radiosonde, and above-canopy tower measurements, we quantify the ratio of atmospheric processes to surface processes ($\beta$) for both ecosystems. Atmospheric processes significantly influence the diurnal patterns of carbon cycle tracers. The dominance of the atmospheric processes varies throughout the day, with maximum $\beta$ values above 1 for $CO_2$ (4.40), $O_2$ (6.23), and $\delta^{13}CO_2$ (2.57) during the morning transition periods. The high $\beta$ values show the need to represent and integrate both atmospheric processes and surface processes when analyzing carbon cycle tracers. In particular, subsidence and cloud ventilation are key to interpret DR changes. Finally, we propose the DR, which is easy to measure, as a metric to validate how well (large-scale) atmospheric models represent the combination of surface and atmospheric processes.

# 6.A Supplementary Information for Chapter 6

This supplementary information includes further information on the measurement campaigns (Sect. 6.A.1 and 6.A.2), the initial and boundary conditions of the model setup and validation (Sect. 6.A.3), the vertical $CO_2$ profiles and the observation-based entrainment flux (Sect. 6.A.4), the sensitivity analyses (Sect. 6.A.5), the definition of $O_2$ and $\delta^{13}CO_2$ (Sect. 6.A.6), and the mixed layer equations (Sect. 6.A.7). The Fig. 6.A.1 to 6.A.4 and the Tables 6.A.1 to 6.A.4 support and complete the study. With this appendix, we ensure reproducibility of our observational and modeling findings.

### 6.A.1 Loobos: site and field campaign

Loobos is an ecosystem measurement site located in the Veluwe natural area in the center of the Netherlands (52.1664° N, 5.7436° E, 33 m AMSL). The site is dominated by Scotts pine (*Pinus sylvestris*) with an understory of Black Cherry (*Prunus serotina*) on podzol on fine sandy soil. The ground water level is 3-6 m below ground level. The trees are 20-22 m tall. The measurements in our campaign were done in a 36 m tall tower. In May 2023, the site was given the official ICOS Class 2 Ecosystem Site label (`https://meta.icos-cp.eu/resources/stations/ES_NL-Loo`).

During our campaign in May 2022 (May 17 and 18), the eddy covariance measurements were already compliant with the ICOS ETC guidelines, using a Gill HS-50 sonic anemometer and a LI-7200 closed path $CO_2$ and $H_2O$ analyzer installed at 38.2 m, which is 2.2 m above the highest platform of the tower. The raw data were collected at 20 Hz by a Licor Smartflux-2 system. Table 6.A.1 shows the extra measurements that were performed during the field campaign. Quality control of the eddy covariance measurements was applied using the EddyPro software (Biosciences L, 2019) and the data with quality flag "2" were excluded. To maintain methodological consistency across all carbon cycle tracers, we chose not to apply air storage corrections to the eddy covariance data, because such corrections could not be applied to $O_2$ and $\delta^{13}CO_2$.



**Table 6.A.1:** Additional variables measured during the temperate forest campaign in May 17 and 18, 2022 next to the existing routine measurements.

| Measurement technique | Variables measured | Frequency | Heights |
|---|---|---|---|
| Soundings | temperature, relative humidity, pressure | Hourly | 0 to ∼14000 m |
| Vertical profiles airplane | temperature, $CO_2$, relative humidity, pressure | 10:00 LT and 14:00 LT | 0 to ∼6000 m |
| Flux measurements airplane | SH, $\overline{(w'CO_2')}$ | 10:00 LT and 14:00 LT | 0 to ∼6000 m |
| Flask measurements airplane | $CO_2$, $O_2$, $\delta^{13}CO_2$ | 10:00 LT and 14:00 LT | below + above the boundary layer height |
| Flask measurements tower | $CO_2$, $O_2$, $\delta^{13}CO_2$ | Hourly | 38 m |

**Table 6.A.2:** Variables measured during the CloudRoots-Amazon22 campaign in addition to the routine measurements collected at the measurement site ATTO that were used in this study. For a complete overview, see Vilà-Guerau de Arellano et al. (2024).

| Measurement technique | Variables measured | Frequency | Heights |
|---|---|---|---|
| Soundings | temperature, relative humidity, pressure | Every three hours | 0 to ∼14000 m |
| Vertical profiles airplane | temperature, $CO_2$, relative humidity, pressure | 10:00 LT and 14:00 LT | 0 to ∼6000 m |
| Flask measurements tower | $CO_2$, $O_2$, $\delta^{13}CO_2$ | Hourly | 60 m |

### 6.A.2 CloudRoots-Amazon22: site and field campaign

The campaign in the Amazon (CloudRoots-Amazon22) was conducted from 8 to 21 August 2022. This campaign has been described in Chapter 3 and in Vilà-Guerau de Arellano et al. (2024). It took place in the Amazon Tall Tower Observatory (ATTO; 2.1819° S, 59.0217° W). This site is located in a "terra firme" rainforest, with a mean tree height of 20.7  0.4 m, but with the tallest trees reach up to 36-40 m.

Our observational strategy during the campaign aimed to extend and complete the comprehensive measurements taken routinely at ATTO. In short, there are three tall towers at ATTO: the ATTO tower (323 m), the Triangle tower (81 m) and the INSTANT tower (80 m) at which profiles of key atmospheric state variables (e.g., wind, temperature, and specific humidity) and their turbulent fluxes are continuously measured (Andreae et al., 2015). Shortwave and longwave radiation was measured at 75 m and photosynthetic active radiation (PAR) is measured within and above the canopy (at the INSTANT tower). Turbulent fluxes were measured using an eddy covariance system, and the fluxes were integrated to 30-min averages. To quantify changes in the state variables between the canopy, the sub-cloud layer, the cloud layer, and the free troposphere, we launched balloon soundings with high temporal frequency (every three hours) over the course of the campaign. On August 18, we extended these measurements by additional aircraft measurements of vertical profiles (up to 5000 m) and of horizontal spatial distribution of atmospheric composition ($H_2O$, $CO_2$, CO, $CH_4$) observations during the morning (09-11 LT) and afternoon (13-15 LT), respectively. The aircraft flew in a horizontal grid around the ATTO facility at constant height. Both in the morning and afternoon flights, we selected three representative heights in the sub-cloud layer, the cloud layer, and the free troposphere, and integrated the measurements at constant heights for long, horizontal paths ($\approx$ 20 km). Table 6.A.2 shows more details on the extra measurements that were done during the campaign days.

During the ATTO campaign, the weather was characterized by clear skies during the morning that transitioned to cloudy skies during the afternoon, which on siz days were categorized as shallow-cumulus. Complete information of the continuous measurements, the field campaign, and its main goals can be found in Vilà-Guerau de Arellano et al. (2024).

### 6.A.3 Model setup and validation

The initial settings and parameters of the numerical experiments for the Loobos and Amazon cases are shown in Tables 6.A.3 and 6.A.4. Table 6.A.3 describes the initial vertical profiles of temperature, specific humidity, wind, carbon cycle tracers ($CO_2$,$O_2$ and $\delta^{13}CO_2$), as well as the boundary conditions of the free troposphere. The initial vertical profiles are based on a combination of radiosonde, flasks and continuous tower measurements. Advection of colder air and subsidence at Loobos were estimated by downscaling ERA5 data with a doubly-periodic large eddy simulation following van Stratum et al. (2014) (Fig. 6.A.1). Advection of colder air and divergence were assumed constant during the CLASS run with values of -0.5 K $h^{-1}$ and 2.5 $\cdot$ $10^{-5}$ $s^{-1}$ respectively. The divergence is related to the subsidence, see Eq. (6.A.10). For the Amazon case, we assumed no subsidence, but instead we included the effect of the shallow cumulus clouds. Table 6.A.4 describes the location, initial time and the vegetation and soil parameters. Vegetation and soil parameters are based on (1) prescribed values for the corresponding type of forest (ECMWF, 2014; Vilà-Guerau de Arellano et al., 2015), (2) previous observations at the sites, or (3) leaf gas exchange observations acquired during the campaigns.

An elaborate comparison between the model results and observations for both locations is shown in Fig. 6.A.2. The diurnal cycle of the surface fluxes, potential temperature, and specific humidity compare well to the observations for both locations. The surface flux of $\delta^{13}CO_2$ was measured during the Amazon campaign (Fig. 6.A.2j) (Moonen et al., 2023). The comparison between the modeled and observed $\delta^{13}CO_2$ surface flux suggests that the CLASS model can reproduce the processes behind the DR of $\delta^{13}CO_2$ well. Unfortunately, no $O_2$ gradient or surface flux measurements were done, and therefore we could not validate the $O_2$ surface flux for these cases. However, Faassen et al. (2024) already showed that CLASS is able to reproduce satisfactorily the processes behind the DR of $O_2$ for boral forest located in Finland.

Three periods (P1, P2, P3) were determined based on the growth of the boundary layer height (Fig. 6.A.3). We defined the periods based on whether the boundary layer growth is faster or slower than a threshold (100 m $h^{-1}$). P1 corresponds to the beginning of the day when the ABL grows slowly and the vegetation slowly starts to take up $CO_2$. In our classification, we define this period from the beginning of the day until the moment when the ABL starts growing at a rate larger than 100 m $h^{-1}$. P2 corresponds to the highest growth of the ABL, this part of the day is associated with high entrainment of air from the free troposphere into the ABL and high surface fluxes. P2 is defined as the period when the growth of the boundary layer exceeds 100 m $h^{-1}$. The last period, P3, occurs when the ABL growth becomes smaller than 100 m $h^{-1}$ again. In this period the ABL stagnates or it starts shrinking. P3 reflects the period when both the entrainment and surface fluxes decrease, while the ABL is still deep. The resulting periods for the temperate forest case are: sunrise - 09:30 LT (P1), 09:30 LT - 13:18 LT (P2), and 13:18 LT - sunset (P3). In turn, the resulting periods for the tropical forest case are: sunrise - 08:43 LT (P1), 08:43 LT - 13:50 LT (P2), and 13:50 LT - sunset (P3).

**Table 6.A.3:** Initial and boundary conditions of atmospheric variables, $CO_2$, $O_2$, and $\delta^{13}CO_2$ used to represent the temperate forest case (18 May 2022) and tropical forest case (15 August 2022) numerical experiments in CLASS. The initial conditions are prescribed in CLASS at 06:00 UTC (07:00 local winter time) for the temperate forest case and at 11:00 UTC (07:00 LT) for the tropical forest case. z indicates the height of the modeled variable: in the mixed layer ($h_0 > z > h_c$), or in the free troposphere ($z > h_0$).

| | Loobos | Amazon |
|---|---|---|
| Initial boundary layer height ($h_0$) | 400 m | 385 m |
| Horizontal large scale divergence of wind ($\nabla \cdot U$) | $2.5 \cdot 10^{-5}$ $s^{-1}$ | 0 $s^{-1}$ |
| Entrainment ratio of virtual potential temperature | 0.2 | 0.2 |
| *Potential temperature* | | |
| $h_0 > z > h_c$ | 289.8 K | 301 K |
| $z > h_0$ | 293.1 + $3.5 \cdot 10^{-3}(z - h_0)$ | 301.9 + $3.8 \cdot 10^{-3}$ $(z - h_0)$ K |
| *Specific humidity* | | |
| $h_0 > z > h_c$ | 7.9 $g_w$ $kg_a^{-1}$ | 16 $g_w$ $kg_a^{-1}$ |
| $z > h_0$ | 9.1 - $1.6 \cdot 10^{-3}(z - h_0)$ $g_w$ $kg_a^{-1}$ | 15.2 - $3.3 \cdot 10^{-3}(z - h_0)$ $g_w$ $kg_a^{-1}$ |
| *Zonal wind* | | |
| $h_0 > z > h_c$ | non-applicable | $-1$ |
| $z > h_0$ | non-applicable | $-3.14 - 7.8 \cdot 10^{-4}(z - h_0)$ m $s^{-1}$ |
| *Meridional wind* | | |
| $h_0 > z > h_c$ | non-applicable | $-2$ |
| $z > h_0$ | non-applicable | $-2.85 - 3.0 \cdot 10^{-4}(z - h_0)$ m $s^{-1}$ |
| *Carbon dioxide* | | |
| $h_0 > z > h_c$ | 458.02 ppm | 445.00 ppm |
| $z > h_0$ | 420.12 ppm | 420.72 ppm |
| *Oxygen using* $ER_A = -0.96$ *and* $ER_R = -1.03$[(1)] | | |
| $h_0 > z > h_c$ | $-225$ ppmEq | $-190.00$ ppmEq |
| $z > h_0$ | $-177.8$ ppmEq | $-171.46$ ppmEq |
| $^{13}CO_2$ *using* $R^{13}_{VPDB} = 0.011057$[(2)] | | |
| $h_0 > z > h_c$ | 5.011 ppm, $\delta = -10.53$ ‰ | 4.872 ppm, $\delta = -9.83$ ‰ |
| $z > h_0$ | 4.603 ppm, $\delta = -9.10$ ‰ | 4.612 ppm, $\delta = -8.58$ ‰ |
| *Advection* | | |
| Advection of potential temperature | -0.5 K $h-1$ | 0 K $h^{-1}$ |
| *Shallow cumulus* | | |
| Transition layer thickness ($\Delta z$) | non-applicable | 193 m |
| Cloud cover fraction | non-applicable | 0 |

(1) The oxygen exchange ratios for assimilation ($ER_A$) and respiration ($ER_R$) were derived by Faassen et al. (2023) for Hyytiälä forest

(2) This value is for $CO_2$ = $^{12}CO_2$ + $^{13}CO_2$. The value for $^{12}CO_2$ as basis is $R^{13}_{VPDB}$=0.0111797.

**Table 6.A.4:** Initial and boundary conditions for the vegetation and soil parameters used to represent the temperate forest (18 May 2022) and tropical forest (15 August 2022) numerical experiments in CLASS.

| Variable | Description and units | Loobos | Amazon |
|---|---|---|---|
| *Geographic and time* | | | |
| Lat | Latitude [deg] | 52.17 | -2.14 |
| Lon | Longitude [deg] | 5.74 | -59.00 |
| $f_c$ | Coriolis parameter [$s^{-1}$] | $10^{-4}$ | $-5.5 \cdot 10^{-6}$ |
| DOY | Day of year [-] | 138 | 226 |
| Time | Initial time [h in UTC] | 6 | 11 |
| *Vegetation* | | | |
| $z_{0m}$ | Roughness length for momentum [m] | 2 | 0.5 |
| $z_{0h}$ | Roughness length for heat and moisture [m] | 2 | 0.11 |
| $\alpha$ | Surface albedo [-] | 0.11 | 0.12 |
| LAI | Leaf area index of vegetated surface fraction [-] | 1.5 | 5 |
| $C_{veg}$ | Vegetation cover [-] | 0.75 | 0.9 |
| c3c4 | Plant type [-] | c3 | c3 |
| $c_\beta$ | Curvature plant-water stress factor [-] | 0.25 | 0 |
| $a_d$ | Regression coefficient to calculate $C_{frac}$ [$kPa^{-1}$] | 0.07 | 0.07 |
| $f_0$ | Maximum value of $C_{frac}$ [-] | 0.89 | 0.89 |
| $g_{min}$ | Cuticular (minimum) conductance to water vapor [mm $s^{-1}$] | 0.25 | 0.25 |
| $A_{max,298}$ | $CO_2$ maximal primary productivity at 298 K [mg $CO_2$ $m^2_{leaf}$ $s^{-1}$] | 2.2 | 1.83 |
| $g_{m,298}$ | Mesophyll conductance at 298 K [mm $s^{-1}$] | 3 | 2 |
| $\alpha_0$ | Light use efficiency at low light conditions [mg $J^{-1}$] | 0.017 | 0.017 |
| $\Gamma_{298}$ | $CO_2$ compensation concentration at 298 K [mg $CO_2$ $m^{-2}$] | 82.2 | 82.2 |
| $K_x$ | Extinction coefficient of PAR inside the canopy [$m_{ground}$ $m^{-1}_{leaf}$] | 0.7 | 0.7 |
| $Q_{10,CO2}$ | Temperature response coefficient to calculate $\Gamma$ [-] | 1.5 | 1.5 |
| $Q_{10,gm}$ | Temperature response coefficient to calculate $g_m$ [-] | 2.0 | 2.0 |
| $Q_{10,Ammax}$ | Temperature response coefficient to calculate $A_{mmax}$ [-] | 2.0 | 2.0 |
| $T_{1,gm}$ | Low reference temperature to calculate $g_m$ [K] | 278 | 301 |
| $T_{1,Ammax}$ | Low reference temperature to calculate $A_{mmax}$ [K] | 281 | 281 |
| $T_{2,gm}$ | High reference temperature to calculate $g_m$ [K] | 305 | 301 |
| $T_{2,Ammax}$ | High reference temperature to calculate $A_{mmax}$ [K] | 311 | 311 |
| $W_l$ | Equivalent water layer depth for wet vegetation [m] | 0 | 0 |
| *Soil* | | | |
| $T_S$ | Initial surface temperature [K] | 288 | 299 |
| $T_{soil1}$ | Temperature top soil layer [K] | 286 | 298.6 |
| $T_{soil2}$ | Temperature deeper soil layer [K] | 284 | 298.7 |
| $w_{sat}$ | Saturated volumetric water content [$m^3$ $m^{-3}$] | 0.22 | 0.472 |
| $w_{fc}$ | Volumetric water content field capacity [$m^3$ $m^{-3}$] | 0.17 | 0.4 |
| $w_{wilt}$ | Volumetric water content wilting point [$m^3$ $m^{-3}$] | 0.02 | 0.171 |
| $w_{soil1}$ | Volumetric water content top soil layer [$m^3$ $m^{-3}$] | 0.04 | 0.3 |
| $w_{soil2}$ | Volumetric water content deeper soil layer [$m^3$ $m^{-3}$] | 0.04 | 0.34 |
| a | Clapp and Hornberger retention curve parameter [–] | 0.387 | 0.219 |
| b | Clapp and Hornberger retention curve parameter [–] | 4.05 | 4.9 |
| p | Clapp and Hornberger retention curve parameter [–] | 4 | 4 |
| $CG_{sat}$ | Saturated soil conductivity for heat [K $m^{-2}$ $J^{-1}$] | $3.22 \cdot 10^{-6}$ | $3.56 \cdot 10^{-6}$ |
| $C1_{sat}$ | Coefficient force term moisture [-] | 0.082 | 0.132 |
| $C2_{ref}$ | Coefficient restore term moisture [-] | 3.9 | 1.8 |
| $\Lambda$ | Thermal diffusivity skin layer [W $m^{-2}$ $K^{-1}$] | 20 | 40 |
| $R_{10}$ | Soil respiration at 10°C [mg $CO_2$ $m^{-2}$ $s^{-1}$] | 0.1 | 0.1 |
| $r_{s,soil,min}$ | Minimum resistance soil evaporation [s $m^{-1}$] | 50 | 50 |

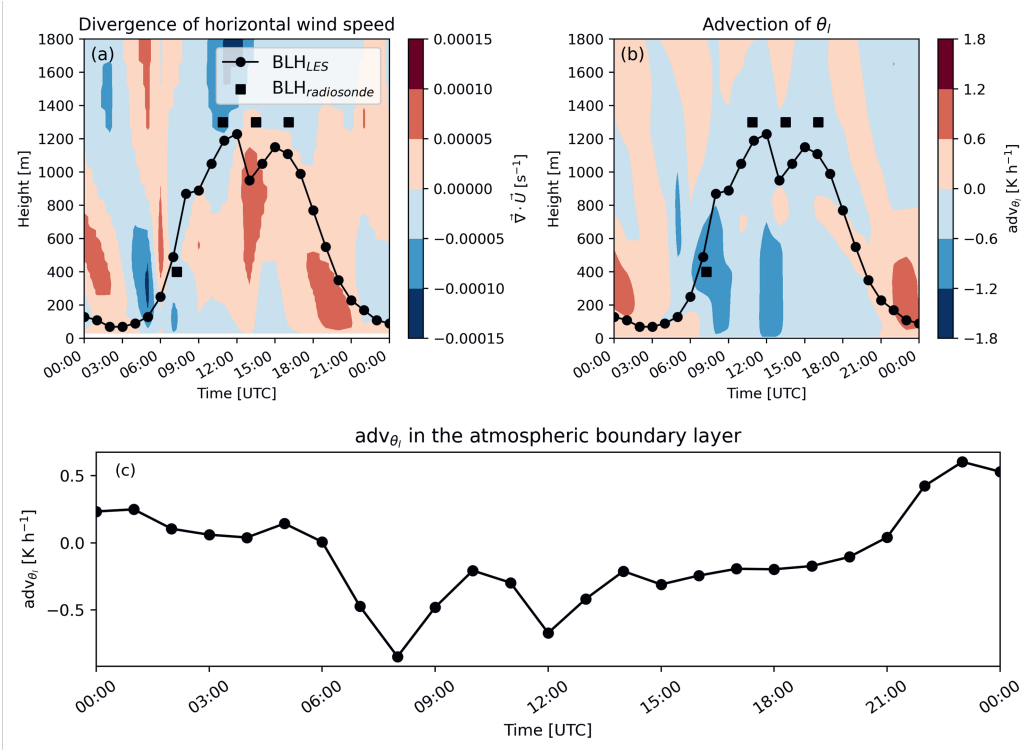



**Figure 6.A.1:** The divergence of wind speed ($\vec{\nabla} \cdot \vec{U}$) (a), and advection of liquid water potential temperature (adv$_{\theta_l}$) (b), per height, and adv$_{\theta_l}$ averaged inside the boundary layer over time (c). The variables correspond to ERA5 data downscaled with a doubly-periodic large eddy simulation following van Stratum et al. (2014) for the temperate forest case. The Boundary Layer Height (BLH) based on the downscaled ERA5 data, and on the observations from the radiosondes is also shown in panels (a) and (b) with dots and squares.

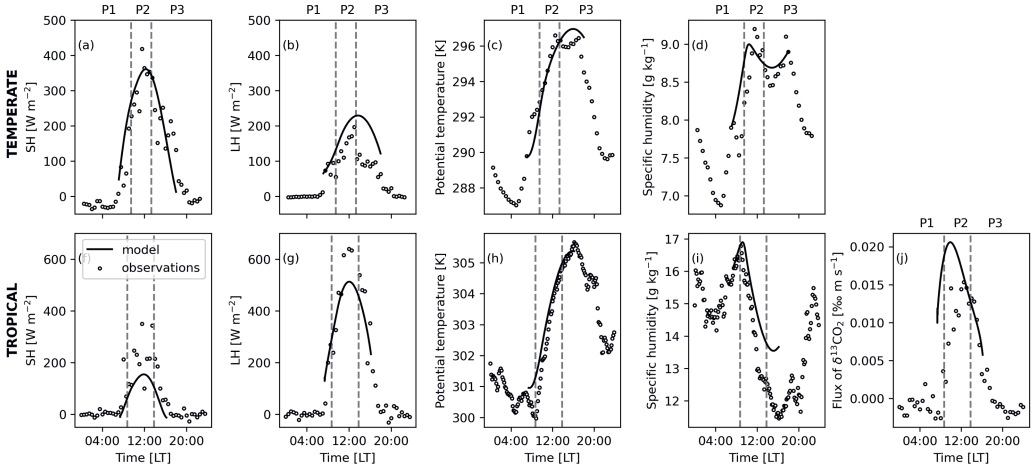



**Figure 6.A.2:** Comparison between the CLASS model output and the observations for the temperate forest case (panels a-d) and for the tropical forest case (panels f-j). The sensible heat flux (SH), latent heat flux (LH), potential temperature and specific humidity are compared for both cases. The surface flux of $\delta^{13}CO_2$ is specifically modeled and compared with observations that were taken for the tropical forest case (j). The periods P1, P2 and P3 are indicated with the vertical dotted lines. All observations of the temperate forest case are made at 38 m. The SH and LH flux of the Amazon case are measured at 81 m, potential temperature and specific humidity are measured at 316 m and the $\delta^{13}CO_2$ flux at 56 m.

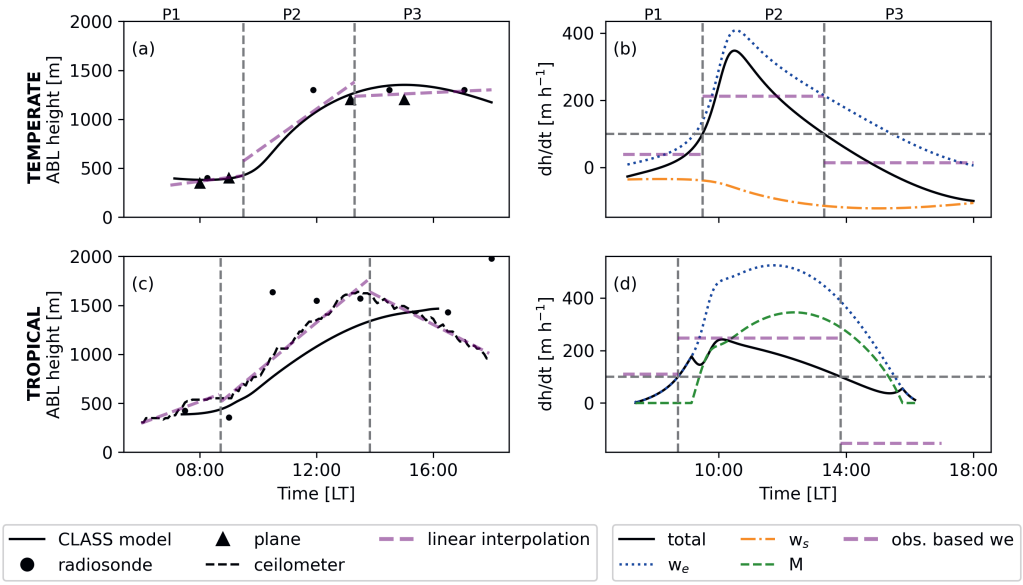



**Figure 6.A.3:** The comparison between the CLASS model output and the observations for the Atmospheric Boundary Layer (ABL) height based on radiosondes, aircraft measurements and ceilometer measurements (left panels), together with the budget components that contribute to the boundary layer height (h) growth (right panels). The purple dotted lines in the left panels indicate the linear regression line through the observations for the three periods (P1, P2 and P3). The purple dotted lines in the right panels indicate the slope of the linear regression line and indicate the entrainment velocity ($w_e$) based on observations. The budget components of the boundary layer growth are: entrainment velocity ($w_e$), subsidence velocity ($w_s$) and the cloud ventilation (M) (see Eq. 6.A.9).

### 6.A.4 Vertical measurements and entrainment calculations

During both campaigns, vertical measurements of meteorological variables and the carbon cycle tracers were simultaneously taken. In this section we explain some of these measurements in more detail and present the method that is used to infer directly and indirectly the entrainment fluxes.

*Vertical continuous $CO_2$ measurements*

Continuous $CO_2$ concentration profiles were measured onboard an aircraft for both the temperate and tropical case (Fig. 2a and 2d). These measurements were obtained with a Li-Cor 7815 closed path trace gas analyser for $CO_2$ and $H_2O$. At both sites, one profile was measured during the morning and one profile was measured in the afternoon.

*Additional temperate forest airplane measurements*

During the temperate forest campaign, the aircraft measured $CO_2$ (and $H_2O$) fluxes with a Li-Cor 7500 open path, high frequency trace gas analyser in combination with a Best Aircraft Turbulence (BAT) probe to measure the high frequency wind (for further details about the instrument see Vellinga et al. (2013)). Covariances between the observed vertical velocity and temperature, moisture or $CO_2$ measured at a 100 HZ rate were integrated over 2 km horizontal windows or roughly 1-min intervals to derive the turbulent fluxes for heat, moisture, and $CO_2$. The plane flew according to two strategies, first vertical profiles were acquired to identify the ABL height. Subsequently, the plane flew in two sets of horizontal laps at different heights within the ABL, one in the morning, and another in the afternoon. In the morning, the plane flew the horizontal laps from 07:00 to 07:41 UTC, at heights of 61 m (200 ft), 152 m (500 ft), and 305 m (1000 ft). In the afternoon, the plane flew from 12:19 to 12:56 UTC at heights of 61 m (200 ft), 152 m (500 ft), 305 m (1000 ft), 607 m (2000 ft) and 1219 m (4000 ft). All horizontal laps were approximately 10 km long and they were made by flying back and forth between [52.20° N, 5.850° E] and [52.11° N, 5.953° E ], producing 11 individual high-frequency meteorological and $CO_2$ flux measurements.

Additionally, air samples were collected from the airplane during the temperate forest campaigns and analyzed for the carbon cycle tracers in the laboratory. These flask measurements were then taken below and above the boundary layer height two times during the day, one in the morning and another in the afternoon.

*Entrainment calculations*

The entrainment flux was directly measured or inferred through indirect methods. For the temperate forest case, we directly estimated the entrainment flux of potential temperature and $CO_2$ using the vertical flux measurements from the aircraft (red crosses in Fig. 6.A.4).

We used these to calculate the horizontal turbulent fluxes at each level, shown in Fig. 6.A.5a. Making use of the assumption that under well-mixed conditions the increase/decrease of turbulent flux of conserved variables is constant with height, the relationship of the horizontally averaged turbulent flux with height was determined using a linear regression, and extrapolated to the estimated BLH to determine the entrainment flux (Vilà-Guerau de Arellano et al., 2004). Only flux measurements made below the BLH were included in this regression.

For the tropical forest case, we did not have flux measurements from aircraft. Therefore, we used the eddy covariance measurements acquired at the ATTO tower to determine the vertical profile of the turbulent fluxes for the Amazon (Fig. 6.A.5b). We calculated the hourly average of the turbulent fluxes at heights of 50 m, 81 m, 196 m, and 316 m during the 6 days that were characterized by shallow convection (Vilà-Guerau de Arellano et al., 2024). We used the measurements between 07:30-08:30, 09:30-10:30 and 13:30-14:30 to determine the average flux for the time periods that are presented in Fig. 6.A.5b. Again a linear regression was used to determine the relationship between the average $CO_2$ flux and height, and to determine the entrainment flux at the BLH.

We also inferred the entrainment flux using flask measurements of the carbon cycle tracers in and above the boundary layer, in combination with the boundary layer height (the triangles in Fig. 6.A.5a and 6.A.5b). The calculation is based on the representation of the entrainment flux as a function of the entrainment velocity ($w_e$), and the jump at the interface between the mixed-layer and the free troposphere (Eq. 6.A.6). We estimated the BLH growth using a linear interpolation of boundary layer height measurements of potential temperature or ceilometer measurements (Fig. 6.A.3). The slope of the linear regression line was assumed to be the entrainment velocity during P1, P2 or P3 (Fig. 6.A.3b and 6.A.3d). Fig. 6.A.3 shows that this approach works well for a first estimate of the entrainment velocity because the modeled and observed $w_e$ are relatively close.

The vertical continuous and flask measurements of $CO_2$, shown in Fig. 6.2a and 6.2d were used to calculate the jump ($\Delta_{(ft-bl)}$). Additionally, vertical continuous measurements from the radiosonde were used to calculate the jump of potential temperature. For the temperate forest case, the values from the free troposphere aircraft flask measurements were used together with the assumption that the lapse rate of the carbon cycle tracers is zero. For the Amazon case only the morning tower flask measurements could be used to get a value for the free troposphere, with the assumption that the highest height is located in the residual layer and the lower heights in the boundary layer. Both the $CO_2$ jump and the observed boundary layer growth are used in Eq. 6.A.6 to calculate the $CO_2$ entrainment flux for both the temperate and tropical forest case.

For potential temperature, the model is able to reproduce the observed entrainment flux and the $\beta$ values well (Fig. 6.A.4a and 6.A.4e). For $CO_2$, we can only validate the modeled entrainment fluxes during the times of the aircraft flights, at two times of the day. No measurements are available at the end of P1 and during P2 when the modeled entrainment fluxes and $\beta$ have the highest values (Fig. 6.A.4b and 6.A.4f). Despite having no observations during P2, we evaluate the entrainment flux during its peak by studying the magnitude and

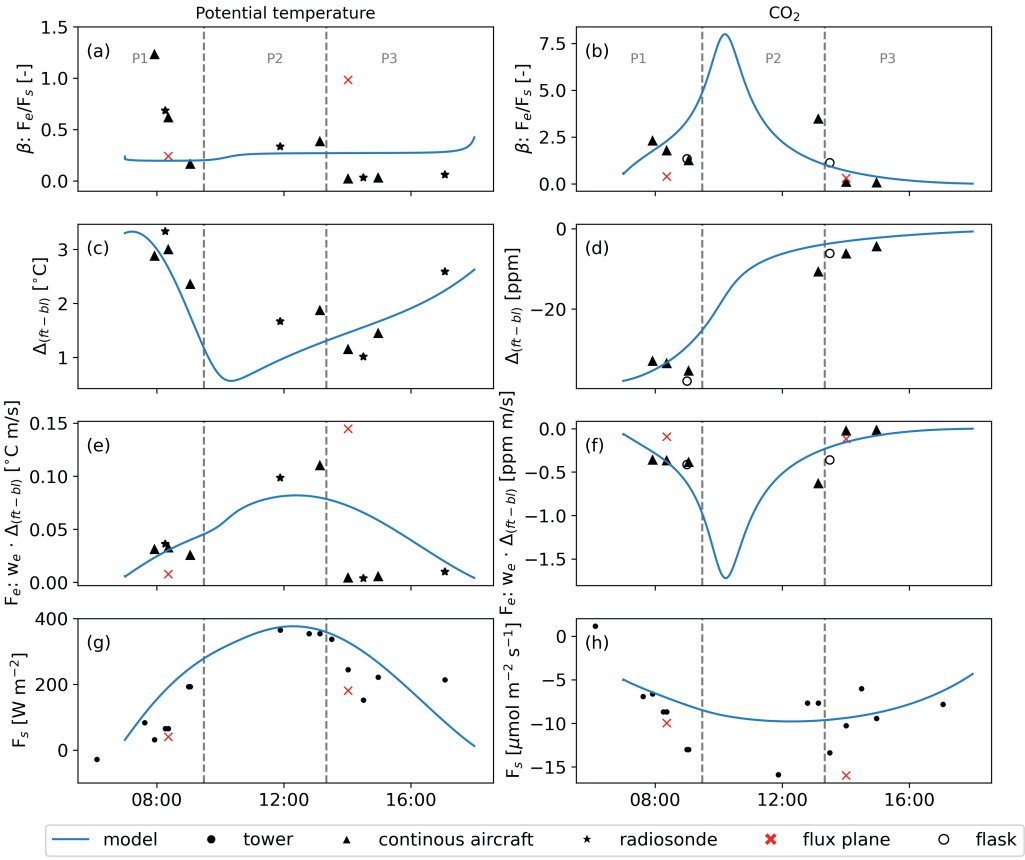



**Figure 6.A.4:** Comparison between the CLASS model and observations of different variables related to the diurnal evolution of potential temperature (left column), and $CO_2$ (right column) for the temperate forest case. These variables include $\beta$, which is the ratio between the entrainment flux and the surface flux (a,b), the jump between the free troposphere and the boundary layer (c,d), the entrainment flux (e,f), and the surface flux (g,h).

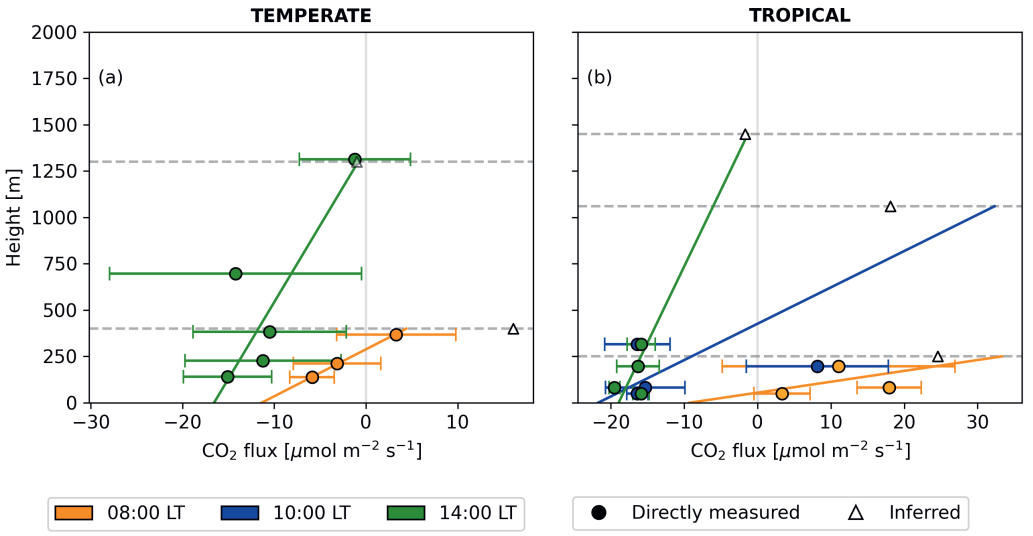



**Figure 6.A.5:** Observed vertical profiles of the $CO_2$ flux observations (circles) and inferred fluxes calculated using observations and Eq. 6.A.6 are indicated with the triangles. The dashed gray horizontal lines show the boundary layer height (BLH) at the measurement times derived from radiosondes

evolution of the $CO_2$ jump at the top pf the boundary layer (Fig. 6.A.4d), which is driven by the boundary layer height and the entrainment velocity (Fig. 6.A.3 and 6.A.4). The model and observations are in agreement in periods P1 and P3 when observations were available. The same strategy can be applied for the boundary layer height. The observed boundary layer height is accurately modeled during P1 and P3. This satisfactory agreement between the $CO_2$ jump and the entrainment shows that the representation of the entrainment fluxes is sufficiently accurate for our purpose of analyzing the magniture and evolution of the diurnal range (DR).

### 6.A.5 DR under different free tropospheric conditions

For the sensitivity analysis of the temperate forest case (Sect. 6.3.2), we changed the model input of the lapse rate of potential temperature ($\gamma_\theta$) and the divergence term (DivU) (Fig. 6.A.6) to understand the influence of a high pressure system. DivU is the horizontal wind divergence, which relates to the subsidence velocity through Eq. 6.A.10. For the sensitivity analysis, we used values of DivU ranging from 0 $s^{-1}$ to $3.15{\cdot}10^{-5}$ $s^{-1}$. We based this range on the study by Williams et al. (2011), the initial value of DivU in Table 6.A.3 and a typical boundary layer height of 1000 m. We used $\gamma_\theta$ values ranging from $10^{-4}$ K $m^{-1}$ (less stable FT) to $10^{-3}$ K $m^{-1}$ (strong stable FT), based on the study by Pino et al. (2012). Fig. 6.A.6 gives the complete overview of the resulting diurnal ranges and the $\beta$ values of P1 and P3 for every combination of the changing values for $\gamma_\theta$ and DivU. The cross indicates the temperate

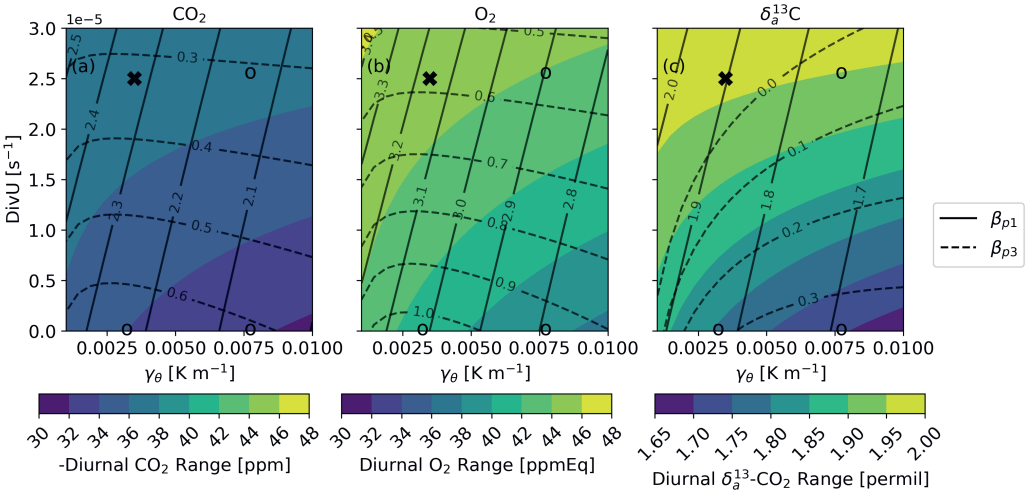



**Figure 6.A.6:** Sensitivity analysis of the diurnal range (colors) of $CO_2$ (a), $O_2$ (b) and $\delta^{13}CO_2$ (c) to the horizontal wind divergence (DivU) and the lapse rate of potential temperature ($\gamma_\theta$). Additionally, $\beta$ values are shown during P1 (continuous lines) and P3 (dashed lines). This sensitivity analysis is based on the temperate forest case, and the cross indicates the default case for the temperate forest (18 May 2022). The circles indicate the sensitivity cases that are shown in Fig. 6.4.

forest case and the circles are the cases that are shown in Fig. 6.4. The $O_2$ and $\delta^{13}CO_2$ results can be found in Fig. 6.A.7.

### 6.A.6 Oxygen and $^{13}$C stable isotope measurements

The flask measurements of $O_2$ are expressed in "per meg" on the Scripps Institution of Oceanography 2017 scale and normally given in $\delta O_2/N_2$, which is defined as:

$$\delta(O_2/N_2) = \left( \frac{(O_2/N_2)_{\text{sample}}}{(O_2/N_2)_{\text{reference}}} - 1 \right) \cdot 10^6 \tag{6.A.1}$$

To directly compare the $O_2$ and $CO_2$ measurements, we converted the $\delta O_2/N_2$ per meg values to ppm equivalents (ppmEq) by multiplying with a conversion factor of 0.20946 (Machta & Hughes, 1970; Kozlova & Manning, 2009). In the main text, we referred to $\delta O_2/N_2$ as $O_2$.

The $\delta^{13}CO_2$ stable isotopes are on the VPDB scale and are expressed in per mil (‰), which is defined as:

$$\delta^{13}CO_2 = \left( \frac{(^{13}CO_2/^{12}CO_2)_{\text{sample}}}{(^{13}CO_2/^{12}CO_2)_{\text{reference}}} - 1 \right) \cdot 10^3 \tag{6.A.2}$$

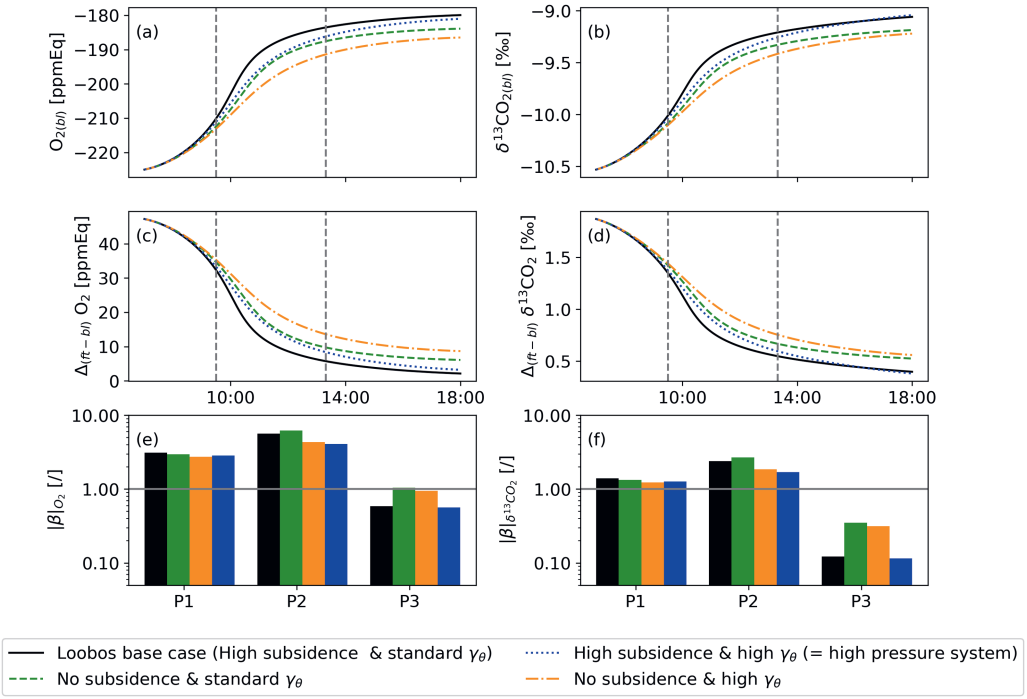



**Figure 6.A.7:** Similar as Fig. 6.4e, 6.4f and 6.4g but now for $O_2$ and $\delta^{13}CO_2$.

Where $^{13}CO_2/^{12}CO_2$ is the ratio of the stable isotopologues $^{13}$C-$CO_2$ to $^{12}$C-$CO_2$.

### 6.A.7 Mixed-layer equations

In the section, we show several governing equations used in the CLASS model (Vilà-Guerau de Arellano et al., 2015). The following equation describes the temporal evolution of a specific scalar ($\phi$):

$$\frac{d\phi}{dt} = \frac{F(\phi)_s - F(\phi)_e - F(\phi)_M}{h} \tag{6.A.3}$$

Where $F(\phi)_s$ is the surface flux, $F(\phi)_e$ is the entrainment flux, which includes the effect of subsidence, $F(\phi)_M$ is the cloud-mass flux that we refer to as the cloud ventilation flux, and h is the boundary layer height. By combining $F(\phi)_e$ and $F(\phi)_M$ into $F(\phi)_a$ and integrating over time between the minimum value of $\phi$ (occurred at $t_{min}$; $\phi_{min} = \phi(t_{min})$) and the maximum value of $\phi$ (occurred at $t_{max}$; $\phi_{max} = \phi(t_{max})$), we obtain:

$$\int_{t_{min}}^{t_{max}} \frac{d\phi}{dt} dt = \int_{t_{min}}^{t_{max}} \frac{F(\phi)_s}{h} dt - \int_{t_{min}}^{t_{max}} \frac{F(\phi)_a}{h} dt \tag{6.A.4}$$

By integrating the change of $\phi$ over time we get the expression for the diurnal range (DR):

$$\int_{t_{min}}^{t_{max}} \frac{d\phi}{dt} dt = \phi(t_{max}) - \phi(t_{min}) = DR \tag{6.A.5}$$

By combing Eq. (6.A.4) and (6.A.5), we obtain Eq. 6.2. The entrainment flux can be written as:

$$F(\phi)_e = -w_e \cdot \Delta_{(ft-bl)}\phi \tag{6.A.6}$$

Where $w_e$ is the entrainment velocity and $\Delta_{(ft-bl)}$ is the jump. The jump is the difference between the free troposphere abundance just above the sub-cloud layer ($\overline{\phi}(h^+)$) and the mixed-layer abundance ($< \phi >$):

$$\Delta_{(ft-bl)}\phi = \overline{\phi}(h^+) - < \phi > \tag{6.A.7}$$

The cloud ventilation flux can be determined with:

$$F(\phi)_M = M \cdot (\phi_{cc} - < \phi >) \tag{6.A.8}$$

Where $M$ is the cloud mass flux in m s$^{-1}$, $\phi_{cc}$ is the mole fraction within the cloud core. The difference between $\phi_{cc}$ and $< \phi >$ is normally represented as a function of the deviation of $\phi$. For more details see van Stratum et al. (2014). Both $M$, $w_e$ and t$w_s$ influence the growth of the boundary layer:

$$\frac{dh}{dt} = w_e + w_s - M \tag{6.A.9}$$

Note that in absence of subsidence and cloud ventilation flux, the entrainment velocity can be calculated with only the boundary layer growth ($\frac{dh}{dt}$). The subsidence velocity is not a constant value but depends on the boundary layer height:

$$w_s = -Div(U_h) \cdot h \tag{6.A.10}$$

Where $Div(U_h)$ is the horizontal wind divergence in s$^{-1}$ and $(U_h)$ is the horizontal mean wind in m s$^{-1}$ at the BLH.

By combining Eq. (6.A.3), (6.A.6), (6.A.7), (6.A.8) and (6.A.9), we obtain the final budget equation of $\phi$ that can be used to disentangle the different processes of the surface, subsidence, boundary layer dynamics and the cloud ventilation. The equation reads:

$$\frac{d\phi}{dt} = \frac{\overbrace{F(\phi)_s}^{\text{Surface}}}{h} - \frac{\overbrace{w_s \cdot \Delta_{(ft-bl)}\phi}^{\text{Subsidence}}}{h} + \frac{\overbrace{dh/dt \cdot \Delta_{(ft-bl)}\phi}^{\text{Boundary layer dynamics}}}{h} - \frac{\overbrace{M \cdot (\phi_{cc} - \overline{\phi}(h^+))}^{Cloud\ ventilation}}{h} \tag{6.A.11}$$

This is a general equation that is valid for any tracers expressed in mole fractions. Fig. 6.A.8 shows the contribution of the terms of the equation for the carbon cycle tracers for the tropical and temperate cases. However, to determine the budget of $\delta^{13}CO_2$, we performed some extra steps because it is a relative quantity which depends on the budget of $CO_2$.

The CLASS model calculates the budget of $^{13}CO_2$ in ppb and the budget of $^{12}CO_2$ in ppm. Observations are normally presented by $\delta^{13}CO_2$ in permil, as a relative value between $^{13}C$ and $^{12}C$. Eq. (6.A.2) is used to convert ppb values to permil by using a constant value for $(^{13}CO_2/^{12}CO_2)_{\text{reference}}$ of 0.011057 (Coplen, 2011; Wehr et al., 2013). To calculate $\delta^{13}CO_2$ from Eq. (6.A.3), the following equation has to be solved:

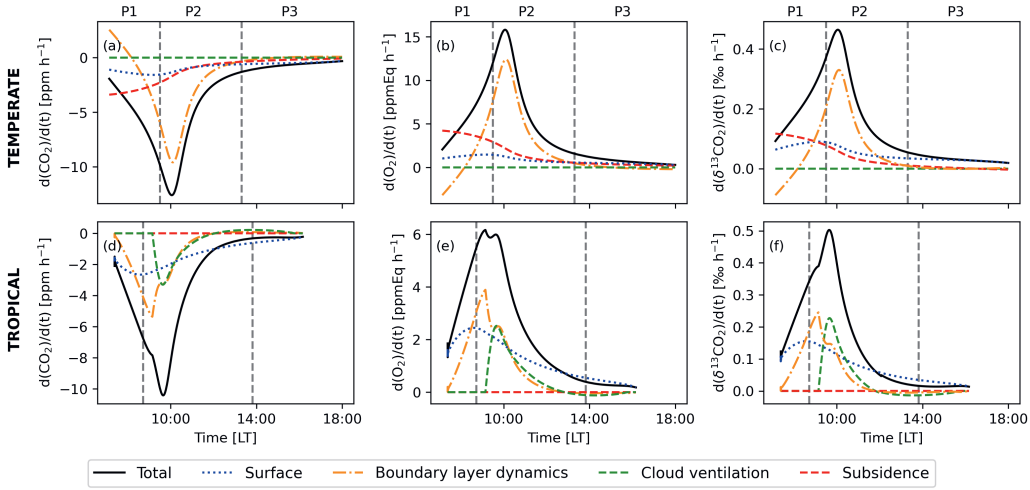



**Figure 6.A.8:** Contribution of the biophysical processes to the diurnal variability of $CO_2$, $O_2$ and $\delta^{13}CO_2$ calculated by the CLASS model for the temperate forest (panels a-c) and the tropical forest (panels d-f) cases. The different budget components are based on Eq. 6.A.11. A more detailed example for $\delta^{13}CO_2$ is given by Eq. 6.A.13.

$$\frac{d(\delta^{13}C)}{d(t)} = \frac{d}{dt}\left(\frac{^{13}C/^{12}C}{R_{ref}} - 1\right) = \frac{1}{R_{ref}}\frac{d}{dt}\left(\frac{^{13}C}{^{12}C}\right) = \frac{1}{R_{ref}}\frac{1}{(^{12}C)^2}\left(^{12}C\frac{d^{13}C}{dt} - ^{13}C\frac{d^{12}C}{dt}\right) \tag{6.A.12}$$

The budget equation for $\delta^{13}C$ can be determined by combining Eq. 6.A.11 and 6.A.12 applied to $^{13}C$ and $^{12}C$. As an example, we provide the surface contribution:

$$\left[\frac{d(\delta^{13}C)}{d(t)}\right]_{surf} = \overbrace{\frac{1}{R_{ref}}\frac{1}{^{12}C}\left(\frac{F(^{13}C)_s}{h} - \frac{^{13}C}{^{12}C}\frac{F(^{12}C)_s}{h}\right)}^{\text{Surface}} \tag{6.A.13}$$

The budget components of the $\delta^{13}C$ tendency for the subsidence, boundary layer dynamics and cloud ventilation can be obtained similarly by combining Eq. 6.A.11 and 6.A.12.

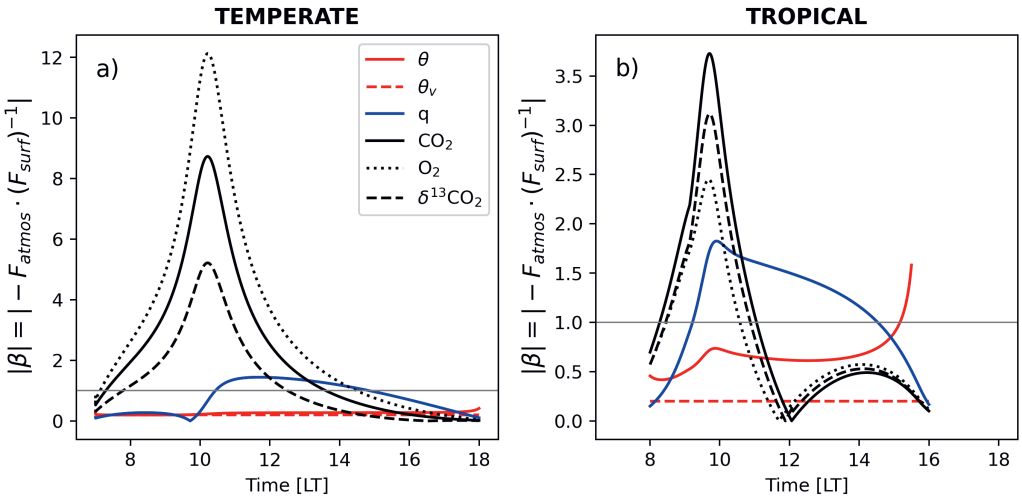



**Figure 6.A.9:** The ratio between the entrainment and the surface flux ($\beta$) over time for different meteorological variables and carbon cycle tracers for the modelled temperate (a) and tropical forest cases (b).

# Chapter 7

# Synthesis

## 7.1 Research outcomes

Throughout this thesis, we have investigated, described and quantified how coupled biophysical and atmospheric processes regulate the interactions between the vegetation and the atmospheric boundary layer over the diurnal cycle, including the effects of shallow-cumulus clouds. To do so, we combined a hierarchy of modeling approaches with comprehensive observational datasets spanning spatial scales from leaf surfaces to ecosystems and the atmospheric boundary layer. This final chapter synthesizes the overarching scientific outcomes of the thesis. In this section, we address the research questions introduced in Sect. 1.4. We then discuss, in Sect. 7.2, broader implications and emerging themes that extend beyond the individual content chapters. Finally, we conclude with key take-home messages that summarize the contributions of the thesis in Sect. 7.3. Below, we summarize the main findings corresponding to the specific research question raised in Sect. 1.4.

*Which environmental factors drive the daytime cycle of transpiration and $CO_2$ assimilation at leaf and canopy level? To what extent?*

In Chapter 2, we showed that the diurnal evolution of stomatal conductance and net $CO_2$ assimilation rate was primarily driven by photosynthetically active radiation (PAR). Air temperature (T) acted as a secondary control on net $CO_2$ assimilation, while both T and vapor pressure deficit (VPD) influenced stomatal conductance. Leaf transpiration responded to PAR, T, and VPD with comparable strength, although PAR dominated during the early morning and late afternoon. In contrast, the temporal variability of the fluxes was only weakly sensitive to changes in atmospheric $CO_2$ mole fractions. Our results also showed that radiative perturbations, such as cloud shading, strongly influence the diurnal evolution of assimilation. These effects occur not only through reduced radiation but also through associated decreases in T.

These findings were obtained for an alfalfa field using a combination of field observations, numerical experiments with a conceptual land-atmosphere model, and a newly developed framework based on tendency equations for the leaf gas exchange. While the quantitative results are site-specific, the methodological framework is transferable and enables detailed analysis of temporal dynamics of surface fluxes at other sites. Importantly, this framework allows us to disentangle direct and indirect effects. For example, cloud shading directly reduces assimilation by lowering incoming radiation, while it can indirectly amplify this reduction through cooling of the surface. Such process-level insights improve the interpretation of temporal dynamics in land-surface schemes and support the development of more realistic surface representations.

*How does canopy microclimate change over canopy depth? How does this vertical variability shape the transpiration and $CO_2$ assimilation rates?*

In Chapter 3, we documented distinctive observed vertical profiles of leaf traits and microclimate for a tropical rainforest. Photosynthetic capacity ($V_{c,\max}$ and $J_{\max}$) increased with canopy height, indicating vertical variation in leaf biochemistry. These gradients likely reflect optimal nitrogen and Rubisco allocation in response to the vertical light environment. The forest microclimate also varied strongly with height. Radiation decreased towards the forest floor, while humidity and $CO_2$ concentrations increased with canopy depth. We observed a persistent within-canopy temperature inversion that limited air mixing between the upper third of the canopy and the lower layers.

Using a three-layer canopy approach constrained by these observations, we found that the ecosystem fluxes of water and $CO_2$ were dominated by the upper third of the canopy, particularly for the $CO_2$ fluxes. Our analysis also highlighted the challenges of interpreting turbulent fluxes during transient atmospheric periods, such as the morning transition, when canopy ventilation, entrainment of tropospheric air, and ecosystem fluxes interact simultaneously.

*How is radiation transferred within canopies? How sensitive is the shortwave radiative transfer to external (atmospheric) and internal (canopy) factors?*

In Chapter 4, we revised and extended the canopy radiative transfer scheme of the canopy-resolving LES can-DALES. The updated scheme simulates both shortwave and longwave radiation, and resolves four shortwave spectral bands - ultraviolet radiation (UV; 280-400 nm), PAR (400-700 nm), far-red radiation (700-750 nm) and near-infrared radiation (NIR; 750-4000 nm) - that are transferred independently through the canopy.

Using this framework, we explored how within-canopy radiation depends on wavelength, external atmospheric forcings, and internal canopy structure. Light extinction with canopy depth was strongest for PAR and UV spectral bands, and weaker for far-red and NIR bands, allowing deeper penetration of the latter spectral bands. External atmospheric factors, such as the solar zenith angle and the direct-to-diffuse radiation ratio, also altered the radiative transfer by shaping canopy reflectance, canopy absorptance, and the distribution of radiation among leaves. Internal canopy factors, including leaf area index and leaf area density, further controlled which canopy layers received most of the incoming radiation.

The updated scheme shows good agreement with observations of shortwave and longwave radiation, PAR, and canopy reflectance acquired in a tropical rainforest, This builds confidence in the ability of can-DALES to represent the canopy radiative environment. Importantly, the inclusion of UV and far-red radiation opens new opportunities to investigate their roles in photosynthesis and surface fluxes. Despite these advancements, a limitation remains: the scheme does not explicitly represent woody biomass and its effects on shortwave and longwave radiative transfer.

*To what extent are turbulent resolving models able to represent the vegetation-air-cloud system? What insights about forest-atmosphere interactions can be gained from them?*

In Chapter 5, we evaluated the ability of the canopy-resolving LES can-DALES, to reproduce land-atmosphere interactions over a tropical rainforest during a day characterized by shallow-cumulus clouds. The model succesfully captured the observed evolution of canopy microclimate, leaf- and ecosystem-scale fluxes, and the development of the atmospheric boundary layer and of the shallow-cumulus clouds. In particular, the simulation reproduced observed $CO_2$ dynamics with high fidelity, owing to its explicit representation of leaf ecophysiology and within-canopy turbulence. The model resolved key processes such as $CO_2$ ventilation events, the storage flux, and the formation of a stable within-canopy air layer that evolved diurnally in response to the canopy radiative transfer.

By realistically representing both the canopy and the boundary-layer clouds, canopy-resolving LES can capture the buffering between radiative-driven ecosystem responses and the surface turbulent forcing (to the atmosphere). This buffering could, in principle, influence the diurnal evolution and properties of shallow cumulus clouds. Although beyond the scope of Chapter 5, canopy-resolving LES enable analysis of three-dimensional airflow fields, offering opportunities to disentangle radiative and turbulent feedbacks between the forest and boundary-layer clouds.

*To what extent do surface and atmospheric processes alter the diurnal evolution of carbon cycle tracers?*

In Chapter 6, we quantified the role of atmospheric processes and surface processes in shaping the diurnal amplitude of three carbon cycle tracers, $CO_2$, $O_2$, and $\delta^{13}CO_2$. We analyzed two contrasting ecosystems: a tropical rainforest in the Amazon (ATTO site, Brazil), and a temperate forest (Loobos site, the Netherlands). The results revealed that atmospheric processes - including entrainment, subsidence, advection, and cloud ventilation - can contribute more than twice as much as the surface processes to the diurnal range. The relative contribution of atmospheric processes and surface processes changed over the course of a day. The contribution of atmospheric processes was largest during the morning and early afternoon (until approximately 13:00-14:00 LT), when the atmospheric boundary layer was experiencing its largest growth. In turn, surface processes became more influential later in the day, when boundary-layer growth slowed and eventually reversed.

The study introduce a metric, the diurnal amplitude range, based on the diurnal maximum and minimum mole fractions of carbon tracers. Because calculating this metric is simple for both Earth system models and observations, this metric can be useful to assess how Earth system models represent the couplings between the vegetation and atmospheric boundary layer dynamics.

## 7.2 General discussion

This dissertation comprises five interconnected studies (Chapters 2, 3, 4, 5, and 6), each with its own results and limitations discussed in the respective chapters. Here, we place these findings in a broader context and outline future research directions. In particular, we identify opportunities to extend this work by addressing its current limitations and to advance the study of vegetation-atmosphere interactions more generally. Where possible, we distinguish between developments that appear achievable in the short term and those that may become feasible over longer timescales.

### 7.2.1 Enhancing the observational coverage

This dissertation combines modeling approaches with observational datasets collected during comprehensive field campaigns. The observational campaigns were conducted at research sites with long-term monitoring of meteorology and atmospheric composition (CloudRoots-Amazon22 at ATTO site, and Loobos field campaign at Loobos site), or as part of a large coordinated initiative that deployed extensive instrumentation for several months (LIAISE field campaign). Together, these efforts integrated measurements of meteorology, atmospheric composition, soil conditions, and surface energy fluxes with additional high frequency radiosonde launches, aircarft observations, and leaf ecophysiological observations. This multi-scale observational strategy provides a detailed description of the soil-vegetation-atmospheric boundary layer system. We consider that dedicated field campaigns at established observational sites are valuable for scientific research, as they generate comprehensive observational datasets that can serve as test beds for evaluating and improving model representations.

Balancing observational representativeness and comprehensiveness with the feasibility and duration of field campaigns remains challenging. This trade-off is particularly evident for leaf ecophysiological measurements, since canopies exhibit biological diversity in leaf traits that we aim to capture, yet measurements are labor intensive and not automatized. In this thesis, we combined measurements of photosynthetic response curves to intercellular $CO_2$ mole fractions and to PAR with stomatal conductance measurements acquired with a LI-6400XT system (reported in Chapter 2 and Chapter 3). The newer LI-6800 portable photosynthesis system (Licor Inc., Lincoln, NA, USA), together with recently developed measurement protocols (Stinziano et al., 2017) can substantially reduce the measurement time. Photosyntetic response curves to incellular $CO_2$ concentrations can now be acquired in approximately 5 min, compared with about 30 min for traditional measurements, as those reported in this dissertation, (Stinziano et al., 2017). This increased efficiency would allow larger leaf sample sizes in field campaigns, improving the representativeness of canopy measurements. The time gained could also enable additional ecophysiological measurements, such as photosynthetic temperature-response curves (Garen & Michaletz, 2024). These measurements are relevant because temperature controls photosynthesis (Chapter 2) yet they are rarely acquired during field campaigns. Furthermore, the reduced measurement noise of the LI-6800 system (Lynch

& Morgan, 2016) improves the reliability of the derived ecophysiological parameters and thus, it can ensure more accurate calibration of leaf gas exchange models.

Increasing sample size is especially important for stomatal conductance, which responds within minutes to changes in radiation, temperature, vapour pressure deficit, and $CO_2$. Complementing portable photosynthesis systems (LI-6400XT or LI-6800) with porometers (e.g. the LI-600) could greatly expand stomatal conductance sampling (LI-COR, 2022). Larger datasets would enable more detailed analyses of stomatal dynamics and their role in land-atmosphere interactions, such as those presented in Chapter 2.

In terms of microclimate, characterizing the within-canopy light environment remains challenging because radiation exhibit strong spatial (horizontal and vertical) heterogeneity. A network of radiometers at the forest floor could help to quantify light transmittance (Parker et al., 2019). In this context, the develpment of low-cost sensors - such as the FROST radiometers used in this thesis (Heusinkveld et al., 2023, Chapter 3) - is particularly valuable, as deploying 10-40 instruments becomes feasible. Ground-based lidar measurements (Parker et al., 2004; Béland & Kobayashi, 2021) can further characterize canopy structure, including leaf area density, outer canopy rugosity, and vertical profiles of foliage clumping, all of which drive spatial variability in radiation. Ideally, these new insights should be combined with multi-layer canopy models capable of representing spatial heterogeneity and its effects on photosynthesis and transpiration (Béland & Baldocchi, 2021).

Beyond radiation, several measurements techniques offer promising opportunities for studying land-atmosphere interactions, in particular when combined with canopy-resolving LES (Chapter 5). Distributed temperature sensing (Van de Giesen et al., 2012), for example, can provide high resolution temperature vertical profiles (from 1.3 mm to 25 cm depending on the setup; ter Horst et al., 2025), with temporal resolution of 5 s and temperature resolution of 0.1 °C. Scintillometers are another valuable addition, enabling turbulent flux estimes at higher temporal resolution ($\approx$ 1 min) than eddy-covariance systems (Hartogensis et al., 2002; Van Kesteren et al., 2013). Such high-frequency flux observations provide insights into vegetation response times to radiative and turbulent atmospheric perturbations (Vilà-Guerau de Arellano et al., 2020), thereby offering observational constraints on the vegetation-atmosphere coupling that can be compared with turbulent-resolving simulations.

Stable isotopologues of water and $CO_2$ provide another useful observational constraint on the vegetation-atmosphere system (Lee et al., 2009; Griffis, 2013). They can track biophysical processes and, as a result, help to partition ecosystem fluxes into the soil and vegetation contributions. Their use at diurnal timescales remains challenging, as it requires measurements of atmospheric isotopic composition, isofluxes, and fractionation coefficients associated to individual processes. Nevertheless, partitioning ecosystem fluxes using isotope measurements is becoming increasingly feasible in dedicated field campaigns that also constrain leaf ecophysiology (Moonen et al., 2025a). This was demonstrated during CloudRoots-Amazon22, where measurements of intercellular and atmospheric $CO_2$ mole fractions were crucial for flux partitioning (Moonen et al., 2025a). This example highlights the value of comprehen-

sive field campaigns for advancing process-level understanding of land-atmosphere interactions.

Vertical profiles of turbulent fluxes obtained from eddy-covariance systems provide another important perspective. While flux measurements acquired at approximately 1.5-3 canopy heights are typically considered most representative of the ecosystem exchange, measurements at additional heights contain valuable information regarding the atmospheric surface layer. In Chapter 5, multiple eddy-covariance systems allowed us to characterize turbulence within and above the canopy. Such measurements are particularly useful for studying the vegetation-atmosphere coupling on diurnal timescales in forest ecosystems.

Overall, we consider that comprehensive datasets from well-established observational sites complemented by dedicated field campaigns enhance our understanding of the land-atmosphere system. They provide test beds for evaluating model representations, and deliver the observational constraints needed to study complex vegetation-atmosphere interactions. Inevitably, however, observational representativeness and comprehensiveness must be balanced against the temporal duration and spatial coverage of measurement strategies - a trade-off addressed in the following section.

### 7.2.2 Extending the temporal scales and spatial scales

This dissertation primarily focused on daytime conditions, when photosynthesis is active and the atmospheric boundary layer is strongly turbulent. However, nighttime conditions are equally important in the study of land-atmosphere interactions. Nighttime ecosystem respiration represent a major component of the terrestrial carbon cycle (e.g., Lavigne et al., 1997), and its accurate representation is essential for predicting how terrestrial ecosystems respond to environmental changes. Additionally, nighttime conditions also set the initial state for the following day, thereby influencing the subsequent daytime evolution of the atmospheric boundary layer, and the clouds development, including the formation of shallow cumulus and the transition to deep convection. At night, the atmospheric boundary layer becomes stable, and shear and longwave cooling govern air movement. These processes strongly influence the coupling between within-canopy and above-canopy air and shape the nocturnal forest microclimate. Turbulent-resolving models, as can-DALES (Chapter 5), offer a promising pathway to better interpret nighttime turbulent flux observations and their links to the ecosystem exchange.



We have performed an initial characterization of the nighttime conditions during CloudRoots-Amazon22 in the work presented by Huitema et al. (2026). This observational study can be complemented by can-DALES simulations of nocturnal dynamics, which could potentially capture the interaction between the longwave radiative cooling and the shear production occurring at the canopy top. Nighttime simulations would also provide a valuable test bed for model development, particularly for the longwave radiative transfer scheme and the future canopy heat storage parameterizations, which play a more prominent role at night than during the day. Achieving a realistic representation of nighttime conditions in canopy-resolving

LES would enable simulations of consecutive days. This capability would open the door to study the influence of multi-day processes on land-atmosphere interactions, including dry spells, day-to-night and night-to-day dynamics, and the impact of shallow convection on the atmospheric state of subsequent days.

Regading spatial scales, our work can be expanded in several directions. Here we highlight two: the inclusion of surface horizontal heterogeneity in canopy structure, topography, and land cover; and the influence of mesoscale and synoptic atmospheric patterns.

In our multi-layer canopy approaches, the canopy has been treated as horizontally homogeneous. Horizontal variability in canopy height, leaf area density, leaf area index, or leaf traits has therefore not been explicitly represented. In Chapter 5, the simulated canopy experienced horizontal variability in the environmental forcing (e.g., radiative and temperature perturbations induced by clouds), but not in canopy structure itself. This approximation yields realistic horizontally averaged turbulent properties and turbulent fluxes for a tropical forest site (Chapter 5), and enables detailed process-level analysis. However, real canopies exhibit horizontal variability in canopy structure (e.g., Parker & Russ, 2004; Parker et al., 2019), which influences both the within-canopy radiative transfer and the turbulent transport.

The radiative effects of canopy spatial heterogeneity can be partly represented through the clumping index, which quantifies foliage aggregation. The clumping index can be quantified at different spatial scales - such as branch and plot level -, and it seems to vary based on environmental conditions (Béland & Baldocchi, 2020) and vertically within the canopy (Béland & Baldocchi, 2021). The can-DALES radiative transfer scheme already includes the clumping factor (Chapter 4), providing a first step towards representing the effects of foliage aggregation on ecosystem exchange.

Horizontal heterogeneity also influences turbulent transport, with both topography and forest patchniess playing important roles (Chen et al., 2019; Bannister et al., 2022). In addition, land cover heterogeneity such as the presence of a river near a forest can cause local circulations which advect air masses with different properties (Ye et al., 2022). Although beyond the scope of this dissertation, these factors likely contribute to discrepancies between observations and results from LES with horizontally homogeneous forest canopies. Bannister et al. (2022) comprises a remarkable recent review on how realistic forests (including patchiness and topography) differ from idealized forests in the forest-atmosphere exchanges. As they point out in their discussion regarding “Future Challenges”, moving beyond idealized horizontally homogeneous forest canopies is challenging and it likely will require interdisciplinary collaboration across scientific disciplines - such as forest ecology, fluid mechanics, plant physiology, meteorology and climatology, and air and water quality -, together with coordinated observational and modeling efforts.

The canopy-resolving LES presented in Chapter 5 can be viewed as an idealized yet comprehensive representation of the soil-canopy-atmosphere system. Despite the horizontally-simplified canopy structure and topography, these canopy-resolving simulations: (1) capture

realistic boundary-layer dynamics, including shallow cumulus cloud fields (Chapter 5); (2) represent dynamic horizontal heterogeneities in environmental forcings; and (3) resolve key biophysical processes. These simulations are valuable for identifying canonical mechanisms of land-atmosphere coupling that can later be tested under spatially heterogeneous canopy configurations, in which the underlying mechanisms may be more difficult to identify.

This thesis, particularly Chapter 5, is at the forefront of simulating the soil-vegetation-atmospheric boundary layer system at diurnal and sub-kilometric spatiotemporal scales. Large-scale atmospheric forcings have been included to some extent through the vertical and horizontal advective terms (Chapter 2 and Chapter 6), but further developments can aid at better representing mesoscale and synoptic influences.

One promising pathway is to embed the LES in limited area mesoscale models, through the use of open boundary conditions and domain nesting (e.g., Liqui Lung et al., 2024). This development allows for realistic large-scale forcings while retaining the high spatial resolution needed to resolve canopy-scale turbulence. Another opportunity is to extend the model hierarchy presented here with mesoscale models that include dynamical vegetation schemes (Agustí-Panareda et al., 2014; Ma & Liu, 2019). These models can accurately capture the non-local atmospheric transport and its influence on local conditions. For example, the European Centre for Medium-Range Weather Forecasts (ECMWF) Integrated Forecasting System (IFS) now includes $CO_2$ surface fluxes and transport while maintaining high skill in simulating synoptic variability (Agustí-Panareda et al., 2014). Although biases in surface $CO_2$ fluxes remain, such models allow the study of diurnal surface fluxes across a wider range of weather conditions than those studied in this thesis.

Finally, we would like to contextualize our temporal conception of land-atmosphere interactions. This thesis has studied them on diurnal scales, where vegetation responds dynamically to environmental conditions but does not acclimate to them. Over longer timescales, vegetation also interacts adaptively with the atmosphere, through changes in leaf traits and canopy architecture. These diverse timescales in land-atmosphere interactions raise a question: *Where do short-term "static" vegetation responses meet the long-term adaptive vegetation responses?* Although this question remains open, it provides a direction to orientate future research by placing the static land-atmosphere interactions studied in this thesis within a seasonal and climatic perspective. Canopy-resolving LES studies could include sensitivity analyses to seasonal changes and climatic scenarios that include both vegetation acclimatation and changing atmospheric conditions. In that way, LES experiments could provide process-based snapshots of the longer-term land-atmosphere interactions while retaining detailed representation of small-scale coupling. Such framework could, for example, help to quantify how shallow cumulus clouds over land respond to warming, rising atmospheric $CO_2$, or changes in plant ecophysiology. Early work in this direction used LES with simplified canopy representations (Sikma et al., 2019); the canopy-resolving LES used in this thesis now enable similar studies with a more realistic representation of within-canopy processes.

### 7.2.3 Developing process representation in land-atmosphere models

In this thesis, we have employed a hierarchy of modeling approaches with diverse degrees of complexity on their treatment of the land-atmosphere system. In terms of the land-surface, we used a big-leaf model approach, a three-layer canopy model, and a multi-layer (three-dimensional) canopy scheme embedded in a LES approach. For the atmosphere, we used a conceptual model based on mixed-layer theory, representative of a column in a classical global Earth system model, and a turbulent-resolving LES model. When modeling the land-atmosphere system, we have attempted to strike a balance between process comprehensiveness and the integration with observations. In doing so, we placed emphasis on important biophysical processes that could be constrained with observational evidence acquired during field campaigns. Inevitably, some processes fell outside the scope of the analyses presented here. In the following paragraphs, we discuss processes that were not studied in this dissertation but that play a role in daytime diurnal dynamics, and their potential future inclusion, particularly in canopy-resolving LES.

As mentioned in the discussion sections of Chapter 4 and Chapter 5, the biomass heat storage flux is non-negligible in forest ecosystems and contributes to the canopy energy balance. It is also recognized as essential when examining the influence of forests on diurnal temperature variations (Meier et al., 2019). In this thesis, we neither included this process in our modeling framework nor quantified it with observations. Therefore, we strongly recommend its inclusion in the next canopy-resolving DALES version. This development should be feasible in the short-term by adapting biomass heat storage implementations from other multi-layer canopy models, such as that reported by Swenson et al. (2019). We expect its inclusion will improve the morning and nighttime boundary layer transitions in can-DALES simulations over forested areas, and it will make nighttime modeling increasingly feasible.

Radiative transfer within canopies is essential to accurately represent water, energy and $CO_2$ fluxes. The canopy-radiative transfer model in can-DALES (Chapter 4) can be considered state of the art among canopy radiative transfer schemes in land-surface models, as it accounts to some extent for three-dimensional vegetation canopy structure (through the clumping index), and resolves four spectral bands in the shortwave range. Future developments could include differentiating between wood and leafy components of canopy biomass, and accounting for their distinct optical properties (Béland, 2025). Additionally, another avenue for development could be to move beyond the primarily one-dimensional radiative transfer and explicitly account for three-dimensional radiative transfer above and within the canopy (Kobayashi et al., 2012; Veerman et al., 2020). Three-dimensional radiative transfer may play a role in vegetation-cloud dynamics by, for example, altering the length scale of thermals and shallow cumulus clouds (Veerman et al., 2020). However, this advancement requires balancing the physical realism gained with the increased computational cost.

A key advantage of canopy-resolving LES, compared to other atmospheric models, is its ability to resolve explicitly part of the turbulence within and above the canopy, enabling realistic three-dimensional distributions of chemical compounds. This capability has applications

for studying atmospheric chemistry over vegetated areas and for investigating stable isotopologues of water and $CO_2$. As mentioned above, measurements of stable isotopologues of water and $CO_2$ allow the quantification of a large uncertainty in Earth system models: the partitioning of ecosystem fluxes into the soil and vegetation contributions. Instrumental developments are making increasingly feasible to measure isofluxes under field conditions, as demonstrated during LIAISE and CloudRoots-Amazon22 field campaigns (Moonen et al., 2023, 2025b). Combining this type of observations with canopy-resolving LES could help to disentangle how isotopic empirical constrains can be used to advance our mechanistic understanding of the ecosystem exchanges.

Regarding atmospheric chemistry, because canopy-resolving LES capture organized canopy-scale turbulent structures and realistic physical separation of chemical reactants, they can be used to study the influence of turbulence on in-canopy chemical loss and dry deposition (Clifton et al., 2022). Including chemical reactions in can-DALES is feasible in the near future and would require adapting the current chemistry module in the DALES framework (Heus et al., 2010; Ouwersloot et al., 2011) to account for deposition rates and emission sources across canopy layers. Representing secondary aerosol formation in canopy-resolving LES also paves the way to study how particles emitted by forests contribute to cloud formation trough their role as cloud condensation nuclei (Durand et al., 2026). In this way, the methodological framework could be extended to include vegetation-cloud interactions related to the cloud microphysics.

In this thesis, we studied vegetation-atmosphere interactions in clear and cloudy skies. However, we focused on one type of (mostly) non-precipitating cloud: the shallow cumulus. Investigating vegetation-shallow cumulus interactions remains relevant (Sikma & Vilà-Guerau de Arellano, 2019) due to the tight coupling of these clouds and the local plant dynamical reponses, which is often not well-represented in Earth system models, and the prevalence of shallow cumulus over land (with approximately 25 % occurrence in midlatitude and tropical continental regions; Eastman & Warren, 2014). Nonetheless, studying land-atmosphere interactions under other cloud regimes and aerosol loading is also important, particularly regarding cloud and aerosol perturbations to surface irradiance that influence gross primary productivity through the diffuse fertilization effect (van Diepen et al., 2025).



Beyond radiative perturbations, clouds also interact with the canopy and soil through precipitation. Coupling can-DALES with precipitating clouds is not yet possible due to some remaining technical challenges. One hurdle is the computational constraint associated with achieving sufficiently high resolution to resolve canopy dynamics while simultaneously covering domains large enough to accurately simulate cloud dynamics, such as precipitating shallow cumulus convection (Lamaakel et al., 2023) and deep convection. Although it may already be possible to simulate some precipitating clouds using domains of approximately $25 \times 25$ km$^2$ in can-DALES, larger domains will become increasingly feasible with the development of open boundary conditions in atmospheric LES (e.g., Liqui Lung et al., 2024) and domain nesting. A second technical hurdle is representing rainfall interception within the canopy, which would require implementing a multi-layer rainfall interception scheme in

can-DALES (Muzylo et al., 2009).

More generally, and also related to liquid water, revisiting the can-DALES formulation to represent dew and fog formation would be good practice. Although water can condensate within the canopy in can-DALES, it would be valuable to revise how dew formation, in-canopy fog, canopy radiative trasfer, and canopy ecophysiology interact within the can-DALES framework. Revisions of these formulations in can-DALES together with full diurnal cycle simulations enable the study of morning fog layers and its infuence on the daytime evolution over forested areas. This type of cloud is thought to be important for land-atmosphere interaction, for example, for the Amazon climate during the wet season (Anber et al., 2015).

We conclude this discussion of missing processes by considering the representation of biophysical processes within the canopy. In this thesis, we focused on the leaf gas exchange, which constitutes a major contribution to the ecosystem fluxes over vegetated areas. Within this topic, we placed emphasis on stomatal responses to the microclimate. This work can be extended in several ways; here we breifly highlight one unexplored mechanism: the stomatal response times. In this thesis, we assumed that stomata respond instantaneously to environmental disturbances. However, stomata do not adapt instantaneously to changing light; their response can take between 5 and 30 minutes depending on the plant functional type and climate (Vico et al., 2011). Accounting for this process (already implemented in can-DALES; Vilà-Guerau de Arellano et al., 2014; Sikma et al., 2018) in future simulations can enable further exploration of differences between canopy layers and help to verify previous studies about its impact under a more realistic canopy representation (Sikma et al., 2018).

In this section, we have focused on missing processes and their potential future inclusion in can-DALES. While increasing process completness enables the study of land-atmosphere interactions under a wider range of realistic environmental conditions, it can also lead to over-parametrization, where the biopysical processes cannot be accurately constrained by observations. Over-parametrization may also hinder the identification of essential generic land-atmosphere processes from particular features at specific sites. In the next section, we discuss how this thesis addressed the trade-off between process completeness and parameter simplicity by using a hierarchy of modeling approaches of varying complexity constrained by observations.

### 7.2.4 Towards an integrated framework for studying vegetation-atmospheric boundary layer interactions

In this thesis we consolidate a methodological framework to study vegetation-atmosphere interactions by bridging comprehensive observational datasets with a hierarchy of modeling approaches, and by interpreting them through diagnostic tools and metrics. Rather than relying on a single modeling strategy, this work shows the value of combining complementary approaches to capture processes acting across scales.

Across the chapters, we have combined a conceptual model (Chapters 2 and 6), an observa-

tional constrained three-layer canopy scheme (Chapter 3), and a realistic canopy-resolving LES (Chapters 4 and 5). This hierarchy proved useful because it is challenging that a single model simultaneously offer mechanistic interpretability (as the conceptual model in Chapters 2 and 6), observational constraints (as the three-layer canopy scheme in Chapter 3), and complex-process realism (as the canopy-resolving LES in Chapters 4 and 5). Conceptual and reduced-complexity models provide flexibility and enhanced interpretation of processes, while canopy-resolving LES capture complex processes at high spatiotemporal resolution, enabling a detail description of the coupled dynamics between land and atmosphere. Anchoring this hierarchy with observational constrains provided guidance for parameter ranges, helped constrain model behaviour, and supported the identification of dominant mechanisms governing vegetation-atmosphere interactions.

Beyond the models themselves, this thesis highlights the importance of diagnostic tools for interpreting complex model and observational output. We applied tendency budget equations of the leaf gas exchange (Chapter 2) and of the carbon cycle tracers (Chapter 6), together with metrics such as the diurnal range of carbon cycle tracers (Chapter 6). These tools facilitated the quantification of essential mechanisms driving land-atmosphere interactions at diurnal scales. Additionally, we consider that such tools enable process-based comparisons among models and observations, and provide a systematic strategy to identify missing or misrepresented processes.

Finally, this thesis emphasize the value of coupling observations and modeling. We consider both strategies useful for disclosing or gradually approaching the "true or real" land-atmosphere system. Observations can be viewed as a benchmark against which models can be judged, providing empirical facts about the system. Yet, even when they acquire high precision, they can have limitations in representativeness or in the underlying instrumental or setup assumptions. In turn, models are simplified representations of a system, which offer a controlled environment in which processes can be isolated, quantified, and tested. Yet, without observational constrains, model undergo the risk of diverging from the real land-atmosphere system due to process underrepresentation or omission. In this thesis, therefore, we have treated observations and models as complementary tools within a unified research strategy.



## 7.3 Final remarks

Vegetation-atmosphere interactions play a central role in regulating exchanges of energy, water, and carbon between the land surface and the atmospheric boundary layer. Despite decades of research, large uncertainties remain in how these exchanges are represented in Earth system models, particularly regarding their diurnal evolution, vertical variability within canopies, and sensitivity to clouds. Addressing these challenges requires treating vegetation and atmosphere as a tightly coupled, multi-scale system in which plant ecophysiology, microclimate, turbulence, radiation, and clouds interact continuously.

In this thesis, we investigated vegetation-atmosphere interactions with a unified diurnal and multi-scale framework, linking leaf-scale processes to canopy and atmospheric boundary layer dynamics. By combining comprehensive field observations with a hierarchy of modeling approaches, ranging from conceptual mixed-layer models to observation-constrained multi-layer canopy schemes and canopy-resolving LES, this work developed and applied an integrated methodology to study the coupled soil-vegetation-atmosphere system.

The results demonstrate that diurnal variations in ecosystem water and $CO_2$ exchange are strongly controlled by microclimatic drivers, particularly radiation, temperature, and vapor pressure deficit, while vertical-variability in microclimate plays a key role in modulating these responses. Persistent within-canopy stratification can decouple lower canopy layers from the atmosphere above, influencing storage and ventilation of $CO_2$. The development of a multi-spectral canopy radiative transfer scheme in a canopy-resolving LES advances the physical representation of radiation within vegetation canopies and open new opportunities to investigate the role of spectral composition in regulating canopy microclimate and photosynthesis. By integrating detailed canopy processes with turbulence and shallow-cumulus cloud dynamics using a canopy-resolving LES, this thesis provides one of the first process-based investigations of forest-atmosphere coupling under realistic representations of both a forest canopy and clouds.

Together, these findings highlight the importance of representing diurnal, vertical, and cloud-related processes in land-atmosphere models and demonstrate the potential of canopy-resolving approaches to bridge ecosystem-scale processes and atmospheric dynamics. In this way, the investigation presented here contributes to narrowing the gap between leaf ecophysiology and atmospheric processes, advancing our understanding of how interactions between stomata and clouds shape the functioning of the Earth system.

# References


Adekanmbi, A. A., & Sizmur, T. (2022). *Importance of Diurnal Temperature Range (DTR) for predicting the temperature sensitivity of soil respiration*. https://doi.org/10.3389/fsoil.2022.969077

Agustí-Panareda, A., Massart, S., Chevallier, F. et al. (2014). *Forecasting global atmospheric CO2*. https://doi.org/10.5194/acp-14-11959-2014

Alekseychik, P., Mammarella, I., Launiainen, S. et al. (2013). *Evolution of the nocturnal decoupled layer in a pine forest canopy*. https://doi.org/10.1016/j.agrformet.2013.01.011

Anav, A., Friedlingstein, P., Beer, C. et al. (2015). *Spatiotemporal patterns of terrestrial gross primary production: A review*. https://doi.org/10.1002/2015RG000483

Anber, U., Gentine, P., Wang, S., & Sobel, A. H. (2015). *Fog and rain in the Amazon*. https://doi.org/10.1073/pnas.1505077112

Andreae, M. O., Acevedo, O. C., Araùjo, A. et al. (2015). *The Amazon Tall Tower Observatory (ATTO): overview of pilot measurements on ecosystem ecology, meteorology, trace gases, and aerosols*. https://doi.org/10.5194/acp-15-10723-2015

Anhuf, D., & Rollenbeck, R. (2001). *Canopy structure of the Rio Surumoni rain forest (Venezuela) and its influence on microclimate*.

Araújo, A. C., Nobre, A. D., Kruijt, B. et al. (2002). *Comparative measurements of carbon dioxide fluxes from two nearby towers in a central Amazonian rainforest: The Manaus LBA site*. https://doi.org/10.1029/2001JD000676

Artaxo, P., Hansson, H.-C., Andreae, M. et al. (2022). *Tropical and Boreal Forest Atmosphere Interactions: A Review*. https://doi.org/10.16993/tellusb.34

Asner, G. P., Scurlock, J. M. O., & A. Hicke, J. (2003). *Global synthesis of leaf area index observations: implications for ecological and remote sensing studies*. https://doi.org/10.1046/j.1466-822X.2003.00026.x

Aubinet, M., Feigenwinter, C., Heinesch, B. et al. (2012). *Nighttime Flux Correction*. https://doi.org/10.1007/978-94-007-2351-1_5

Ball, J. T., Woodrow, I. E., & Berry, J. A. (1987). A model predicting stomatal conductance and its contribution to the control of photosynthesis under different environmental conditions. In *Progress in photosynthesis research: volume 4 proceedings of the VIIth international congress on photosynthesis providence, Rhode Island, USA, august 10–15, 1986*, (pp. 221–224). Springer.

Bannister, E. J., MacKenzie, A. R., & Cai, X.-M. (2022). *Realistic Forests and the Modeling of Forest-Atmosphere Exchange*. https://doi.org/10.1029/2021RG000746

Belcher, S. E., Harman, I. N., & Finnigan, J. J. (2012). *The wind in the willows: Flows in forest canopies in complex terrain*. https://doi.org/10.1146/annurev-fluid-120710-101036

Best, M. J., Abramowitz, G., Johnson, H. R. et al. (2015). *The Plumbing of Land Surface Models: Benchmarking Model Performance*. https://doi.org/10.1175/JHM-D-14-0158.1

Binks, O., Finnigan, J., Coughlin, I. et al. (2021). *Canopy wetness in the Eastern Amazon*. https://doi.org/10.1016/j.agrformet.2020.108250

Biosciences L (2019). *Eddy covariance processing software (version 7.0. 6)[software]*.

Bonan, G. (2019). *Radiative Transfer*, (p. 228–259). Cambridge University Press.

Bonan, G. B. (2008). *Forests and Climate Change: Forcings, Feedbacks, and the Climate Benefits of Forests*. https://doi.org/10.1126/science.1155121

Bonan, G. B., Burns, S. P., & Patton, E. G. (2026). *Beyond surface fluxes: Observational and computational needs of multilayer canopy models - A walnut orchard test case*. https://doi.org/10.1016/j.agrformet.2025.110960

Bonan, G. B., Lucier, O., Coen, D. R. et al. (2024). *Reimagining Earth in the Earth system*. https://doi.org/10.1029/2023MS004017

Bonan, G. B., Patton, E. G., Finnigan, J. J. et al. (2021). *Moving beyond the incorrect but useful paradigm: reevaluating big-leaf and multilayer plant canopies to model biosphere-atmosphere fluxes – a review*. https://doi.org/10.1016/j.agrformet.2021.108435

Boone, A. A., Bellvert, J., Best, M. et al. (2021). *Updates on the International Land Surface Interactions with the Atmosphere over the Iberian Semi-Arid Environment (LIAISE) field campaign*.

Boone, A. A., Best, M., Cuxart, J. et al. (2019). *Land surface Interactions with the Atmosphere over the Iberian Semi-arid Environment (LIAISE)*.

Botía, S., Gerbig, C., Marshall, J. et al. (2020). *Understanding nighttime methane signals at the Amazon Tall Tower Observatory (ATTO)*. https://doi.org/10.5194/acp-20-6583-2020

Botía, S., Komiya, S., Marshall, J. et al. (2022). *The CO2 record at the Amazon Tall Tower Observatory: A new opportunity to study processes on seasonal and inter-annual scales*. https://doi.org/10.1111/gcb.15905

Boussetta, S., Balsamo, G., Beljaars, A. et al. (2013). *Natural land carbon dioxide exchanges in the ECMWF integrated forecasting system: Implementation and offline validation*. https://doi.org/10.1002/jgrd.50488

Bowling, D., Burns, S. P., Conway, T. J. et al. (2005). *Extensive observations of CO2 carbon isotope content in and above a high-elevation subalpine forest*. https://doi.org/10.1029/2004GB002394

Butt, N., New, M., Malhi, Y. et al. (2010). *Diffuse radiation and cloud fraction relationships in two contrasting Amazonian rainforest sites*. https://doi.org/10.1016/j.agrformet.2009.12.004

Béland, M. (2025). *Mapping wood area in forests from ground lidar and estimating their light interception using radiative transfer modeling*. https://doi.org/10.1016/j.agrformet.2025.110883

Béland, M., & Baldocchi, D. D. (2020). *Is foliage clumping an outcome of resource limitations within forests?*. https://doi.org/10.1016/j.agrformet.2020.108185

Béland, M., & Baldocchi, D. D. (2021). *Vertical structure heterogeneity in broadleaf forests: Effects*

*on light interception and canopy photosynthesis*. https://doi.org/10.1016/j.agrformet.2021.108525

Béland, M., & Kobayashi, H. (2021). *Mapping forest leaf area density from multiview terrestrial lidar*. https://doi.org/10.1111/2041-210X.13550

Calvet, J.-C., Noilhan, J., Roujean, J.-L. et al. (1998). *An interactive vegetation SVAT model tested against data from six contrasting sites*. https://doi.org/10.1016/S0168-1923(98)00091-4

Cao, S., Li, M., Zhu, Z. et al. (2023). *Spatiotemporally consistent global dataset of the GIMMS leaf area index (GIMMS LAI4g) from 1982 to 2020*. https://doi.org/10.5194/essd-15-4877-2023

Carswell, F. E., Meir, P., Wandelli, E. V. et al. (2000). *Photosynthetic capacity in a central Amazonian rain forest*. https://doi.org/10.1093/treephys/20.3.179

Casso-Torralba, P., Vilà-Guerau de Arellano, J., Bosveld, F. et al. (2008). *Diurnal and vertical variability of the sensible heat and carbon dioxide budgets in the atmospheric surface layer*. https://doi.org/10.1029/2007JD009583

Chamecki, M., Freire, L. S., Dias, N. L. et al. (2020). *Effects of Vegetation and Topography on the Boundary Layer Structure above the Amazon Forest*. https://doi.org/10.1175/JAS-D-20-0063.1

Chen, B., Chamecki, M., & Katul, G. G. (2019). *Effects of topography on in-canopy transport of gases emitted within dense forests*. https://doi.org/10.1002/qj.3546

Chen, T. H., Henderson-Sellers, A., Milly, P. et al. (1997). *Cabauw Experimental Results from the Project for Intercomparison of Land-Surface Parameterization Schemes*. https://doi.org/10.1175/1520-0442(1997)010<1194:CERFTP>2.0.CO;2

Chi, Y., Zhao, C., Yang, Y. et al. (2024). *Global characteristics of cloud macro-physical properties from active satellite remote sensing*. https://doi.org/10.1016/j.atmosres.2024.107316

Clifton, O. E., Patton, E. G., Wang, S. et al. (2022). *Large eddy simulation for investigating coupled forest canopy and turbulence influences on atmospheric chemistry*. https://doi.org/10.1029/2022MS003078

Collatz, G. J., Ball, J. T., Grivet, C., & Berry, J. A. (1991). *Physiological and environmental regulation of stomatal conductance, photosynthesis and transpiration: a model that includes a laminar boundary layer*. https://doi.org/10.1016/0168-1923(91)90002-8

Combe, M., de Arellano, J. V.-G., Ouwersloot, H. G., & Peters, W. (2016). *Plant water-stress parameterization determines the strength of land–atmosphere coupling*. https://doi.org/10.1016/j.agrformet.2015.11.006

Coplen, T. B. (2011). *Guidelines and recommended terms for expression of stable-isotope-ratio and gas-ratio measurement results*. https://doi.org/10.1002/rcm.5129

Culf, A., Fisch, G., Malhi, Y., & Nobre, C. (1997). *The influence of the atmospheric boundary layer on carbon dioxide concentrations over a tropical forest*. https://doi.org/10.1016/S0168-1923(96)02412-4

Davidson, E. A., de Araújo, A. C., Artaxo, P. et al. (2012). *The Amazon basin in transition*. https://doi.org/10.1038/nature10717

Davis, K. J., Lenschow, D. H., Oncley, S. P. et al. (1997). *Role of entrainment in surface-atmosphere interactions over the boreal forest*. https://doi.org/10.1029/97JD02236

de Castro, F. (2000). *Light spectral composition in a tropical forest: measurements and model*. https://doi.org/10.1093/treephys/20.1.49

de Feiter, V. S., Janssens, M., de Haas, S. E. M. et al. (2025). *Turbulent Exchange of CO2 in the Lower Tropical Troposphere Across Clear-to-Cloudy Conditions*. https://doi.org/10.1029/2025JD044231

Denning, A. S., Randall, D. A., Collatz, G. J., & Sellers, P. J. (1996). *Simulations of terrestrial carbon metabolism and atmospheric CO2 in a general circulation model: Part 2: Simulated CO2 concentrations*. https://doi.org/10.1034/j.1600-0889.1996.t01-1-00010.x

Dickinson, R. E. (1983). *Land surface processes and climate—surface albedos and energy balance*. https://doi.org/10.1016/S0065-2687(08)60176-4

Dolman, A., Gash, J. H., Roberts, J., & Shuttleworth, W. (1991). *Stomatal and surface conductance of tropical rainforest*. https://doi.org/10.1016/0168-1923(91)90011-E

Dolman, A., Moors, E., & Elbers, J. (2002). *The carbon uptake of a mid latitude pine forest growing on sandy soil*. https://doi.org/10.1016/S0168-1923(02)00024-2

dos Santos Michiles, A. A., & Gielow, R. (2008). *Above-ground thermal energy storage rates, trunk heat fluxes and surface energy balance in a central Amazonian rainforest*. https://doi.org/10.1016/j.agrformet.2008.01.001

Doutriaux-Boucher, M., Webb, M., Gregory, J. M., & Boucher, O. (2009). *Carbon dioxide induced stomatal closure increases radiative forcing via a rapid reduction in low cloud*. https://doi.org/10.1029/2008GL036273

Dupont, S., & Brunet, Y. (2008). *Edge Flow and Canopy Structure: A Large-Eddy Simulation Study*. https://doi.org/10.1007/s10546-007-9216-3

Dupont, S., Irvine, M. R., & Bidot, C. (2024). *Morning transition of the coupled vegetation canopy and atmospheric boundary layer turbulence according to the wind intensity*. https://doi.org/10.1175/jas-d-23-0201.1

Durand, M., Lintunen, A., & Ezhova, E. (2026). *Forest canopy interactions with aerosols: important considerations in approaching future impacts and climate management*. https://doi.org/10.1111/nph.70636

Eastman, R., & Warren, S. G. (2014). *Diurnal cycles of cumulus, cumulonimbus, stratus, stratocumulus, and fog from surface observations over land and ocean*. https://doi.org/10.1175/JCLI-D-13-00352.1

Echer, F. R., & Rosolem, C. A. (2015). *Cotton leaf gas exchange responses to irradiance and leaf aging*. https://doi.org/10.1007/s10535-015-0484-3

ECMWF, I. (2014). *Documentation—Cy40r1 Part IV: Physical Processes*.

Elbers, J. A., Jacobs, C. M., Kruijt, B. et al. (2011). *Assessing the uncertainty of estimated annual totals of net ecosystem productivity: A practical approach applied to a mid latitude temperate pine forest*. https://doi.org/10.1016/j.agrformet.2011.07.020

Evans, J. R., & Santiago, L. S. (2014). *Prometheuswiki gold leaf protocol: gas exchange using li-cor 6400*. https://doi.org/10.1071/FP10900

Faassen, K. A. P., Nguyen, L. N. T., Broekema, E. R. et al. (2023). *Diurnal variability of atmospheric O2, CO2, and their exchange ratio above a boreal forest in southern Finland*. https://doi.org/10.

5194/acp-23-851-2023

Faassen, K. A. P., Vilà-Guerau de Arellano, J., González-Armas, R. et al. (2024). *Separating above-canopy CO2 and O2 measurements into their atmospheric and biospheric signatures*. https://doi.org/10.5194/bg-21-3015-2024

Farquhar, G., O'Leary, M., & Berry, J. (1982). *On the relationship between carbon isotope discrimination and the intercellular carbon dioxide concentration in leaves*. https://doi.org/10.1071/PP9820121

Farquhar, G. D., Ehleringer, J. R., & Hubick, K. T. (1989). *Carbon Isotope Discrimination and Photosynthesis*. https://doi.org/10.1146/annurev.pp.40.060189.002443

Farquhar, G. D., von Caemmerer, S., & Berry, J. A. (1980). *A biochemical model of photosynthetic CO2 assimilation in leaves of C3 species*. https://doi.org/10.1007/BF00386231

Fehsenfeld, F., Calvert, J., Fall, R. et al. (1992). *Emissions of volatile organic compounds from vegetation and the implications for atmospheric chemistry*. https://doi.org/10.1029/92GB02125

Finnigan, J. J., Shaw, R. H., & Patton, E. G. (2009). *Turbulence structure above a vegetation canopy*. https://doi.org/10.1017/S0022112009990589

Fitzjarrald, D. R., Moore, K. E., Cabral, O. M. R. et al. (1990). *Daytime turbulent exchange between the Amazon forest and the atmosphere*. https://doi.org/10.1029/JD095iD10p16825

Foken, T., Leuning, R., Oncley, S. et al. (2012). Eddy covariance method. In M. Aubinet, T. Vesala, & D. Papale (Eds.) *Eddy covariance: A practical guide to measurement and data analysis*, vol. 10, (pp. 1–19). Springer.

Friedlingstein, P., Cox, P., Betts, R. et al. (2006). *Results from the C4MIP model intercomparison*. https://doi.org/10.1175/JCLI3800.1

Friedlingstein, P., O'sullivan, M., Jones, M. W. et al. (2024). *Global carbon budget 2024*. https://doi.org/10.5194/essd-17-965-2025

Froelich, N., Grimmond, C., & Schmid, H. (2011). *Nocturnal cooling below a forest canopy: Model and evaluation*. https://doi.org/10.1016/j.agrformet.2011.02.015

Garen, J. C., & Michaletz, S. T. (2024). *Fast Assimilation-Temperature Response: a FAsTeR method for measuring the temperature dependence of leaf-level photosynthesis*. https://doi.org/10.1111/nph.19405

Garratt, J. R. (1992). *The Atmospheric Boundary Layer*. Cambridge, UK: Cambridge University Press.

Gentine, P., Green, J. K., Guérin, M. et al. (2019). *Coupling between the terrestrial carbon and water cycles—a review*. https://doi.org/10.1088/1748-9326/ab22d6

Giangrande, S. E., Feng, Z., Jensen, M. P. et al. (2017). *Cloud characteristics, thermodynamic controls and radiative impacts during the Observations and Modeling of the Green Ocean Amazon (GoAmazon2014/5) experiment*. https://doi.org/10.5194/acp-17-14519-2017

Gibert, F., Schmidt, M., Cuesta, J. et al. (2007). *Retrieval of average CO2 fluxes by combining in situ CO2 measurements and backscatter lidar information*. https://doi.org/10.1029/2006JD008190

Gomes Alves, E., Aquino Santana, R., Quaresma Dias-Júnior, C. et al. (2023). *Intra- and interannual changes in isoprene emission from central Amazonia*. https://doi.org/10.5194/acp-23-8149-2023

Gonsamo, A., Chen, J. M., Wu, C., & Dragoni, D. (2012). *Predicting deciduous forest carbon uptake phenology by upscaling FLUXNET measurements using remote sensing data*. https://doi.org/10.1016/j.agrformet.2012.06.006

González-Armas, R., Vilà-Guerau de Arellano, J., Mangan, M. R. et al. (2024). *Impact of canopy environmental variables on the diurnal dynamics of water and carbon dioxide exchange at leaf and canopy level [Suppl.]*. https://doi.org/10.5194/bg-21-2425-2024

Goudriaan, J. (1977). *Crop micrometeorology : a simulation study*. Ph.D. thesis, Wageningen. https://edepot.wur.nl/166537

Goudriaan, J. (1986). *A simple and fast numerical method for the computation of daily totals of crop photosynthesis*. https://doi.org/10.1016/0168-1923(86)90063-8

Goudriaan, J. (1988). *The bare bones of leaf-angle distribution in radiation models for canopy photosynthesis and energy exchange*. https://doi.org/10.1016/0168-1923(88)90089-5

Goudriaan, J., Van Laar, H., Van Keulen, H., & Louwerse, W. (1985). *Photosynthesis, CO2 and plant production*. https://doi.org/10.1007/978-1-4899-3665-3_10

Goudriaan, J., & Van Laar, H. H. (1994). *Radiation in crops*, (pp. 95–119). Dordrecht: Springer Netherlands. https://doi.org/10.1007/978-94-011-0750-1_6

Grace, J., Lloyd, J., McIntyre, J. et al. (1995). *Fluxes of carbon dioxide and water vapour over an undisturbed tropical forest in south-west amazonia*. https://doi.org/10.1111/j.1365-2486.1995.tb00001.x

Graven, H., Keeling, R., Piper, S. et al. (2013). *Enhanced seasonal exchange of CO2 by northern ecosystems since 1960*. https://doi.org/10.1126/science.1239207

Griffis, T. J. (2013). *Tracing the flow of carbon dioxide and water vapor between the biosphere and atmosphere: A review of optical isotope techniques and their application*. https://doi.org/10.1016/j.agrformet.2013.02.009

Gu, L., Baldocchi, D., Verma, S. B. et al. (2002). *Advantages of diffuse radiation for terrestrial ecosystem productivity*. https://doi.org/10.1029/2001JD001242

Gu, L., Baldocchi, D. D., Wofsy, S. C. et al. (2003). *Response of a Deciduous Forest to the Mount Pinatubo Eruption: Enhanced Photosynthesis*. https://doi.org/10.1126/science.1078366

Gueymard, C., et al. (1995). *SMARTS2: a simple model of the atmospheric radiative transfer of sunshine: algorithms and performance assessment*, vol. 1. Florida Solar Energy Center Cocoa, FL.

Harrison, S. P., Cramer, W., Franklin, O. et al. (2021). *Eco-evolutionary optimality as a means to improve vegetation and land-surface models*. https://doi.org/10.1111/nph.17558

Hartogensis, O. K., De Bruin, H. A. R., & Van De Wiel, B. J. H. (2002). *Displaced-beam small aperture scintillometer test. part ii: Cases-99 stable boundary-layer experiment*. https://doi.org/10.1023/A:1019620515781

Haverd, V., Cuntz, M., Leuning, R., & Keith, H. (2007). *Air and biomass heat storage fluxes in a forest canopy: Calculation within a soil vegetation atmosphere transfer model*. https://doi.org/10.1016/j.agrformet.2007.07.006

Helbig, M., Gerken, T., Beamesderfer, E. R. et al. (2021). *Integrating continuous atmospheric boundary*

*layer and tower-based flux measurements to advance understanding of land-atmosphere interactions*. https://doi.org/10.1016/j.agrformet.2021.108509

Henderson-Sellers, A., Pitman, A., Love, P. et al. (1995). *The project for intercomparison of land surface parameterization schemes (PILPS): Phases 2 and 3*. https://doi.org/10.1016/S0921-8181(98)00044-7

Henkes, A., Fisch, G., Machado, L. A. T., & Chaboureau, J.-P. (2021). *Morning boundary layer conditions for shallow to deep convective cloud evolution during the dry season in the central Amazon*. https://doi.org/10.5194/acp-21-13207-2021

Heus, T., van Heerwaarden, C. C., Jonker, H. J. J. et al. (2010). *Formulation of the dutch atmospheric large-eddy simulation (dales) and overview of its applications*. https://doi.org/10.5194/gmd-3-415-2010

Heusinkveld, B. G., Mol, W. B., & van Heerwaarden, C. C. (2023). *A new accurate low-cost instrument for fast synchronized spatial measurements of light spectra*. https://doi.org/10.5194/amt-16-3767-2023

Hikosaka, K. (2014). *Optimal nitrogen distribution within a leaf canopy under direct and diffuse light*. https://doi.org/10.1111/pce.12291

Holtslag, A., Svensson, G., Baas, P. et al. (2013). *Stable atmospheric boundary layers and diurnal cycles: challenges for weather and climate models*. https://doi.org/10.1175/BAMS-D-11-00187.1

Horn, H. S. (1971). *The adaptive geometry of trees*. 3. Princeton University Press.

Huang, X., Dunn, R. J. H., Li, L. Z. X. et al. (2023). *Increasing Global Terrestrial Diurnal Temperature Range for 1980–2021*. https://doi.org/10.1029/2023GL103503

Huitema, A. C., de Feiter, V. S., González-Armas, R. et al. (2026). *CO2 and Heat exchange across the Nocturnal Canopy-Atmosphere interface in the Amazon rainforest*. https://doi.org/10.5194/egusphere-2026-684

Iacono, M. J., Delamere, J. S., Mlawer, E. J. et al. (2008). *Radiative forcing by long-lived greenhouse gases: Calculations with the AER radiative transfer models*. https://doi.org/10.1029/2008JD009944

Ishidoya, S., Murayama, S., Kondo, H. et al. (2015). *Observation of O2:CO2 exchange ratio for net turbulent fluxes and its application to forest carbon cycles*. https://doi.org/10.1007/s11284-014-1241-3

Jacobs, C. M., & de Bruin, H. A. (1997). *Predicting regional transpiration at elevated atmospheric CO2: influence of the PBL–vegetation interaction*. https://doi.org/10.1175/1520-0450(1997)036<1663:PRTAEA>2.0.CO;2

Jacobs, C. M. J. (1994). *Direct impact of atmospheric CO2 enrichment on regional transpiration*. Ph.D. thesis, Wageningen.
https://edepot.wur.nl/206972

Jans, T. B., Mossink, L., Wassenaar, M. et al. (2025). *Coupling Modelling and Experiments to Analyse Leaf Photosynthesis Under Far-Red Light*. https://doi.org/10.1111/pce.15340

Jarvis, P. G., & McNaughton, K. (1986). Stomatal control of transpiration: scaling up from leaf to region. In *Advances in ecological research*, vol. 15, (pp. 1–49). Elsevier.

Kaimal, J. C., & Finnigan, J. J. (1994). *Atmospheric boundary layer flows: their structure and measurement*. Oxford university press.

Kariyathan, T., Bastos, A., Reichstein, M. et al. (2024). *How atmospheric CO2 can inform us on annual and decadal shifts in the biospheric carbon uptake period*. https://doi.org/10.5194/egusphere-2024-1382

Kivalov, S. N., & Fitzjarrald, D. R. (2018). *Quantifying and modelling the effect of cloud shadows on the surface irradiance at tropical and midlatitude forests*. https://doi.org/10.1007/s10546-017-0301-y

Knohl, A., & Baldocchi, D. D. (2008). *Effects of diffuse radiation on canopy gas exchange processes in a forest ecosystem*. https://doi.org/10.1029/2007JG000663

Kobayashi, H., Baldocchi, D. D., Ryu, Y. et al. (2012). *Modeling energy and carbon fluxes in a heterogeneous oak woodland: A three-dimensional approach*. https://doi.org/10.1016/j.agrformet.2011.09.008

Kozlova, E. A., & Manning, A. C. (2009). *Methodology and calibration for continuous measurements of biogeochemical trace gas and $O_2$ concentrations from a 300-m tall tower in central Siberia*. https://doi.org/10.5194/amt-2-205-2009

Kretschmer, R., Gerbig, C., Karstens, U. et al. (2014). *Impact of optimized mixing heights on simulated regional atmospheric transport of CO2*. https://doi.org/10.5194/acp-14-7149-2014

Kruijt, B., Malhi, Y., Lloyd, J. et al. (2000). *Turbulence Statistics Above And Within Two Amazon Rain Forest Canopies*. https://doi.org/10.1023/A:1002401829007

Lamaakel, O., Venters, R., Teixeira, J., & Matheou, G. (2023). *Computational domain size effects on large-eddy simulations of precipitating shallow cumulus convection*. https://doi.org/10.3390/atmos14071186

Lamour, J., Davidson, K., Ely, K. et al. (2020). *Leaf spectral reflectance and transmittance, san lorenzo, panama, 2020*. https://doi.org/10.15486/ngt/1781003

Larson, V. E., & Volkmer, H. (2008). *An idealized model of the one-dimensional carbon dioxide rectifier effect*. https://doi.org/10.1111/j.1600-0889.2008.00368.x

Latham, J., Cumani, R., Rosati, I., & Bloise, M. (2014). *Global land cover share (GLC-SHARE) database beta-release version 1.0-2014*.

Lavigne, M. B., Ryan, M. G., Anderson, D. E. et al. (1997). *Comparing nocturnal eddy covariance measurements to estimates of ecosystem respiration made by scaling chamber measurements at six coniferous boreal sites*. https://doi.org/10.1029/97JD01173

Lee, X., Griffis, T. J., Baker, J. M. et al. (2009). *Canopy-scale kinetic fractionation of atmospheric carbon dioxide and water vapor isotopes*. https://doi.org/10.1029/2008GB003331

Lefèvre, M., Schroedter-Homscheidt, M., & Arola, A. (2019). *Improving the mcclear model estimating the downwelling solar radiation at ground level in cloud-free conditions – mcclear-v3*. https://doi.org/10.1127/metz/2019/0946

Leuning, R., van Gorsel, E., Massman, W. J., & Isaac, P. R. (2012). *Reflections on the surface energy imbalance problem*. https://doi.org/10.1016/j.agrformet.2011.12.002

LI-COR, I. (2022). *Complimentary Leaf Physiology Measurments with the LI-600 and LI-6800*. Applica-

tion Note.
https://www.licor.com/support/AppNotes/complementary-photosynthesis-measurements.html#

Lilly, D. K. (1968). *Models of cloud-topped mixed layers under a strong inversion*. https://doi.org/10.1002/qj.49709440106

Lindroth, A., Lagergren, F., Aurela, M. et al. (2008). *Leaf area index is the principal scaling parameter for both gross photosynthesis and ecosystem respiration of Northern deciduous and coniferous forests*. https://doi.org/10.1111/j.1600-0889.2006.00330.x

Lindroth, A., Mölder, M., & Lagergren, F. (2010). *Heat storage in forest biomass improves energy balance closure*. https://doi.org/10.5194/bg-7-301-2010

Lindvall, J., & Svensson, G. (2015). *The diurnal temperature range in the CMIP5 models*. https://doi.org/10.1007/s00382-014-2144-2

Liqui Lung, F., Jakob, C., Siebesma, A. P., & Jansson, F. (2024). *Open boundary conditions for atmospheric large-eddy simulations and their implementation in DALES4.4*. https://doi.org/10.5194/gmd-17-4053-2024

Liu, C., Calders, K., Meunier, F. et al. (2022). *Implications of 3D Forest Stand Reconstruction Methods for Radiative Transfer Modeling: A Case Study in the Temperate Deciduous Forest*. https://doi.org/10.1029/2021JD036175

Lloyd, J., Grace, J., Miranda, A. C. et al. (1995). *A simple calibrated model of amazon rainforest productivity based on leaf biochemical properties*. https://doi.org/10.1111/j.1365-3040.1995.tb00624.x

Lloyd, J., Patiño, S., Paiva, R. Q. et al. (2010). *Optimisation of photosynthetic carbon gain and within-canopy gradients of associated foliar traits for Amazon forest trees*. https://doi.org/10.5194/bg-7-1833-2010

Lynch, Y. L. S. A. A. T., D., & Morgan, P. (2016). *LI-6800 Instrument Performance In Physiological Parameter Estimation*. LI-COR, Inc., Lincoln, NA, USA. Poster.
https://licor.app.boxenterprise.net/s/hdhjvo7m24syayd2v9qsgwuqgg1ebmhv

Ma, Y., & Liu, H. (2019). *An Advanced Multiple-Layer Canopy Model in the WRF Model With Large-Eddy Simulations to Simulate Canopy Flows and Scalar Transport Under Different Stability Conditions*. https://doi.org/10.1029/2018MS001347

Machado, L. A., Kesselmeier, J., Botía, S. et al. (2024). *How rainfall events modify trace gas mixing ratios in central Amazonia*. https://doi.org/10.5194/acp-24-8893-2024

Machta, L., & Hughes, E. (1970). *Atmospheric oxygen in 1967 to 1970*. https://doi.org/10.1126/science.168.3939.1582

Mahrt, L. (1999). *Stratified Atmospheric Boundary Layers*. https://doi.org/10.1023/A:1001765727956

Malhi, Y., Nobre, A. D., Grace, J. et al. (1998). *Carbon dioxide transfer over a Central Amazonian rain forest*. https://doi.org/10.1029/98JD02647

Mangan, M. R., Hartogensis, O., Boone, A. et al. (2023a). *The surface-boundary layer connection across spatial scales of irrigation-driven thermal heterogeneity: An integrated data and modeling study of the*

*LIAISE field campaign*. https://doi.org/10.1016/j.agrformet.2023.109452

Mangan, M. R., Hartogensis, O., van Heerwaarden, C., & Vilà-Guerau de Arellano, J. (2023b). *Evapotranspiration controls across spatial scales of heterogeneity*. https://doi.org/10.1002/qj.4527

Martin, C. L., Fitzjarrald, D., Garstang, M. et al. (1988). *Structure and growth of the mixing layer over the Amazonian rain forest*. https://doi.org/10.1029/JD093iD02p01361

Martín-Gómez, V., Ruprich-Robert, Y., Tourigny, E. et al. (2023). *Large spread in interannual variance of atmospheric CO2 concentration across CMIP6 Earth System Models*. https://doi.org/10.1038/s41612-023-00532-x

Mason, P. J. (1989). *Large-eddy simulation of the convective atmospheric boundary layer*. https://doi.org/10.1175/1520-0469(1989)046<1492:LESOTC>2.0.CO;2

Masson, V., Le Moigne, P., Martin, E. et al. (2013). *The SURFEXv7.2 land and ocean surface platform for coupled or offline simulation of earth surface variables and fluxes*. https://doi.org/10.5194/gmd-6-929-2013

McCree, K. J. (1981). *Photosynthetically Active Radiation*, (pp. 41–55). Berlin, Heidelberg: Springer Berlin Heidelberg.
https://doi.org/10.1007/978-3-642-68090-8_3

McPherson, R. A. (Jun 2007). *A review of vegetation–atmosphere interactions and their influences on mesoscale phenomena*. https://doi.org/10.1177/0309133307079055

Meier, R., Davin, E. L., Swenson, S. C. et al. (2019). *Biomass heat storage dampens diurnal temperature variations in forests*. https://doi.org/10.1088/1748-9326/ab2b4e

Mercado, L. M., Bellouin, N., Sitch, S. et al. (2009). *Impact of changes in diffuse radiation on the global land carbon sink*. https://doi.org/10.1038/nature07949

Meyers, T. P., Finkelstein, P., Clarke, J. et al. (1998). *A multilayer model for inferring dry deposition using standard meteorological measurements*. https://doi.org/10.1029/98JD01564

Mol, W. B., Heusinkveld, B., Mangan, M. R. et al. (2024). *Observed patterns of surface solar irradiance under cloudy and clear-sky conditions*. https://doi.org/10.1002/qj.4712

Mol, W. B., van Stratum, B. J., Knap, W. H., & van Heerwaarden, C. C. (2023). *Reconciling observations of solar irradiance variability with cloud size distributions*. https://doi.org/10.1029/2022JD037894

Monin, S., Andreĭ, & Obukhov, A. M. (1954). *Basic laws of turbulent mixing in the surface layer of the atmosphere*.

Monsi, M., & Saeki, T. (2005). *On the Factor Light in Plant Communities and its Importance for Matter Production*. https://doi.org/10.1093/aob/mci052

Monteith, J. L., & Unsworth, M. H. (2013). *Principles of Environmental Physics: Plants, Animals, and the Atmosphere*. Oxford, UK: Academic Press, 4 ed.

Moonen, R. P., Adnew, G. A., Hartogensis, O. K. et al. (2023). *Data treatment and corrections for estimating H2O and CO2 isotope fluxes from high-frequency observations*. https://doi.org/10.5194/amt-16-5787-2023

Moonen, R. P. J., Adnew, G. A., Vilà-Guerau de Arellano, J. et al. (2025a). *CO2 and H2O isotope*

*exchange and flux partitioning in Amazonia*. https://doi.org/10.5194/egusphere-2025-5969

Moonen, R. P. J., Adnew, G. A., Vilà-Guerau de Arellano, J. et al. (2025b). *Amazon rainforest ecosystem exchange of CO2 and H2O through turbulent understory ejections*. https://doi.org/10.5194/acp-25-12197-2025

Moore, C., & Fisch, G. (1986). *Estimating heat storage in Amazonian tropical forest*. https://doi.org/10.1016/0168-1923(86)90055-9

Muzylo, A., Llorens, P., Valente, F. et al. (2009). *A review of rainfall interception modelling*. https://doi.org/10.1016/j.jhydrol.2009.02.058

Niinemets, Ü. (2010). *A review of light interception in plant stands from leaf to canopy in different plant functional types and in species with varying shade tolerance*. https://doi.org/10.1007/s11284-010-0712-4

Niyogi, D., Chang, H.-I., Saxena, V. et al. (2004). *Direct observations of the effects of aerosol loading on net ecosystem CO2 exchanges over different landscapes*. https://doi.org/10.1029/2004GL020915

Noilhan, J., & Planton, S. (1989). *A simple parameterization of land surface processes for meteorological models*. https://doi.org/10.1175/1520-0493(1989)117<0536:ASPOLS>2.0.CO;2

Norman, J. M. (1979). Modelling the complete crop canopy. In B. J. Barfield, & J. F. Gerber (Eds.) *Modification of the Aerial Environment of Crops*, no. 2 in ASAE Monograph. American Society of Agricultural Engineers (ASAE).

North, P. (1996). *Three-dimensional forest light interaction model using a Monte Carlo method*. https://doi.org/10.1109/36.508411

Oke, T. R. (1987). *Boundary Layer Climates*. London, UK: Routledge, 2 ed.

Oshio, H., & Asawa, T. (2023). *Simulating the 3D Distribution of Absorbed Shortwave Radiation in a Tree Crown: Comparison of Simplified and Monte Carlo Models*. https://doi.org/10.1029/2023JD038612

Ouwersloot, H. G., de Arellano, J. V.-G., H. van Stratum, B. et al. (2013). *Quantifying the transport of subcloud layer reactants by shallow cumulus clouds over the amazon*. https://doi.org/10.1002/2013JD020431

Ouwersloot, H. G., Moene, A. F., Attema, J. J., & de Arellano, J. V.-G. (2017). *Large-Eddy Simulation Comparison of Neutral Flow Over a Canopy: Sensitivities to Physical and Numerical Conditions, and Similarity to Other Representations*. https://doi.org/10.1007/s10546-016-0182-5

Ouwersloot, H. G., Vilà-Guerau de Arellano, J., Nölscher, A. C. et al. (2012). *Characterization of a boreal convective boundary layer and its impact on atmospheric chemistry during HUMPPAC-COPEC-2010*. https://doi.org/10.5194/acp-12-9335-2012

Ouwersloot, H. G., Vilà-Guerau de Arellano, J., van Heerwaarden, C. C. et al. (2011). *On the segregation of chemical species in a clear boundary layer over heterogeneous land surfaces*. https://doi.org/10.5194/acp-11-10681-2011

Park, H.-T., Hattori, S., & Tanaka, T. (1998). *Development of a numerical model for evaluating the effect of litter layer on evaporation*. https://doi.org/10.1007/BF02760289

Park, S.-W., Kug, J.-S., Jun, S.-Y. et al. (2021). *Role of cloud feedback in continental warming response to CO2 physiological forcing*. https://doi.org/10.1175/JCLI-D-21-0025.1

Parker, G. G., Fitzjarrald, D. R., & Sampaio, I. C. G. (2019). *Consequences of environmental heterogeneity for the photosynthetic light environment of a tropical forest*. https://doi.org/10.1016/j.agrformet.2019.107661

Parker, G. G., Harding, D. J., & Berger, M. L. (2004). *A portable LIDAR system for rapid determination of forest canopy structure*. https://doi.org/10.1111/j.0021-8901.2004.00925.x

Parker, G. G., & Russ, M. E. (2004). *The canopy surface and stand development: assessing forest canopy structure and complexity with near-surface altimetry*. https://doi.org/10.1016/j.foreco.2003.09.001

Patton, E. G., Sullivan, P. P., Shaw, R. H. et al. (2016). *Atmospheric Stability Influences on Coupled Boundary Layer and Canopy Turbulence*. https://doi.org/10.1175/JAS-D-15-0068.1

Pedruzo-Bagazgoitia, X., Ouwersloot, H., Sikma, M. et al. (2017). *Direct and diffuse radiation in the shallow cumulus–vegetation system: Enhanced and decreased evapotranspiration regimes*. https://doi.org/10.1175/JHM-D-16-0279.1

Pedruzo-Bagazgoitia, X., Patton, E., Moene, A. et al. (2023). *Investigating the Diurnal Radiative, Turbulent, and Biophysical Processes in the Amazonian Canopy-Atmosphere Interface by Combining LES Simulations and Observations*. https://doi.org/10.1029/2022MS003210

Piao, S., Liu, Z., Wang, Y. et al. (2018). *On the causes of trends in the seasonal amplitude of atmospheric CO2*. https://doi.org/10.1111/gcb.13909

Piao, S., Wang, X., Wang, K. et al. (2020). *Interannual variation of terrestrial carbon cycle: Issues and perspectives*. https://doi.org/10.1111/gcb.14884

Pieruschka, R., Huber, G., & Berry, J. A. (2010). *Control of transpiration by radiation*. https://doi.org/10.1073/pnas.0913177107

Pino, D., Vilà-Guerau de Arellano, J., Peters, W. et al. (2012). *A conceptual framework to quantify the influence of convective boundary layer development on carbon dioxide mixing ratios*. https://doi.org/10.5194/acp-12-2969-2012

Pugliese, G., Ingrisch, J., Meredith, L. K. et al. (2023). *Effects of drought and recovery on soil volatile organic compound fluxes in an experimental rainforest*. https://doi.org/10.1038/s41467-023-40661-8

Qu, M., Wan, J., & Hao, X. (2014). *Analysis of diurnal air temperature range change in the continental United States*. https://doi.org/10.1016/j.wace.2014.05.002

Raupach, M., & Finnigan, J. (1988). *"single-layer models of evaporation from plant canopies are incorrect but useful, whereas multilayer models are correct but useless": discuss*. https://doi.org/10.1071/PP9880705

Raupach, M. R., Finnigan, J. J., & Brunei, Y. (1996). *Coherent eddies and turbulence in vegetation canopies: The mixing-layer analogy*. https://doi.org/10.1007/BF00120941

Renner, M., Brenner, C., Mallick, K. et al. (2019). *Using phase lags to evaluate model biases in simulating the diurnal cycle of evapotranspiration: a case study in Luxembourg*. https://doi.org/10.5194/hess-23-515-2019

Renner, M., Kleidon, A., Clark, M. et al. (2021). *How Well Can Land-Surface Models Represent the Diurnal Cycle of Turbulent Heat Fluxes?*. https://doi.org/10.1175/JHM-D-20-0034.1

Restrepo-Coupe, N., Levine, N. M., Christoffersen, B. O. et al. (2017). *Do dynamic global vegetation models capture the seasonality of carbon fluxes in the Amazon basin? A data-model intercomparison*. https://doi.org/10.1111/gcb.13442

Ronda, R., De Bruin, H., & Holtslag, A. (2001). *Representation of the canopy conductance in modeling the surface energy budget for low vegetation*. https://doi.org/10.1175/1520-0450(2001)040<1431:ROTCCI>2.0.CO;2

Santana, R. A., Dias-Júnior, C. Q., da Silva, J. T. et al. (2018). *Air turbulence characteristics at multiple sites in and above the Amazon rainforest canopy*. https://doi.org/10.1016/j.agrformet.2018.05.027

Santana, R. A. S. d., Dias-Júnior, C. Q., Vale, R. S. d. et al. (2017). *Observing and Modeling the Vertical Wind Profile at Multiple Sites in and above the Amazon Rain Forest Canopy*. https://doi.org/10.1155/2017/5436157

Santanello, J. A., Dirmeyer, P. A., Ferguson, C. R. et al. (2018). *Land–Atmosphere Interactions: The LoCo Perspective*. https://doi.org/10.1175/BAMS-D-17-0001.1

Sarma, A. N., Satheesh, S. K., & Moorthy, K. K. (2022). *Land-atmosphere interactions at a semi-arid region in the deccan plateau*. https://doi.org/10.1029/2022jd037211

Schilperoort, B., Coenders-Gerrits, M., Jiménez Rodríguez, C. et al. (2020). *Decoupling of a Douglas fir canopy: a look into the subcanopy with continuous vertical temperature profiles*. https://doi.org/10.5194/bg-17-6423-2020

Schuh, A. E., & Jacobson, A. R. (2023). *Uncertainty in parameterized convection remains a key obstacle for estimating surface fluxes of carbon dioxide*. https://doi.org/10.5194/acp-23-6285-2023

Séférian, R., Delire, C., Decharme, B. et al. (2016). *Development and evaluation of CNRM Earth system model–CNRM-ESM1*. https://doi.org/10.5194/gmd-9-1423-2016

Seibt, U., Rajabi, A., Griffiths, H., & Berry, J. A. (2008). *Carbon isotopes and water use efficiency: sense and sensitivity*. https://doi.org/10.1007/s00442-007-0932-7

Sellers, P., Randall, D., Collatz, G. et al. (1996). *A revised land surface parameterization (SiB2) for atmospheric GCMs. Part I: Model formulation*. https://doi.org/10.1175/1520-0442(1996)009<0676:ARLSPF>2.0.CO;2

Sellers, P. J. (1985). *Canopy reflectance, photosynthesis and transpiration*. https://doi.org/10.1080/01431168508948283

Seo, E., & Dirmeyer, P. A. (2022). *Understanding the diurnal cycle of land–atmosphere interactions from flux site observations*. https://doi.org/10.5194/hess-26-5411-2022

Serbin, S., Meng, R., Wu, J., & Ely, K. (2019). *Ngee tropics gliht puerto rico campaign leaf spectral reflectance and transmittance march 2017*. Data set. Available online from the Ecological Spectral Information System (EcoSIS).
http://ecosis.org

Shaw, R. H., & Schumann, U. (1992). *Large-eddy simulation of turbulent flow above and within a forest*. https://doi.org/10.1007/BF02033994

Shuttleworth, W. J. (1984). *Observations of radiation exchange above and below Amazonian forest*. https://doi.org/10.1002/qj.49711046623

Shuttleworth, W. J. (1985). *Daily variations of temperature and humidity within and above Amazonian forest*. https://doi.org/10.1002/j.1477-8696.1985.tb07489.x

Shuttleworth, W. J., Leuning, R., Black, T. A. et al. (1989). *Micrometeorology of temperate and tropical forest*. https://doi.org/10.1098/rstb.1989.0050

Siebesma, A. P., Bony, S., Jakob, C., & Stevens, B. (2020). *Clouds and Warming*, (p. 356–388). Cambridge University Press.

Sikma, M., Ouwersloot, H., Pedruzo-Bagazgoitia, X. et al. (2018). *Interactions between vegetation, atmospheric turbulence and clouds under a wide range of background wind conditions*. https://doi.org/10.1016/j.agrformet.2017.07.001

Sikma, M., & Vilà-Guerau de Arellano, J. (2019). *Substantial reductions in cloud cover and moisture transport by dynamic plant responses*. https://doi.org/10.1029/2018GL081236

Sikma, M., Vilà-Guerau de Arellano, J., Pedruzo-Bagazgoitia, X. et al. (2019). *Impact of Future Warming and Enhanced [CO2] on the Vegetation-Cloud Interaction*. https://doi.org/10.1029/2019JD030717

Sterck, F. J., Duursma, R. A., Pearcy, R. W. et al. (2013). *Plasticity influencing the light compensation point offsets the specialization for light niches across shrub species in a tropical forest understorey*. https://doi.org/10.1111/1365-2745.12076

Stinziano, J. R., Morgan, P. B., Lynch, D. J. et al. (2017). *The rapid A–Ci response: photosynthesis in the phenomic era*. https://doi.org/10.1111/pce.12911

Stocker, B. D., Wang, H., Smith, N. G. et al. (2020). *P-model v1.0: an optimality-based light use efficiency model for simulating ecosystem gross primary production*. https://doi.org/10.5194/gmd-13-1545-2020

Stull, R. B. (1988). *An introduction to boundary layer meteorology*, vol. 13. Springer Science & Business Media.

Sun, Y., Fu, R., Dickinson, R. et al. (2015). *Drought onset mechanisms revealed by satellite solar-induced chlorophyll fluorescence: Insights from two contrasting extreme events*. https://doi.org/10.1002/2015JG003150

Swenson, S. C., Burns, S. P., & Lawrence, D. M. (2019). *The Impact of Biomass Heat Storage on the Canopy Energy Balance and Atmospheric Stability in the Community Land Model*. https://doi.org/10.1029/2018MS001476

Tang, H., Ganguly, S., Zhang, G. et al. (2016). *Characterizing leaf area index (LAI) and vertical foliage profile (VFP) over the United States*. https://doi.org/10.5194/bg-13-239-2016

Tennekes, H. (1973). *A model for the dynamics of the inversion above a convective boundary layer*. https://doi.org/10.1175/1520-0469(1973)030<0558:AMFTDO>2.0.CO;2

Tennekes, H., & Driedonks, A. (1981). *Basic entrainment equations for the atmospheric boundary layer*. https://doi.org/10.1007/BF00122299

ter Horst, C. G. B., Vis, G. A., Jongen-Boekee, J. et al. (2025). *An adaptable DTS-based parametric method to probe near-surface vertical temperature profiles at millimeter resolution*. https://doi.org/10.5194/amt-18-6853-2025

Thomas, C., & Foken, T. (2007). *Organised Motion in a Tall Spruce Canopy: Temporal Scales, Structure*

*Spacing and Terrain Effects*. https://doi.org/10.1007/s10546-006-9087-z

Tohjima, Y., Machida, T., Watai, T. et al. (2005). *Preparation of gravimetric standards for measurements of atmospheric oxygen and reevaluation of atmospheric oxygen concentration.*. https://doi.org/10.1029/2004JD005595

Tolk, J. A., Evett, S. R., & Howell, T. A. (2006). *Advection influences on evapotranspiration of alfalfa in a semiarid climate*. https://doi.org/10.2134/agronj2006.0031

Valladares, F., & Niinemets, Ü. (2007). *The architecture of plant crowns: from design rules to light capture and performance*, (pp. 101–150). CRC Press Boca Raton.

Van de Giesen, N., Steele-Dunne, S. C., Jansen, J. et al. (2012). *Double-Ended Calibration of Fiber-Optic Raman Spectra Distributed Temperature Sensing Data*. https://doi.org/10.3390/s120505471

van Diepen, K. H. H., Goudriaan, J., Vilà-Guerau de Arellano, J., & de Boer, H. J. (2022). *Comparison of C3 Photosynthetic Responses to Light and CO2 Predicted by the Leaf Photosynthesis Models of Farquhar et al. (1980) and Goudriaan et al. (1985)*. https://doi.org/10.1029/2021MS002976

van Diepen, K. H. H., Kaiser, E., Hartogensis, O. K. et al. (2025). *When do clouds and aerosols lead to higher canopy photosynthesis?*. https://doi.org/10.1016/j.agrformet.2025.110597

van Heerwaarden, C. C., de Arellano, J. V.-G., Gounou, A. et al. (2010). *Understanding the daily cycle of evapotranspiration: A method to quantify the influence of forcings and feedbacks*. https://doi.org/10.1175/2010JHM1272.1

van Heerwaarden, C. C., Vilà-Guerau de Arellano, J., Moene, A. F., & Holtslag, A. A. (2009). *Interactions between dry-air entrainment, surface evaporation and convective boundary-layer development*. https://doi.org/10.1002/qj.431

Van Kesteren, B., Hartogensis, O., van Dinther, D. et al. (2013). *Measuring h2o and co2 fluxes at field scales with scintillometry: Part ii – validation and application of 1-min flux estimates*. https://doi.org/10.1016/j.agrformet.2013.01.010

van Stratum, B. J., Vilà-Guerau de Arellano, J., van Heerwaarden, C. C., & Ouwersloot, H. G. (2014). *Subcloud-layer feedbacks driven by the mass flux of shallow cumulus convection over land*. https://doi.org/10.1175/JAS-D-13-0192.1

Veerman, M. A., Pedruzo-Bagazgoitia, X., Jakub, F. et al. (2020). *Three-Dimensional Radiative Effects By Shallow Cumulus Clouds on Dynamic Heterogeneities Over a Vegetated Surface*. https://doi.org/10.1029/2019MS001990

Vellinga, O. S., Dobosy, R. J., Dumas, E. J. et al. (2013). *Calibration and quality assurance of flux observations from a small research aircraft*. https://doi.org/10.1175/JTECH-D-11-00138.1

Vico, G., Manzoni, S., Palmroth, S., & Katul, G. (2011). *Effects of stomatal delays on the economics of leaf gas exchange under intermittent light regimes*. https://doi.org/10.1111/j.1469-8137.2011.03847.x

Vilà-Guerau de Arellano, J., Ney, P., Hartogensis, O. et al. (2020). *Cloudroots: integration of advanced instrumental techniques and process modelling of sub-hourly and sub-kilometre land–atmosphere interactions*. https://doi.org/10.5194/bg-17-4375-2020

Vilà-Guerau de Arellano, J., Ouwersloot, H. G., Baldocchi, D., & Jacobs, C. M. (2014). *Shallow cumulus rooted in photosynthesis*. https://doi.org/10.1002/2014GL059279

Vilà-Guerau de Arellano, J., Van Heerwaarden, C., Van Stratum, B., & Van Den Dries, K. (2015). *Atmospheric boundary layer: Integrating air chemistry and land interactions*. Cambridge University Press Cambridge.

Vilà-Guerau de Arellano, J., Gioli, B., Miglietta, F. et al. (2004). *Entrainment process of carbon dioxide in the atmospheric boundary layer*. https://doi.org/10.1029/2004JD004725

Vilà-Guerau de Arellano, J., Hartogensis, O., Benedict, I. et al. (2023). *Advancing understanding of land-atmosphere interactions by breaking discipline and scale barriers*. https://doi.org/10.1111/nyas.14956

Vilà-Guerau de Arellano, J., Hartogensis, O. K., de Boer, H. et al. (2024). *CloudRoots-Amazon22: Integrating clouds with photosynthesis by crossing scales*. https://doi.org/10.1175/BAMS-D-23-0333.1

Vilà-Guerau de Arellano, J., Koren, G., Ouwersloot, H. G. et al. (2019). *Sub-diurnal variability of the carbon dioxide and water vapor isotopologues at the field observational scale*. https://doi.org/10.1016/j.agrformet.2019.05.014

Vilà-Guerau de Arellano, J., van Heerwaarden, C. C., van Stratum, B. J. H., & van den Dries, K. (2015). *Atmospheric Boundary Layer: Integrating Air Chemistry and Land Interactions*. Cambridge University Press.

Vilà-Guerau de Arellano, J., Wang, X., Pedruzo-Bagazgoitia, X. et al. (2020). *Interactions Between the Amazonian Rainforest and Cumuli Clouds: A Large-Eddy Simulation, High-Resolution ECMWF, and Observational Intercomparison Study*. https://doi.org/10.1029/2019MS001828

Wang, B., Yue, X., Zhou, H., & Zhu, J. (2022a). *Impact of diffuse radiation on evapotranspiration and its coupling to carbon fluxes at global FLUXNET sites*. https://doi.org/10.1016/j.agrformet.2022.109006

Wang, C.-T., Campbell, P. C., Makar, P. et al. (2025). *Quantifying forest canopy shading and turbulence effects on boundary layer ozone over the United States*. https://doi.org/10.5194/acp-25-16631-2025

Wang, X., Wu, J., Chen, M. et al. (2018). *Field evidences for the positive effects of aerosols on tree growth*. https://doi.org/10.1111/gcb.14339

Wang, Y., Braghiere, R. K., Yin, Y. et al. (2024). *Beyond the visible: Accounting for ultraviolet and far-red radiation in vegetation productivity and surface energy budgets*. https://doi.org/10.1111/gcb.17346

Wang, Y., Zhang, J., Trentmann, J. et al. (2022b). *Observations and Implications of Diurnal Climatology and Trends in Direct and Diffuse Solar Radiation Over China*. https://doi.org/10.1029/2022JD036769

Wehr, R., Munger, J., McManus, J. et al. (2016). *Seasonality of temperate forest photosynthesis and daytime respiration*. https://doi.org/10.1038/nature17966

Wehr, R., Munger, J., Nelson, D. et al. (2013). *Long-term eddy covariance measurements of the isotopic composition of the ecosystem–atmosphere exchange of CO2 in a temperate forest*. https://doi.org/10.1016/j.agrformet.2013.07.002

Williams, I., Riley, W., Torn, M. et al. (2011). *Using boundary layer equilibrium to reduce uncertainties*

*in transport models and CO2 flux inversions*. https://doi.org/10.5194/acp-11-9631-2011

Williams, I. N., & Torn, M. S. (2015). *Vegetation controls on surface heat flux partitioning, and land-atmosphere coupling*. https://doi.org/10.1002/2015GL066305

Winderlich, J., Chen, H., Gerbig, C. et al. (2010). *Continuous low-maintenance $co_2$/$ch_4$/$h_2o$ measurements at the Zotino Tall Tower Observatory (ZOTTO) in Central Siberia*. https://doi.org/10.5194/amt-3-1113-2010

Wofsy, S. C., Harriss, R. C., & Kaplan, W. A. (1988). *Carbon dioxide in the atmosphere over the Amazon Basin*. https://doi.org/10.1029/JD093iD02p01377

Wu, Y., Brashers, B., Finkelstein, P. L., & Pleim, J. E. (2003). *A multilayer biochemical dry deposition model. 1. Model formulation*. https://doi.org/10.1029/2002JD002293

Xiao, H., Berg, L. K., & Huang, M. (2018). *The Impact of Surface Heterogeneities and Land-Atmosphere Interactions on Shallow Clouds Over ARM SGP Site*. https://doi.org/10.1029/2018MS001286

Xu, K., Pingintha-Durden, N., Luo, H. et al. (2019). *The eddy-covariance storage term in air: Consistent community resources improve flux measurement reliability*. https://doi.org/10.1016/j.agrformet.2019.107734

Ye, J., Batista, C. E., Zhao, T. et al. (2022). *River winds and transport of forest volatiles in the Amazonian riparian ecoregion*. https://doi.org/10.1021/acs.est.1c08460

Yi, C., Davis, K. J., Bakwin, P. S. et al. (2004). *Observed covariance between ecosystem carbon exchange and atmospheric boundary layer dynamics at a site in northern Wisconsin*. https://doi.org/10.1029/2003JD004164

Zhao, H., Dolman, H., Elbers, J. et al. (2025). *The loobos ecosystem first tower dataset: meteorology, turbulent fluxes and net ecosystem exchange (1996 to 2021)*. https://doi.org/10.5194/essd-2025-372

Zhen, S., van Iersel, M. W., & Bugbee, B. (2022). *Photosynthesis in sun and shade: the surprising importance of far-red photons*. https://doi.org/10.1111/nph.18375

# Acknowledgements

I am immensely grateful to the people who have guided and accompanied me during my PhD journey. First of all, I want to express my gratitude to Jordi and Hugo, who have given me the opportunity to initiate this journey and who have been anchors for support along the journey. Jordi, I met you during my MSc studies in Wageningen, where, as many people that know you, I was fascinated by the dynamism in which you teach the wonders of the atmospheric boundary layer. Since then, you have always been generous with me, sharing scientific challenges and projects to tackle. I am grateful to have learned from the knowledge that you have accumulated over the years but most importantly, for learning by witnessing how you carry out science in a very human and caring manner. I still cannot comprehend how you seem to multiply the hours of a day, but I am immensely grateful for your continuous guidance throughout the whole process, even if it was only ten minutes to, in your own words, 'keep the momentum'. Thanks for the opportunities, for giving importance to bring 'modelers' to field campaigns, and for your humor, which helps lighten any heavy meeting.

Hugo, I met you when applying for the PhD position, and soon after, we had the opportunity to get to know each other better in the first field campaign of the project. Thanks to you, I have learned to appreciate the complexity and beauty of vegetation and have grown interested in how plant biology communicates with atmospheric physics and chemistry. Because of that, now in my mind, the atmospheric models seem more alive. I am also grateful for your clarity of thought, which has helped me improve my scientific writing in structure and clarity. In addition, your clear explanations and practical advice have been essential on the journey. Last but not least, I am grateful for the time together in Lleida, Loobos and the Amazon, where I have experienced the thrill of field work, as well as the anecdotes that naturally emerge from field campaigns.

The topic of this dissertation is at the intersection of different scientific specializations and combines modeling efforts with observations, making collaboration fundamental. At the beginning of this project, I felt the challenge on my shoulders as a big, ambiguous, and almost intractable goal. Now, at the end, I feel this challenge, as well as future ones, to be attainable and enjoyable, thanks to the collaboration of researchers, technicians, and colleagues. During these five years, I have collaborated with a multitude of people and I am grateful to all of them. Oscar, you have been a fundamental piece in the research carried out here, bringing immense knowledge and experience in field work, providing key feedback to the work, and beyond. Mary Rose, you have also helped shaping my research through your great field work experience and the invaluable discussions we have held about LIAISE field campaign, about atmospheric turbulence, and micrometeorology in general. Robbert, you have been the other half of the CloudRoots project, sharing challenges, and I owe to you all I know about water and carbon dioxide isotopologues. I am grateful to Kim and Ingrid, for helping me understand the atmospheric oxygen dynamics and for sharing the challenge of writing a concise manuscript about

a vast topic. Menno, I am grateful to have collaborated tightly with you in the last stages of my PhD, trying to tackle together within-canopy radiation. I have learned a lot by simply trying to keep the pace of your 'speed of light' thinking and of your coding proficiency. I am grateful also to Xabi, who has handed me the relay of the multi-layer canopy model and shared with me its details in numerous online meetings. I also want to extend my gratitude to all the BSc and MSc students with whom I have collaborated - Koen, Vincent, Sebastiaan, Guido, Däniel, and Anna -, many of who have become afterward dear colleagues. Finally, to all the people that have contributed to the success of the field-campaingns and of the research presented here, such as Thomas, Getachew, David, Hella, Komi, and including the essential ATTO and INPA researchers and staff.

In general, I extend my thanks to my MAQ (Meteorology and Air Quality) colleagues and friends. During these years, I have been able to learn about the atmosphere by simply listening to high quality tea-talks, smaller group meetings, and symposiums. I am grateful for the sportive culture of the group, which has encouraged me to do a few races and even some triathlons. Above all, I am grateful to have established some friends along the way; many of them have already been mentioned. Martin, you supervised my MSc thesis and then became a colleague and a friend. You are, to me, a source of inspiration due to your knowledge, motivation, and caring way of collaborating and carrying out research. Wouter, you are to me a dear friend, my PhD started with a car trip with you to a field campaign in Spain, and during the majority of the PhD journey you have been by my side, literally and figuratively speaking, offering support from the closest office desk. Francisca, Mar and Ámbar, you are other sources of inspiration to me. I was able to witness your PhD journeys, and I am deeply impressed by how you withstand challenges, by your determination, and leadership. And finally, to all my other dear colleagues, Anh, Anne-Wil, Felipe, Santiago, Mirjam, Astrid, Jan, Kevin, Ariadna, Chiel, Wiebke, Marc, Bernard, Sarah, Thomas, Farhan, Lucas, Ewout, Mohamadreza, Marnix, Reinaart, and many others.

I am also grateful to all the people who have supported my PhD journey without necessarily knowing the technical details of my job. I particularly thank the housemates I have had along the years, who have made 101 a home for me: Lucía, Jonne, Áureo, Iacopo, Lucas, Claudia, Mo, Mellie, Nellie, Jorge, Rianne, Luca... I am fortunate for the many moments shared with you, most of them eating delicious home-made food. Among millions of reasons for my gratitude, I thank Claudia for opening the doors of 101 and for sharing with me now my beloved islands, thanks Jonne for building me stairs and making insects look like the coolest animals on Earth, Lu for your warmth and chill energy that makes me feel incredibly supported, and Áureo for being to me a sometimes annoying but always deeply loved big brother. I also thank other beloved friends and family, Arianna, Ainhoa, Sandra, Andrea, Marta, Yaiza, Candela, and Arume.

I dedicate this thesis, as any merit, to my mother, father, sister, and my extended family. To my mum, for being always there, no matter what. To my father, for letting me witness the passion for mathematics, which seems to be contagious. And to my sister, for being my biggest supporter and for warming my heart. Finally, I also dedicate this dissertation to Joost, because a breeze swiftly and recently brought you into my life, and I feel fortunate to have met you.

I am aware that these words cannot capture the gratitude that I profess towards all the people involved in this particular PhD journey and in my life. I hope, therefore, that my gratitude can extend beyond these pages and reach you all through my actions and intentions.

# List of publications

Author lists of project reference articles are shortened to *[First author] et al.*, refer to the online article for a full list.

## Articles

**González-Armas R.**, Vilà-Guerau de Arellano, J., de Boer, H. J., Pedruzo-Bagazgoitia, X. & Veerman, M. A. *Development and Evaluation of a Multi-Spectral Canopy Radiation Transfer Scheme in a Canopy-Resolving Large Eddy Simulation* [In Preparation]

**González-Armas R.**, Pedruzo-Bagazgoitia, X., de Boer, H. J., de Feiter, V., Veerman, M. A., Hartogensis, O., Dias-Júnior, C. Q., & Vilà-Guerau de Arellano, J. *Forest-Atmosphere Coupling and Boundary-Layer Processes Revealed by Canopy-Resolving Large Eddy Simulations and Observations* [In Preparation]

Huitema, A. C., de Feiter, V. S., **González-Armas, R.**, Hartogensis, O. K., van Asperen, H., Dias-Júnior, C. Q., Vilà-Guerau de Arellano, J. (2026). *$CO_2$ and heat exchange across the nocturnal canopy-atmosphere interface in the Amazon rainforest*. Atmospheric Chemistry and Physics [Submitted]. https://doi.org/10.5194/egusphere-2026-684

Faassen, K. A. P., **González-Armas, R.**, Koren, G., Adnew, A., van Asperen, H., de Boer, H. J., Botía, S., de Feiter, V. S., Hartogensis, O., Heusinkveld, B. G., Hulsman, L. M., Hutjes, R. W. A., Jones, S. P., Kers, B. A. M., Komiya, S., Machado, L. A. T., Martins, G., Miller, J. B., Mol, W., van der Molen, M., Moonen, R., Dias-Junior, C., Röckmann, T., Snellen, H., Luijkx, I. T., & Vilà-Guerau de Arellano, J. (2025). *Tracing diurnal variations of atmospheric $CO_2$, $O_2$ and $\delta^{13}CO_2$ over a tropical and a temperate rainforest*. Geophysical Research Letters. https://agupubs.onlinelibrary.wiley.com/doi/full/10.1029/2025GL118016

**González-Armas, R.**, Rikkers, D., Hartogensis, O. K., Dias-Júnior, C. Q., Komiya S., Pugliese, G., Williams, J., van Asperen, H., Vilà-Guerau de Arellano J. & de Boer, H. J. (2025). *Daytime water and $CO_2$ exchange within and above the Amazon rainforest*. Agricultural and Forest Meteorology. https://doi.org/10.1016/j.agrformet.2025.110621

Vilà-Guerau de Arellano, J. et al. (2024). *CloudRoots-Amazon22: Integrating clouds with photosynthesis by crossing scales*. Bulletin of the American Meteorological Society. https://doi.org/10.1175/bams-d-23-0333.1

Faassen K. A. P., Vilà-Guerau de Arellano J., **González-Armas, R.**, Heusinkveld B. G., Mammarella I., Peters. W., & Luijkx I. T. (2023). *Separating above-canopy $CO_2$ and $O_2$ measurements into their atmospheric and biospheric signatures*. Biogeosciences. https://doi.org/10.5194/bg-21-3015-2024

**González-Armas R.**, Vilà-Guerau de Arellano, J., Mangan M. R., Hartogensis O. K. & de Boer H. J. (2024). *Impact of canopy environmental variables on the diurnal dynamics of water and carbon dioxide exchange at leaf and canopy level*. Biogeosciences. https://doi.org/10.5194/bg-21-2425-2024

Vilà-Guerau de Arellano, J., et al. (2023). *Advancing understanding of land-atmosphere interactions by breaking discipline and scale barriers*. Annals of the New York Academy of Sciences. https://doi.org/10.1111/nyas.14956

# About the author



Raquel González Armas was born on May 2$^{nd}$ 1997 in La Laguna (Tenerife, Spain). As a kid, she was always keen on studying and learning, a reality that until today remains true. After graduating with honors in high school, she pursued a degree on Physics in the Universidad de La Laguna, in her home city in Tenerife. During the program, she enjoyed quite much the wide range of subjects as well as the mathematical challenges. Afterwards, she decided to specialize in Atmospheric Science, as she liked the idea of being able to make more tangible her study topic, as well as, for the relevance of understanding the Earth system under climate change and increasing anthropogenic influence. To accomplish this goal, she pursued her MSc studies in Wageningen University (Earth and Environment MSc, with the specialization of meteorology and air quality), of which she graduated as cum laude. During the last months of her MSc, she received the opportunity to pursue a PhD, whose result is this dissertation.

During her PhD, she was part of field campaigns on different areas, on the Iberian Peninsula in an heterogeneous area marked by high irrigation contrast, on a temperate forest, and on the Amazon tropical forest. She deepened in her knowledge of the atmospheric boundary layer and on land-atmospheric interactions, as well as, on the value of integrating modeling approaches with observational datasets. The PhD journey also trained her to teach in a wide range of settings - participating in lectures, supporting courses, and supervising student research projects - and to comunicate science via written manuscripts and oral presentations.

Her thirst of understanding is not confined to Earth System Science. In general, Raquel has great pleasure while learning. She enjoys reading from a variety of topics - philosophy essays, classical literature, books about society, nature and human relationships, or science-fiction -, as she understand reading as a gentle way of accessing the mind of the writer, and experiencing the world with a new sight. She enjoys contemplative activities, crafting - such as knitting, crocheting, and making macrame pieces -, and any kind of activity that involves movement - such as hiking, swimming, running, dancing, climbing, stretching, or strength training.

She enjoys sharing time with people and have a deep interest in understanding the human experience and relationships, as well as the way in which nurturing communities are built and maintained. Finally, she is interested in social justice and in how we can remain hopeful, caring, and creative under challenging structural situations.

*Netherlands Research School for the*
*Socio-Economic and Natural Sciences of the Environment*

# D I P L O M A

***for specialised PhD training***

The Netherlands research school for the
Socio-Economic and Natural Sciences of the Environment
(SENSE) declares that

## *Raquel González Armas*

born on 2 May 1997 in San Cristóbal de La Laguna, Santa Cruz de Tenerife, Spain

has successfully fulfilled all requirements of the
educational PhD programme of SENSE.

Wageningen, 1 July 2026

SENSE coordinator PhD education

Dr Ir Peter Vermeulen

The SENSE Director

Dr Jampel Dell'Angelo

The SENSE Research School declares that **Raquel González Armas** has successfully fulfilled all requirements of the educational PhD programme of SENSE with a work load of 40.2 EC, including the following activities:

## Academic knowledge and skills

| | |
|---|---|
| o Writing the PhD project proposal | |
| o Attending the Buys Ballot Research School Autumn Symposium (2021, 2022,2024) | Institute of Marine and Atmospheric Research Utrecht |
| o Big data exploration and object-oriented programming with Python (2024) | WIMEK |
| o Scientific writing (2024) | Wageningen Graduate Schools |
| o Peer review of a journal manuscript (2022) | |
| o Oral presentation: Water and carbon turbulent land-atmospheric exchange across scales: from leaf to canopy field scale (2023) | First LIAISE conference and determining evapotranspiration crosscut workshop |
| o Oral presentation: On the impact of leaf-level processes on the water and carbon canopy-turbulent fluxes (2023) | European Geosciences Union General Assembly 2023 |
| o Oral presentation: Vertical Variability in Leaf Traits and Environmental Conditions: Implications for Evapotranspiration and Net Ecosystem Exchange above the Amazon Rainforest (2024) | European Geosciences Union General Assembly 2024 |
| o Oral presentation: Moisture and Carbon Dioxide Turbulent Exchange within and above the Amazon Rainforest: a Multi-layer Modelling and Observational Perspective (2025) | 25th Conference on Boundary Layers and Turbulence |

## Transferable Professional Skills

| | |
|---|---|
| o A1: introduction to personal leadership in your PhD (2022) | SENSE |

## Societal impact

- o A2: Organising a two day course 'Land-atmosphere interactions' in Manaus (2025)
- o Writing a blog of Cloudroots-Amazon22 Field campaign and participating in CloudRoots-Amazon22 Field campaign video (2022)
- o Supervising 1 BSc and 2 MSC students with thesis (2022-2025)
- o Lecturing in the BSc/MSc course 'Clouds in a present and changing climate'(2025)

## Career perspectives

| | |
|---|---|
| o Basic Dutch 2 (2024) | Wageningen In'to Languages |

- o Participation in LIAISE Field Campaign (2021) and CloudRoots22-Loobos Field Campaign (2022)
- o Participation in DALES developer meeting (2025)
- o Participation in Boundary layer and Turbulence meetings (2025) and ATTO seminar (2025)

The presented research received funding from the Dutch Research Council (NWO) project *CloudRoots - Clouds rooted in a heterogeneous biosphere* (project no. OCENW.KLEIN.407)

Financial support from Wageningen University for printing this thesis is gratefully ackowledged.

Cover design by Emily Matena
Printed by ProefschriftMaken

